From a rough flow to experiments : a path towards probing spontaneous stochasticity

Antoine Barlet

THESE DE DOCTORAT

NNT : 2024UPASP104

From a rough flow to experiments: a path towards probing spontaneous stochasticity

D'un écoulement irrégulier aux expériences : un chemin vers la mesure de la stochasticité spontanée

Thèse de doctorat de l'université Paris-Saclay et de l'Instituto de Matemática Pura e Aplicada (IMPA)

École doctorale n° 564, Physique en île-De-France (EDPIF)
Spécialité de doctorat : Physique
Graduate School : Physique. Référent : Faculté des sciences d'Orsay

Thèse préparée dans les unités de recherche **SPEC** (Université Paris-Saclay, CEA, CNRS) et l'**Instituto Nacional de Matemática Pura e Aplicada** (IMPA), sous la direction de **François DAVIAUD**, directeur de recherche, la co-direction d'**Alexei MAILYBAEV**, directeur de recherche, et le co-encadrement d'**Adam CHEMINET**, ingénieur CEA

Thèse soutenue à Paris-Saclay, le 11 Octobre 2024, par

Antoine BARLET

Composition du jury

Membres du jury avec voix délibérative

Caroline NORE Professeure, Université Paris-Saclay	Présidente
Jérémie BEC Directeur de recherche, INRIA Sophia Antipolis	Rapporteur & Examinateur
Théodore DRIVAS Maître de conférences, Stony Brooks University	Rapporteur & Examinateur
Khadim MBACKE WAR Professeur, IMPA	Examinateur
Étienne MÉMIN Directeur de recherche, INRIA Rennes	Examinateur
Laure SAINT-RAYMOND Directrice de recherche, CNRS	Examinatrice

université PARIS-SACLAY | ÉCOLE DOCTORALE Physique en Île-de-France (PIF)

Titre : D'un écoulement irrégulier aux expériences : un chemin vers la mesure de la stochasticité spontanée

Mots clés : stochasticité spontanée, singularités, transport turbulent, anomalie de dissipation

Résumé : Les systèmes chaotiques sont caractérisés par une séparation exponentielle des paires de particules. C'est en outre cette propriété qui rend ces systèmes imprédictibles sur une fenêtre de temps infinie. Pour autant, il est certain que ce phénomène n'est pas à l'origine du caractère aléatoire de la turbulence. On observe en effet que les paires de particules en expérience se séparent de manière algébrique, suivant une loi cubique indépendante de la séparation initiale. Ce régime, dit de Richardson, suggère que la stochasticité devrait arriver en un temps fini, contrairement à ce qui est observé dans le chaos. Ce phénomène est intitulé « stochasticité spontanée » et tient sa source du caractère irrégulier de la dynamique sous-jacente. C'est en tout cas un candidat théorique qui pourrait expliquer la nature aléatoire de la turbulence elle-même. Alors que la stochasticité spontanée est bien formalisée dans des modèles simplifiés, il n'existe pas à ce jour de procédure ou d'outils précis qui pourraient quantifier efficacement ce phénomène.

Dans cette thèse, nous nous intéressons à un écoulement 3d irrégulier, inspiré de la fonction de Weierstrass, intitulé « modèle WABC ». On montre que des trajectoires lagrangienne possèdent une dispersion en temps finie même dans la limite de dispersion initiale infinitésimale. Cette observation directe de la stochasticité spontanée est néanmoins impossible à mettre en place dans les écoulements réels à cause des contraintes numériques ou expérimentales. Inspiré de notre modèle, nous proposons un critère basé sur les probabilités de transition pour mesurer en pratique la stochasticité spontanée dans les écoulements réels. On vérifie dans un premier temps si ce critère est bien sensible à ce phénomène dans le modèle WABC. On l'applique enfin à des données expérimentales où des résultats préliminaires mettent en évidence des traces de stochasticité spontanée.

université PARIS-SACLAY

ÉCOLE DOCTORALE
Physique en
Île-de-France (PIF)

Title: From a rough flow to experiments: a path towards probing spontaneous stochasticity

Keywords: spontaneous stochasticity, singularities, turbulent transport, anomalous dissipation

Abstract: Chaotic systems are characterised by exponential separation between close-by trajectories, which in particular leads to deterministic unpredictability over an infinite time-window. It is now believed, that such butterfly effect is not fully relevant to account for the type of randomness observed in turbulence. For example, tracers in homogeneous isotropic flows are observed to separate algebraically, following a universal cubic growth, independent from the initial separation. This regime, known as Richardon's regime, suggests that at the level of trajectories, and unlike in chaos theory, randomness may in fact emerge in finite-time. This phenomenon called 'spontaneous stochasticity' originates from the singular nature of the underlying dynamics, and provides a candidate framework for turbulent randomness and transport. While spontaneous stochasticity has been mathematically formalised in simplified turbulence models , a precise and systematic tool for quantifying the various facets of this phenomenon is to this day missing.

We introduce in this thesis a 3d rough flow inspired by the Weierstrass function, entitled 'the WABC model'. We show that Lagrangian trajectories in this model have a finite-time dispersion, even in the limit of infinitesimal initial dispersion. This direct observation of spontaneous stochasticity is impossible to perform in real flows due to numerical or experimental constraints. To circumvent this technical issue, we adapt the definition of spontaneous stochasticity in our model to create a criterion based on transition probabilities. We show that this criterion is more suited for the analysis of real flows. We verify its sensibility to spontaneous stochasticity in the WABC model. This criterion is then applied on experimental data, where preliminary results tend to highlight traces of spontaneous stochasticity.

À Manou, mon étoile.

Acknowledgments

Un voyage entre deux pays, entre deux domaines commence nécessairement par une singularité. Je voudrais ainsi remercier en premier lieu Bérengère Dubrulle pour son expérience à gérer les étudiants stochastiques et surtout pour m'avoir donné l'opportunité de poursuivre mes rêves d'aventures. Cette intense partie de ma vie aurait pu mal finir sans une bonne régularisation. Je remercie tout particulièrement Adam Cheminet qui a cru dans mes idées, dans mes dynamiques. Son soutien inébranlable a été déterminant, surtout quand on est loin de ses conditions initiales. Merci infiniment. Je voudrais également remercier Simon Thalabard avec qui j'ai créé beaucoup d'entropie. C'est toujours un plaisir d'échanger avec toi et j'espère que nos discussions perdureront.

Ce travail n'aurait pas pu être possible sans le soutien additionnel de François Daviaud qui a su redresser certaines trajectoires un peu perdues. Je remercie également Alexei Mailybaev pour les discussions intéressantes que nous avons eu.

I particularly thank my two reviewers Jérémie Bec and Théodore Drivas. They kindly accepted to review my work, and brought, each, their own interesting expertise to this complex subject that is spontaneous stochasticity. The questions they raised are still haunting me, and I hope I have the chance someday to continue debating about those. I cannot avoid mentioning the other members of the jury who were kind enough to follow a bit of my adventure and with whom I had very interesting discussions along the way: Caroline Nore, Khadim War, Laure Saint-Raymond and Etienne Mémin. Thank you very much to all of you.

Mon voyage a commencé de manière déterministe en France dans l'équipe du Sphynx. Dans le chaos qu'est la thèse, il est bon de se savoir écouté et soutenu. Je voudrais particulièrement remercier François Ladieu pour sa patience, son écoute et les mots doux qui peuvent résonner chez un étudiant à la dérive. Je ne peux également oublier les deux cartographes de ma thèse qui m'ont accompagné : Sébastien Aumaitre et Romain Monchaux. Merci pour votre soutien et pour les beaux échanges que nous avons eu.

Avoir un pied en physique et l'autre en mathématiques n'est pas de tout repos. En particulier quand on oscille également entre l'expérience et la théorie. Mais j'ai eu la chance à Saclay d'être entouré de personnes talentueuses dans ces deux domaines. Je remercie d'abord Ben, Jean, Marceau et Marco avec qui j'ai eu de passionnantes discussions sur leurs expériences respectives. Mes pensées vont aussi au groupe des « log-lattice », qui m'ont accueilli dans leurs aventures « tchoupesques »: Abhishek, Adrien, Amaury, Guillaume, Lucas.

Ce travail n'aurait pu voir le jour sans l'aide de Vincent (pour l'expérience), Claude (pour l'informatique) et surtout Cécile (pour tout). Leur expérience fut précieuse et je vous remercie tous de votre patience avec moi.

Enfin je souhaite remercier tous les autres membres du Sphynx. Ces deux ans passés avec vous furent riches et j'ai eu vraiment beaucoup de plaisir à échanger avec chacun d'entre vous. D'abord avec mes co-thésards et post-docs : Alexandre, Éden, Émile, Enzo,

Gabriel, Julie, Laura, Michael, Murukesh, Pricille, Romain, Sumeja, Thibault, Tiago et Xiaolong. Je remercie aussi tous les chercheurs permanents qui m'ont toujours réservé un accueil exceptionnel : Caroline, Cindy, Daniel, Hervé, Hugues, Laure, Sawako (Saco), Thuy et Vadim. Merci à tous, sincèrement. Pour finir, je tiens à remercier personnellement René pour ses précieux enseignements qui me poursuivront, certainement à vie.

When arriving in Rio, I really started to understand how different spontaneous stochasticity was from chaos. Because while everything was deterministic in France, in Brazil it is most of the times quite stochastic (at low scales). Fortunately, I have been very well supported from the very beginning. Aos meus amigos brasileiros: foi um imenso prazer de encontrar vocês. Eu não tenho os palavras para descrever os sentimentos que eu sentei durante o meu viaje no Rio. Particularmente, muito obrigado aos Marlon, Júlia y Arthur. Muito obrigado para tudo y especialmente pra ajuda que vocês me deu quando eu fiquei lá, perdido. Y para todas as experiências incríveis que eu vivei com vocês, muito obrigado a: Andersen, André, Antoinette, 'Berto', Breino, Bruno (os dois), Ciro, Emerson, Hugo, Iago, Ivan, Karl, Sergei, Txai, Yangrui, Yulia y Zhifey.

Muito obrigado também a Sérgio para a ajuda com o serviços informáticos do IMPA. Obrigado ao IMPA em geral, que fui muito implicado em o sucesso da minha particular tese!

Je souhaite remercier enfin mes parents et ma sœur pour tout le soutien qu'ils m'ont fourni malgré la distance (réelle et de nos domaines). J'ai également une pensée pour mon amie Ada qui s'est donnée corps et âme à la relecture de mon manuscrit. Je sais que les périodes sont difficiles pour toi, mais je te remercie du fond du cœur pour ce que tu es. Je remercie Quentin d'avoir tenté de sauver une troupe de théâtre en perdition. En espérant qu'elle te soutiendra en retour pour cette troisième et dernière année de thèse. Une pensée va également à mes chers amis Nicolas, mes "partner in crimes". Merci à vous deux pour ces belles amitiés qui m'animent sincèrement.

Je tiens enfin à remercier Damien Geneste, mon ex co-bureau mais néanmoins ami. Je ne peux oublier ces précieux échanges que nous avons eu, et je te suis reconnaissant pour toutes les choses que tu m'as apporté pour m'en sortir durant ces trois ans. Merci, vraiment.

Mes derniers mots vont à ma chère Alexandrine. Ta présence à mes côtés me rassure, me guide et m'élève. Merci pour ce que tu es et puissent nos chemins continuer de s'entrelacer tendrement.

Contents

Preamble

In 'Essai philosophique sur les probabilités', published in 1814, Pierre Simon de Laplace wrote: *'Une intelligence qui pour un instant donné, connaîtrait toutes les forces dont la nature est animée, et la situation respective des êtres qui la composent, si d'ailleurs elle était assez vaste pour soumettre ces données à l'analyse, embrasserait dans la même formule les mouvements des plus grands corps de l'univers et ceux du plus léger atome : rien ne serait incertain pour elle, et l'avenir comme le passé, serait présent à ses yeux.'*. For the large majority of scientists (like Laplace) of the time, physics was deterministic: one cause could only lead to a single consequence. And as Laplace puts it: if we knew every single forces in the universe, we would be able to predict exactly its whole evolution, in all its details.

However, this perspective started to crackle when Brown observed in 1827 some random rough movements of pollen grains. Thanks to some physicists such as Einstein, we understood that those erratic dynamics could be formally explained by statistical tools. He particularly thought that this movement was due to the collisions of molecules on the grain. But at its core, nothing was considered to be truly stochastic: the dynamics of the molecules was simply way too complex to comprehend with deterministic tools.

The final blow to determinism as a global paradigm was given by the emergence of quantum mechanics. In this theory, statistics were elevated to the foundation of physics at infinitely small scales. Physicists started to split, as some of them, like Bohr, considered that this theory was proof of our incapacity of predicting the laws of Nature with an infinite precision. Some others, like Einstein, still thought that this was just a theory and that the world could not be intrinsically stochastic. This point of view was challenged in the 60s when J. Bell enunciated a theorem that would prove, whether some hidden variables, characteristic of a missing deterministic understanding, could be unveiled. And in 1982, a brilliant experiment lead by A. Aspect proved that Bell's inequalities were not respected, shattering the last hopes promised by determinism[1].

Quantum mechanics represent the exception though, as it only accounts for the dynamics at the infinitely small scales, and, quantum noise appears to be totally negligible at a macroscopic level (at least in full generality). For a long time, researchers agreed that the complexity of systems is at the core of their unpredictability. Especially, chaos theory showed that in some deterministic systems a slight perturbation could lead to very different dynamics. The unpredictability of turbulence, for instance, appeared for a long time as our failure to solve its complex dynamics with great accuracy.

This last statement got challenged however by E. Lorenz in 1969, when he conjectured that some too complex systems can show some extreme amplification of a small perturbation. He presented what he called the 'butterfly effect' and this phenomenon got confused with chaos for a long time. We now know that it is stronger than chaos as even an infinitesimal noise could lead to completely different dynamics in a finite-time [67]. This 'real butterfly effect' is concerning since, with the amplification of the quantum noise, some macroscopic phenomenons (as climate) could truly be unpredictable by nature.

[1] A brief review of the history of unpredictability in physics can be found in an interesting paper by F. Ladieu [58].

In this thesis, we explore Lorenz' statement and question if this 'real butterfly effect' could occur in turbulence. We build a simple model of a flow reproducing Lorenz' observations in order to understand what this phenomenon, named 'spontaneous stochasticity', is about. The approach that we adopt in this thesis is to experimentally observe and analyse such phenomenon. To this aim, we use the above model as a source of inspiration to create a criterion to investigate spontaneous stochasticity in experimental turbulence. We mainly try to extend what has been explored theoretically so far to probe this phenomenon in real flows.

After an introduction of unpredictability in turbulence in chapter 1, we introduce in chapter 2 the main ingredient of spontaneous stochasticity: irregularities. We then describe the phenomenon in chapter 3, in order to analyse what is at its core. This detailed description allows us to build a model of a flow that exhibits spontaneous stochasticity, presented in chapter 4. We also give some of its important features, especially about turbulent transport. The definition of spontaneous stochasticity in this model is presented in chapter 5. We also analyse this definition and create our experimental criterion, called the 'transition deviation criterion'. It exploits the possible link that spontaneous stochasticity has with the anomalous dissipation that can be observed in turbulence. After describing in chapter 6 the mathematical tools that we used, we check numerically the presence of spontaneous stochasticity in our model. This is done in chapter 7, where we also test how our criterion performs in this model. Finally, chapter 8 gives some insights regarding the use of the transition deviation criterion in experimental data. While this study is incomplete, it gives a proof of concept for investigating spontaneous stochasticity in experiments.

Part I

From unpredictability to spontaneous stochasticity

1 - Unpredictability of turbulence

For more than 200 years, physicists have been trying to predict turbulent flows. And yet, we are still unable to forecast with high certainty the weather after a few days. This comes as a surprise since we know the exact deterministic equations of motions for fluids, which are the Navier-Stokes equations

$$\frac{\partial \boldsymbol{u}}{\partial t} + (\boldsymbol{u}.\nabla)\boldsymbol{u} = -\frac{1}{\rho}\nabla P + \nu\Delta\boldsymbol{u} + \boldsymbol{F}. \tag{1.1}$$

In this thesis, we suppose that the fluid is incompressible (preserving the volume)

$$\nabla.\boldsymbol{u} = 0. \tag{1.2}$$

Equations (1.1) with this added condition are called the 'incompressible Navier-Stokes equations' (INSE). Those equations describe the evolution of the velocity field $\boldsymbol{u}$ in time and space, when there is an external forcing $\boldsymbol{F}$ that continuously injects energy. The injected energy is then dissipated by viscosity ν at the smallest scales.

An example of a flow slice is presented in Figure 1.1. We observe that a turbulent flow: 1. is made of global structures, 2. involves different scales (see for instance the small structures in the inset), 3. seems random or 'chaotic'. Taking into account all of those features is the main challenge when it comes to weather forecasting for instance.

In the end, what is really at the origin of unpredictability in turbulence? In this chapter, we will explore this question by first defining the concept of chaos from dynamical systems theory. We will observe that chaos is not the driving factor in the apparent stochasticity of turbulence. The latter will then be broached, exploring the influence of thermal noise on the macroscopic dynamics. We will particularly see that the underlying process is more complex than expected, implying intermittency and potential singular events.

1.1 . Chaos and turbulence

1.1.1 . Dynamical systems

Definition – In the following, we call a smooth dynamical system, any dynamics governed by the differential equation

$$\dot{\boldsymbol{x}} = \boldsymbol{f}(\boldsymbol{x}(t)), \tag{1.3}$$

where $\boldsymbol{f}$ is a $\mathcal{C}^1(\mathbb{R}^{d+1})$ function, d being the dimension of space. We also introduce the notion of continuous maps $\boldsymbol{\Phi}_t$ as the morphisms, such as $\boldsymbol{x}(t) = \boldsymbol{\Phi}_t(\boldsymbol{x}_0)$, where $\boldsymbol{x}(t)$ is solution of equation (1.3) with $\boldsymbol{x}_0$ the associated initial position. We also call those maps 'flows'.

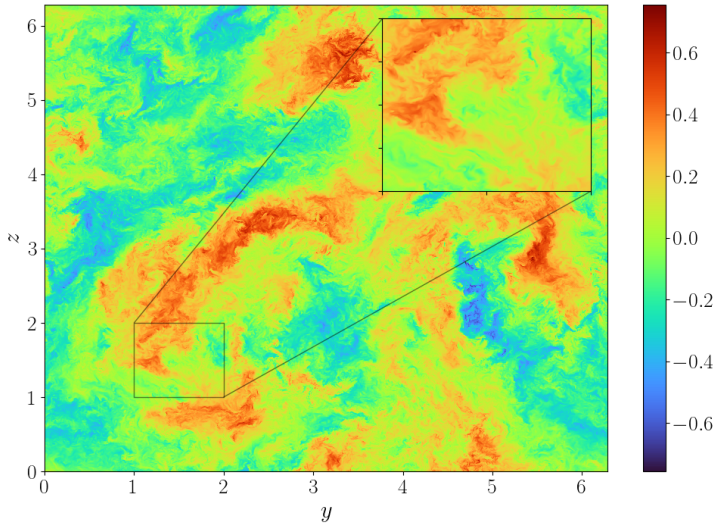

Figure 1.1: Slice across the x-axis of a turbulent velocity field. This was made from a numerical simulation by Bitane et al. [6]. One can notice that turbulence is a multi-scale phenomenon, implying structures over a wide range of scales.

Attractors and chaos – Particles can get trapped in certain regions of phase-space. They could stop at a point, called a sink, or start having a periodic movement. We call those areas 'attractors' since the orbit stays in this subspace for some long-enough time[1]. The trapped trajectories are robust: a small perturbation is generally not sufficient to make the particle escape.

In some cases, the trapped trajectories can have a more complex and unpredictable movement. We call those 'strange attractors'[73, 32] . As an example, we introduce the Lorenz 63 system as

$$\begin{cases} \frac{dx}{dt} = \sigma(y - x) \\ \frac{dy}{dt} = \rho x - y - xz \\ \frac{dz}{dt} = xy - \beta z. \end{cases} \tag{1.4}$$

This system has some fixed points, especially sinks, for many values of the parameters. But some of them, like $(\sigma, \rho, \beta) = (16, 45.92, 4)$, exhibit a non-trivial attractor. This is depicted in Figure 1.2 which represents a trajectory in this 'butterfly' attractor tracked for a very long time. The unpredictability here lies in the impossibility to predict when the tracked particle will switch from one 'wing' of the attractor to another.

Such unpredictability is a signature of chaos. This phenomenon is characterised by the loss of information about the long-term past. For long enough times, those systems appear to behave randomly. This apparent randomness should not be confused with

[1]Some more precise mathematical definition can be found in [32, 83]. We here only give a phenomenological one.

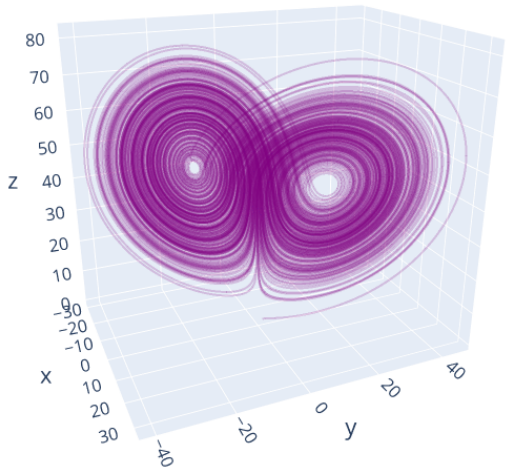

Figure 1.2: The Lorenz 63 strange attractor. We represent here the tracking of a single particle in time. Trajectories are trapped in this particular subspace. We also note that it is impossible to predict when a particle will switch from one 'wing' to another. This is what we call 'chaos'.

true stochastic processes. In fact, the randomness here is only apparent since from one initial condition, there exists only one possible outcome (being a consequence of Cauchy's theorem for smooth differential equations). Many simple systems exhibit great complexity due to chaos (double pendulum, three-body problem, etc...).

Poincaré maps – In practice, it is often difficult to tell if a system is chaotic or not. A qualitative evaluation is however possible through the analysis of Poincaré maps. Consider a $3d$ trajectory represented by the points $(x_p(t),\, y_p(t),\, z_p(t))$ for a given dynamical system (the Lorenz63 model for instance). Then, pick a cut axis and position, for example $z_c = 1$. We can then obtain a set of points such that

$$\mathcal{P}_s = \{(x_p(t_i),\, y_p(t_i)) \mid z_p(t_i) = z_c\}. \tag{1.5}$$

This corresponds to plotting a point on a x-y slice where the trajectory hits $z_p(t) = z_c$. In the attractors, the trajectory has a coherent movement which translates into a coherent structure in the Poincaré map. Scarcer points show places where the trajectory explores this phase-space area only for a few times. This is often a signature of chaos, since small perturbations of the system can quickly lead to extreme changes of behaviours.

We present in Figure 1.3, an example of a Poincaré map in the Lorenz 63 system. They represent sections of the butterfly observed in Figure 1.2. There are less streamlines near $x = 0$ and $y = 0$. A particle coming from one of the butterfly's wings can spontaneously be attracted by the other wing of the attractor. The few dots on the bottom of the x-z

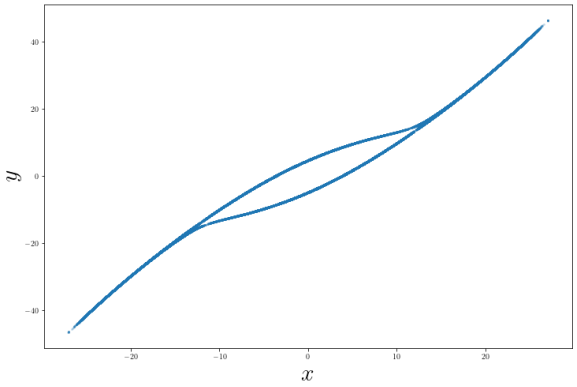

(a) x-y section with $z = 41$

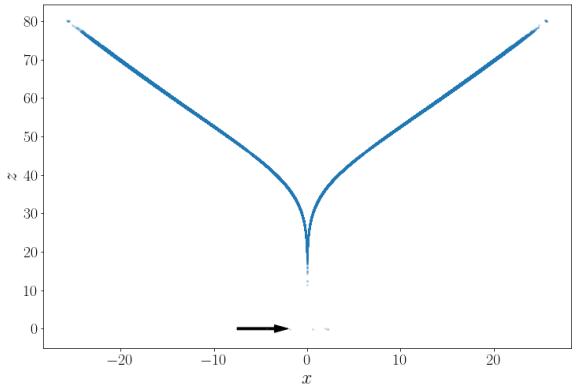

(b) x-z section with $y = 0$

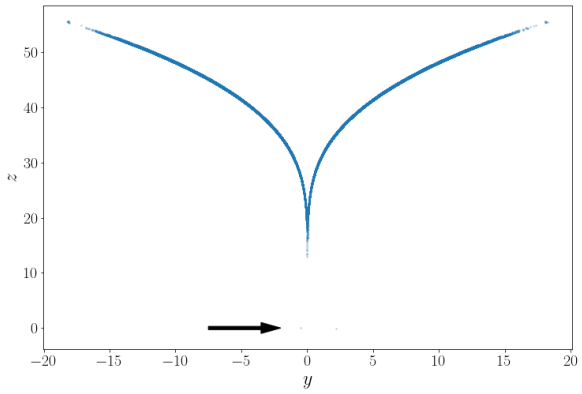

(c) x-y section with $x = 0$

Figure 1.3: Poincaré sections of the Lorenz 63 system given in equations (1.4). The black arrows indicate the points where the trajectories suddenly change wings, symbol of chaos. A total of 20 particles were used to simulate the streamlines here.

and y-z sections show this very chaotic behaviour (indicated by the black arrows on the figures).

1.1.2 . Lyapunov dispersion

The exponential amplification of small initial perturbations is a very important consequence of chaos. This phenomenon is called here 'Lyapunov dispersion'.

Definition – Considering a perturbation around a reference trajectory $\boldsymbol{x} = \boldsymbol{x}_p + \boldsymbol{\delta x}$, we obtain the linearised version of equation (1.3) such as:

$$\dot{\delta x_i} = \delta x_j \, J_i^j(\boldsymbol{x}_p(t)), \tag{1.6}$$

where $J_i^j(\boldsymbol{x}_p(t)) = \partial_j f_i(\boldsymbol{x}_p(t))$ is the Jacobian of the system evaluated at $\boldsymbol{x}_p$. The exponential evolution of such perturbation at large times is prescribed by its maximum global growth rate called 'Lyapunov exponent':

$$\lambda \doteq \lim_{t\to\infty} \frac{1}{t} \log \frac{||\boldsymbol{\delta x}(t)||}{||\boldsymbol{\delta x}(0)||} \tag{1.7}$$

By the Oseledets theorem, this coefficient exists and depends on the initial position [72]. In practice, it gives the average rate of separation of two particles. If we consider two particles $\boldsymbol{x}_1(t)$ and $\boldsymbol{x}_2(t)$ initially separated by $D_0 \doteq ||\boldsymbol{x}_2(0) - \boldsymbol{x}_1(0)||$, then their separation at time t is given by

$$D(t) \doteq ||\boldsymbol{x}_2(t) - \boldsymbol{x}_1(t)|| = D_0\, e^{\lambda t}. \tag{1.8}$$

In the following, we will refer to this phenomenon as 'Lyapunov dispersion'. As an example, we give in Figure 1.4 the evolution of $\delta x(t)$ as a function of t for the Lorenz 63 system. We observe that on average, the pair dispersion has an exponential increase with time.

Instantaneous Lyapunov exponent – In practice, a dynamical system can have several attractors. As a consequence, trajectories can jump from one onto another. The infinite time limit seems therefore hard to reach since the tracked trajectory needs to stay in the same attractor during the whole measurement. A way to circumvent this difficulty is to define the 'instantaneous Lyapunov Exponent' (iLE), which corresponds to the short-time counterpart of the regular Lyapunov exponent. It is defined as:

$$\lambda^i(t) \doteq \frac{\partial}{\partial t}\left[\log \frac{||\boldsymbol{\delta x}(t)||}{||\boldsymbol{\delta x}(0)||}\right] \tag{1.9}$$

The Lyapunov exponent can therefore be understood as the time average of the iLE for trajectories remaining in the same attractor:

$$\lambda = \lim_{t\to\infty} \frac{1}{t} \int_0^t \lambda^i(t')\, dt'. \tag{1.10}$$

As for the Lyapunov exponent, the iLE characterises the instantaneous dispersion rate of pairs of particles at time t:

$$D(t+dt) \underset{dt\to 0}{=} D(t) e^{\lambda^i(t)t} \tag{1.11}$$

1.1.3 . Is turbulence chaotic?

Observations – From the above conclusions about chaos and Lyapunov dispersion, we observe that chaos does not rule turbulence. This is illustrated in Figure 1.4, showing the time evolution of pair dispersion in a turbulent flow. We notice two main differences with the Lorenz 63 system:

- Pair dispersion in turbulence does not depend on initial position any more after some characteristic time.
- The growth rate of the separation does not correspond to an exponential amplification, but to an algebraic t^3 law.

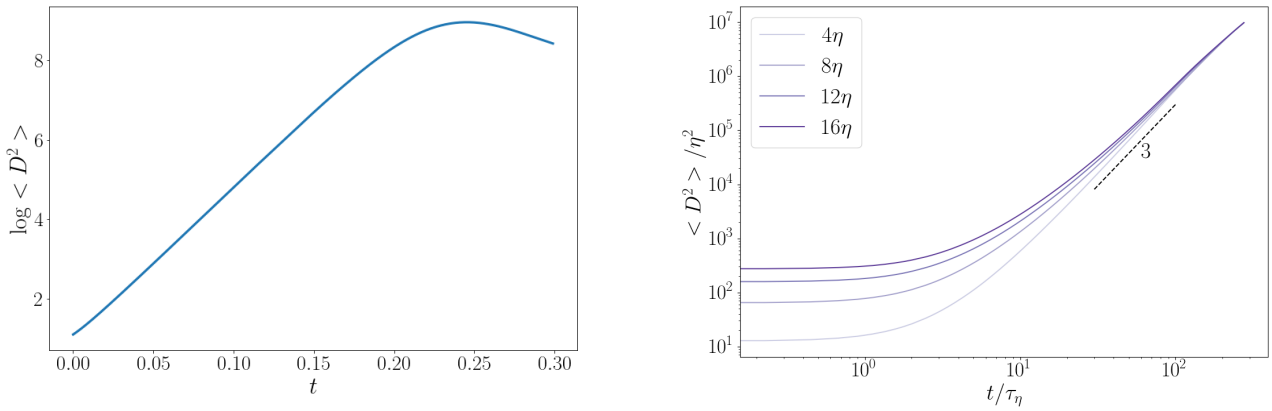

Figure 1.4: Evolution of average square pair dispersion $< D^2 >$ as a function of time for the Lorenz 63 system (Left) and a turbulent simulation [6] (Right). We observe that the Lyapunov dispersion is driving the chaotic system. However turbulence seems to show a regime that: 1. is not exponential, 2. do not seem to depend on initial separation. This underlines that this regime (Richardson) cannot be explained by chaos only.

Historical context – The algebraic regime was first observed by Richardson in 1926 [71] for atmospheric tracers. This regime was later refined by Batchelor [10] who proved that Richardson's regime should emerge after a characteristic time t_B (Batchelor's time) that depends on initial separation and average dissipation in the flow. The Batchelor regime happening before that time is highly dependent on initial dispersion and shows a t^2 law. This regime would be much closer to Lyapunov dispersion in the case of an infinitesimal t.

1.2 . Stochasticity in turbulence

1.2.1 . Stochasticity and unpredictability

Introduction to stochasticity – It appears that chaos is not the main driving phenomenon in turbulence. If so, what is at the origin of unpredictability in turbulence? To get a grasp of it, let us compare a turbulent signal with a chaotic (Lorenz 63) and a stochastic one (Brownian motion). The turbulent signal is obtained from hot-wire measurements in a wind tunnel [13]. We show those three time series in Figure 1.5.

We first observe that, macroscopically, the turbulent signal seems to be closer to a Brownian motion. In contrast, the chaotic signal seems to be too regular: microscopic fluctuations are totally absent (by construction) from the observed signal. Whether turbulence is a real stochastic process or a more complex system than chaos, the use of stochastic tools seems suited.

In addition, turbulence is a multi-scale phenomenon. We can observe this property in the pair dispersion curve, since we can distinguish two regimes (low times and large

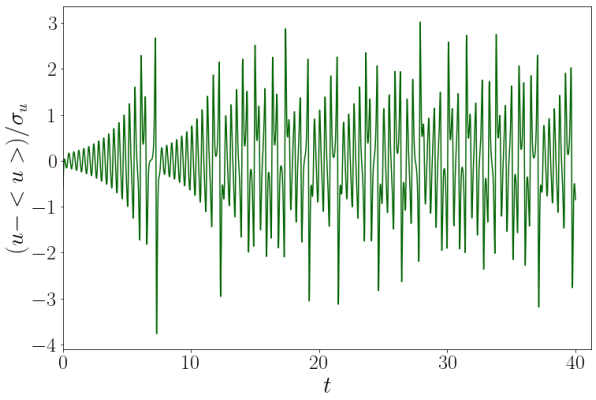

(a) Lorenz 63

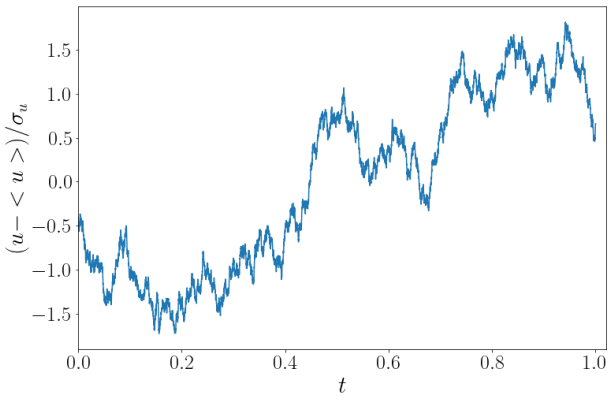

(b) Brownian motion

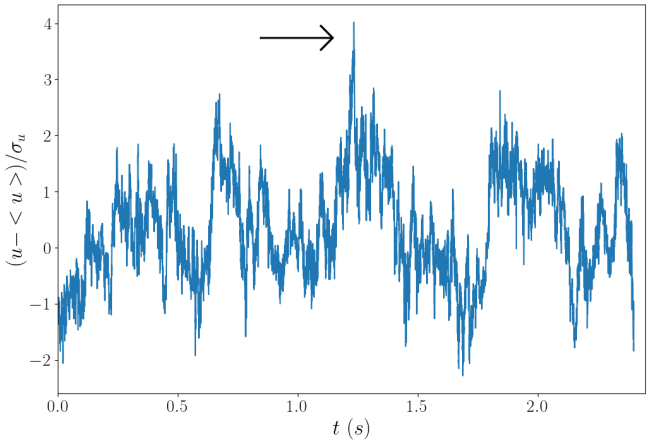

(c) Hot-Wire measurement

Figure 1.5: Comparison of time series from different types of processes, centred and normalised by their standard deviation σ: a chaotic one (Lorenz 63), a purely stochastic one (Brownian motion) and an experimental measurement (with a hot-wire) of a turbulent velocity field (data from Modane experiment [13]). On this last one is represented an arrow pointing at a burst of velocity, characteristic in turbulence which is intermittent.

times). The hot-wire signal given in Figure 1.5 also shows both microscopic fluctuations (i.e the fast changing velocities) and larger macroscopic changes.

Self-similarity and intermittency – The fluctuations are however not uniform across the scales since at time $t = 1.2s$ a larger perturbation arises, driving the system towards 4σ. We say that turbulence is not 'self-similar', in the sense that zooming in the dynamics does not lead to exactly the same system.

To quantify such deviations, let us consider a turbulent flow from the perspective of Euler (i.e. we follow the flow itself and not the particles). We build below the longitudinal structure functions as

$$S_p^{\parallel}(\boldsymbol{r}) = \left\langle (u_{\parallel}(\boldsymbol{x}+\boldsymbol{r},t) - u_{\parallel}(\boldsymbol{x},t))^p \right\rangle \tag{1.12}$$

where the $< . >$ symbol refers to a spatial average and $u_{\parallel} = \boldsymbol{u}.\frac{\boldsymbol{r}}{||\boldsymbol{r}||_2}$. One can also define the structure functions in the transversal direction, that we note S_p^T. In case of a self-similar process, we should expect $S_p \sim r^{\beta p}$ for both types, which was first derived by Kolmogorov in 1941 [56]. However, experimental measurements (see Figure 1.6) tend to show that

$$S_p(r) \sim r^{\zeta(p)}, \tag{1.13}$$

where approximately $\zeta(p) = \alpha p^2 + \beta p + \gamma$ with $\alpha \neq 0$. Such deviation from self-similar behaviour is called intermittency, as it is connected with intermittent 'burst' of fluctuations in the velocity signal.

1.2.2 . Thermal noise: a microscopic paradox

Observations – From the previous observations, we wonder if turbulence can be driven by microscopic noises. The small movement of molecules due to thermal fluctuations is very small compared to the scales at which turbulence builds. One can evaluate the order of magnitude at which thermal noise can have an effect compared to the inter-particle distance l_{int} such as [4]

$$\frac{l}{l_{int}} \sim (Ma)^{\frac{-2}{3}}, \tag{1.14}$$

where $Ma = U/c_s$ is the Mach number representing the ratio between the average flow velocity compared to the speed of sound. For instance, in a teacup, average velocities can reach $\sim 0.2m.s^{-1}$. The sound velocity in water is $c_s \sim 1500m.s^{-1}$. As a result we deduce that in a teacup, the scale at which thermal noise becomes important is approximately $l/l_{int} \sim 330$. The inter-particle distance in water is of the order of several nm. Thermal noise in this teacup has therefore an effect at most at the order of μm, way lower than the cup scale. All stochastic effects therefore appear as negligible compared to the macroscopic lengths. However, as G. Eyink argues, it still has an impact on eddies of comparable size. A small perturbation could therefore lead to changes of the fluid dynamics, at least microscopically. But as Lorenz conjectured in 1969 for atmospheric flows [60], those fluctuations could have effects on the larger scales as well.

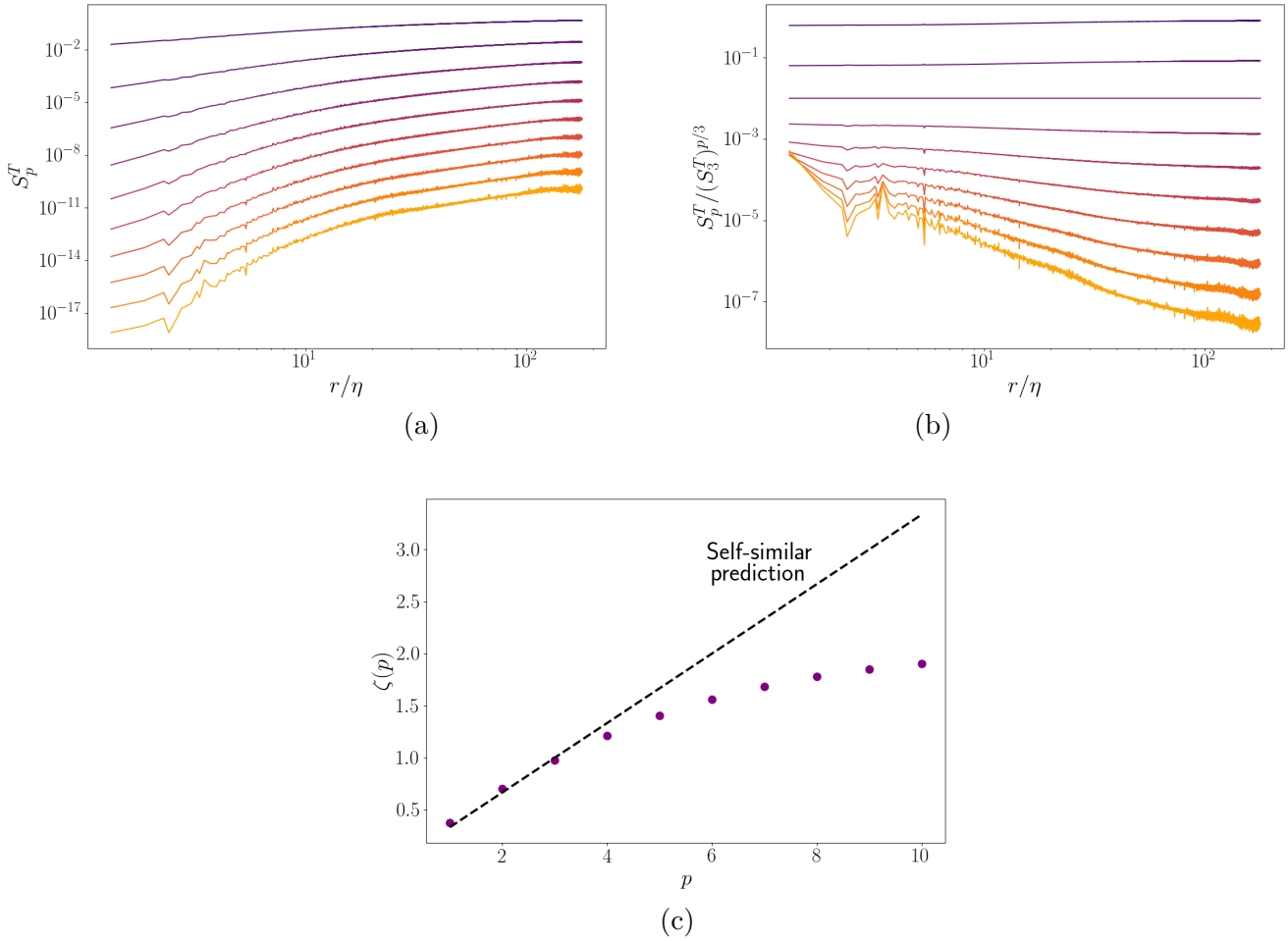

Figure 1.6: (a) and (b): transverse velocity structure functions (in arbitrary units) across scales r/η from experimental data [22]. The curves range from $p = 1$ (purple) to $p = 9$ (yellow). The right picture corresponds to structure functions normalised by S_3^T, to highlight deviations from self-similarity. In the latter case, all curves should be constant. (c): evolution of $\zeta(p)$ from equation (1.13) as a function of p. The black dotted line corresponds to the self-similar case.

A paradox? – This conjecture was stated as:

> *[...] certain formally deterministic fluid systems which possess many scales of motion are observationally indistinguishable from indeterministic systems; specifically, that two states of the system differing initially by a small "observational error" will evolve into two states differing as greatly as randomly chosen states of the system within a finite time interval, which cannot be lengthened by reducing the amplitude of the initial error.*

There is a paradox then, since thermal noise is supposed to be negligible compared to the large scales dynamics of turbulence. In his paper, Lorenz explores this conjecture through a model of atmospheric turbulence, looping back to Richardson's first observations and linking the loss of memory of the initial conditions to irregularities in the flow.

The 1969 Lorenz paper sets the ground of the 'true butterfly effect' [67], by which an infinitely small scale noise is amplified to the extreme. Such phenomenon explains why modern forecasting relies on stochastic predictions. The measurement of thermal noise in turbulence is of particular interest to that regard. A method for measuring such effects is described in Appendix A. In this thesis, we focus on exploring the building of this 'true butterfly effect' in multi-scale irregular systems. Next chapter will be dedicated to introducing the necessary mathematical tools to both deal with the multi-scale property of turbulence and the potential irregularities that can develop inside.

2 - Turbulence and singularities

2.1 . Finite-time blow-ups

2.1.1 . Introduction

Intuitions – Chaos is not sufficient for explaining the unpredictability of turbulence. It is however the only mechanism that can effectively produce entropy in smooth dynamical systems (from an information theory perspective, see Appendix B). Consequently, either an additional random forcing (thermal noise) is perturbing the flow, or turbulence is not a smooth dynamical system.

As an introductory example, consider again the Richardson's regime. Taking heuristic square root, we get as an order of magnitude that $\delta x = Ct^{3/2}$, where C is a constant. Differentiating in time, we get:

$$\delta\dot{x} = \frac{3C}{2}t^{1/2}, \tag{2.1}$$

and changing t for δx, we obtain

$$\delta\dot{x} = \frac{3C^{2/3}}{2}\delta x^{1/3}. \tag{2.2}$$

The flow on the right side becomes non-differentiable in space. We say it is 'irregular'. This simple argument suggests that turbulent flows might indeed be non-smooth in the Richardson regime.

Anomalous dissipation and Onsager's conjecture – Interestingly enough, there is another property of turbulence that points towards singular behaviours. Onsager, in 1949, was the first to emit this hypothesis after observing some curious phenomenon in dissipation [66].

All energy injected at large scales in turbulence is transmitted to the smaller scales (this is what we call 'Richardson's cascade'). This energy is finally dissipated by viscous forces around the smallest scale of turbulence, the Kolmogorov scale η. One may argue that, if we lower viscosity ν to 0, we should not have any more dissipation. Experimental observations contradict this statement. As depicted in Figure 2.1, when the Reynolds number $Re = \frac{UL}{\nu}$ (i.e. ν large) is low, dissipation decreases in proportion to viscosity, as expected. However, for large enough Reynolds number, dissipation does not decrease any more and saturates towards a finite value. In other words, there is still some dissipation in the limit of infinite Re, which is paradoxical regarding the negligible effect of viscous forces in this limit.

To solve this paradox, Onsager conjectured the existence of irregularities that dissipate energy. The corresponding phenomenon is called 'anomalous dissipation'. In the sequel, we provide a more rigorous statement of this conjecture, using a formalism adapted from Leray 1934 and Duchon and Robert 2000.

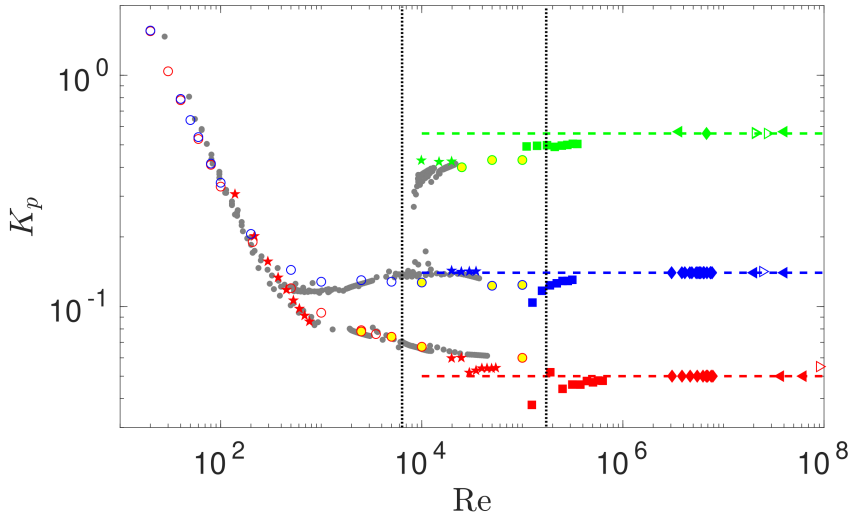

Figure 2.1: Dissipation measured through torque K_p in Von Kàrman type flows as a function of Re. The dotted lines indicated the range of Reynolds numbers investigated in this thesis. Red symbols correspond to contra case, Blue symbols to non-bifurcated anti case and Green symbols to bifurcated anti case. The ★ correspond to results obtained in VK2 experiment with a mix of glycerol and water. The results from the same experiment but with only water are displayed with the ■. The grey • represent results from the same experiment but with turbines equipped with 16 blades instead of 8. The ◀ correspond to Helium 4 at $T = 2.3K$ while the ▷ to Helium 4 at $T = 2K$ (superfluid phase) in SHREK experiment. The ♦ correspond to unpublished work from the VKS collaboration (M. Faure, N. Bonnefoy, S. Miralles, N. Plihon, J-F. Pinton, Ph. Odier, G. Verhille, M. Bourgoin, S. Fauve, F. Petrelis, M. Berhanu, N. Mordant, B. Gallet, S. Aumaitre, F. Daviaud, A. Chiffaudel, R. Monchaux, P. Gutierrez). Finally the ∘ correspond to numerical experiment where white are DNS data and yellow LES data. Figure adapted from [30, 74].

2.1.2 . Blow-ups in Euler

Intuitions – A typical case of singularity occurs when gradients are ill-defined or blow-up. This situation is typical when viscosity is zero, i.e. for Euler flows. Indeed, consider the enstrophy

$$\Omega = \left\langle \frac{1}{2}||\boldsymbol{\omega}||^2 \right\rangle, \tag{2.3}$$

where $\boldsymbol{\omega} = \nabla \times \boldsymbol{u}$ is the vorticity. One can show that enstrophy is related to dissipation $\epsilon[I]$ through energy balance (see Frisch [42]):

$$\Omega = \frac{1}{2\nu}\epsilon[I]. \tag{2.4}$$

Since dissipation saturates when $\nu \to 0$, we expect Ω to diverge in ν^{-1}. In the limit of Euler equations (i.e. $\nu = 0$), there is therefore a blow-up of enstrophy. This intuitive argument goes in favour of observing blow-ups in Euler equations[1].

Numerical investigations – The previous argument is only based on an empirical law of turbulence, the anomalous dissipation. When it comes to mathematical proofs, the situation is less clear, especially for the viscous case. There are however increasing numerical evidences of the existence of finite-time blow-up for the Euler equations. For example, Hou et. al. [54, 17] showed that in the case of axisymmetric inviscid flows, a blow-up can occur at the axis, or near a stagnation point near the boundary.

An even clearer evidence of finite-time blow-up upon Euler equation has been recently obtained by Campolina and Mailybaev [12, 68], for flows projected on a logarithmic lattice (with exponential spacing).

Weak formulation – Since some solutions of Navier-Stokes (or Euler) equations are possibly ill-defined because of finite-time blow-ups, we have to look at another space of solutions. Those solutions were introduced by Leray in 1934 and termed 'weak solutions' [59]. Physically, it corresponds to smoothing the ill-defined solutions with a filter in order to limit blow-ups. Mathematically, we choose two test functions $\boldsymbol{\psi}(\boldsymbol{x}, t)$ and $\Phi(\boldsymbol{x}, t)$ in the space of infinitely differentiable with compact support functions. We say that $\boldsymbol{u}$ is a weak solution of the incompressible Navier-Stokes equations (without any external forcing) if and only if $\boldsymbol{u}$ verifies

$$\int_{\mathbb{R}^3}\int_{\mathbb{R}} u_i \partial_t \psi_i + \int_{\mathbb{R}^3}\int_{\mathbb{R}} u_i u_j \partial_j \psi_i = -\frac{1}{\rho}\int_{\mathbb{R}^3}\int_{\mathbb{R}} P\partial_i\psi_i - \nu\int_{\mathbb{R}^3}\int_{\mathbb{R}} u_i \partial_k\partial_k\psi_i, \tag{2.5}$$

$$\int_{\mathbb{R}^3}\int_{\mathbb{R}} u_i \partial_i \Phi = 0. \tag{2.6}$$

The same formalism also applies to the incompressible Euler equations, by setting $\nu = 0$. In this thesis, we will extensively refer back to those solutions when differentiability in space might be broken.

[1] We note that it is not necessarily a finite-time blow-up here. Some observations show that a smooth initial flow can become singular in the limit of infinite Reynolds number for some numerical setups [28].

2.2 . How to detect the most irregular locations in a velocity field?

In this section, we summarise a technique developed in the SPHYNX group[2] to detect locations of the most irregular points in the flow. For this, we need to quantify the degree of irregularity needed to observe anomalous dissipation. In this chapter, we rely on the simple notion of Hölder continuity. We say that a function $\boldsymbol{f}$ is h-Hölder continuous if and only if

$$\exists C > 0, \ \ \forall (\boldsymbol{x}, \boldsymbol{y}) \in \mathbb{R}^{2d}, \ \ ||\boldsymbol{f}(\boldsymbol{x}) - \boldsymbol{f}(\boldsymbol{y})|| \leq C||\boldsymbol{x} - \boldsymbol{y}||^h. \tag{2.7}$$

From this definition, we get that $\boldsymbol{f}$ is Lipschitz continuous for $h = 1$. If $\boldsymbol{f}$ is differentiable, then $h \geq 1$. Physically, the larger the h, the more regular the function is.

2.2.1 . Duchon-Robert approach

In this thesis, we will heavily use a formalism introduced by Duchon and Robert in 2000 to help us detect the most irregular locations of the flow. We thus introduce a smoothing function ψ^l infinitely differentiable, compact support, even and positive. Then we define a smoothed velocity field such as

$$\boldsymbol{u}^l(\boldsymbol{x}, t) \doteq (\boldsymbol{u} * \psi^l)(\boldsymbol{x}, t) = \int_{\mathbb{R}^3} \boldsymbol{u}(\boldsymbol{x} + \boldsymbol{\xi}) \psi^l(\boldsymbol{\xi}) \, d\boldsymbol{\xi}, \tag{2.8}$$

and also introduce the velocity increments $\delta_\xi \boldsymbol{u}$ as

$$\delta_\xi \boldsymbol{u} \doteq \boldsymbol{u}(\boldsymbol{x} + \boldsymbol{\xi}) - \boldsymbol{u}(\boldsymbol{x}). \tag{2.9}$$

Using the filtered incompressible Navier-Stokes equations (INSE) and the definition of velocity increments, we get:

$$\begin{cases} \partial_t u_i^l + \partial_j (u_i u_j)^l = -\partial_i P^l + \nu \partial_k \partial_k u_i^l, \\ \partial_j u_j^l = 0. \end{cases} \tag{2.10}$$

Using this equation with the non-filtered INSE, one can deduce the energy budget that Duchon and Robert [31] were able to obtain:

$$\frac{1}{2} \partial_t u_i u_i^l + \partial_i T_i^l = \frac{1}{2} \nu \partial_i \partial_j (u_i u_i^l) - \nu \partial_j u_i \partial u_i^l - \Pi^l, \tag{2.11}$$

where

$$T_i^l \doteq \frac{1}{2} \left[u_j u_j^l u_i + P^l u_i + P u_i^l \right] + \frac{1}{4} \left[(u_i u_j u_j)^l - (u_j u_j)^l u_i \right], \tag{2.12}$$

represents spatial energy transport and

$$\Pi^l \doteq \frac{1}{4} \int \nabla \psi^l(\boldsymbol{\xi}) . \delta_\xi \boldsymbol{u} \, ||\delta_\xi \boldsymbol{u}||_2^2 \, d\boldsymbol{\xi} \tag{2.13}$$

the energy transfers towards scales below l. Duchon and Robert proved that Π^l corresponds, in the inviscid limit and $l \to 0$, to the anomalous dissipation:

$$\lim_{l \to 0} \lim_{\nu \to 0} \Pi^l = \epsilon[I], \tag{2.14}$$

[2] CEA Paris-Saclay.

which can be physically interpreted as being the dissipation due to irregularities in the flow. We note that $\Pi^l \geq 0$ and is a local quantity (i.e. we can compute it at any position in space).

Weak Karman Monin Howarth energy balance – As noted by Paul Debue and Bérengère Dubrulle [23, 30], equation (2.14) is, however, not suited for dealing with experimental flows. We introduce instead the weak Karmàn Howarth Monin equation (see Dubrulle 2019 for further details) as

$$\frac{1}{2}\partial_t u_i u_i^l + \partial_i J_i^l = -D_\nu^l - \Pi^l, \tag{2.15}$$

where $J_i^l = T_i^l - \frac{1}{2}\nu\partial_i \left[(u_j u_j)^l + u_j u_j^l\right] + \nu(u_j \partial_i u_j^l)$ and

$$D_\nu^l \doteq \frac{\nu}{2}\int \Delta\psi^l(\boldsymbol{\xi})\, ||\delta_\xi \boldsymbol{u}||_2^2 \, d\boldsymbol{\xi}. \tag{2.16}$$

This last term represents dissipation due to viscosity. We can then adapt equation 2.14 to get the following theorem

$$\lim_{l\to 0}\lim_{\nu\to 0}\left(D_\nu^l + \Pi^l\right) = \epsilon[I]. \tag{2.17}$$

In this thesis, we will extensively use Π^l as an indicator for possible locations of dissipative singularities in the flow by tracking points where this coefficient does not tend to zero as l tends to zero.

Scalings with h – We can refine the degree of irregularities of the dissipative singularities by simple dimensional arguments [31, 66]. Indeed, suppose that norm $||\boldsymbol{\xi}|| \sim l$ and $\boldsymbol{u}$ is h-Hölder continuous. Then, we get $||\delta_\xi \boldsymbol{u}|| \sim l^h$ which therefore leads to the following scaling laws for Π^l and D_ν^l:

$$\Pi^l = O(l^{3h-1}), \tag{2.18}$$

The dimensional argument shows that as soon as $\boldsymbol{u}$ is more regular than 1/3-Hölder, there can be no anomalous dissipation [66]. Tracking areas where Π^l does not converge to zero as l is decreased therefore enables us to track dissipative singularities, with $h \leq 1/3$.

From this point of view, we understand why Π^l accounts only for irregularities with Hölder exponent $h \leq 1/3$: those are the only available h for which Π^l does not go to 0 in the limit $l \to 0$. Because of intermittency, turbulence does not have a unique Hölder exponent h. We know from multi-fractal theory, introduced by Frisch, that h is a random field, function of space and time. A Lagrangian particle travelling will therefore endure different 'intensities' of irregularities on its path. Only the irregularities showing $h \leq 1/3$ are considered to be dissipative.

2.2.2 . Experimental observations

The application of this technique to experimental flows was initiated in the thesis of D. Kuzzay [76, 57]. Measurements of experimental velocities were injected into the formula

(2.13), using a filter ψ^l with decreasing width. The corresponding value of Π^l was then tracked in space and time, to search for locations where this quantity took the highest value, as the filter width was decreasing. The analysis of vorticity around these locations showed that an interconnection between two vortices were happening at the same place. A broader description of the structures next to those events can be found in Paul Debue's thesis [23]. Those events are rare and one needs a lot of data to achieve a good statistical convergence.

3 - Spontaneous stochasticity

3.1 . Introduction

3.1.1 . Introductory example

What does happen after a blow-up? In general, we cannot build solutions after those. When the dynamics is filtered however, the blow-up gets regularised and the solutions exist. The trajectories (or fields in the Eulerian point of view) obtained after a blow-up, are weak solutions in the limit of vanishing regularisation. In this chapter, we introduce the concept of spontaneous stochasticity, a transient phenomenon that explains what happens for the weak solutions in the limit of a vanishing stochastic regularisation.

We here start with a simple example[1] in order to get some intuition. We consider the following rough potential (represented in Figure 3.1)

$$V(x) = (1 - ||x||^{1+h})^2. \tag{3.1}$$

We consider specifically the over damped dynamic of a particle set in such potential:

$$\dot{x} = -\nabla_x V. \tag{3.2}$$

The above equation is well defined if $h \geq 1$ since it is differentiable only for this range of h. In particular, the $h = 1$ case corresponds to the classical over damped dynamic of a particle inside a classical double well. This case is well-known: if no additional perturbation is given, a particle starting exactly on top of the hill ($x(0) = 0$) will stay there indefinitely. A random infinitesimal perturbation would push the particle to go in one of the wells.

If $h < 1$, equation (3.1) presents a singularity for $x = 0$. In order to define and solve the dynamics (3.2) in the presence of a singularity, we regularise the potential by introducing a cut-off norm such as:

$$||x||_\eta = \begin{cases} |x| & \text{if } |x| > \eta \\ \frac{x^2}{2\eta} + \frac{\eta}{2} & \text{if } |x| \leq \eta \end{cases} . \tag{3.3}$$

This corresponds to exploring the weak solutions of equation (3.2). In addition to that, we also introduce a small noise $\xi(t)$ that will act as a random perturbation that will trigger the particle to fall into one of the wells:

$$\dot{x} = -\nabla_x V + \sqrt{2\kappa}\xi(t). \tag{3.4}$$

where κ is a diffusion term[2]. We consider a particle on top of this potential. Due to the random perturbation, a particle will reach one of the wells' bottom in a finite time. We assume that the noise scales with regularisation as

[1] A candid example initially proposed in a private conversation by Simon Thalabard.

[2] This stochastic regularisation was already studied for other singular ODEs in the probability theory literature [51, 3, 40].

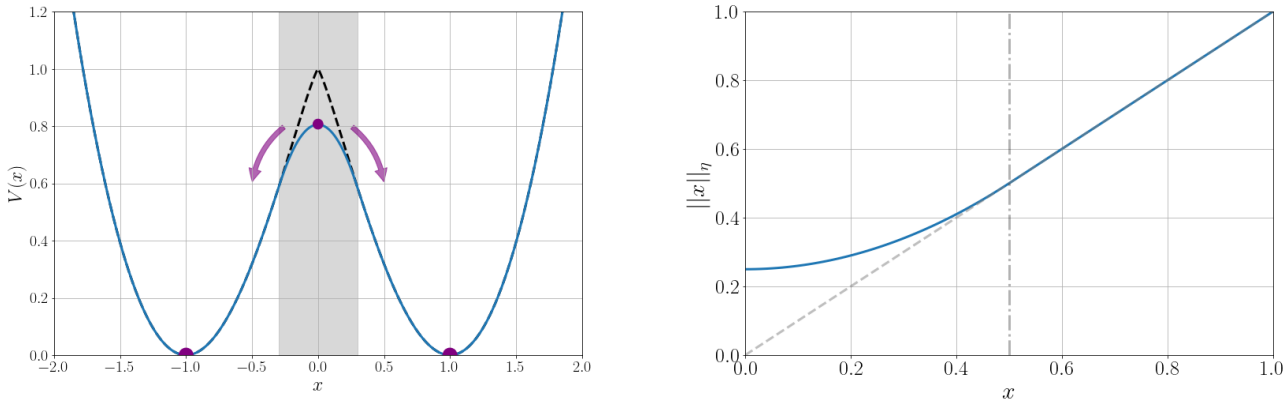

Figure 3.1: (Left): the singular double well potential defined in equation (3.1). The black dotted curve is the true potential while the blue curve corresponds to the regularised version using the norm defined by equation (3.3). A particle situated on top of the potential (in purple) cannot move unless there is an additional random force or perturbation. (Right): the regularised norm defined in equation (3.3).

$$\kappa = \eta^{1+h}. \tag{3.5}$$

Let us now investigate what happens in the limit of vanishing regularisation in the case where $h < 1$. In this limit, we expect to retrieve a similar behaviour as in the classical case: the particle remaining stuck at $x = 0$. Instead we observe that the particle tends to escape from $x = 0$ in a finite time, regardless of regularisation, as presented in Figure 3.2. This counter-intuitive result is what we call 'spontaneous stochasticity'. Physically, it corresponds to a transient amplification of an infinitesimal perturbation (represented here by the noise). It is a specific way to build the different non-unique weak solutions after a finite-time blow-up.

3.1.2 . Historical context

First steps: the Kraichnan model – The notion of spontaneous stochasticity appeared in the late 90's. It originated from the study of pair dispersion in the Kraichnan model [5]. In this model[3], Lagrangian trajectories are advected by a random Gaussian field with a specific correlation function

$$\left\langle v^i(t, \boldsymbol{r}) v^j(t', \boldsymbol{r}') \right\rangle \doteq (D_0 \delta_{i,j} - D^{ij}(\boldsymbol{r} - \boldsymbol{r}'))\delta(t - t'), \tag{3.6}$$

[3]The study of this model is not in the scope of this thesis. We note however that it is able to reproduce many different aspects of Lagrangian turbulence. An interested reader could find some additional information in [45].

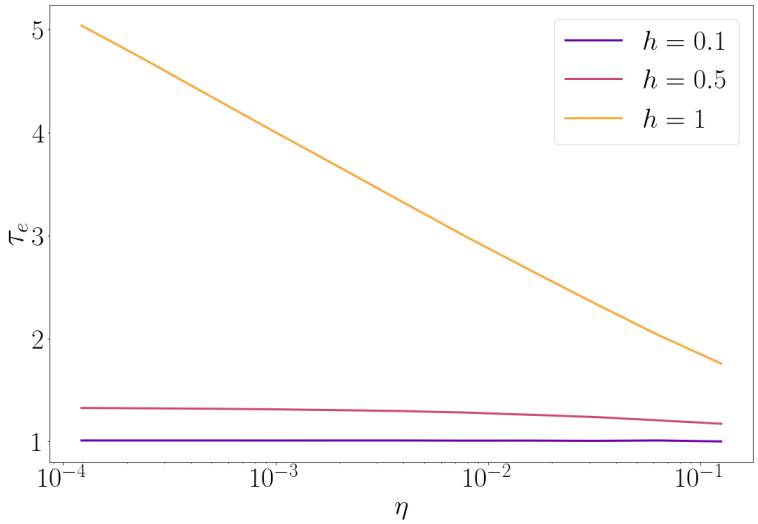

Figure 3.2: Evolution of exit time τ_η (average time to reach either -1 or 1) as a function of regularisation η for the Lagrangian particle driven by the force derived from the potential shown in Figure 3.1. The case $h = 1$ diverges as $\eta \to 0$, which is to be expected since $\tau_\eta = \infty$ for $\eta = 0$ in the classical double well potential. The cases $h < 1$ show a convergence of this exit time, being a signature of spontaneous stochasticity.

where $D^{ij}(\boldsymbol{r}) \propto r^{2\alpha}$, with α being the Hölder exponent here. One can then show that pair dispersion obeys a Richardson algebraic law as:

$$\left\langle \delta x(t)^2 \right\rangle \propto t^{\frac{1}{1-\alpha}}. \tag{3.7}$$

This example was further investigated later on, and a deterministic regime was found for a given range of parameters. In this regime, the particles were not separating any more and tended to stick together instead [82, 39]. It was proven that this model experiences phase transitions between those different regimes. While the term of 'intrinsic stochasticity' was first chosen to represent this unusual transient phenomenon, Falkovich introduced the term of 'spontaneous stochasticity' in 2001.

An Eulerian point of view – While spontaneous stochasticity was originally observed in Lagrangian statistics, this phenomenon can also be observed in an Eulerian context. We illustrate this point by taking the example of shell models. Those models are representations in Fourier modes of PDEs. The existence of weak solutions was shown for Sabra and Gledzer-Okhitani-Yamada (GOY) [19, 20] models, which are representations of Navier-Stokes equations. In 2016, Mailybaev presented an adaptation of GOY model by considering purely imaginary shells [61], leading to

$$\frac{du_n}{dt} = \left(\frac{1}{2}k_{n-1}u_{n-1}u_{n-2} + \frac{1}{2}k_n u_{n+1}u_{n-1} - k_{n+1}u_{n+2}u_{n+1}\right) - \nu k_n^2 u_n, \tag{3.8}$$

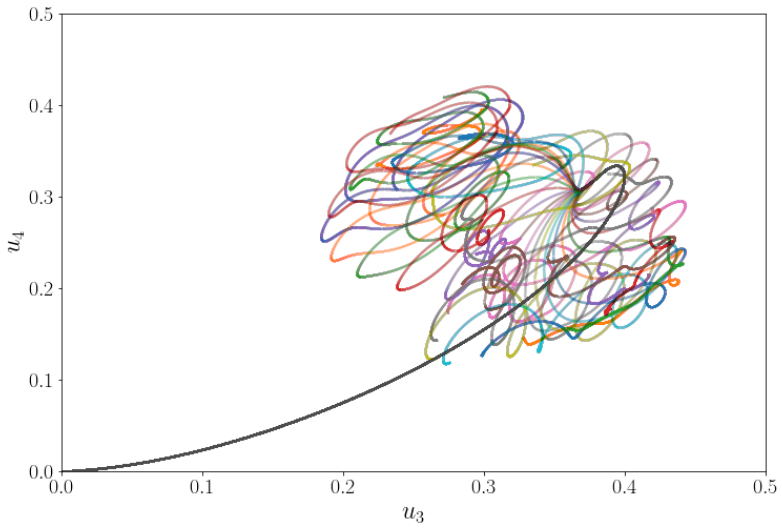

Figure 3.3: Evolution of modes u_3 and u_4 as a function of time for different infinitesimal variation of viscosity μ. Trajectories, represented each by different colours, tend to stick together until blow-up happens at time $t_B \sim 2.35$.

in which Navier-Stokes velocities $\tilde{u}(k,t)$ in Fourier modes are discretised and represented by the sequence $\{u_i\}_{1\leq i\leq N}$. Some boundary conditions, i.e. $u_0 = cte$ and $u_{-1} = cte$ are added and a cut-off N (considered to be large enough) is imposed. Mailybaev showed that Sabra model exhibits a finite-time blow-up in the inviscid limit. To construct different solutions of equation (3.8) after the blow-up, one may add a small regularisation by adding a random viscous term of decreasing amplitude. The resulting Poincaré section (u_3, u_4) is displayed in Figure 3.3. One observes that, before the blow-up time, all trajectories collapse onto a single curve. After this time, they all diverge from each other, tracing the different many possible solutions post blow-up. Then, the solution is not deterministic any more, but can be represented by a probability distribution function, hence the name of 'spontaneous stochasticity'.

Apart from shell models, other models exhibit the same behaviour in the Eulerian framework such as the shear layer problem [79].

3.2 . Towards an experimental observation?

All previous examples are either theoretical or numerical, based on simulations of Navier-Stokes or related equations. From an experimental point of view, however, evidence of spontaneous stochasticity is lacking. In fact, even the simple Richardson regime has never been observed. There are many technical reasons explaining such difficulties. In this thesis, we address them thoroughly, and devise a procedure enabling the exploration of spontaneous stochasticity in experimental flows. For this, we first need to discuss the

necessary ingredient for observing spontaneous stochasticity.

3.2.1 . Ingredients

Characterisation – Let us first have a look at the models displaying spontaneous stochasticity. We observe that they can involve some key features of turbulence such as energy cascade (see shell models) or intermittency (see Kraichnan models). They can also appear in simple Ordinary Differential Equations (as in our introductory model). From their very core they can even be intrinsically stochastic (see Kraichan model) or not. We can at least identify some important features to build spontaneous stochasticity:

- an irregularity that implies an irreversibility;
- a stochastic regularisation/perturbation (otherwise it does not work, see the Arnold's cat map example from Mailybaev [62]);
- a non-unicity of weak solutions.

Those ingredients are however not sufficient to fully characterise this transient phenomenon. There is no general recipe to create a spontaneously stochastic model. This is paradoxical since we know that chaotic systems and some stochastic processes can be characterised and arranged by their complexity. The unpredictability of systems such as the ones presented in Figure 1.5 can be decomposed and deeply understood. Since spontaneous stochasticity seems to sit in between those two worlds, we wonder if we can characterise it the same way.

Lagrangian determinism – In this thesis we will focus only on the Lagrangian point of view of spontaneous stochasticity. The questions about its characterisation will not be treated in the main text. An interested reader could find some interesting investigations in Appendix B, in which we try to extend the notions of information theory to understand this phenomenon. Instead, we focus here on building a toy model for spontaneous stochasticity from which we can get intuitions to create a good observable for experimental data.

The most promising model so far is the Kraichnan model, inherently stochastic. Real turbulence might be influenced by thermal noise, but it is still deterministic in its core (as represented by Navier-Stokes equations). Some $1d$ spontaneous stochastic models for Lagrangian spontaneous stochasticity have been developed in the past [29]. But there is currently no $3d$ flow that shows similar results while being irregular everywhere. Such model would be interesting to explore, especially to better understand the mechanisms of the sweeping of small scales displacements, closer to a turbulent dispersion [15].

3.2.2 . Thesis plan

This thesis will be dedicated to building such a $3d$ deterministic flow that shows Lagrangian spontaneous stochasticity:

1. A first chapter is dedicated to justifying and defining this model, called 'WABC model'. We will additionally present some of its interesting properties.

2. This will lead us to a second chapter in which we will analyse what it means to be spontaneously stochastic in this model. Especially, we will derive a promising criterion to explore this phenomenon in both experimental or simulated flows.

3. A short chapter will follow explaining in details the statistical tools that we use to quantitatively test for spontaneous stochasticity in the simulated WABC model.

4. A chapter dedicated to the numerical integration of the WABC model will then be presented. We will first introduce the general numerical methods employed to integrate the model. Results will come in the next chapter. In the process, we will quantitatively test the built criterion to check if it is really related to spontaneous stochasticity.

5. A final chapter will then present some observations on experimental and simulated flows. We will first present the used data. Finally, we will introduce the results and compare them with what was observed in our toy model.

Part II

The WABC model: definitions, criterium and methodology

4 - The WABC flow

We introduce in this chapter the WABC model which we build specifically to simulate spontaneous stochasticity. We will start by introducing the ABC flow, a simple chaotic flow that serves as a base for our model. We will then define the WABC model and introduce a stochastic regularisation for the integration. Finally, we will discuss its properties and see if we can observe Richardson's regime in it.

4.1 . From chaos...

4.1.1 . Introduction

We here introduce the 'ABC flow', a flow that was created by V. Arnold in 1965 following the work of E. Beltrami, S. Childress and himself. It is an important foundation of our toy model [2]. It is defined as

$$\boldsymbol{U}(\boldsymbol{x}) = \begin{cases} A\sin(z) + C\cos(y) \\ B\sin(x) + A\cos(z) \\ C\sin(y) + B\cos(x), \end{cases} \tag{4.1}$$

where A, B and C are constants. This flow solves the incompressible stationary Euler equations on the torus $[0, 2\pi]^3$ and has the special property of having vorticity $\boldsymbol{\omega}$ equal to velocity (a simple case of Beltrami property where $\boldsymbol{\omega} \propto \boldsymbol{U}$). This solution of Euler equation has the advantage of being simple and analytical.

As pointed out by Dombre et al. [24], the following system of equations for Lagrangian particles

$$\begin{cases} \dot{x} = A\sin(z) + C\cos(y) \\ \dot{y} = B\sin(x) + A\cos(z) \\ \dot{z} = C\sin(y) + B\cos(x), \end{cases} \tag{4.2}$$

remains unchanged under the following symmetries

$$\begin{cases} S_1 : \ x \to x', \ y \to \pi - y', \ z \to -z', \ t \to -t' \\ S_2 : \ x \to -x', \ y \to y', \ z \to \pi - z', \ t \to -t' \\ S_3 : \ x \to \pi - x', \ y \to -y', \ z \to z', \ t \to -t'. \end{cases} \tag{4.3}$$

A flow invariant under those transformations is considered to be time-reversible following Birkhoff's definition.

4.1.2 . Chaos and streamlines

Poincaré section – The ABC flow is of particular interest since Lagrangian chaos can appear for some special A, B and C coefficients. Hénon et al. in 1966 [53] were first to observe such properties when setting $A = \sqrt{3}$, $B = \sqrt{2}$ and $C = 1$. They use theoretical

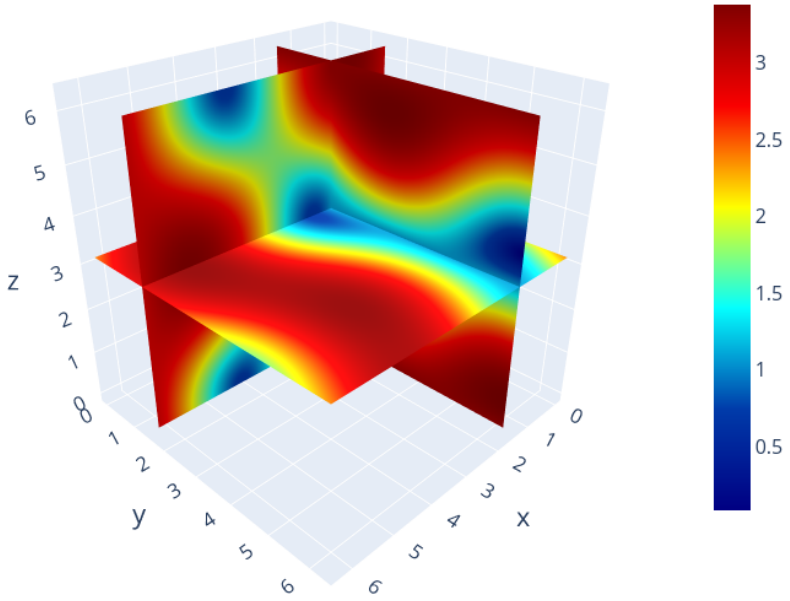

Figure 4.1: $||\boldsymbol{U}||_2$ slices of ABC flow.

and numerical analysis of streamlines to show that the flow is indeed chaotic. In the sequel, we focus on the case where $A = \sqrt{3}$, $B = 1.314$ and $C = 1$ which were chosen arbitrarily. We first test chaos by representing Poincaré sections of several streamlines, represented in Figure 4.2.

We can see from those graphs the presence of attractors (the structured regions), where the trajectories tend to get trapped for several moments, and chaotic areas in which the streamlines wander in a random fashion (the dotted areas). This shows that the chosen coefficients make the model chaotic as Hénon et al. showed in 1966 [53]. This also shows that the Lyapunov exponent depends on initial position: a trajectory can end up in several different attractors associated with different invariant measures.

Instantaneous Lyapunov exponent – To further illustrate this point, we present here the computations of the instantaneous Lyapunov exponent λ^i. The results are presented in Figure 4.3. We observe that the distribution in space of the λ^i is not homogeneous: there are places where those coefficients are higher than others.

4.2 . The WABC model

4.2.1 . Model definition

The assumption of having a smooth dynamical setup has to be broken to build a spontaneous stochastic model: we need irregularities. This idea is not new: as early as

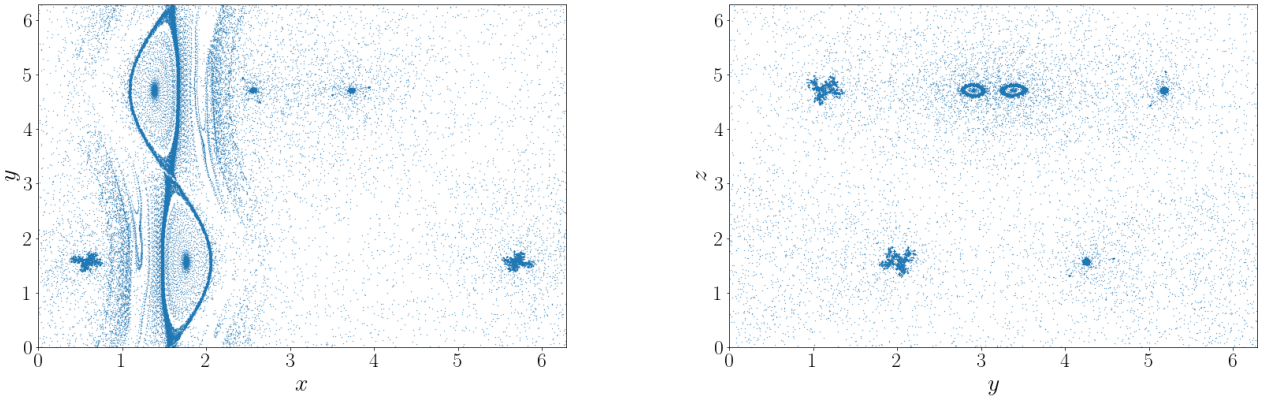

Figure 4.2: Poincarré sections of the ABC flow for $z = \pi$ (left) and $x = \pi$ (right) obtained from 20 trajectories.

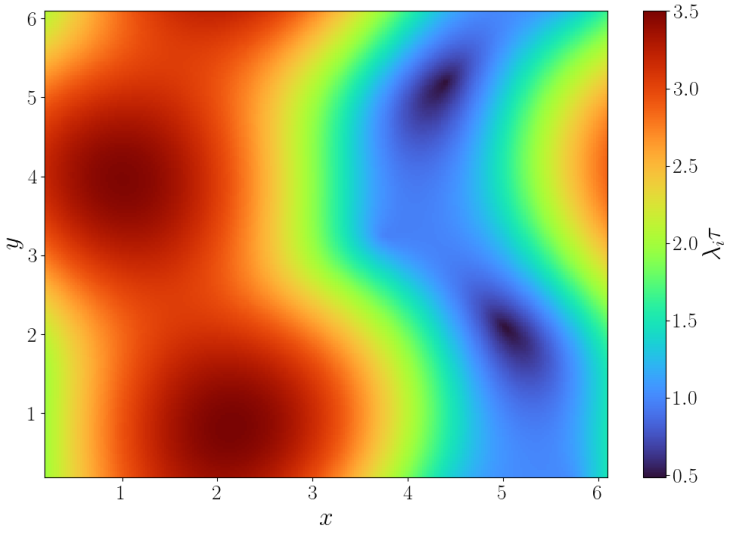

Figure 4.3: Slice for $z = \pi$ of the ABC flow's iLE field.

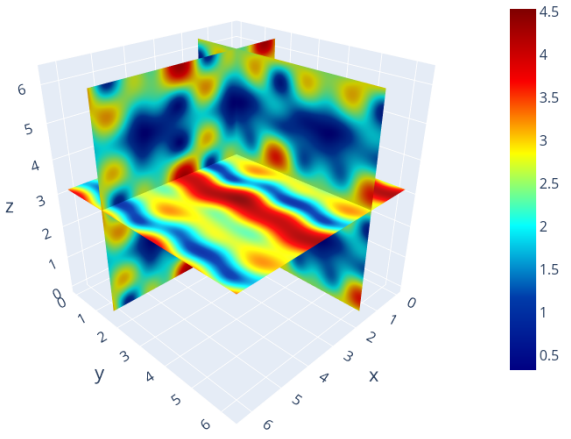

(a) $N = 2$

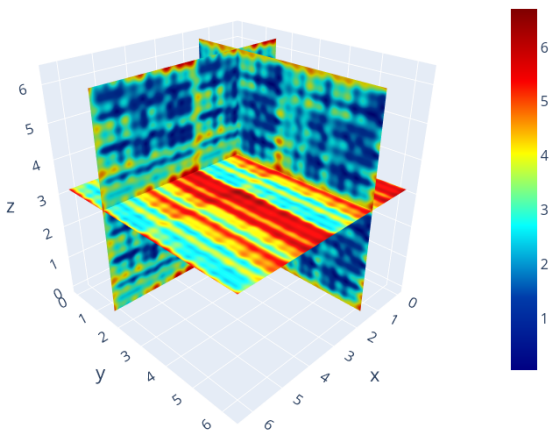

(b) $N = 4$

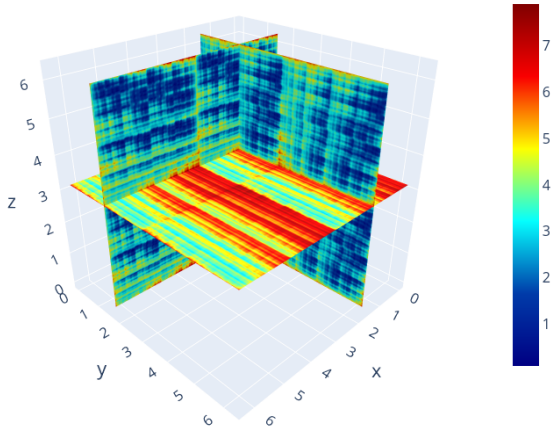

(c) $N = 6$

Figure 4.4: $||\boldsymbol{u}_W||_2$ slices of the WABC flow for increasing number of modes N.

1926, Richardson introduced an irregular toy model to interpret his famous dispersion law [71]. He took the example of an infinitesimal 'particle of air' for which positions are modelled by the Weierstrass' function

$$v_{a,b}(t) = \sum_{i=0}^{+\infty} a^i \cos(b^i t). \tag{4.4}$$

This function has the particularity to be h_0-Hölder continuous for any time t, where $h_0 = -\ln a / \ln b$ [84]. As a result, he showed that defining a velocity in that context is not possible. This shows the necessity to use statistics as a smooth measurement of particles' dispersion. In the present section, we build on Richardson's idea and construct a $3d$ 'Weierstrass' velocity field with irregularities in space. The elementary brick is the ABC flow, having similarities with other models [33, 37]. We call this model the 'Weierstrass-Arnold-Beltrami-Childress' or 'WABC' and define it as:

$$\boldsymbol{u}_W(\boldsymbol{x}) = \sum_{i=1}^{+\infty} \frac{\omega_i}{k_i} \boldsymbol{U}(k_i \boldsymbol{x}). \tag{4.5}$$

where $k_i = \lambda^i$ and $\omega_i = \lambda^{(1-h)i}$, having $\lambda > 1$.

The above velocity field is bounded by the exponential series $\sum_i^\infty \lambda^{-hi}$ which converges if and only if $h > 0$. This stationary $3d$ flow is a succession of layers each representing a smaller version of the ABC flow (see Figure 4.4).

We note that this flow does not solve Euler equations, even in its weak formulation, since the non-linear term $(\boldsymbol{u}_W.\boldsymbol{\nabla})\boldsymbol{u}_W$ breaks the superposition theorem. Also, since it is deeply connected to the Weierstrass function, one can show that the WABC flow is h-Hölder continuous. As a result, almost all spatial derivatives are undefined for $h < 1$. This leads to an exploding vorticity in that range of Hölder exponents. This flow is still incompressible for any h by linearity of divergence,

$$\boldsymbol{\nabla}.\boldsymbol{u}_W = \sum_{i=1}^{+\infty} \frac{\omega_i}{k_i} \boldsymbol{\nabla}.\boldsymbol{U}(k_i \boldsymbol{x}) = 0. \tag{4.6}$$

Since the flow is not differentiable, we need to introduce a regularisation in order to solve the Lagrangian dynamics. We decide to impose a stochastic regularisation through the addition of a cut-off scale $k_{max}^{-1} = k_N^{-1}$. This is modelled by a white noise $\boldsymbol{W}(t)$ (Wiener process) for which

$$\mathbb{E}(W_i(t) W_j(t')) = \delta_{i,j} \delta(t - t'). \tag{4.7}$$

We can then transform the dynamics into a Langevin-type equation as follows

$$d\boldsymbol{x}_N(\boldsymbol{x}, t) = \sum_{i=1}^{N} \frac{\omega_i}{k_i} \boldsymbol{U}(k_i \boldsymbol{x}) dt + \sqrt{2\kappa_N} d\boldsymbol{W}(t), \tag{4.8}$$

where κ_N is a diffusion term that should decrease with the 'number of modes' N. This kind of equation usually represents the dynamics of a particle that is affected by a small random forcing $f_w(t) = \sqrt{2\kappa_N} d\boldsymbol{W}(t)$ [43]. We will refer to equation (4.8) in the following as 'Langevin-WABC'.

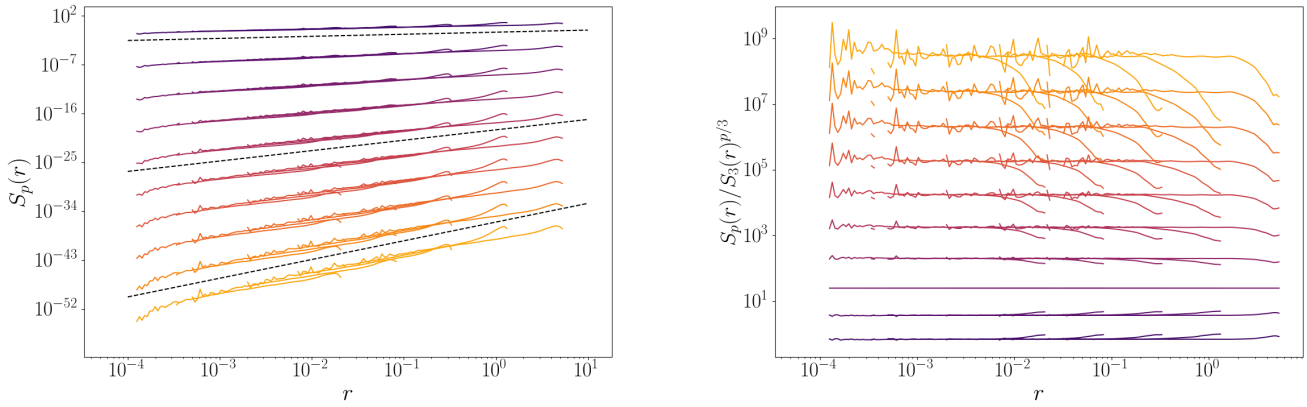

(a) (b)

Figure 4.5: Eulerian structure functions $S_p(r) = ||\delta_r u||^p$ as a function of distance r, not normalised (a) and normalised by $S_3(r)^{p/3}$ (b) for the WABC flow with $h = 1/3$ and $N = 14$. Increasing p are displayed by colours, ranging from $p = 1$ (dark purple) to $p = 10$ (light orange). The dotted lines are linear fits displaying a $0.38 \times p$ slope (close to the expected slope of hp).

4.3 . General properties

4.3.1 . Symmetries

Symmetries S_1, S_2 and S_3 are broken under the addition of modes of ABC flows. Therefore, the WABC flow cannot be seen as time reversible contrary to the original ABC model. 2π-periodicity is however conserved by linearity of the sum only in the case of an integer λ.

Due to contributions of all modes, Beltrami's property breaks for any $h \neq 1$.

4.3.2 . Self-similarity

Structure functions – Even though the full self-similarity is broken, WABC model still has a partial self-similarity property since:

$$\boldsymbol{u}_W(\lambda \boldsymbol{x}) = \lambda^h \left(\boldsymbol{u}_W(\boldsymbol{x}) + \lambda^{-2h} \boldsymbol{U}(\lambda^2 \boldsymbol{x}) \right), \tag{4.9}$$

which suggests that we could find self-similar structures. The analysis of Eulerian structure functions $S_p(r) = ||\delta_r \boldsymbol{u}_W||^p$ for the WABC flow with $h = 1/3$, presented in Figure 4.5, confirms such expectations. We indeed see that the flow is self similar with exponent $\zeta(p) = hp$ for scales larger than the cut-off (the inertial range of our flow).

Self-similar attractors – We can also observe the self-similar property with the attractors that we can spot on the Poincaré sections in Figure 4.6. For a strong regularisation ($N = 2$), we observe similar structures to those in the regular ABC flow. As N increases, the flow becomes more and more chaotic, presenting smaller and smaller attractors until

precision is not sufficient to distinguish them. This indicates that there will be, in the limit of vanishing regularisation, an infinite amount of attractors. They all have their own invariant measure and Lyapunov exponent. Consequently, Lagrangian trajectories experience fast jumps from different attractors.

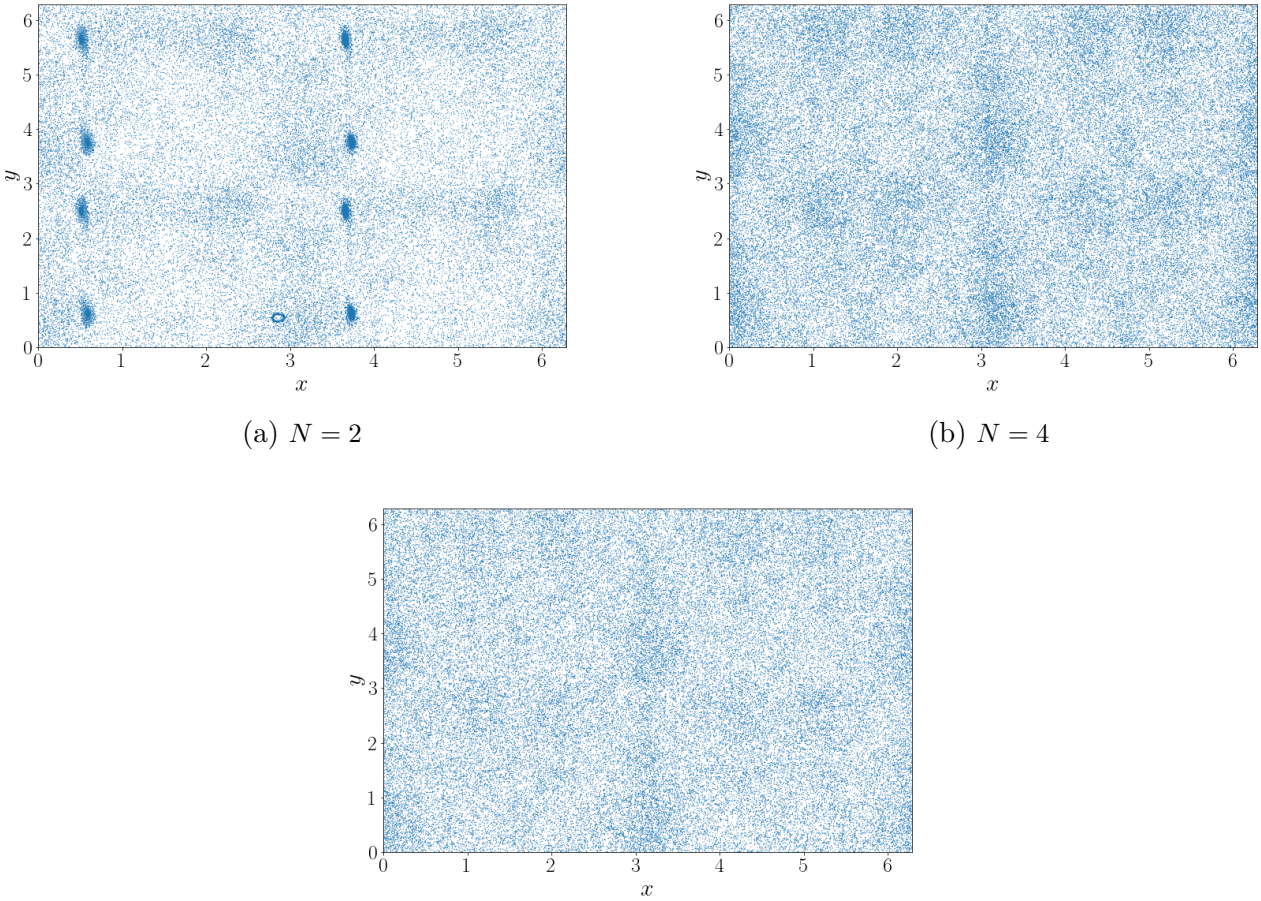

(a) $N = 2$

(b) $N = 4$

(c) $N = 6$

Figure 4.6: Poincaré $x - y$ sections for $z = \pi$ obtained from 20 trajectories and for increasing number of modes N for the WABC flow where $h = 1/3$. The small structures in $N = 2$ represent attractors of the flow: the trajectories stay in those areas for several moments. Those structures are self-similar and appear in the $N = 4$ case as well. We cannot distinguish them in the displayed observation window for the $N = 6$ case.

4.3.3 . Instantaneous Lyapunov exponents

To illustrate this last point, we present different maps of instantaneous Lyapunov Exponent (iLE) in Figure 4.7. We also show in Figure 4.8 different projections of integrated trajectories coloured by iLE for $N = 8$. The obtention of those coefficients is further explained in Appendix D. We observe that the distribution of iLEs is far from being

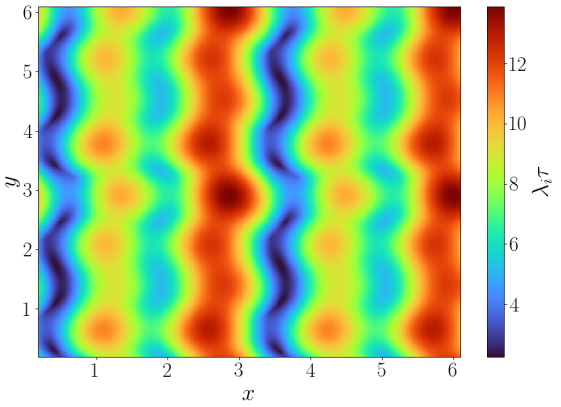

(a) $N = 2$

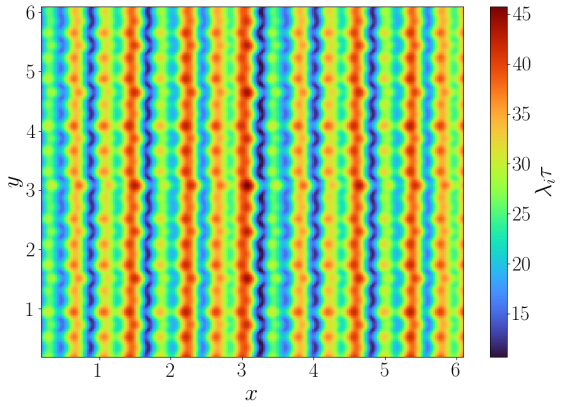

(b) $N = 4$

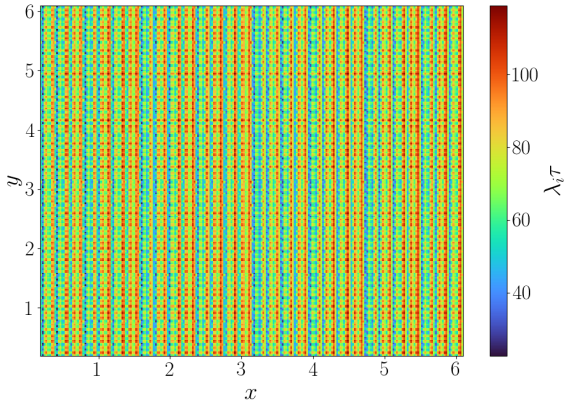

(c) $N = 6$

Figure 4.7: Slices on the z-axis of iLE fields for different number of modes in the WABC model for $h = 1/3$. The structures are entirely self-similar.

homogeneous. As a result, trajectories experience very different intensities of dispersion as they develop in the flow. We can therefore imagine that some trajectories could go through more extreme dispersions than others.

4.3.4 . 'Anomalous dissipation'

Definition – The notion of anomalous dissipation can be extended to the WABC model even though the flow is not a weak solution of either Navier-stokes or Euler equations. Indeed, equation (2.13) is still defined but we loose its regular interpretation as being a dissipative term. It is still sensitive to irregularities, as we recall that

$$\Pi^l = O(l^{3h-1}), \tag{4.10}$$

where h is the WABC's Hölder exponent. Therefore, for $h > \frac{1}{3}$, this coefficient tends to 0 in the limit of vanishing regularisation. In the dissipative case, i.e. $h < \frac{1}{3}$, this coefficient

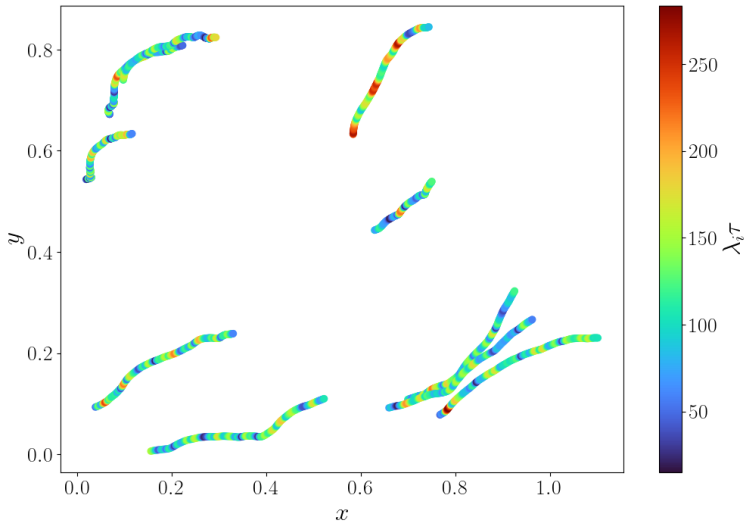

Figure 4.8: Typical trajectories projected onto the $x-y$ plan of the WABC flow for $h = 1/3$ and $N = 8$, coloured by instantaneous Lyapunov exponent.

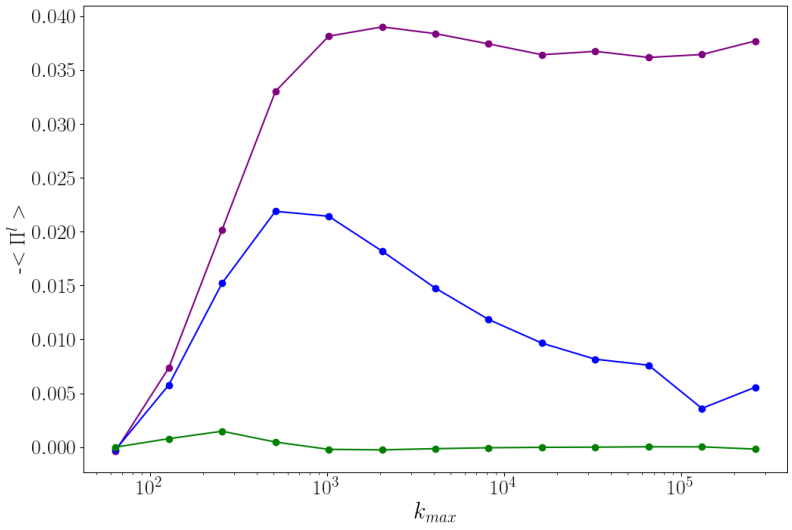

Figure 4.9: Evolution of anomalous dissipation $\left\langle \Pi^l \right\rangle$ as a function of k_{max} for the WABC model when: $h = \frac{1}{3}$ (purple), $h = \frac{2}{5}$ (blue) and $h = 1$ (green).

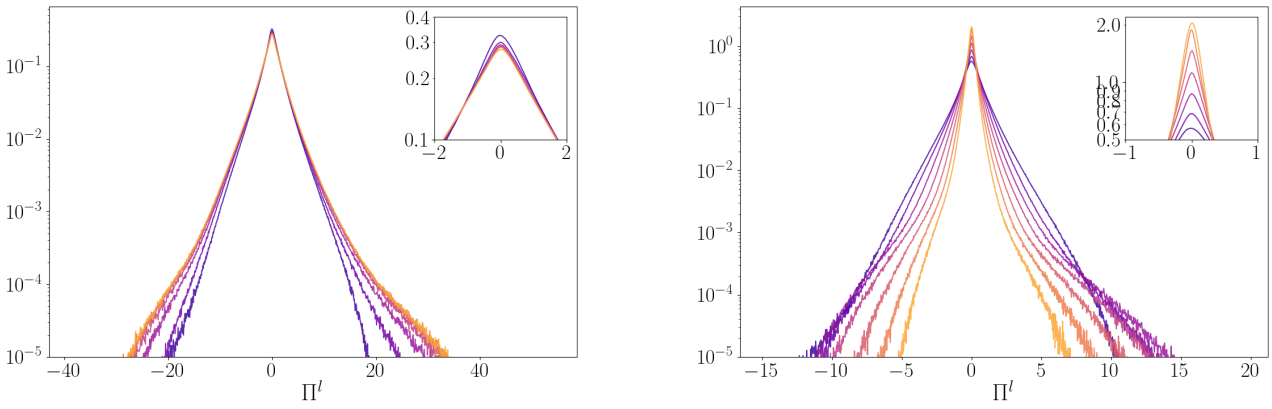

(a) $h = \frac{1}{3}$ (b) $h = \frac{2}{5}$

Figure 4.10: Probability distribution of Duchon-Robert coefficient Π^l as a function of N, ranging from $N = 6$ (dark purple) to $N = 18$ (yellow) for two different Hölder exponents of the WABC flow.

is not bounded any more. Those observations were already studied in another similar Weierstrass-type flow by G. Eyink [34].

Observations – We scale l with N by setting $l = 2.8k_{max}^{-1} = 2.8k_N^{-1}$. We show in Figure 4.9 the evolution of $< \Pi^l >$ as a function of k_{max} for $h = 1/3$, $h = 2/5$ and $h = 1$. As expected, for $h > \frac{1}{3}$, the curves tend to vanish in the limit of $k_{max} \to \infty$. For $h = 1/3$ the curve reaches a plateau of dissipation, coherent with the presence of dissipative singularities[1]. This is confirmed by Figure 4.10 which shows the evolution of $p(\Pi^l)$ as a function of N: the probability distributions become more and more peaked when converging towards the inviscid limit. When $h = \frac{1}{3}$, the distributions seem to collapse onto a unique non-Gaussian distribution. We identify $N \simeq 9$ to be the turning point where $\left\langle \Pi^l \right\rangle$ starts to decrease.

4.3.5 . Trajectories and Richardson's regime

To complete our tour of the general properties of the WABC flow, we test for Richardson's regime in this flow. For a given initial separation D_0, we integrate 1000 pairs of particles. Their initial position in space is random, we make sure that the pairs themselves have a D_0. The numerical integration procedure is explained in Chapter 7. The results are displayed in Figure 4.12 and we also show in Figure 4.11 an example of some trajectories coming from a same initial position. The time evolution of the pair dispersion displays a cubic power law. We conclude that the WABC flow can develop the Richardson regime for pair dispersion.

[1]We note that Π^l should not necessarily be positive here since the positivity was only proven for the Navier-Stokes and Euler equations.

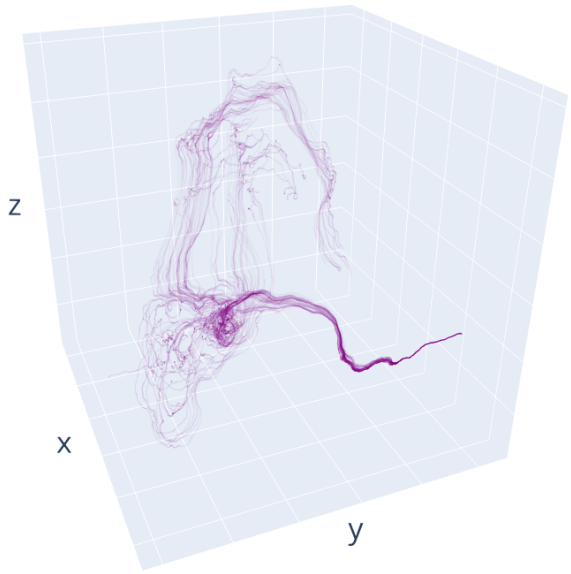

Figure 4.11: An example of trajectories all coming from a same initial position in the case $h = 1/3$ and $N = 20$, illustrating the exploding dispersion observed in the WABC model.

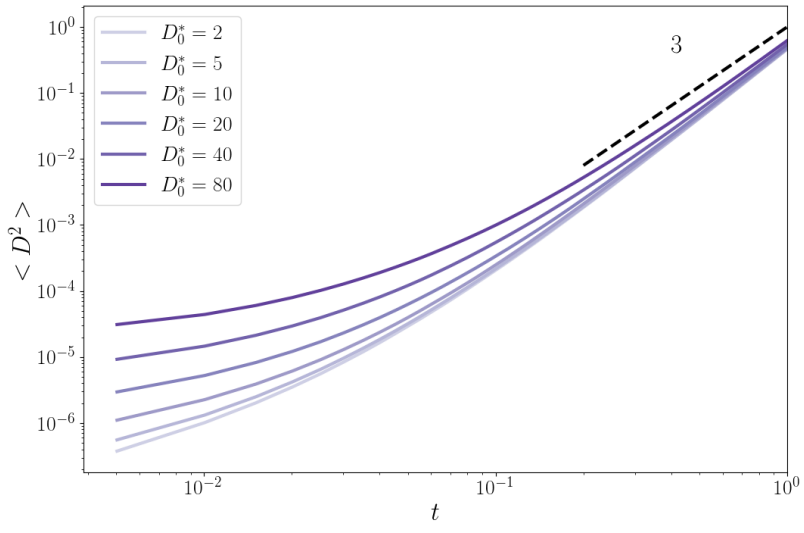

Figure 4.12: Square pair dispersion D^2 as a function of time for trajectories in the WABC model for $h = 1/3$ and $N = 14$ and different initial separation $D_0^* = D_0 k_N$. We identify here the typical cubic law of the Richardson regime.

	ABC Flow	WABC Flow
Incompressibility	x	x
Differentiability	x	Only for $h \geq 1$
Beltrami property	x	
Periodicity	x	Only for integer λ
S_1, S_2 and S_3 symmetries	x	Broken
Self-similarity		Partial
Chaos	x	x
Richardson regime		x

Table 4.1: Summary of properties of ABC and WABC flows.

4.3.6 . Summary of properties

In this chapter, we built a promising model for simulating spontaneous stochasticity. This needs to be numerically tested, which will be done in Chapter 7. As a summary, we give in Table 4.1 a comparison between the WABC flow and the regular ABC model regarding their properties.

5 - Building a criterion for spontaneous stochasticity

In this chapter we build a criterion to observe spontaneous stochasticity in experimental flows based on simple phenomenology. We first define and analyse what it means to be spontaneously stochastic in the WABC model. We will then present the constraints that make the use of this definition impossible in real flows. The identified problems will then be solved by constructing a criterion based on transition probabilities, conditioned to extreme events of dissipation. The numerical tools to compute all those observables will be presented in next chapter.

5.1 . Spontaneous stochasticity in WABC

5.1.1 . Definition

Spontaneous stochasticity – We recall the regularised Lagrangian dynamics 'Langevin-WABC'

$$d\boldsymbol{x}_N(\boldsymbol{x},t) = \sum_{i=1}^{N} \frac{\omega_i}{k_i} \boldsymbol{U}(k_i\boldsymbol{x})dt + \sqrt{2\kappa_N}\boldsymbol{dW}(t), \tag{5.1}$$

where $\kappa_N \underset{N\to\infty}{=} 0$. We consider an initial density probability distribution $p_0^L(\boldsymbol{x}) = \delta(\boldsymbol{x} - \boldsymbol{x}_0)$, where all particles start in $\boldsymbol{x}_0$. We define the density probability distribution at time t with N modes $p_N^L(\boldsymbol{x},t)$.

We will therefore say that we have Lagrangian spontaneous stochasticity if and only if, given a set of initial positions $\boldsymbol{x}_0$ such as, for any N, $p_N(\boldsymbol{x},0) = p_0^L(\boldsymbol{x})$, we have for $h < 1$

$$\exists t_s^{x_0} > 0,\ \forall t > t_s^{x_0} \quad \lim_{N\to\infty} p_N^L(\boldsymbol{x},t) = p^L(\boldsymbol{x},t) \neq \delta(\boldsymbol{x} - \boldsymbol{m}(t)), \tag{5.2}$$

where

$$\boldsymbol{m}(t) = \mathbb{E}(\boldsymbol{x}) = \int_{\mathbb{R}^d} \boldsymbol{x}\, p^L(\boldsymbol{x},t)\, d\boldsymbol{x}. \tag{5.3}$$

This means that the solutions of equation (5.1) are still non-deterministic in the limit $N \to \infty$ (vanishing noise), given that all particles start at the same initial position[1].

Universality – We note that condition (5.2) is not restrictive and could be universal under the change of several parameters in the WABC model.

- *Universality of regularisation:* Observations made on other spontaneously stochastic models tend to show that the limiting probability distribution should not depend on regularisation (or noise type) [29].

[1] We note that equation (5.2) depends on the initial position a priori where the spontaneous stochastic characteristic time $t_S^{x_0}$ depends on it.

- *Universality of continuity:* We expect spontaneous stochasticity to happen for any h-Hölder continuity where $h < 1$.

- *Universality of initial position:* Since the WABC model is non-differentiable everywhere, we expect it to be spontaneously stochastic for any initial position x_0.

We shall check condition (5.2) and test those three universal conditions numerically. The methods and results will be introduced in further chapters.

5.1.2 . Experimental constraints

From reading the above definition and conditions to match, any astute experimentalist could argue that checking those conditions is impossible in a real experimental setting since:

1. We cannot have the same exact initial state for each new measurement. It means that we cannot compute the probability distributions depicted in condition (5.2).

2. Experiments are bounded either physically (walls) or by measurement's constraints (thin laser sheet). Consequently we cannot track particles for a very long time $t > t_s^{x_0}$[2].

3. Due to the particle tracking method, we are able to either follow a lot of particles for a short time or a few of them for a very long time. The first scenario is convenient for statistics but only the second is needed to test condition (5.2).

Those constraints motivate the finding of a specific criterion that can be used in practice to test spontaneous stochasticity. From the above observations, we deduce that this criterion would first need to be local in space and time in order to exploit the available large number of short tracks. But more importantly, we would need this criterion to overcome the limitation of having access to only one realisation of the same flow.

5.2 . The transition deviation criterion

5.2.1 . Locality

Introduction – We consider the following scenario: some Lagrangian trajectories, all coming from a same initial position, move towards an isolated regularised singularity (see Figure 5.1). This matches with the spontaneously stochastic scenario observed in the non-Lipschitz dynamical system introduced by Drivas, Mailybaev and Raibekas [29].

In this model, particles emanating from $\boldsymbol{x}_0$ at time $t = 0$ are tracked until at least the singular event has been passed. In real flows, the tracked Lagrangian trajectories have many different initial positions. As a consequence, it is hard to isolate the ones that will go through a singularity from the others: we have a continuum of possible initial positions. A better idea would be to consider jumps from position $\boldsymbol{x}$ at time t to positions $\boldsymbol{x}'$ at

[2]This is what prevents researchers to actually observe Richardson's regime experimentally.

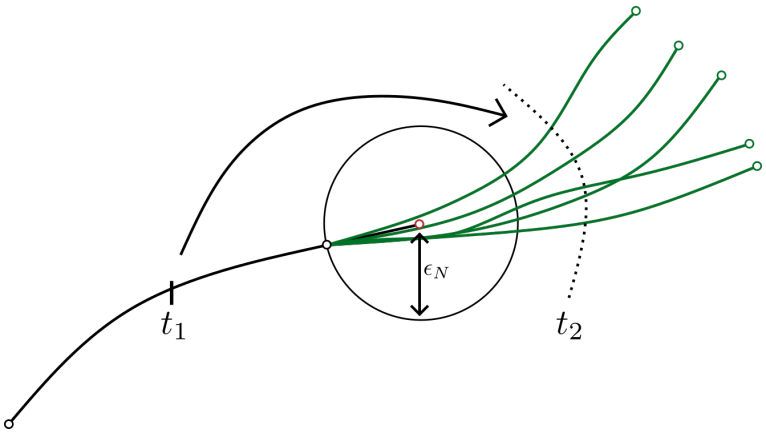

Figure 5.1: Schematic of an isolated regularised singularity. We consider a particle reaching a singularity (represented by the red dot) in a finite-time. The stochastic regularisation allows for the emergence of post blow-up non-unique trajectories (in green). The computing of probability transitions between two times, t_1 and t_2, allows for a more flexible approach regarding the analysis of spontaneously stochastic events. This schematic was largely inspired by Drivas, Mailybaev and Raibekas [29].

time $t+\tau$, where τ would need to be sufficiently large to pass the singularity. In the following we will introduce transition probabilities: a dedicated tool to study jumps[3]. We then analyse how those can be connected to condition (5.2). Those discussions will be lead onto the WABC model, which we will generalise to any flow.

Transition statistics – We consider two time-dependant random variables $\boldsymbol{X}(t)$ and $\boldsymbol{X}'(t)$ representing positions of two particles at time t. We introduce the density transition probability p as the probability of a particle jumping from a position $\boldsymbol{x}$ at time t to a position $\boldsymbol{x}'$ at time $t+\tau$

$$p(t,\, \boldsymbol{x},\, t+\tau,\, \boldsymbol{x}') \doteq p(\boldsymbol{X}'(t+\tau) = \boldsymbol{x}' \,|\, \boldsymbol{X}(t) = \boldsymbol{x}). \tag{5.4}$$

We note that by definition of conditional probabilities

$$\int_{\mathbb{R}^d} p(t,\, \boldsymbol{x},\, t+\tau,\, \boldsymbol{x}')\, d\boldsymbol{x}' = \int_{\mathbb{R}^d} \frac{p((\boldsymbol{X}'(t+\tau) = \boldsymbol{x}') \bigcap (\boldsymbol{X}(t) = \boldsymbol{x}))}{p(\boldsymbol{X}(t) = \boldsymbol{x})}\, d\boldsymbol{x}' = 1. \tag{5.5}$$

We define below what we will call in the following the 'transition average'

$$\boldsymbol{m}^\tau(\boldsymbol{x}, t) \doteq \int_{\mathbb{R}^d} \boldsymbol{x}'\, p(t,\, \boldsymbol{x},\, t+\tau,\, \boldsymbol{x}')\, d\boldsymbol{x}', \tag{5.6}$$

and the 'transition standard deviation'

$$(\sigma^\tau(\boldsymbol{x}, t))^2 \doteq \int_{\mathbb{R}^d} ||\boldsymbol{x}' - \boldsymbol{m}^\tau(\boldsymbol{x}, t)||^2\, p(t,\, \boldsymbol{x},\, t+\tau,\, \boldsymbol{x}')\, d\boldsymbol{x}'. \tag{5.7}$$

[3]Originated from the study of Markov processes [43].

Link with spontaneous stochasticity – Since in the Langevin-WABC setup all particles start from the initial position $\boldsymbol{x}_0$, we deduce that if spontaneous stochasticity exists in this setup, using condition (5.2) then

$$\forall \tau > t_s^{x_0}, \quad \lim_{N\to\infty} p_N(\boldsymbol{x},\, \tau) = \lim_{N\to\infty} p_N(t,\, \boldsymbol{x}_0,\, t+\tau,\, \boldsymbol{x}) = p(\boldsymbol{x},\, \tau). \tag{5.8}$$

Consequently, we also get for the transition standard deviation $\sigma_N^\tau(\boldsymbol{x}, t)$

$$\forall \tau > t_s^{x_0}, \quad \lim_{N\to\infty} \sigma_N^\tau(\boldsymbol{x}_0, t) > 0. \tag{5.9}$$

This last equation is a convenient observable since it is local in space. This criterion is however too local since in real flows, particles do not start with an identical initial position. Thus we shall improve it by considering a filtering performed by a coarse-graining.

5.2.2 . Spontaneous stochasticity within a coarse-graining

We here introduce the formalism to take into account the coarse-graining for the building of our criterion. We first introduce formally what we mean by 'coarse-graining'. We then analyse its consequences on the measurement of spontaneous stochasticity.

Setup – We restrict our space to $M \subset \mathbb{R}^d$, where M is bounded. We note μ_L the Lebesgue measure (or volume in an Euclidean set) associated with M. Let us consider a partition of M such as:

$$M = \bigcap_{i=1}^{N_\epsilon} I_i, \tag{5.10}$$

where $\forall (i,j) \in [\![1,\, N_\epsilon]\!]^2,\ I_i \cap I_j = \emptyset$ and $\mu_L(I_i) = \epsilon^d > 0$. It corresponds to having a regular grid with a spatial step ϵ, where N_ϵ is the total number of cells (or 'voxels' in $3d$) I_i. In the following, we refer to this partition as being the 'coarse-graining' of M.

Within this setup, we define the coarse-grained transition probability as

$$\forall i \in [\![1,\, N_\epsilon]\!],\ \ p(t,\, i,\, t+\tau,\, \boldsymbol{x}') \doteq \int_{I_i} p(t,\, \boldsymbol{x},\, t+\tau,\, \boldsymbol{x}')\, d\boldsymbol{x}, \tag{5.11}$$

which corresponds to the probability of the particles situated in I_i at time t to jump to a position $\boldsymbol{x}'$ at time $t+\tau$. This also leads to a new definition for the transition standard deviation

$$\sigma^{\epsilon,\tau}(i,t) \doteq \int_{I_i} \sigma^\tau(\boldsymbol{x}, t)\, d\boldsymbol{x}. \tag{5.12}$$

In the following, we would abusively associate i with the centre $\boldsymbol{x}$ of the cells I_i.

Artificial and intrinsic stochasticity – By imposing a coarse-graining, we lose information about the true dynamics of a system: several particles coming from a same cell I_i can end up in different position $\boldsymbol{x}'$ due to small velocity fluctuations within the cell. We call this phenomenon 'artificial stochasticity', since the coarse-graining represents the lack of information we have about the true system. Spontaneous stochasticity, on the contrary, represents an 'intrinsic stochasticity'.

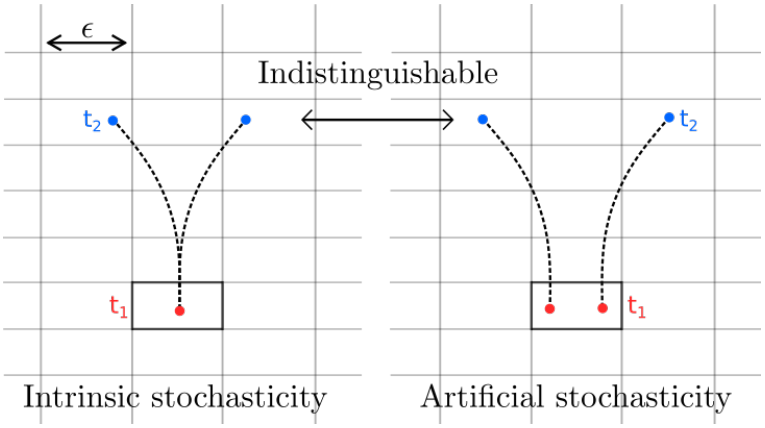

Figure 5.2: Schematic illustrating the distinction between the intrinsic and the artificial stochasticity. The first is a result of the stochastic nature of the dynamics (either by spontaneous stochasticity or any other random forcing). The second is imposed by the coarse-graining of the considered system.

For a given coarse-graining $(I_i)_{i\in[\![1,\,N_\epsilon]\!]}$, it is impossible to distinguish the two types of stochasticity (as illustrated in Figure 5.2). However, we note that

$$p(t,\, i,\, t+\tau,\, \boldsymbol{x}') \underset{\epsilon\to 0}{\sim} p(t,\, \boldsymbol{x},\, t+\tau,\, \boldsymbol{x}'). \tag{5.13}$$

As such, it is possible to distinguish the effect of spontaneous stochasticity from the coarse-graining in their asymptotic behaviours. We shall therefore refine the condition (5.9) as: if the WABC model develops spontaneous stochasticity, then

$$\forall \tau > t_s^{x_0},\ \lim_{\epsilon\to 0}\lim_{N\to\infty} \sigma_N^{\epsilon,\tau}(\boldsymbol{x}_0, t) > 0. \tag{5.14}$$

To ease the above limits, we set $\epsilon = \alpha k_N^{-1} \underset{N\to\infty}{\to} 0$ where α is a constant. We can do the same trick in experiments by setting $\epsilon = \alpha'\eta$, where the same manner $\epsilon \underset{Re\to\infty}{\to} 0$.

A practical criterion – We can compute $\sigma^{\tau,\epsilon}$ at any time in any cell, provided that we have enough particles cell-wise to have good convergence of the transition standard deviation. We note so far that, for a given $\boldsymbol{x}_0$, spontaneous stochasticity implies condition (5.14). The converse is also true: if in the limit $N \to \infty$ (or $Re \to \infty$), $\sigma^{\epsilon,\tau}(\boldsymbol{x}_0, t) = 0$, then there is almost surely no spontaneous stochasticity.

5.2.3 . Dissipation-based statistics

We identified that real flows are problematic since to two different Reynolds numbers correspond two different flow configurations. This prevents us from correctly computing the limits in condition (5.14) which requires to stay in the exact same setup (same initial condition, same flow configuration). In this subsection, we propose a way to circumvent this issue by introducing dissipation-based conditioned statistics, which will allow us to extend the previous discussions to real flows.

Intuitions – We know that, due to Lyapunov dispersion, two particles separate at an exponential rate (for τ small)

$$\delta x(t+\tau) = \delta x(t) e^{\lambda^i(t)\tau}. \tag{5.15}$$

The instantaneous Lyapunov exponents rely on the computation of gradients (assuming they exist within a given regularisation). From equation (5.15), we understand that the larger the gradients, the stronger the dispersion. We deduce that highly irregular places participate more in the dispersion of particles than smooth places. This leads to a question: is it possible to quantitatively group areas that share the same smoothness together?

Anomalous dissipation – To quantify the local smoothness, we use the two coefficients from Duchon and Robert theorem, introduced in Chapter 2. Since they are sensitive to gradients (more exactly to velocity increments), a higher local $\Pi^l(\boldsymbol{x}, t)$ implies a higher $\sigma^{\epsilon,\tau}(\boldsymbol{x}, t)$ as well. It was also already noted by Gawedzki or Eyink that there should exist a relation between anomalous dissipation (Eulerian) and spontaneous stochasticity (Lagrangian) [38]. In particular, Drivas and Eyink were able to prove such relationship for passive scalars in turbulence [26, 27]. From dimensional analysis, for a fine coarse-graining $\epsilon << 1$, we have

$$\sigma^{\epsilon,\tau} \sim \delta_{\boldsymbol{\xi}} u \tau, \tag{5.16}$$

where $||\boldsymbol{\xi}|| \sim \epsilon$ and $\delta_{\boldsymbol{\xi}} u = ||\boldsymbol{u}(\boldsymbol{x}+\boldsymbol{\xi}, t) - \boldsymbol{u}(\boldsymbol{x}, t)||$. Then, by definition of Π^l and D^l_ν (equations (2.13) and (2.16)),

$$\Pi^l \sim \delta_{\boldsymbol{\xi}} u^3, \tag{5.17}$$

and

$$D_\nu \sim \nu \delta_{\boldsymbol{\xi}} u^2. \tag{5.18}$$

We therefore conclude that if we are able to group extreme events of dissipation together, we should have, according to dimensional analysis:

$$\sigma^{\epsilon,\tau} \sim {\Pi^l}^{1/3}, \tag{5.19}$$

and

$$\sigma^{\epsilon,\tau} \sim {D^l_\nu}^{1/2}. \tag{5.20}$$

In this thesis, we will test if those two relations are verified. More generally, we are interested in the possibility to identify a common feature for the observed extreme events of dissipation.

Transition deviation – We assume that indeed $\sigma^{\epsilon,\tau}$ is higher where dissipation is large. We introduce the conditioned transition standard deviation that we will simply call 'transition deviation':

$$\langle \sigma^{\epsilon,\tau} \rangle_\Pi (\gamma) \doteq \int_M \sigma^{\epsilon,\tau}(\boldsymbol{x}, t)\, p(\Pi^l(\boldsymbol{x}, t) = \gamma)\, d\boldsymbol{x}. \tag{5.21}$$

By writing this definition, we question the possible connection between spontaneous stochasticity and the anomalous dissipation. We know that the first cannot imply the

second since spontaneous stochasticity can appear for $h < 1$ in full generality[4], whereas only singularities with $h < 1/3$ are dissipative.

In this thesis, we test if anomalous dissipation implies a spontaneously stochastic event. If this is true, then we shall expect for the WABC model

$$\forall \gamma > 0, \lim_{\epsilon \to 0} \lim_{N \to \infty} \langle \sigma_N^{\epsilon,\tau} \rangle_\Pi (\gamma) > 0. \tag{5.22}$$

For a given $\gamma > 0$, if $\langle \sigma_N^{\epsilon,\tau} \rangle > 0$ in the limit of vanishing regularisation and coarse-graining, then it indicates that trajectories, in average, do not fall onto a deterministic curve in places of strong dissipation. As a consequence, it would clearly show that anomalous dissipation implies spontaneous stochasticity.

In practice, we will test this criterion in the WABC flow on three different Hölder exponents:

- $h = 1/3$, being an example of dissipative singularities;
- $h = 2/5$, being an example of non-dissipative singularities;
- $h = 1$, being our control reference to see if the criterion behaves the same way or not in this case.

5.3 . Summary

In this chapter, we analysed what it means to be spontaneously stochastic in the Lagrangian framework for the WABC model. We identified the key differences this model has with experiments. With this knowledge, we were able to build a practical criterion based on the WABC model. Those definitions were designed to also be applied to real flows (DNS or experimental).

The transition deviation criterion however needs to be tested beforehand. We here summarise the different steps that are needed to certify that the criterion works (see also Figure 5.3 for a visual summary):

1. We will prove that the WABC model shows Lagrangian spontaneous stochasticity for $h = 1/3$. (A)
2. We will verify for its universality under the change of regularisation type, Hölder exponent and initial position.
3. We will check if the transition standard deviation relates to Duchon-Robert dissipation. If this is true, then it confirms the deep relation between transition statistics and singularities. (B)
4. If all of the above conditions are verified, we will finally test whether or not anomalous dissipation leads to events of spontaneous stochasticity. (C)

[4]This needs to be tested for the WABC model though.

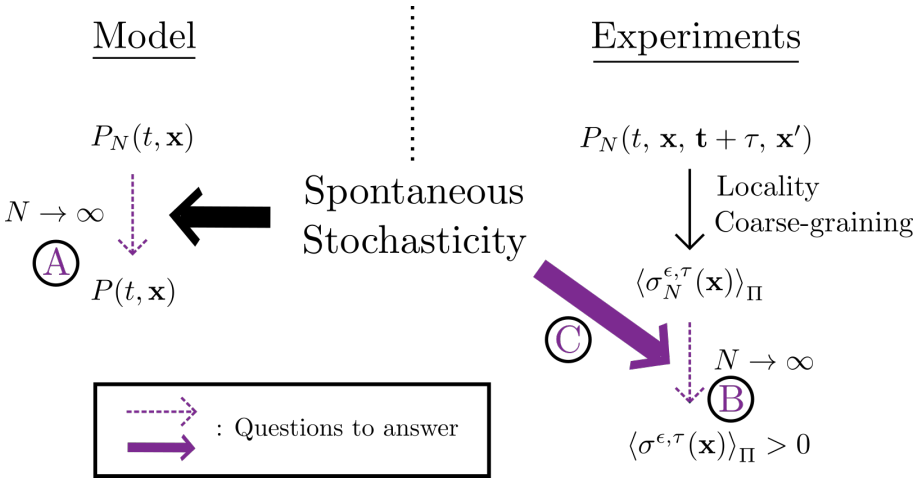

Figure 5.3: Illustration of this thesis' plan. The strategy is to prove first that the WABC model is spontaneously stochastic (A). In the meantime, we determine if the transition deviation criterion is well defined and converges non-trivially towards non zero values (B). Using the knowledge on the two above questions, we will finally test whether the transition deviation criterion is sensitive or not to spontaneous stochasticity (C).

After checking those points, we will compare the results with experimental observations. Condition (5.22) will be tested and we will see to which scenario ($h = 1/3$, $h = 2/5$ or $h = 1$) from the WABC model we are the closest.

To achieve those goals, we will first introduce the numerical tools to compute probability distributions and the transition deviation criterion. We will then present the results for the WABC flow. The experimental and DNS data will then be presented an analysed in the last chapter. We will discuss the results and compare with what was obtained in our reference model.

6 - Computational tools

In this chapter, we introduce the statistical tools that we need, to check spontaneous stochasticity and the transition deviation criterion. We will first show how we can, in practice, compute probability distributions to check their convergence into vanishing regularisation. We will then introduce the 'FlowHisto' method that allows for efficient computation of transition probabilities in real flows.

6.1 . Statistical tools for spontaneous stochasticity

6.1.1 . Standard deviation

Condition (5.2) is about whether probability distributions $p_N(t,x,y,z)$ converge trivially or not. However, statistical convergence in dimensions larger than 2 is in general very difficult to achieve. This phenomenon, known as 'curse of dimensionality', largely limits the investigations in $d > 2$: if 10^3 particles are needed to achieve convergence in $1d$, we would then need the impossible amount of $(10^3)^3 = 10^9$ particles for the $3d$ case. A necessary condition for convergence can however be obtained through first and second cumulant:

$$\boldsymbol{m}_N^{x_0}(t) \doteq \int\int\int \boldsymbol{x}\, p_N(t,x,y,z)\, dx\, dy\, dz, \tag{6.1}$$

$$\sigma_N^{x_0}(t)^2 \doteq \int\int\int ||\boldsymbol{x} - \boldsymbol{m}_N^{x_0}(t)||^2\, p_N(t,x,y,z)\, dx\, dy\, dz. \tag{6.2}$$

If $p_N(x,y,z,t) \underset{N\to\infty}{\to} p(x,y,z,t) \neq \delta(x,y,z,t)$, then we have $\sigma_N^{x_0}(t) \underset{N\to\infty}{\to} \alpha(t) > 0$, with α a function of time. In other words, we say that we observe traces of spontaneous stochasticity if we observe a saturation of $\sigma_N^{x_0}(t)$ in the limit of $N \to \infty$. The calculation of this coefficient is direct and can be computed for any time t. We will therefore use this observable to identify the times at which we suspect the onset of spontaneous stochasticity.

6.1.2 . 1,2-point statistics

Diagnostics using bare standard deviations are limited, since we can have $\sigma_N^{x_0}(t) \underset{N\to\infty}{\to} \alpha(t)$ while the distributions still change with increasing N. In order to get more details about the statistics, we investigate also the one and two point probability distributions, i.e.

$$p_N(t,x) \doteq \int\int p_N(t,x,y,z)\, dy\, dz, \tag{6.3}$$

$$p_N(t,x,y) \doteq \int p_N(t,x,y,z)\, dz. \tag{6.4}$$

If $p_N(x,y,z,t) \underset{N\to\infty}{\to} p(x,y,z,t) \neq \delta(x,y,z,t)$ as expressed by equation (5.2), then $p_N(t,x) \underset{N\to\infty}{\to} p(t,x)$ and $p_N(t,x,y) \underset{N\to\infty}{\to} p(t,x,y)$. The converse is also true: if the one/two point distributions do not converge, then the full distribution $p_N(x,y,z,t)$ should not as well. However, this projection rigorously implies the following statement: if we observe convergence

of one/two point statistics, we cannot be mathematically sure that the full convergence is reached.

6.1.3 . Kullback-Leibler divergence

The n-point statistics give important visual information about convergence of probability distributions. We use Kullback-Leibler divergence to quantify it. It is defined as follows (in 1d):

$$H_{KL}(p,q) = \int p(x) \ln \frac{p(x)}{q(x)} dx, \tag{6.5}$$

where p and q are probability densities. This relative entropy is a divergence and is therefore asymmetric. It also verifies

$$\begin{cases} H_{KL}(p,q) \geq 0 \\ H_{KL}(p,q) = 0 \Leftrightarrow \forall x \in M,\, p(x) = q(x). \end{cases} \tag{6.6}$$

The latter property can be used as an identification tool. If $p_N \underset{N\to\infty}{\to} p$, then we should have

$$|p_N - p_{N+1}| \underset{N\to+\infty}{\to} 0. \tag{6.7}$$

We would therefore observe $H_{KL}(p_N, p_{N+1}) \underset{N\to\infty}{\to} 0$. The advantages of this divergence are that: 1. it is simple to compute, 2. it is mathematically well defined, 3. it gives information about numerical precision. Numerical error, from the numerical scheme or because of the lack of statistics, implies small differences on equation (6.7). This results in H_{KL} not reaching 0 in the limit of $N \to \infty$.

Finally, we can also use Kullback-Leibler divergence to compare Langevin-WABC and other types of regularisations when testing for noise universality.

6.1.4 . Computations of histograms

All histograms will be computed with linear or, in some cases, logarithmic binning. No kernel (i.e. no statistical prior) will be used to smooth the results. We use a number of bins depending on the number of particles simulated. We generally ensure to have at least ~ 100 particles per bin on average. The computations of Kullback-Leibler divergence require a large enough number of bins and we made sure to select a thinner binning for those calculations.

A summary of all statistical tools used is given in Table 6.1.

6.2 . FlowHisto: a coarse-grained method to evaluate probability transitions

6.2.1 . Introduction

To compute the transition deviation criterion, we must be able to compute transition probabilities from Lagrangian data. Computing directly this quantity can be harmful since we need the computer to store an almost empty $6d$ histogram (corresponding to

	$\sigma_N^{x_0}$	$p_N(t,x)$	H_{KL}
Visual	x	x	
Quantification			x
Time analysis	x		
Binning		x	x

Table 6.1: Summary of properties of the used statistical tools.

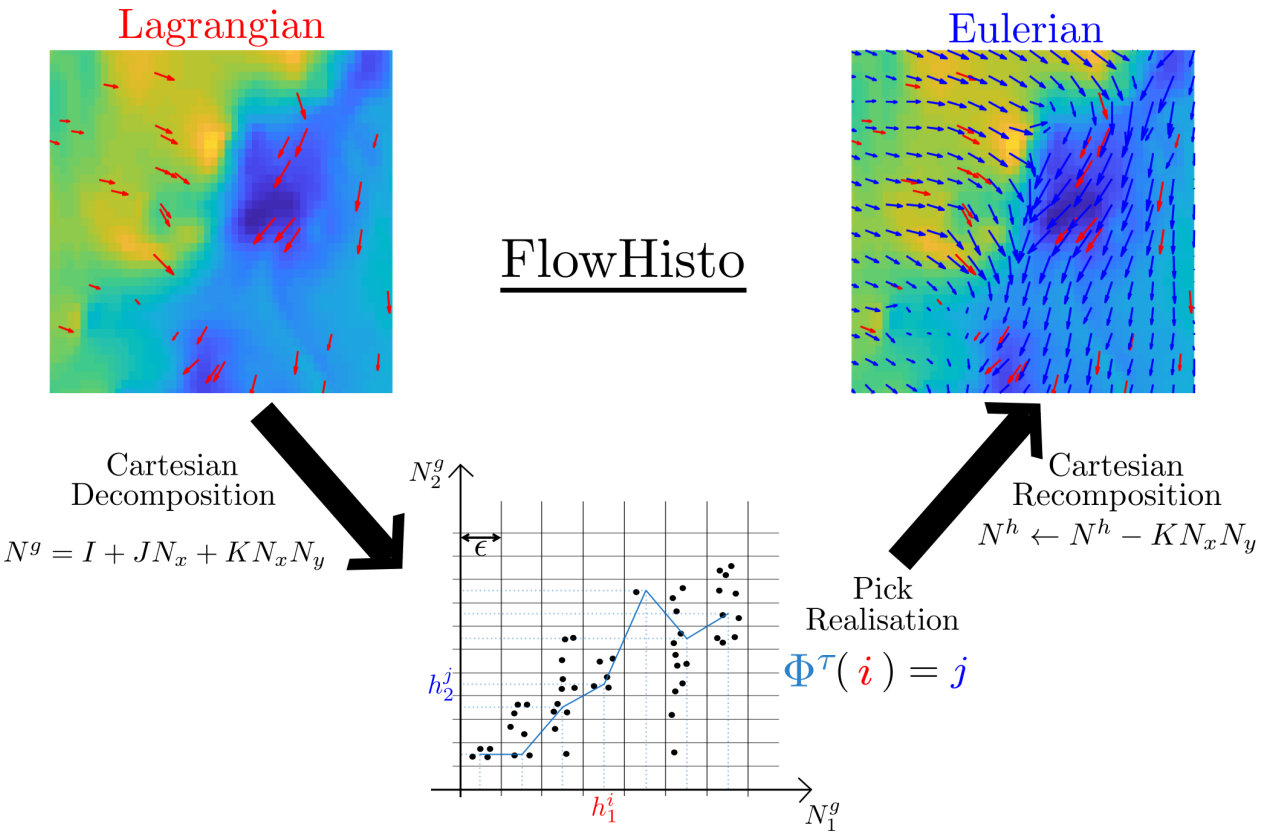

Figure 6.1: Schematic illustrating the FlowHisto algorithm. The aim of this algorithm is to deduce a possible evolution matrix from a given Lagrangian distribution (here displacements). We first perform a Cartesian decomposition defined by equations from 6.9 to 6.12 on Lagrangian data. N_g points are then set into a $2d$ histogram. We can find an evolution matrix by defining the associations between cells h_i and I_j. Using a Cartesian recomposition, we can then get the constructed real evolution matrix of the flow.

all possible transitions between two times). In this section, we introduce the 'FlowHisto' method that aims at performing this numerical task more efficiently.

Definition of evolution matrices – Before getting into the method presentation, we here introduce the notion of evolution matrices, which we will be needed in the following. We consider a discrete system (either deterministic or stochastic) S_N. We define its evolution to S_{N+1} as:

$$S_{N+1} = \Phi^N S_N, \tag{6.8}$$

where Φ^N is an evolution matrix, characterising how the system should evolve if we know in which state it originally was. In the case of a deterministic system, Φ^N is unique, corresponding to the flows from dynamical systems theory. In our case, Φ^N is not unique and is just one possible evolution. We can extend this notion in the case of systems that are time continuous, where we would only consider the function $\Phi_t^{t+\tau}$.

Methodology – The full method is represented in Figure 6.1. It consists of three steps:

1. *Cartesian decomposition*: sampling of positions $\boldsymbol{x}$ at time t_1 and t_2. It is the action of coarse-graining the Lagrangian positions.

2. *Histogram of transitions*: building the transition probabilities in the whole space. A possible transition for all particles, represented as an evolution matrix $\Phi_t^{t+\tau}$, is given as an output.

3. *Cartesian recomposition*: building an Eulerian flow based on the evolution matrix obtained at the end of the previous step.

At the end of step 3, we get one evolution matrix sent into real space. We can start again at step 2 in order to get a new evolution matrix. The accumulation of those different realisations can give an approximate evaluation of $\sigma^{\epsilon,\tau}(\boldsymbol{x}, t)$. In the following, we will introduce in more details all those steps and this final computation. A verification of the method will finally be presented.

6.2.2 . Step 1: Cartesian decomposition

The idea is to flatten n-dimensional vectors into $1d$ numbers. We assume that $d = 3$ and our space has a defined coarse-graining (N_x, N_y, N_z). We assume our domain M to be represented by the boundaries $\{(L_x^-, L_x^+), (L_y^-, L_y^+), (L_z^-, L_z^+)\}$ and we note a position as $\boldsymbol{x} = (x, y, z)$.

We convert x (resp. y and z) into a number I (resp. J and K) such that

$$I = \left\lfloor \frac{x - L_x^-}{L_x^+ - L_x^-} N_x \right\rfloor, \tag{6.9}$$

$$J = \left\lfloor \frac{y - L_y^-}{L_y^+ - L_y^-} N_y \right\rfloor, \tag{6.10}$$

$$K = \left\lfloor \frac{z - L_z^-}{L_z^+ - L_z^-} N_z \right\rfloor. \tag{6.11}$$

We can therefore form a new number that is an image of our position $\boldsymbol{x}$

$$N^g \doteq I + JN_x + KN_xN_y. \tag{6.12}$$

This method works the same for any other number of dimensions, using the exact same procedures. However, one also loses precision on computations from saving memory and time. If the coarse-graining is too strong, i.e. one of the (N_x, N_y, N_z) is too low, then the method fails to correctly encode the positions, resulting in highly discretised flowmaps. Choosing a too fine coarse-graining can lead to having too few particles per voxel preventing any statistical convergence.

6.2.3 . Step 2: Histogram of transitions

Histograms and transition probabilities – We note N_1^g and N_2^g the Cartesian positions obtained at the end of the previous step. They represent all the Lagrangian particles in this space moving from time t_1 to time t_2. We can then create a joint histogram based on those two positions. It corresponds to all possible associations between positions N_1^g and N_2^g. We call $H_{i,j}$ a bin in this space. The associated edges to this bin are the h_1^i and h_2^j, where the $(h_1^i)_i$ and $(h_2^j)_j$ represent the entire histogram's edges.

We pick one h_1^i, selecting all the particles with an initial position $N_1^g \in h_1^i$. Therefore the bin $H_{i,j}$ represents, for any j, the empirical probability to jump from h_1^i to h_2^j in a time τ. In the real space, it corresponds to approximating the computation of $p(t, \boldsymbol{x}, t+\tau, \boldsymbol{x'})$.

Global transition – The approximation of $p(t, \boldsymbol{x}, t+\tau, \boldsymbol{x'})$ is however poor and not useful for computing the transition standard deviation. Instead, we build a random evolution matrix $\Phi_t^{t+\tau}$, such as for any h_1^i we get the association $h_2^{\Phi_t^{t+\tau}(i)}$. It corresponds to a possible global evolution of the system from time t to time $t+\tau$.

6.2.4 . Step 3: Cartesian recomposition

Methodology – We now want to send the evolution matrix back into the real space. We note $N_1^{h,i}$ and $N_2^{h,\Phi_t^{t+\tau}(i)}$ the respective average values of the edges h_1^i and $h_2^{\Phi_t^{t+\tau}(i)}$. We therefore perform the inverse procedure of the one introduced in Step 1, i.e.

1. We isolate K by computing $K = \left\lfloor \frac{N^h}{N_x N_y} \right\rfloor$.
2. We then get z^h by inverting eq. (6.11): $z^h = L_z^- + \frac{K}{N_z}(L_z^+ - L_z^-)$.
3. We do $N^h \leftarrow N^h - KN_xN_y$.
4. We do steps 1 to 3 again to get y^h (dividing by only N_x this time), and finally x^h.

With this, we get a global evolution of the system[1]:

$$\boldsymbol{x}_2^h = \Phi_t^{t+\tau} \boldsymbol{x}_1^h. \tag{6.13}$$

Transition standard deviation – One can repeat the procedure from step 2 as many times as needed. Each time, we would obtain a different possible evolution $\Phi_t^{t+\tau}$. Locally, several realisations of $\Phi_t^{t+\tau}(\boldsymbol{x}, t)$ give the ensemble of possible evolutions from position $\boldsymbol{x}$, which can be used to compute the transition standard deviation as

$$\sigma^{\epsilon,\tau}(\boldsymbol{x}, t)^2 \approx \left\langle \left|\left| \Phi_t^{t+\tau}(\boldsymbol{x}, t) - \left\langle \Phi_t^{t+\tau}(\boldsymbol{x}, t) \right\rangle_\Phi \right|\right|_2^2 \right\rangle_\Phi . \tag{6.14}$$

The amount of necessary realisations to effectively compute equation (6.14) is not obvious. A convergence test is performed for the WABC model and the experimental data and is presented in Appendix E

6.2.5 . Verifying the method

Since the ABC flow (represented by velocity field $\boldsymbol{U}$) is a deterministic field, there exists one unique evolution matrix, given by:

$$\boldsymbol{\Phi}_t^{t+\tau}(\boldsymbol{x}) = \boldsymbol{x} + \int_t^{t+\tau} \boldsymbol{U}(\boldsymbol{x}(t'))dt' \tag{6.15}$$

We use this relation to verify the FlowHisto methodology. The obtained evolution matrices are compared to the theoretical ones, calculated using a Runge-Kutta scheme of order 8 (DOP853). We choose to work on a grid $N_x = N_y = N_z = 100$ with $10M$ particles, leading to an average density of 10 particles per voxel. Slices of absolute values of $\varphi_t^{t+\tau}(\boldsymbol{x}) = \Phi_t^{t+\tau}(\boldsymbol{x}) - \boldsymbol{x}$ are presented in Figure 6.2. We observe that the method performs well globally, exhibiting a small error (up to around 10%). The method fails when lots of scales need to be resolved. It fails to correctly capture the band of zero values as depicted on the maps.

6.3 . Computation of Duchon-Robert coefficients

6.3.1 . Procedure and conventions

Introduction – In this thesis, we will adopt the same procedure as in Paul Debue's thesis [23] regarding the computation of Π^l and D_ν^l. Those two coefficients will be computed using wavelet transforms with a Gaussian kernel:

$$\psi^l(\boldsymbol{x}) = \left(\frac{a}{2\pi l^2}\right)^{d/2} e^{-\frac{a||\boldsymbol{x}||^2}{2l^2}}, \tag{6.16}$$

where we choose $a = 30$. Further details can be found in Paul Debue's thesis [23].

We finally note that the Eulerian grid on which those observables are computed is different from the one in the FlowHisto method. We call ϵ_Π the spatial step for this grid.

[1] For simplicity, we here confound $\Phi_t^{t+\tau}$ in the Cartesian space and in the real space. Do note the difference: in the Cartesian space, $\Phi_t^{t+\tau}$ is a function of indices, and in the real space it is a real matrix.

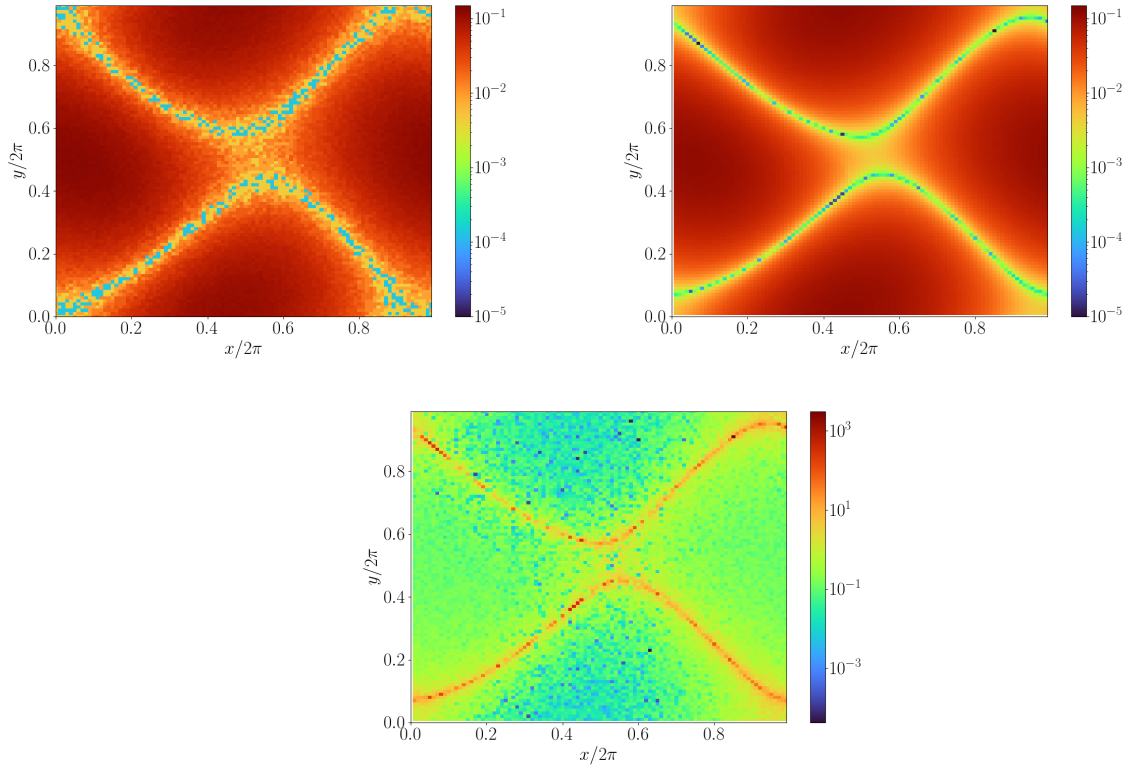

Figure 6.2: Slices of $|\varphi_x^\tau|$ for $z = \pi$ in ABC flow. FlowHisto methodology (top left) is compared to theoretical value (top right). The comparison between the two maps through their difference is provided on the lower picture.

Matching the scales – The FlowHisto method imposes a coarse-graining, which filters all scales below the spatial precision. One can show that the characteristic length scale of this filtering (at a -2dB cut-off) is[2]:

$$l_c = 2.8\epsilon \tag{6.17}$$

In comparison, the -2dB cut-off of the Fourier transform of equation (6.16) (which we recall is also a Gaussian) is:

$$l_s = \frac{\pi}{a \log 2} l \epsilon_\Pi. \tag{6.18}$$

In order to have comparable scales between the FlowHisto method and the filtering from the wavelet transform, we therefore need to select l such as:

$$l \approx \frac{2.8 a \log 2}{\pi} \frac{\epsilon}{\epsilon_\Pi}. \tag{6.19}$$

[2]One has to consider the coarse-graining to be a series of door functions, which are cardinal sinus in Fourier space. The 2.8 coefficient corresponds to -2dB cut-off of the cardinal sinus function. See [41, 48] for further details.

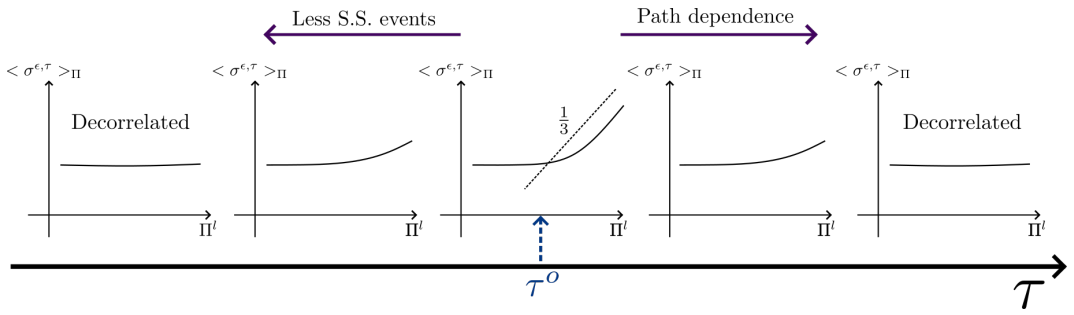

Figure 6.3: Schematic illustrating the evaluation of correlation between $< \sigma^{\epsilon,\tau} >$ and Π^l as a function of time τ. Correlations appear for a range of optimal times. This time is found to be the result of a battle between the isolation of elementary dissipations in trajectories and the rarefaction of spontaneous stochastic events.

In the analysis of the data, we would pick l depending on the ratio between FlowHisto grid size ϵ and the dissipation grid size ϵ_Π.

6.3.2 . UV locality

In the process, a lot of scales are filtered out, especially if l_c is in the inertial range. As Paul Debue pointed out, we can invoke the UV criterium introduced by Eyink [35]. In case of $l_c >> d_{part}$ where d_{part} is the inter-particular distance, we can assume that contributions to Π^l and D^l_ν come from scales close to l_c only.

In our case, we make sure to have a large enough number of particles per voxel d_ϵ to ensure statistical convergence of standard deviations. Since $d_{part} \sim \frac{\epsilon}{d_\epsilon}$, in most cases where $d_\epsilon > 6$ (which is what we aim for), the UV criterion is respected. For cases where $d_\epsilon \sim 1$, we expect Duchon-Robert coefficients to be underestimated as $l_c \sim d_\epsilon$.

6.4 . Paths and transitions

6.4.1 . Dissipation and paths

So far, we did not establish what τ we should choose for the computations of $\sigma^{\epsilon,\tau}$. In the WABC model, spontaneous stochasticity could be observed macroscopically only for $\tau > t_s^{x_0}$ (see Condition (5.2) in Chapter 5). A priori, $t_s^{x_0}$ depends on initial position. As such, we should choose $\tau = \tau^*$ such as

$$\forall \boldsymbol{x}_0 \in M, \;\; \tau^* > t_s^{x_0}, \tag{6.20}$$

in order to take into account all positions. This is however not a good choice. In the argumentation we developed in Chapter 5, we assumed that spontaneous stochasticity occurs at an isolated singularity. If τ is too large, this assumption breaks and one has to consider the whole history of Π^l (or D^l_ν in experiments) to account for the possible encounter of many different singularities.

On the other hand, τ should not be too low since we would limit the number of initial positions where spontaneous stochasticity developed, i.e. the x_0 such as $\tau > t_s^{x_0}$. These two

constraints are summarised in Figure 6.3. In the following, we choose the 'good τ' noted τ^o heuristically, in between these two limits, as we did not find any clear mathematical criterion to select it.

6.4.2 . Normalisation

We additionally note that the correlation times τ_c in both the WABC model and the experimental data decreases with N or Re [3]. As such we should scale τ with N or Re in order to limit the path influence as cited above. We then choose to keep a constant ratio τ/τ_c. For the WABC flow, we consider $\tau_c = \frac{1}{\omega_N}$. For the experimental data, we consider $\tau_c = \tau_\eta$, the limit of Lagrangian ballistic regime.

[3] It also seems that, in experiments, the more extreme the dissipation is, the faster the decorrelation happens. See Appendix F for further information.

Part III

Results

7 - Observations in the WABC flow

7.1 . Numerical integration

In order to simulate the different realisations of equation (5.1) we use a Monte-Carlo method. We here introduce the corresponding numerical methods and the possible issues that one can encounter when using those.

7.1.1 . Strong and weak convergence

Algorithms can be ranked by their weak and strong order of convergence. While weak convergence is related to accuracy of probability distributions and their moments, strong convergence is related to accuracy of the trajectories themselves. Those convergences deeply depend on both time-stepping (just as for Ordinary Differential Equations) and the number of trajectories, at the core of statistical convergence. We note x_t the theoretical points from trajectories at time t, and y_n the discrete approximation of x_t obtained numerically with a time step $\tau = t/n$. We will say that we strongly converge at time t to x_t with order α if there exist $C^s > 0$ and $\delta t_{max} > 0$ such as

$$\mathbb{E}(||y_n - x_t||) \leq C^s \tau^\alpha \quad \forall \tau \leq \delta t_{max} \tag{7.1}$$

Similarly, we will say that we weakly converge at time t to x_t with order β with respect to a class of functions $\mathscr{C}$ if, for each $f \in \mathscr{C}$ there exist $C_f^w > 0$ and $\delta t_{max} > 0$ such as

$$||\mathbb{E}(f(y_n)) - \mathbb{E}(f(x_t))|| \leq C_f^w \tau^\beta \quad \forall \tau \leq \delta t_{max}. \tag{7.2}$$

In the following, we choose the L^2-norm and we pick $f = \mathbb{1}$ for convenience. Good statistical accuracy is crucial when investigating spontaneous stochasticity. This requires numerical schemes that have good weak convergence. We shall particularly show that the number of particles has an important role regarding the convergence of averages.

7.1.2 . Numerical scheme

In case of Langevin-WABC, we use a stochastic method to integrate Lagrangian trajectories following equation (5.1), sticking to Ito's representation.

We use the stochastic solver 'SRA3' from the SciML library, programmed in Julia. This method relies on an optimised Runge-Kutta scheme of strong order 1.5 [69] and claimed to be of weak order 3. Since our noise is diagonal, there is no problem with using this scheme as the diffusion term perfectly commutes. Integration is performed with a fixed time step dt_N to make sure that it scales properly with cut-off N. Later we compare the performances of this algorithm with Euler-Mayurama method. Finally, a series of sampling times t_i are given and used to compare the different simulations. Since the t_i are not necessarily proportional to dt_N, a linear interpolation is performed in order to get the positions at any t_i.

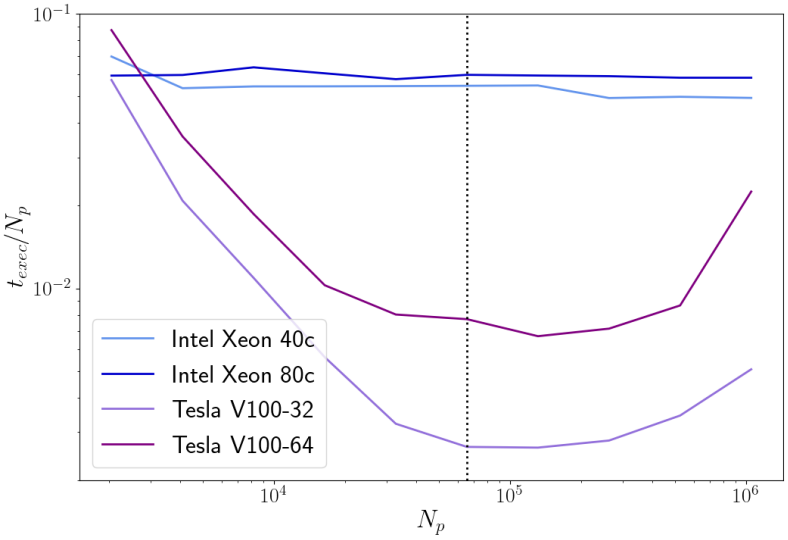

Figure 7.1: Computation time benchmark for integrating the WABC model with the SRA3 algorithm for parameters $N = 12$ and $a = 0.012$. CPU computations are performed for 40 and 80 cores on an Intel Xeon 2.1 GHz. GPU computations are performed in 32 and 64 bits floating point numbers on a Nvidia Tesla V-100.

7.1.3 . GPU accelerated computations

GPU computations – Computations can become heavy when increasing the number of modes N, especially since a large number of particles is needed to ensure weak convergence. For those reasons, CPU[1] computations can be limiting and we decided to switch to GPU[2] computations. Such components are more fitted to handle a large number of parallel tasks. We made use of Julia's library 'DiffEqGPU' combined with the 'EnsembleArray' method, which is a flexible hybrid option using both CPU and GPU.

Precision – The 32 bits precision floats is the norm for GPUs. However, for some parameters (large N, small dt), this precision is limiting. As an example: with $N = 14$ and $a = 0.012$, typical parameters detailed below, the time step $dt \sim 7.34 \times 10^{-7}$ ends up being too close to the lowest possible 32 bits precision, i.e. 1.19×10^{-7}. We therefore switched to a 64 bits precision floats, imposing slower methods than in the 32 bits case.

Benchmark – Switching from CPU to GPU hugely accelerates computations as shown in Figure 7.1. As expected, those computations show an optimal number of tasks to be executed at the same time for GPUs. We evaluate this number to be $2^{16} \sim 65\ 000$, right before the ratio time / Number of particles rises. We decide to use this optimal number of tasks to batch them and not overload the GPU. We finally noticed that a multi-

[1]Central Processing Unit.
[2]Graphics Processing Unit.

threaded version of the above method was also helping a lot during phases of intense CPU computations, especially when sending data to the GPU.

7.2 . Tests of the methods

7.2.1 . Weak convergence on Ornstein-Ulhenbeck process

Definitions – We verify that SciML algorithms give the expected weak convergences. We use as a reference a standard $3d$ Ornstein-Ulhenbeck equation with diagonal noise

$$\boldsymbol{dX} = -\theta(\boldsymbol{X} - \boldsymbol{\mu})dt + \sigma \boldsymbol{dW} \tag{7.3}$$

which we integrate for a fixed time step. The theoretical expectation value for this system is given by [43]

$$\mathbb{E}(\boldsymbol{X}) = \boldsymbol{X}_0 e^{-\theta t} + \boldsymbol{\mu}(1 - e^{-\theta t}), \tag{7.4}$$

which can be compared to results from simulations.

Observations – Tests of weak convergence of both Euler-Mayurama (EM) and SRA3 algorithm using the definition given by equation (7.2) are presented in Figure 7.2. We observe that EM algorithm performs as expected, showing a weak order 1. However SRA3 algorithm performs better than expected compared to the announced weak order 3. This algorithm will be used in the following since, in the case of WABC, it is at least as performant as EM.

Figure 7.2 also shows that the lower dt gets, the larger the required number of particles to display weak order convergence. As a consequence, for a given dt, the number of particles can be limiting when it comes to quantifying weak convergence.

7.2.2 . Sweeping and noise

On a dimensional argument, it would be natural to set $dt_N \sim \omega_N^{-1}$. However this leads to incorrect results. In fact, a displacement with such a time step would be $\delta x \sim \omega_N^{-1}$, essentially carried by the large scales. That way, the particles would not feel the smallest scales for large N, leading to an undesired sweeping effect. Please note that the WABC model does have a zero average velocity field and we refer here to local sweeping due to the specific construction of it by layers. Such phenomenon has been first observed by Thomson [81, 37]. In a similar flow, they observe that a local sweeping can lead to incorrect pair-dispersion law as initially found by Eliott and Majda [33]. The desired displacement here should be $\delta x \sim k_N^{-1}$. Consequently, we decide to set the time step to $dt_N = a k_N^{-1}$.

We define the diffusion term in equation (5.1) as

$$\kappa_N = b^2 \frac{\omega_N^2}{k_N^{2.4}}, \tag{7.5}$$

where $b = \sqrt{a}$. Since $dW \sim \frac{1}{\sqrt{a}}$, the noise term explodes when sending $a \to 0$. b acts as a corrective factor to counterbalance the diverging effect of a. This ensures that the noise always dominates at approximately the same scale. When testing weak convergence, we

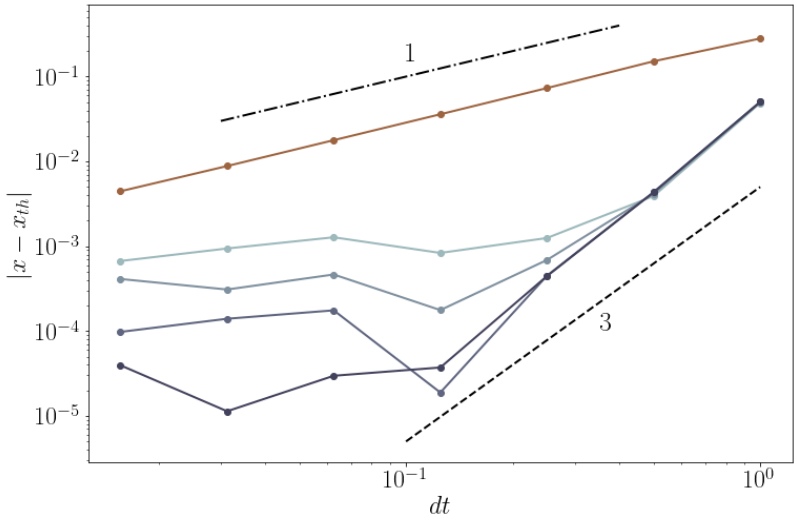

Figure 7.2: Comparison between theory and simulations for Euler-Mayurama (brown curve) and SRA3 (blue curves) for an increasing number of particles N_p, ranging from $N_p = 10^4$ to $N_p = 10^7$ (from light to deep blue). EM algorithm shows a weak order 1 as expected while SRA3 shows a higher weak order than the announced 3.

must set $b = 1$. Otherwise, the integration scheme changes as we decrease a. Numerical convergence is tested both when setting $b = 1$ (the standard way) and $b = \sqrt{a}$ (specific to this model).

We note that the particular noise scaling introduced here was deduced from a comparison with another noise type for $h = 1/3$. The optimisation procedure and the corresponding results are given in Appendix H.

7.2.3 . Weak convergence on the WABC model

Testing integration precision – We now introduce the tests of convergence for the WABC model to check that algorithms behave well. We also want to find the optimal a coefficient that leads to both good accuracy and low calculation time.

Early trials showed that the initial position $\boldsymbol{x}_0^* = (3.3492, 2.8988, 0.7665)$ results in a larger dispersion for solutions computed on $t \in [0, 1]$. We set the initial position $\boldsymbol{x}_0^*$ and we integrate an increasing number of trajectories N_p (from 2^{11} to 2^{20}) using a decreasing time-stepping coefficient a. We use a number of modes $N = 14$, already converging towards non-trivial distributions for large enough times.

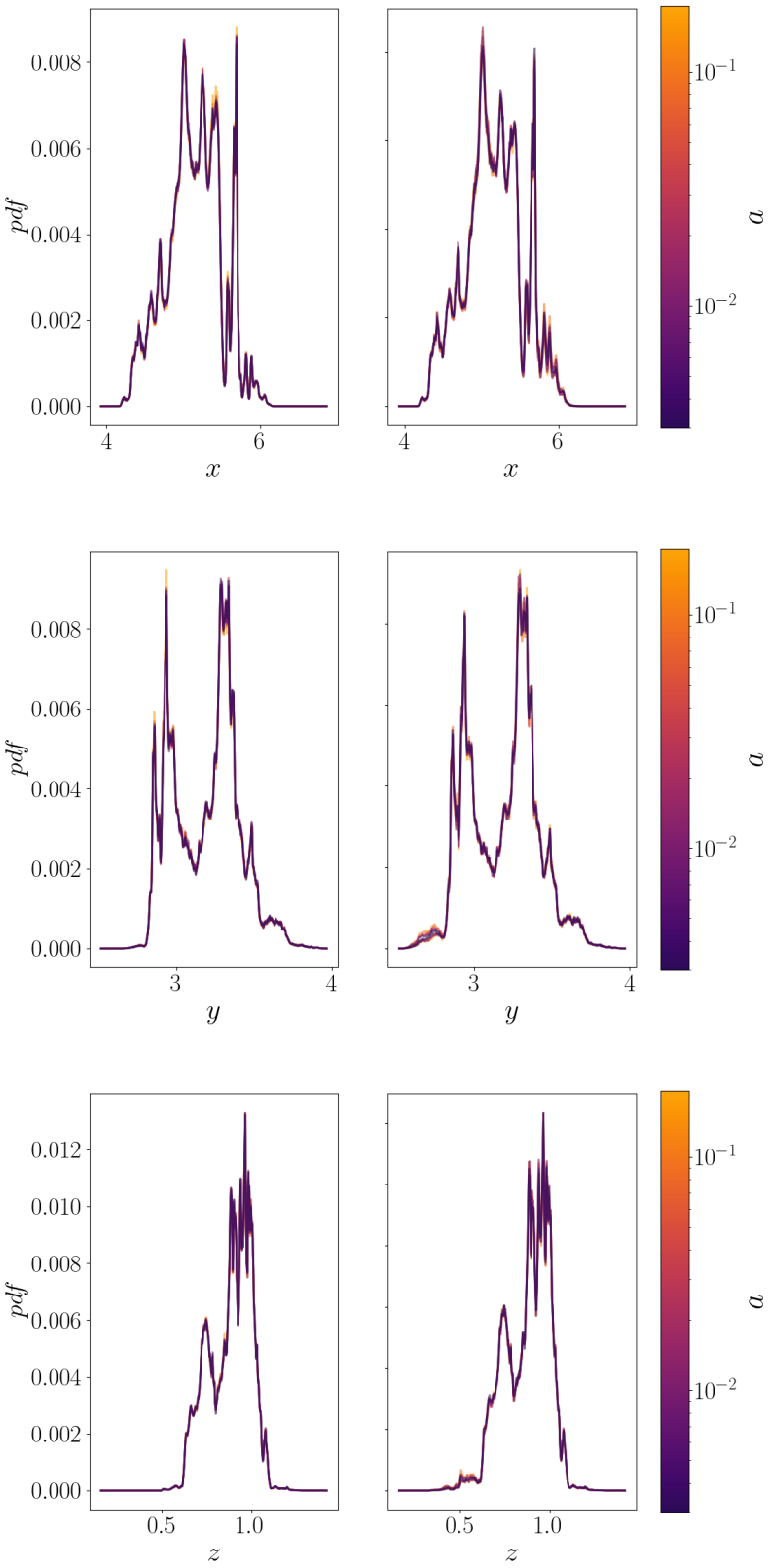

Figure 7.3: One-point statistics of the WABC model where $h = 1/3$ and $N = 14$, with decreasing a coefficient for checking numerical convergence of schemes with: Euler-Mayurama (Left) and SRA3 (Right) algorithms when $b = 1$ and varying a (indicated by the colour bar). From top to bottom, the one points statistics for the 3 coordinates x, y and z are displayed.

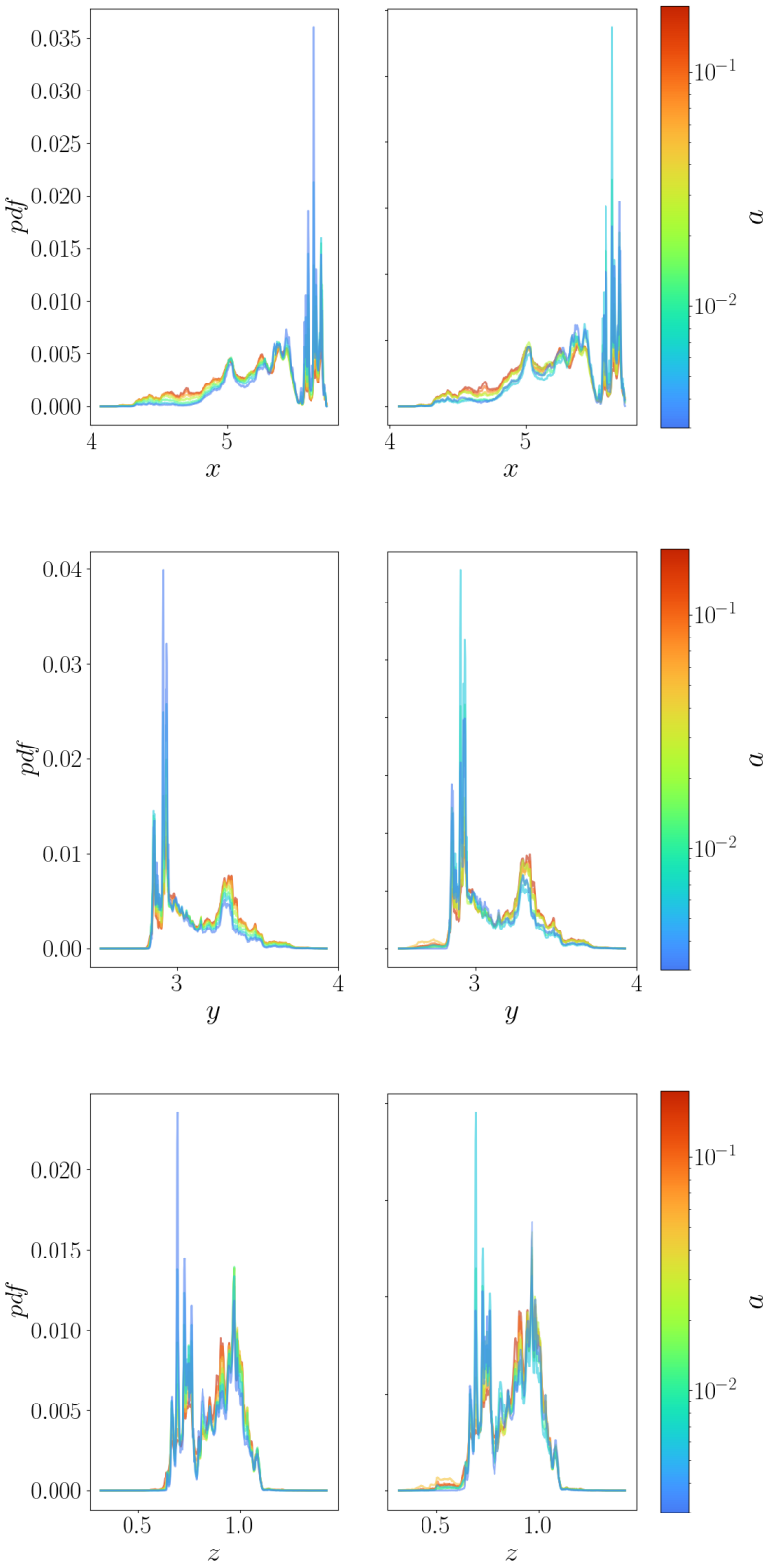

Figure 7.4: One-point statistics of the WABC model where $h = 1/3$ and $N = 14$ with, decreasing a coefficient for checking numerical convergence of schemes with: Euler-Mayurama (Left) and SRA3 (Right) algorithms when $b = \sqrt{a}$ and varying a (indicated by the colour bar). From top to bottom, the one points statistics for the 3 coordinates x, y and z are displayed.

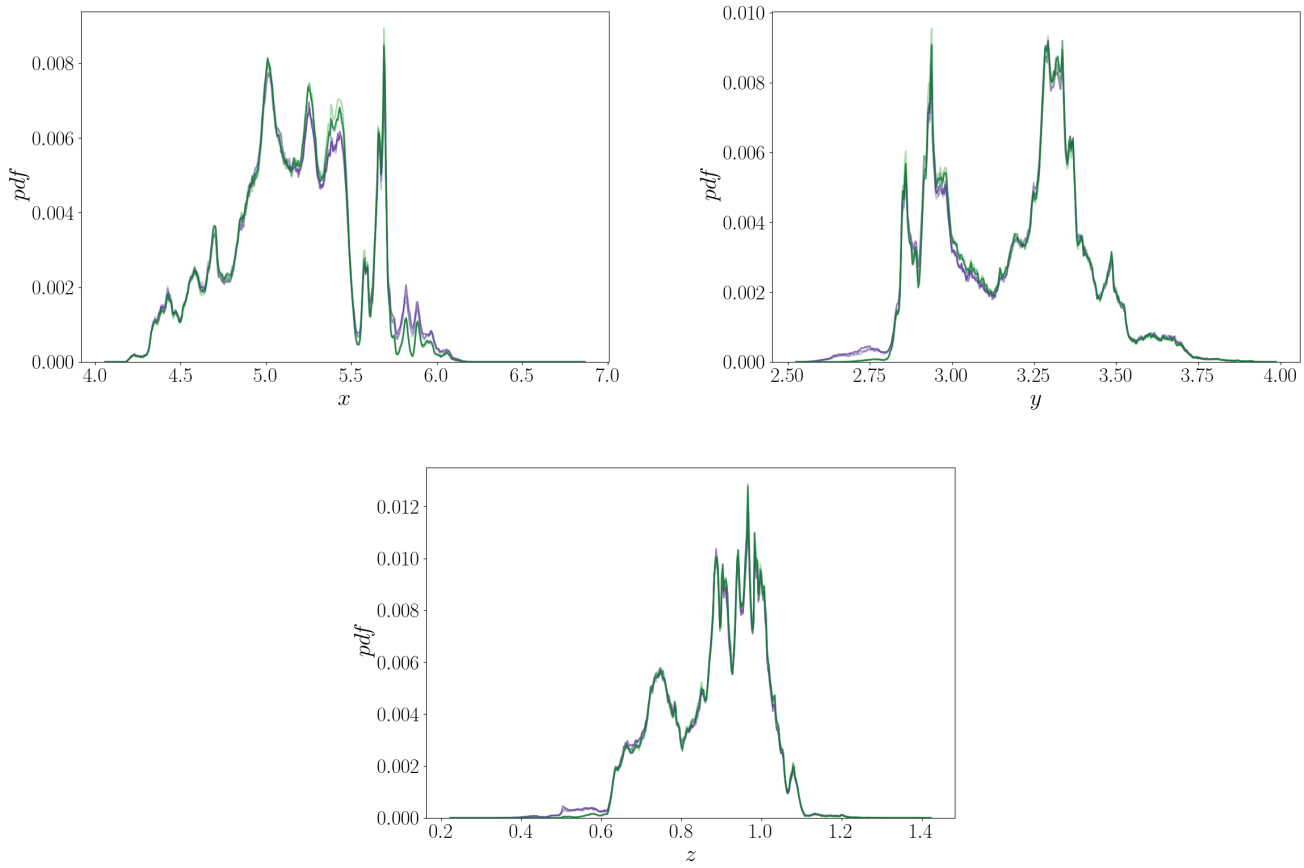

Figure 7.5: Comparison of one-point statistics for different algorithms and setups: Euler-Mayurama in Langevin setup (Purple), SRA3 in Langevin setup (Green) at small enough a for the WABC model with $h = 1/3$ and $N = 14$. From top to bottom, the one points statistics for the 3 coordinates x, y and z are displayed.

Figure 7.3 shows convergence of one point probability distributions for EM and SRA3 when $b = 1$ and decreasing a (i.e. the time step). We first observe that the distributions look similar between the two. A side by side comparison between the two stochastic solvers is displayed in Figure 7.5 and tends to confirm this tendency. We also note that the range of a tested does not seem to have a large influence on accuracy here.

This is further tested in Figure 7.4 where one point statistics of EM and SRA3 are compared in the case $b = \sqrt{a}$ with varying coefficient a. We observe here that a has a small impact on integration accuracy. Convergence appears to be slower than for the $b = 1$ case.

Testing the number of particles – We now want to evaluate the number of particles necessary to achieve statistical convergence. To that aim, we integrate different numbers of trajectories N_p, all emanating from $\boldsymbol{x}_0^*$ using three different time steps: $a_0 = 0.012$,

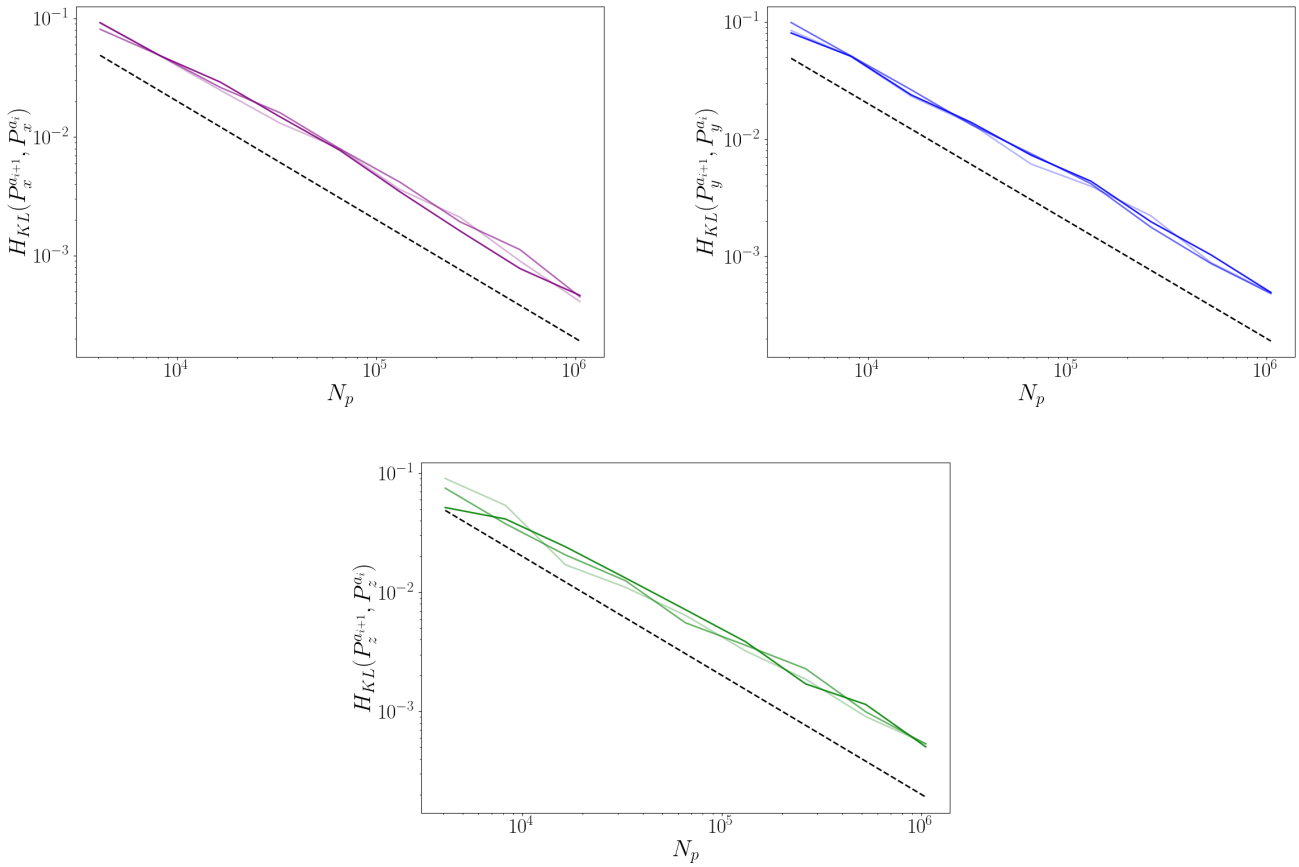

Figure 7.6: Kullback-Leibler divergence between one-point distributions of increasing number of particles for the WABC model where $h = 1/3$ and $N = 14$. All plots show a N_p^{-1} power-law represented by dotted lines.

$a_+ = 4a_0 = 0.048$ and $a_- = \frac{a_0}{4} = 0.003$. We then compute the Kullback-Leibler divergence $H_{KL}(P^{N_p^{i+1}}, P^{N_p^i})$ between distributions of increasing number of particles. We finally compare results between the three time steps to identify if the fluctuations observed in the other figures are due to numerical integration or statistical convergence. Results are presented in Figure 7.6.

The number of particles does indeed decrease statistical error. However, the integration constant a has very little effect on those plots as no saturation or change of regime is observed as a increases.

7.2.4 . Presentation of data

Checking for spontaneous stochasticity – We will first test for spontaneous stochasticity by simulating trajectories starting from x_0*, with h set to $1/3$. From the analysis of weak convergence above, we selected $a = 0.012$ and $N_p = 2^{20}$ which is a good compromise

		h = 1/3	h = 2/5	h = 1	
S.S. ?		x	x		
Dissipative		x			
Density		6	6	6	
l_c (k_{max})		3	3	3	Domain size
τ^*/τ_N	N = 6	0.32	0.17	5×10^{-4}	π
	N = 8	0.32	0.17	5×10^{-4}	$\pi/4$
	N = 10	0.3	0.16	5×10^{-4}	$\pi/16$
	N = 12	0.38	0.15	5×10^{-4}	$\pi/64$
	N = 14	0.32	0.17	5×10^{-4}	$\pi/256$

Table 7.1: Summary of WABC flow parameters and investigated scales. Density being the number of particles per voxel.

between computation time and accuracy of integration[3].

Checking the criterion – In order to test the transition deviation criterion, we perform many ensemble simulations on WABC flow for an increasing number of modes. We use the SRA3 algorithm with precision $a = 0.012$ and without any noise. We carry those studies on $h = \frac{1}{3}$ (rough dissipative case), $h = \frac{2}{5}$ (rough non dissipative case) and $h = 1$ (smooth case). In this scenario, we sample $N_p = 40M$ particles on a smaller and smaller domain $[0, \pi/2^{N-6}]$ so that by defining

$$k_{max} = k_N = 2^{-N}, \tag{7.6}$$

we are always looking at the same scale l_c compared to the lowest one:

$$\frac{l_c}{k_{max}} = 2.8\frac{\epsilon}{k_{max}} = 3. \tag{7.7}$$

We get trajectories on a time span $(0, 0.1)$, leading to 200 time steps.

We choose to have a grid for histograms where $N_x = N_y = N_z = 188$, which corresponds to having $\epsilon = \frac{2\pi}{N_x}$. Coupled with the large number of particles generated, we obtain a high density per voxel $d_\epsilon \approx 6$.

Duchon-Robert's coefficient Π_l is evaluated using the theoretical field. A grid $N_x^\Pi = N_y^\Pi = N_z^\Pi = 400$ is used in order to correctly compute this coefficient. Sides are trimmed up to 16 voxels on each boundary, in order to avoid any numerical artefacts. Using relation 6.19, we deduce $l = 2.8$ is needed to have $l_s \approx l_c$.

A summary of chosen parameters is given in Table 7.1.

7.3 . Results regarding spontaneous stochasticity

[3]We could have chosen a higher a in order to save some valuable computation time: no effect from integration is detected for that N_p. This indicates that the main source of error comes from the lack of particles.

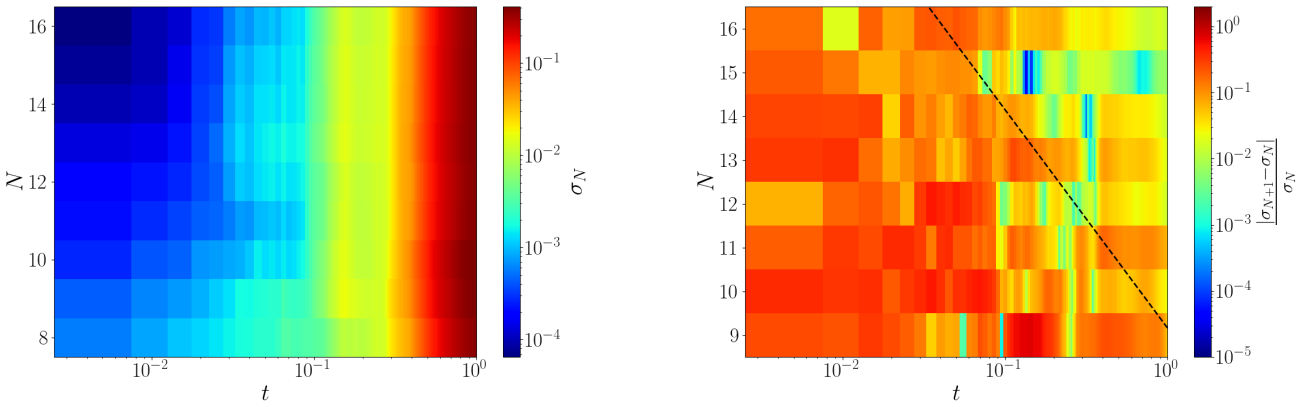

(a) (b)

Figure 7.7: Evolution of standard deviation σ_N (Left) and its rate of convergence $\delta\sigma_N = \frac{|\sigma_{N+1}-\sigma_N|}{\sigma_{N+1}}$ (Right) as a function of both number of modes N and time t for the WABC model with $h = 1/3$ and initial position $\boldsymbol{x}_0^*$. The dashed line represents the $\tau_N = \frac{1}{\omega_N}$ slope.

7.3.1 . Standard deviation study

We now present the evaluation of $\sigma_N^{x_0}$ computed on the Monte-Carlo simulations. It is summarised in Figure 7.7a. This graph shows a clear change of behaviour for approximately $t > 0.1$, from which standard deviation σ_N seems to remain constant as N increases. This is confirmed with Figure 7.7b which shows the rate of convergence $\delta\sigma_N = \frac{|\sigma_{N+1}-\sigma_N|}{\sigma_{N+1}}$. In the following, we decide to evaluate probability distributions at time $t = 0.875 > 0.1$ to quantitatively verify the convergence of statistics.

Finally, those two graphs also indicate a saturation of $\sigma_N^{x_0}$ for $N \geq 12$. We should therefore expect convergence of statistics for $N \geq 12$.

7.3.2 . One,two-points statistics

Qualitative approach – We show here the evolution of one and two-points statistics as the number of modes N increases. Figure 7.8 introduces results of the one-point statistics for the different axes x, y and z. The two-point statistics are represented by slices ($x - y$, $x - z$ and $y - z$) in Figure 7.9, Figure 7.10 and Figure 7.11.

One can notice that both one-point and two-points statistics seem to converge onto unique curves for increasing N. More specifically, the limiting probability is reached for $N \geq 12$, confirming our initial guess using standard deviation. The limit distributions appear to be notably non-trivial.

Kullback-Leibler divergence – We quantify this convergence through the analysis of Kullback-Leibler divergence between one-point statistics. Those results are presented in Figure 7.12 for axes x, y and z. All curves decrease as N increases, and reach a plateau for $N \geq 14$. This saturation was expected, as it corresponds to the non-negligible numerical

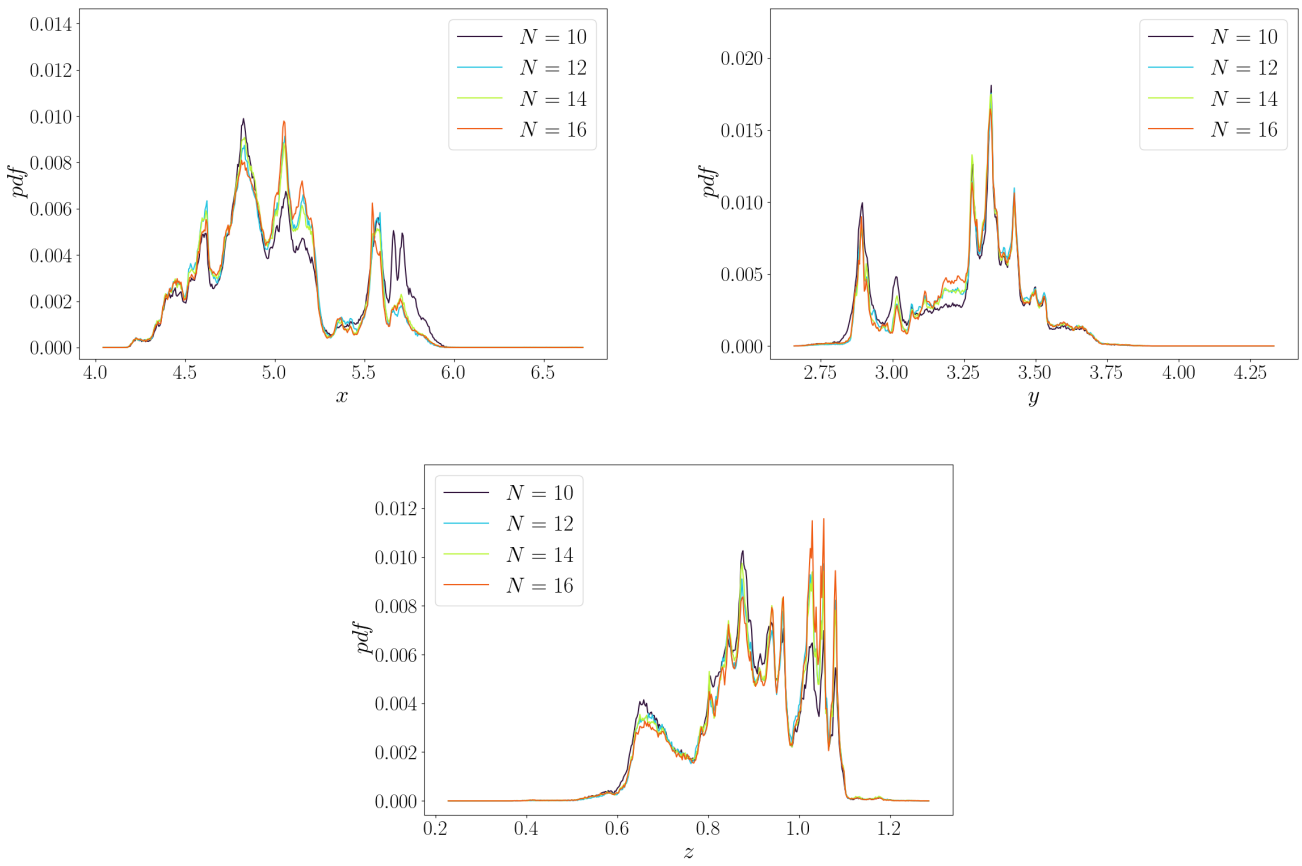

Figure 7.8: Evolution of one-point statistics through the number of modes N for the Langevin-WABC problem with $h = 1/3$ on the three different axes x, y and z.

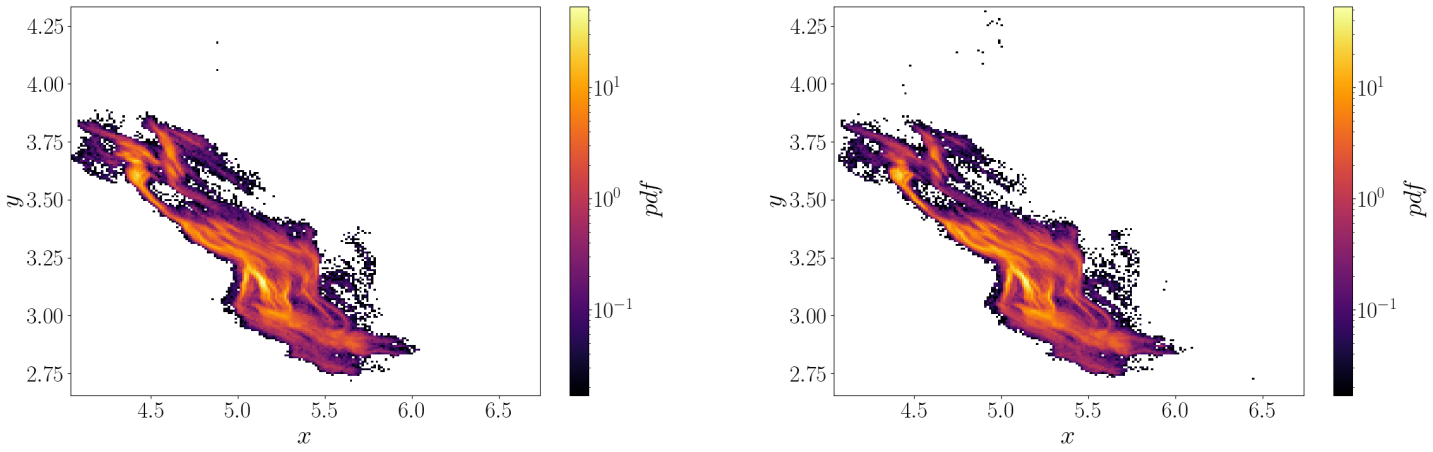

(a) $N = 10$ (b) $N = 12$

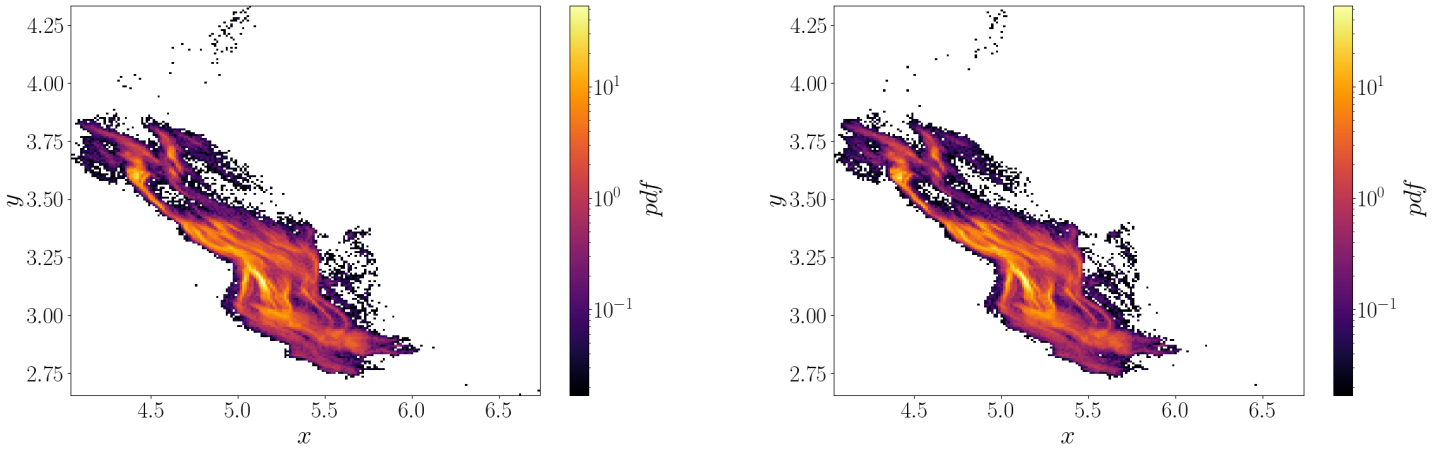

(c) $N = 14$ (d) $N = 16$

Figure 7.9: Evolution of two-points statistics through the number of modes N for the Langevin-WABC problem for the XY-slice and $h = 1/3$.

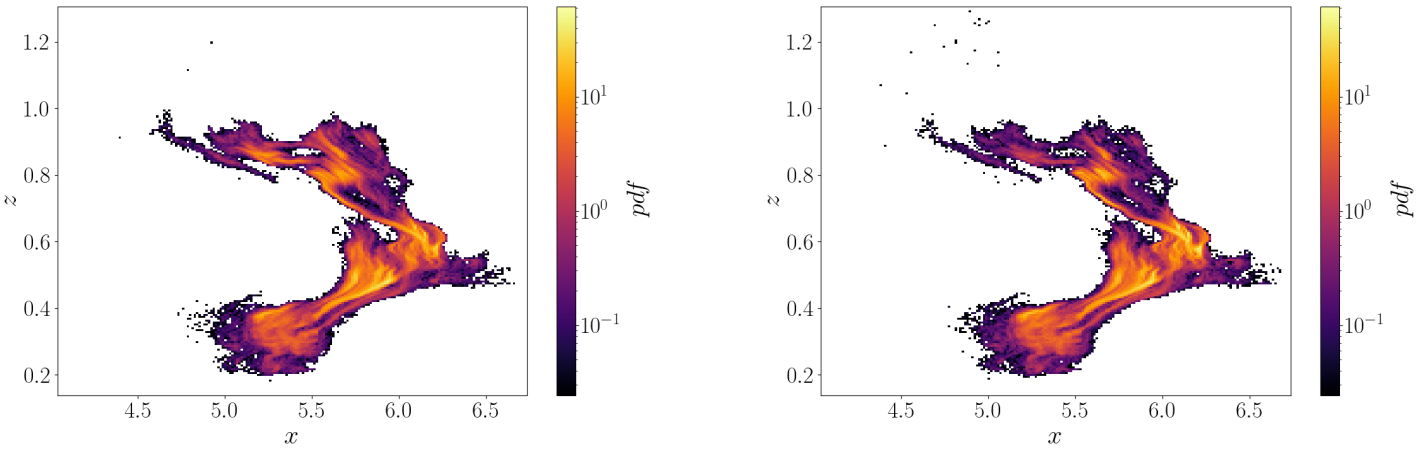

(a) $N = 10$ (b) $N = 12$

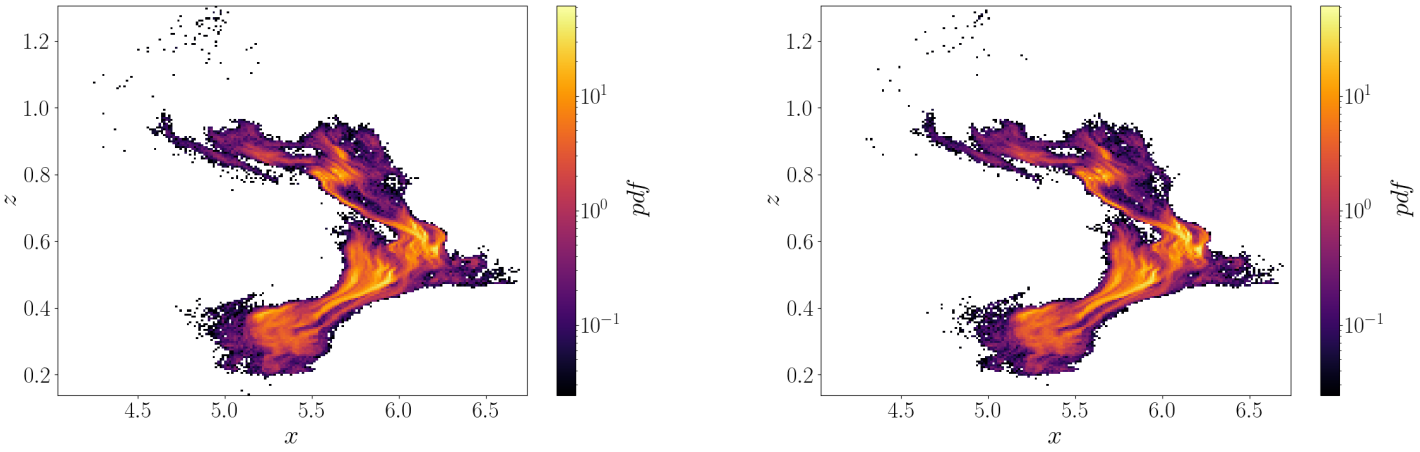

(c) $N = 14$ (d) $N = 16$

Figure 7.10: Evolution of two-points statistics through the number of modes N for the Langevin-WABC problem for the XZ-slice and $h = 1/3$.

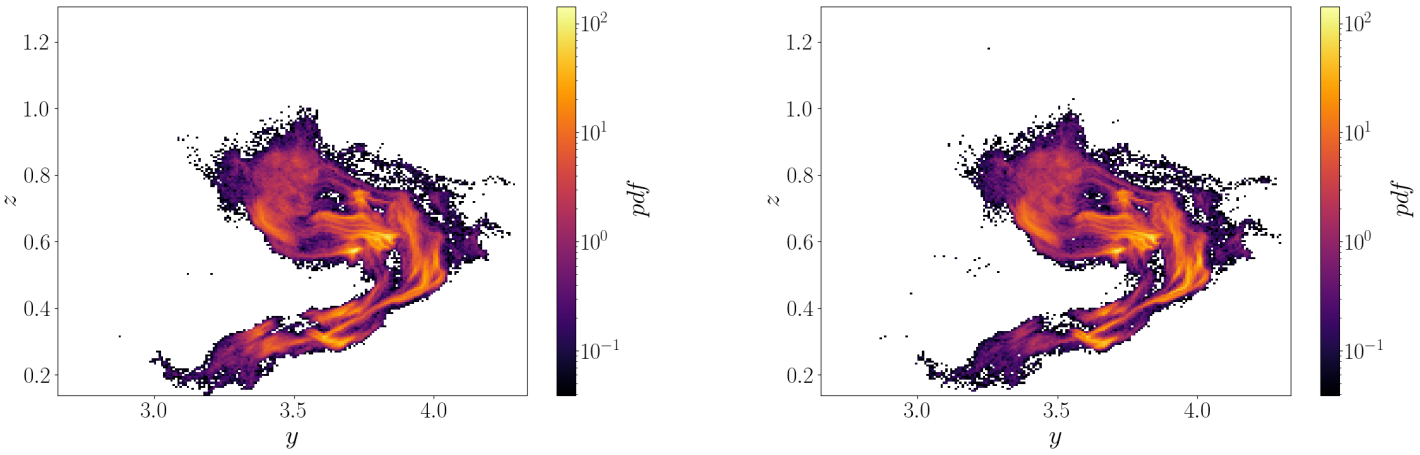

(a) $N = 10$ (b) $N = 12$

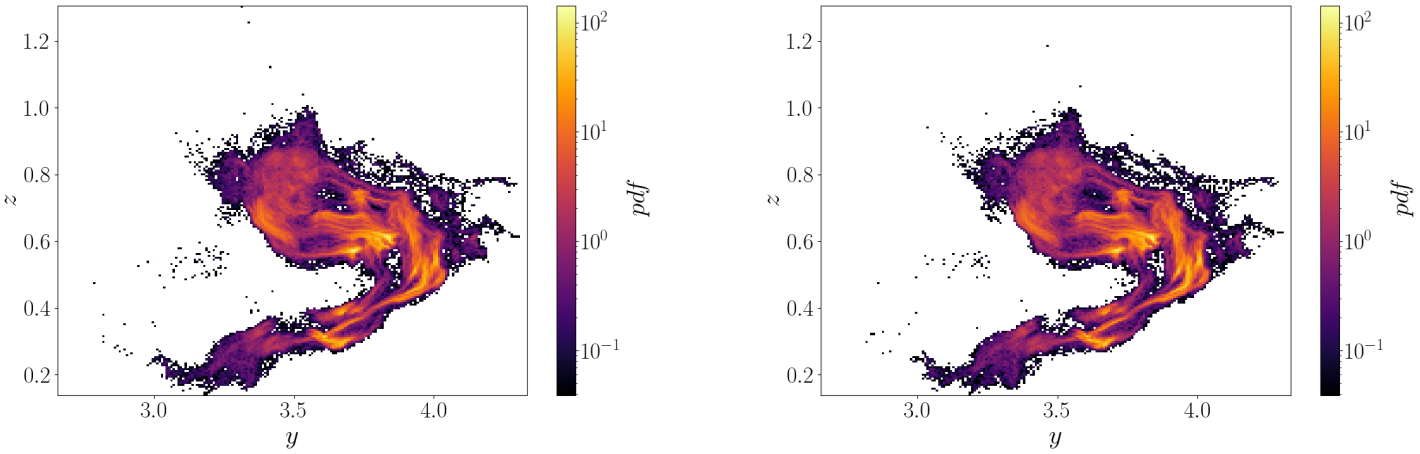

(c) $N = 14$ (d) $N = 16$

Figure 7.11: Evolution of two-points statistics through the number of modes N for the Langevin-WABC problem for the YZ-slice and $h = 1/3$.

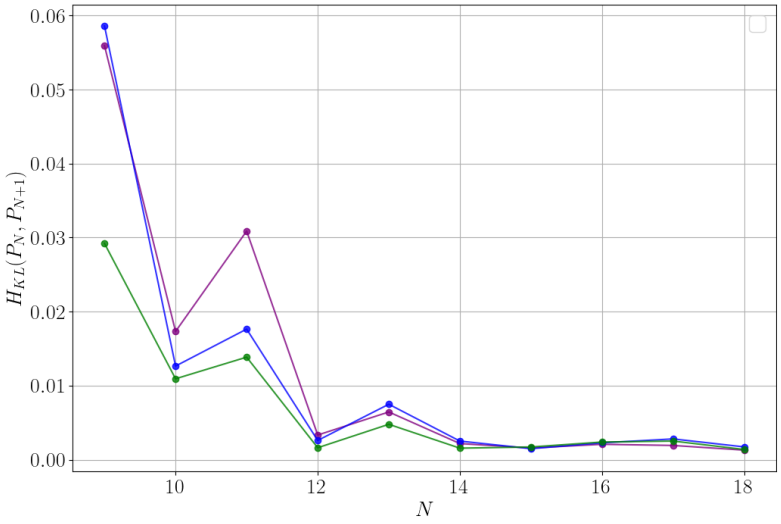

Figure 7.12: Evolution of the Kullback-Leibler divergence between one-point statistics of increasing number of modes N as a function of N for Langevin-WABC with $h = 1/3$ for the x-axis (purple), the y-axis (blue) and the z-axis (green).

errors. In particular, from the results of the previous section, the number of simulated particles is the limiting factor here.

7.4 . Discussions and testing universality

7.4.1 . Analysis of the results

The previous results, obtained for $h = 1/3$, show a convergence of statistics in the limit of numerical errors. The two-points probability distributions are also well converged at the considered N. The limit distributions are highly non-trivial and distinct from simple Diracs. From those results, we conclude that the WABC model can build Lagrangian spontaneous stochasticity in the sense that Lagrangian trajectories appear to be still stochastic in the limit of vanishing noise.

Computational burdens limited us to $N_p = 2^{20}$, which is, at the present, the main limiting factor to the convergence of the Kullback-Leibler divergence. In the event where computational resources increases, allowing for higher values of N_p, the scheme accuracy would become the main limiting factor.

7.4.2 . Influence of noise type

Knowing that spontaneous stochasticity exists in this model, is it possible to extend those results to any other type of noise? This would test universality of the model under the change of regularisation.

Definition – We investigate this possibility by introducing the ensemble of Cauchy problems

$$\begin{cases} d\boldsymbol{x}_N(\boldsymbol{x},t) = \sum_{i=1}^{N} \frac{\omega_i}{k_i} \boldsymbol{U}(k_i \boldsymbol{x}) dt \\ \text{with} \quad \{\boldsymbol{x}(0) = \boldsymbol{x}_0 \,|\, \boldsymbol{x}_0 \in \mathcal{B}(\boldsymbol{x}_0^*, \eta_N)\}, \end{cases} \tag{7.8}$$

where η_N denotes the ball radius. Since the uncertainty on the initial position represents the stochastic regularisation, η_N should decrease with the number of modes N. We choose to have in particular $\eta_N = \frac{10}{k_N}$ [4]. We refer to this setup as 'Cauchy-WABC'. We introduce the probability distribution p_N^C where initial conditions are assumed to be uniformly distributed inside the ball $\mathcal{B}(\boldsymbol{x}_0^*, \eta_N)$

$$p_N^C(\boldsymbol{x}, 0) = \frac{1}{V_{\eta_N}} \Theta_H(\eta_N - ||\boldsymbol{x} - \boldsymbol{x}_0^*||_2) \tag{7.9}$$

with Θ_H the Heaviside function and V_{η_N} the ball volume. In the same way as for Langevin-WABC, we say that spontaneous stochasticity occurs if and only if p_N^C verifies condition 5.2.

Observations – We integrate this problem with a Runge-Kutta method of strong order 4/5 for the same number of particles $N_p = 2^{20}$. The results presented in Figure 7.13 and Figure 7.14 show comparisons of one and two-points statistics between Langevin and Cauchy-WABC. Additional results showing convergence of Cauchy's regularisation are available in Appendix G. We reach identical conclusions as for the Langevin-WABC case: the statistics appear to be converged for $N \geq 12$. The distributions for both regularisations look notably similar, providing evidence of universality of spontaneous stochasticity with respect to regularisation.

7.4.3 . Hölder exponent influence

We showed that the WABC model is spontaneously stochastic for $h = 1/3$. This conclusion should be valid for any other Hölder exponent $h < 1$. We here test this hypothesis by computing one-point statistics for two other Hölder exponents: $h = 1/5$ and $h = 2/5$. We keep the same simulation characteristics as before: we only change the Hölder exponent. We did not test higher coefficients because spontaneous stochasticity appears at longer times for those. The associated results are presented in Figure 7.15.

We note that both cases seem to converge, in the limit of statistical errors. The case $h = 2/5$ does not seem as clear as the $h = 1/5$ case though. Integrating trajectories up to those times comes as a challenge as a larger h requires a large number of particles to reach statistical convergence. We nevertheless conclude that WABC model should be spontaneously stochastic for at least $h \leq \frac{2}{5}$ and initial position $\boldsymbol{x}_0^*$.

Finally, the noise scaling in equation (7.5) was chosen for the $h = 1/3$ case. So far, no theory was built to derive this scaling properly and it was deduced heuristically for the

[4] An elementary cell in this model is given by its smallest scale k_N^{-1}. All particles starting in this cell will have the same initial velocity. The resulting trajectories would inevitably be totally identical for up to a certain time. This phenomenon would ask for longer integration and false durations for the appearance of spontaneous stochasticity.

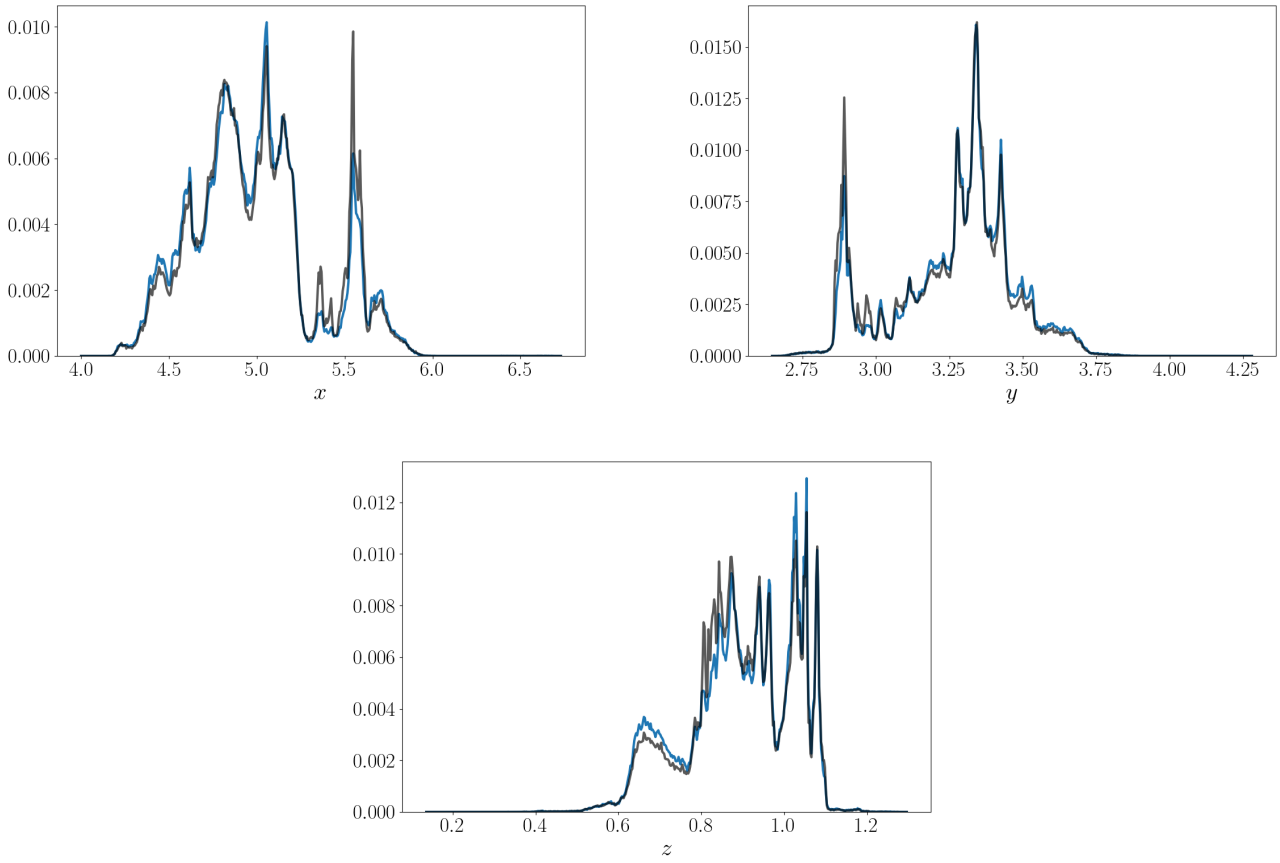

Figure 7.13: Comparison of one-point statistics between Langevin-WABC (Blue) and Cauchy-WABC (Black) for $N = 16$ and $h = 1/3$ on the three different axes x, y and z.

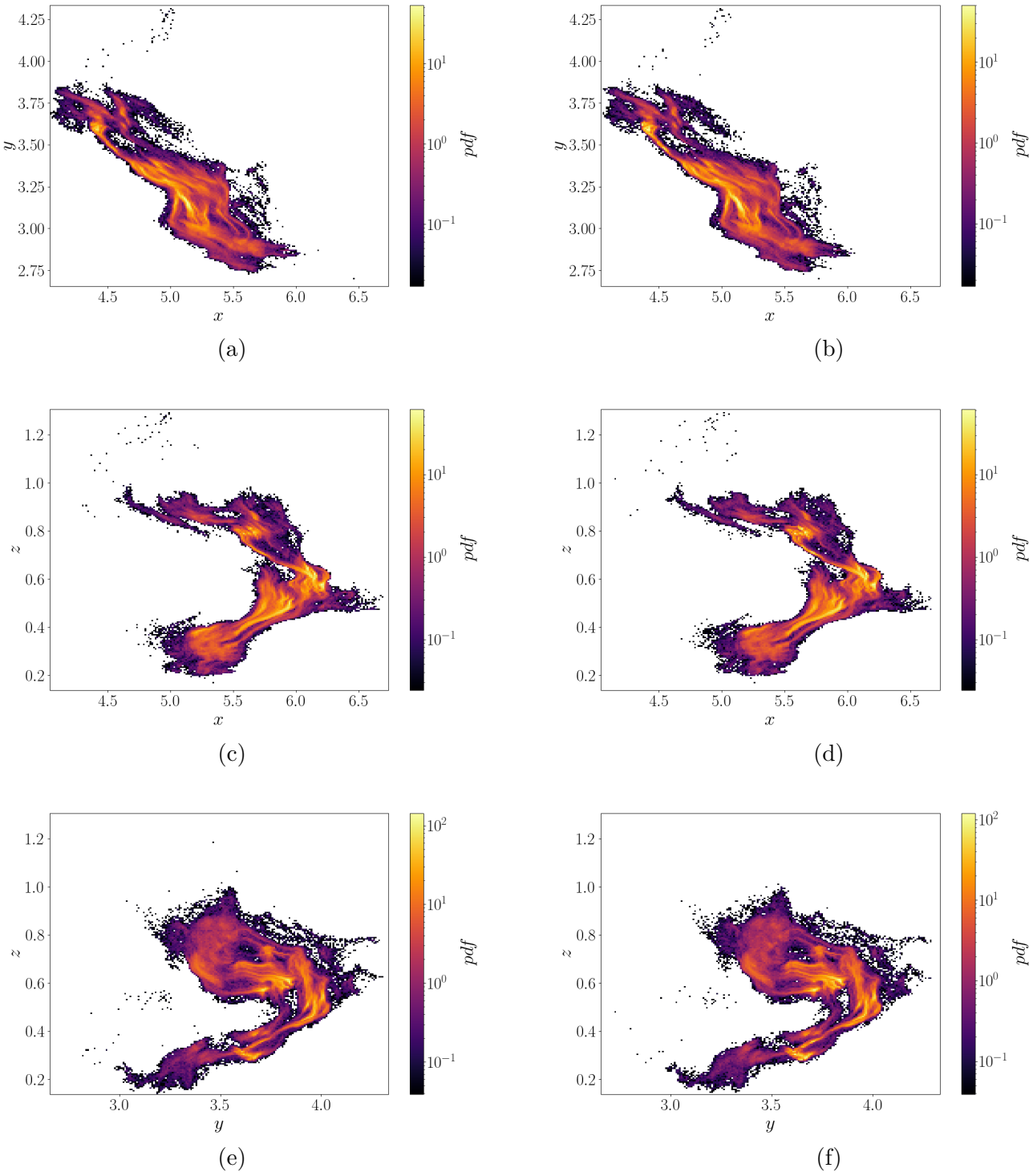

Figure 7.14: Comparison of two-point statistics between Langevin-WABC (Left) and Cauchy-WABC (Right) for $N = 16$ and $h = 1/3$ on the three different slices $x - y$, $y - z$ and $x - z$.

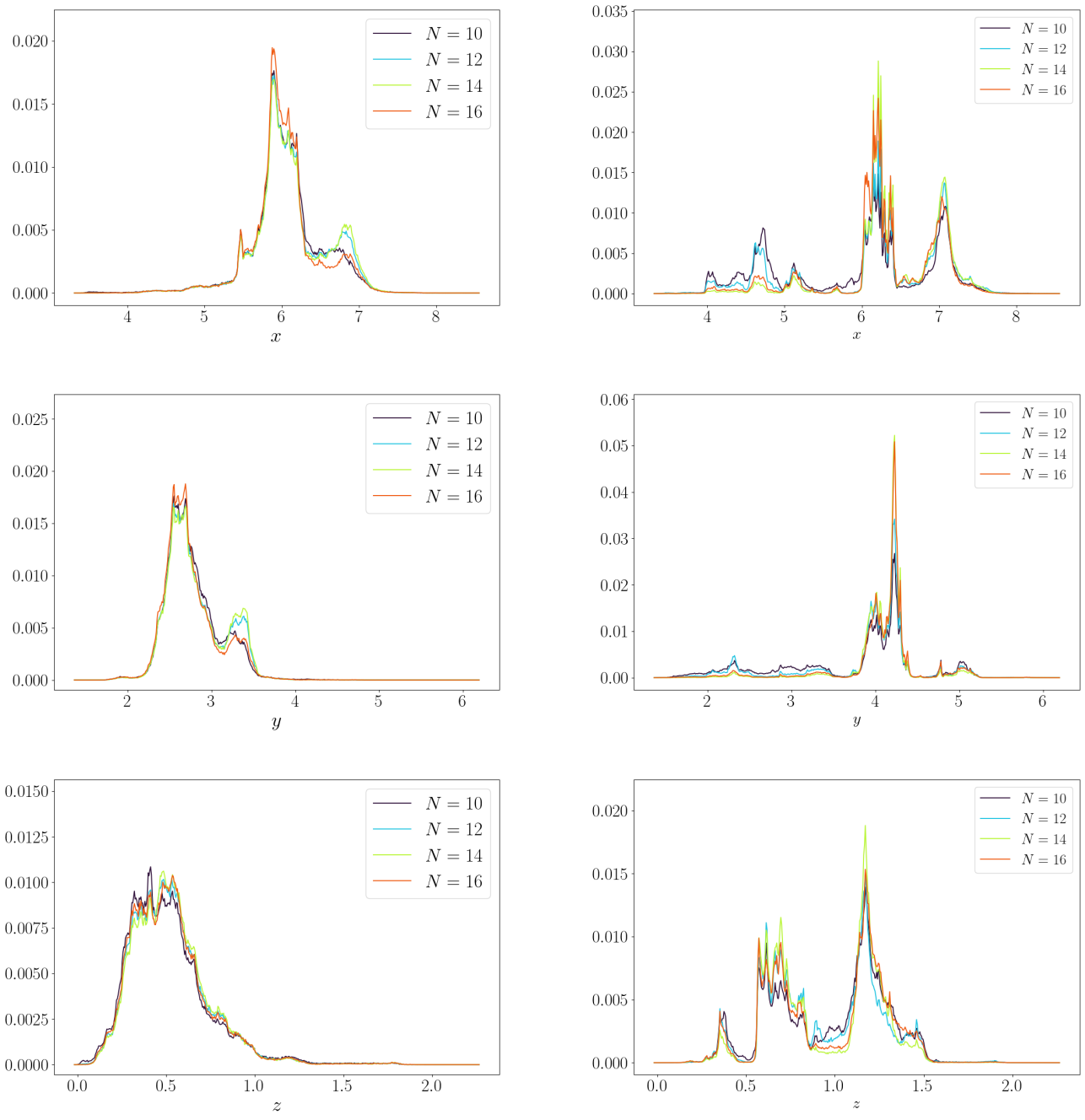

Figure 7.15: One point statistics of WABC-Cauchy problem at $t = 0.875$ where $h = 1/5$ (Left) and $h = 2/5$ (Right). The x, y and z axes are displayed from top to bottom.

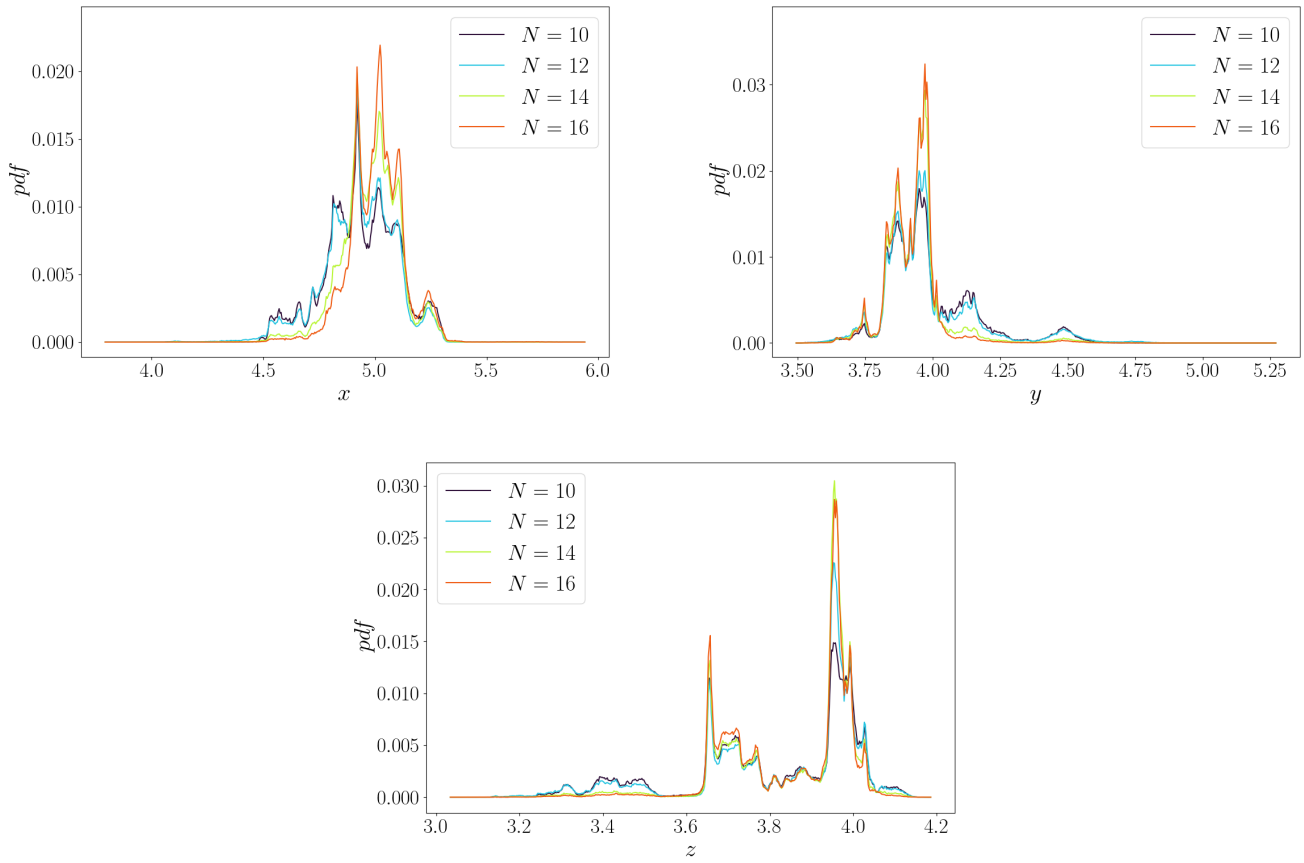

Figure 7.16: Evolution of one point statistics through the number of modes N for initial position $\boldsymbol{x}_0^\pi$ at time $t = 0.875$ for the WABC model with $h = 1/3$.

case h=1/3, under the hypothesis that non-linearities produce non trivial scaling. More investigations are needed to test the scaling and its dependence with respect to h.

7.4.4 . Initial position dependence

First approach – Since the model is singular everywhere, it should present spontaneous stochasticity for any other initial position. This hypothesis can be tested by starting the trajectories from another initial position $\boldsymbol{x}_0^\pi = (\pi, \pi, \pi)$. The corresponding one-point statistics evaluated at $t = 0.875$ are depicted in Figure 7.16. At a similar time, statistics in this case appear less converged than with the other initial condition, suggesting that the time to reach convergence depends on initial position: $t_s^{x_0^\pi} > t_s^{x_0^*}$.

This makes investigations harder, as we need to integrate the trajectories on longer times. Also, particles tend to disperse more, making the construction of histograms harder (having less particles per bins).

Average analysis – To overcome such limitations, we use a simpler procedure to

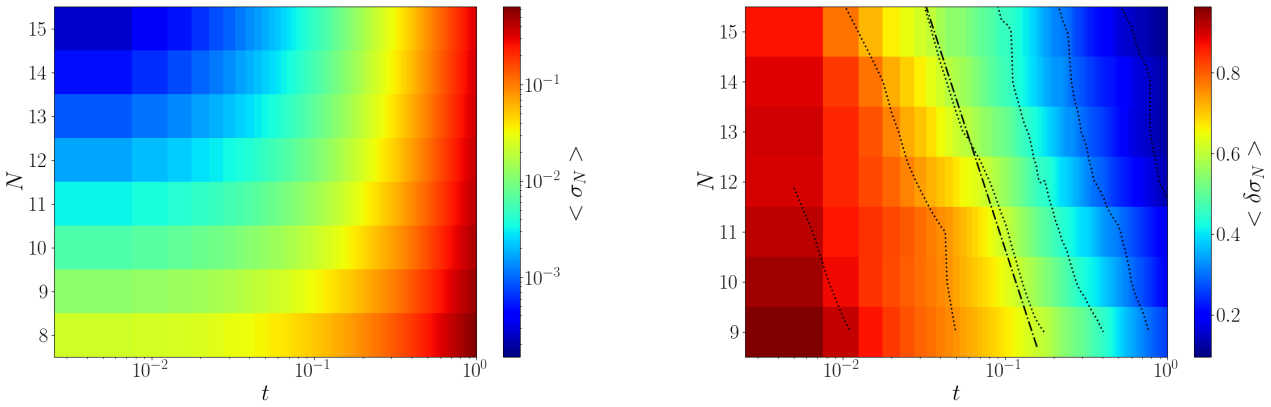

Figure 7.17: Evolution of standard deviation $\langle \sigma_N^{x_0} \rangle_{x_0}$ (Left) and rate of convergence $\langle \delta\sigma_N^{x_0} \rangle_{x_0}$ (Right) averaged over all selected initial position as a function of time and number of modes. Isocontours are represented in dotted lines. The closer to 0, the faster convergence is.

investigate the onset of spontaneous stochasticity: we randomly pick 1000 initial positions within the domain and generate 1000 trajectories for each. We then compute the standard deviation $\sigma_N^{x_0}$ and its rate of convergence $\delta\sigma_N^{x_0}$ for each of those initial positions. We finally calculate an average of those two quantities over positions $\langle \sigma_N^{x_0} \rangle_{x_0}$ and $\langle \delta\sigma_N^{x_0} \rangle_{x_0}$. This gives us a global rate of convergence for which results are presented in Figure 7.17.

Finally, we pick a threshold $\delta\sigma_N^{max} = 10^{-1}$ and evaluate the times τ_σ at which $\delta\sigma_{N_{\tau_\sigma}}^{x_0} < \delta\sigma_N^{max}$ for each $N_{\tau_\sigma} > N$. This acts as a biased rough criterion for convergence: if no time is found to follow the above condition, then the corresponding initial position is discarded. We thus only use this crude criterion to estimate the probability distributions of those times. This will give information about whether those statistics are peaked or spread. The corresponding results are presented in Figure 7.18.

We observe that the global standard deviation seems to converge towards non-zero values, as expected. A clear dependence on the number of modes N appears on the rate of convergence plot. Isocontours show a similar scaling as time increases, seemingly being $\sim \frac{1}{\omega_N^{0.5}}$, larger than characteristic time $\tau_N \sim \frac{1}{\omega_N}$. This suggests that non-linearities and chaos have a large impact on the scaling properties of the observed phenomenon. This also suggests that spontaneous stochasticity takes less and less time to build up in this model as $N \to \infty$.

Distributions of criterion times τ_σ are definitely not peaked but quite spread out as Figure 7.18 depicts. This suggests a high dependence on initial position regarding convergence time, despite the biases brought by the above criterion.

7.5 . Results regarding transition deviation

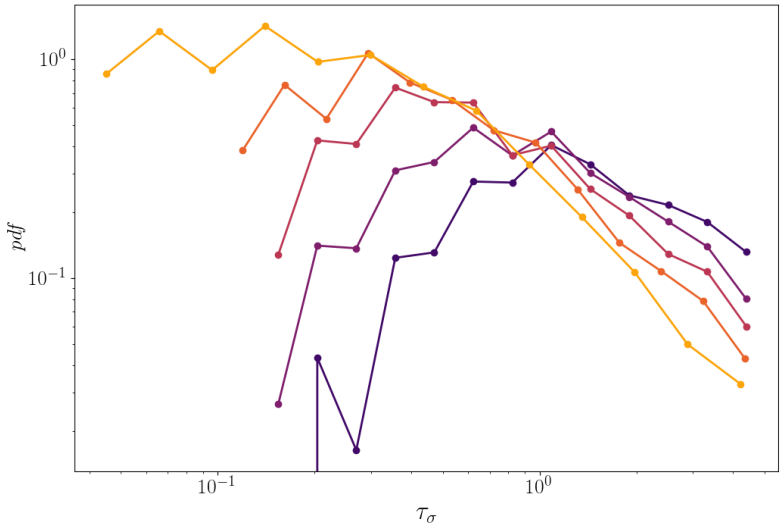

Figure 7.18: Probability distributions of convergence time based on threshold value $\delta\sigma_N^{max} = 10^{-1}$ and Hölder exponent $h = 1/3$ for the WABC model. The lighter the colour, the higher the mode N (from $N = 9$ to $N = 13$).

We showed that the WABC model is spontaneously stochastic. We now move on to testing the transition deviation criterion to see whether it is sensitive to spontaneous stochasticity or not. We will conclude from those observations if our criterion can be used in real flows or not.

7.5.1 . Joint probabilities

We introduce joint probability distributions between $\sigma_N^{\epsilon,\tau^o}$ and Π^l for $h = 1/3$ and $h = 1$ in Figure 7.19. For $h = 1/3$ and $N = 6$, we observe that the joint probability distribution is wider for low Π^l and $\sigma_N^{\epsilon,\tau^o}$. It becomes thinner for larger Π^l and $\sigma_N^{\epsilon,\tau^o}$, showing a correlation between the two quantities. The expected regime $(\Pi^l)^{\frac{1}{3}}$ seems to be respected (for large enough Π^l and $\sigma_N^{\epsilon,\tau^o}$ at least). We note that the distributions do not seem to change drastically when N increases, keeping to the $(\Pi^l)^{\frac{1}{3}}$ law. We do not observe the same behaviour in the $h = 1$ case however. For low N, we observe a similar correlation between the two quantities. When N increases, the distributions start to elongate in the direction of small Π^l. This shows that as N increases, Π^l and $\sigma_N^{\epsilon,\tau^o}$ decorrelate. The expected regime $(\Pi^l)^{\frac{1}{3}}$ ceases to match the data for $N = 14$ in that case.

7.5.2 . Transition deviation criterion

The transition deviation criterion $< \sigma_N^{\epsilon,\tau^o} >_\Pi$ as a function of Π^l is given in Figure 7.20. We observe in all cases that the curves are flat for low Π^l, which confirms the decorrelation between $\sigma_N^{\epsilon,\tau^o}$ and Π^l observed in the study of the joint probabilities. For $h < 1$, we note that the curves become non-flat for a large enough Π^l, for any N. The expected law $(\Pi^l)^{\frac{1}{3}}$

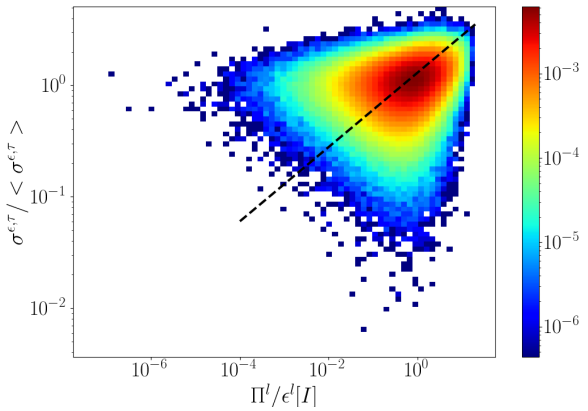

(a) $h = \frac{1}{3}$ and $N = 6$

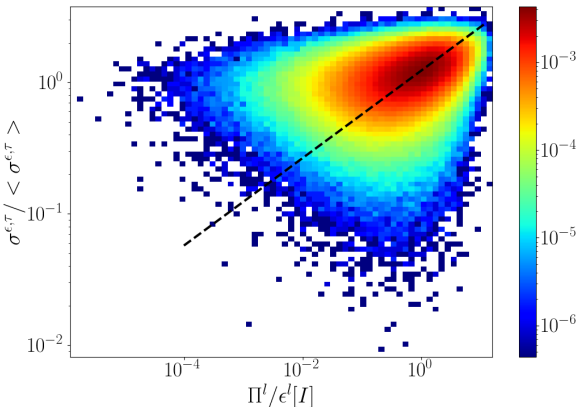

(b) $h = 1$ and $N = 6$

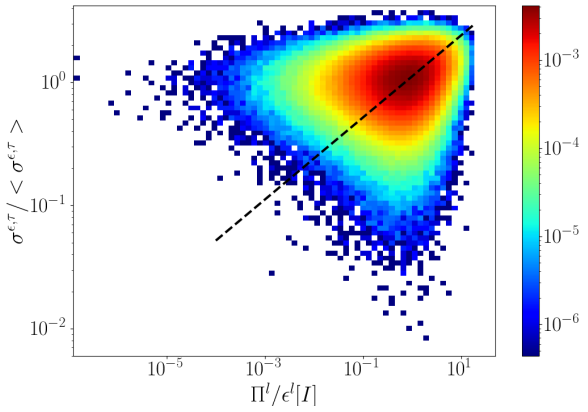

(c) $h = \frac{1}{3}$ and $N = 10$

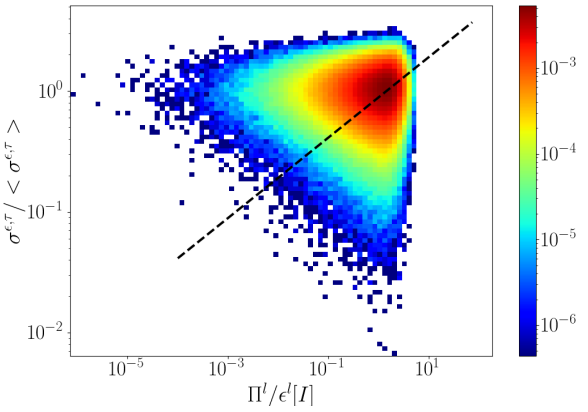

(d) $h = 1$ and $N = 10$

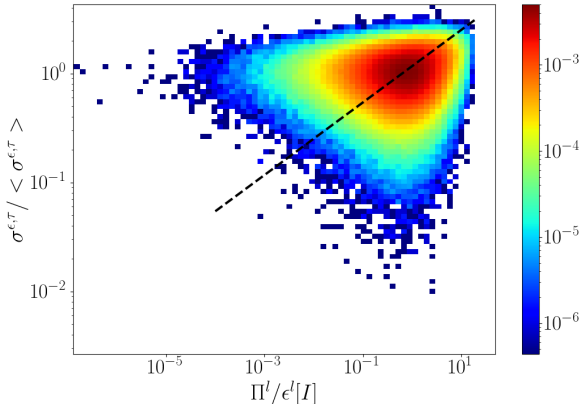

(e) $h = \frac{1}{3}$ and $N = 14$

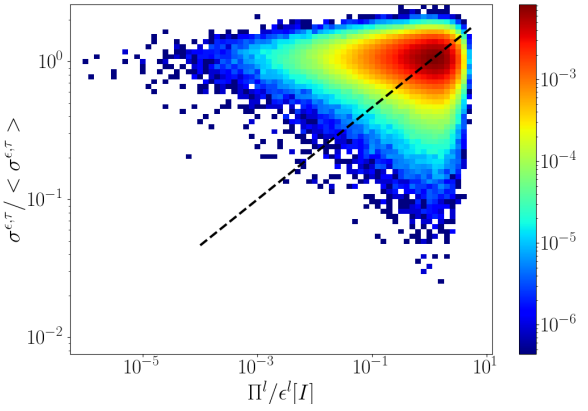

(f) $h = 1$ and $N = 14$

Figure 7.19: Joint probability distribution between σ^{ϵ,τ^o} and Π^l for increasing N and two different Hölder exponents h. The dashed lines correspond to the scaling law provided by equation (5.19).

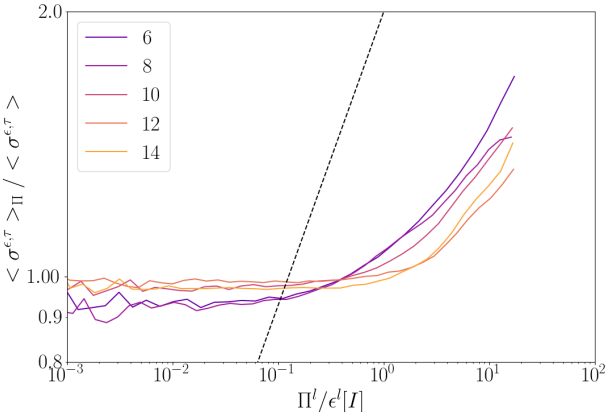

(a) $h = \frac{1}{3}$

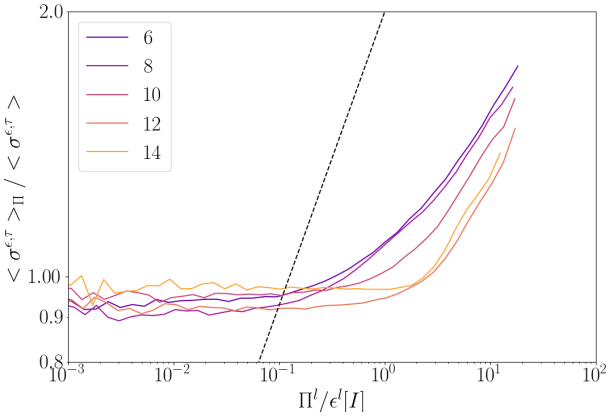

(b) $h = \frac{2}{5}$

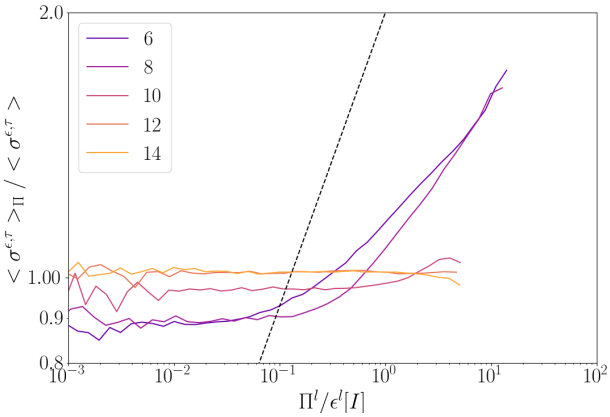

(c) $h = 1$

Figure 7.20: Conditioned average $\langle \sigma^{\epsilon,\tau^o} \rangle_\Pi$ as a function of Π^l for an increasing number of modes N for the WABC model with three different h. The dotted curve corresponds to the $\frac{1}{3}$ determined by equation (5.19).

never seems to be respected. For $h = 1$, a different behaviour appears: as N increases, the curves flatten totally. This underlines the decorrelation already observed for $N = 14$ in the study of joint probabilities.

We finally observe a subtle decrease of the maximum Π^l in the $h = 2/5$ case. This is expected since the irregularities in that case are non-dissipative: $< \Pi^l >$ diminishes as $N \to \infty$.

7.5.3 . Discussion

As expected, the larger Π^l are more correlated to $\sigma_N^{\epsilon,\tau^o}$. In this scope, we observed that the cases $h < 1$ are showing a correlation between the two quantities that do not seem to change with N. This comes in total opposition with what is observed in the case $h = 1$ where the curves show an important dependence on N. We therefore conclude that the transition criterion $< \sigma_N^{\epsilon,\tau^o} >_\Pi > 0$ in the limit $N \to \infty$ works for $h = 1/3$ or $h = 2/5$. Since we showed that the WABC model is spontaneously stochastic for $h = 1/3$ and $h = 2/5$ we also conclude that the transition deviation criterion is sensitive to spontaneous stochasticity.

7.6 . Conclusions

We built a model that presents spontaneously stochastic behaviour within the limits of integration and statistical convergence. The main difficulty with this model is to reach weak convergence. The high number of modes and particles represents a challenge regarding both computation time and storage. Switching to GPU computations allows for a tremendous reduction of computation time. Further reduction in computational cost may be achieved by switching to 32 bits, or by optimising time steps.

This model is universal with respect to change of regularisation. We showed that both Langevin-WABC and Cauchy-WABC converge onto similar distributions in the case of $h = 1/3$. Universality with respect to change of Hölder exponent has also been investigated, by both lowering and increasing h, without noticeable influence on the results. Due to time limitation, we were however not able to test whether spontaneous stochasticity develops for the whole interval $0 < h < 1$. It is also unclear if the noise scaling should depend on h. However, performing such investigations requires the ability to simulate more than $N = 18$ modes, with a large number of particles, in a reasonable computing time.

Using the fact that the WABC model was found to develop Lagrangian spontaneous stochasticity, we were able to check if the transition deviation criterion (5.22) was meaningful. We observed that in the case of an irregular flow ($h = 1/3$ and $h = 2/5$), the criterion reaches non-zero values for large 'dissipation' Π^l, even in the limit of vanishing regularisation. On the contrary, for the regular case $h = 1$, a clear decorrelation appears between the criterion and Π^l, as expected. We concluded that this criterion is well-defined in the inviscid limit and is sensitive to spontaneous stochasticity.

Thanks to this results, we shall now adapt the transition criterion to the experimental

data and compare them with the cases $h = 1/3$ or $h = 1$ obtained for the WABC flow.

8 - Observations in real flows

In this chapter, we introduce the numerical and experimental data that we use to study the transition deviation criterion. We then briefly present the methodology to get the experimental Lagrangian trajectories from the fast movement of the tiny particles in the experiment. An algorithm designed to compute the Eulerian velocity field from the Lagrangian data is then broached.

A last part is dedicated to the analysis of the data. Due to a lack of time, we only present preliminary results. We intend to only give a proof of concept of our methodology. A more detailed study of the transition deviation criterion will be provided for an upcoming publication.

8.1 . Presentation of the data

8.1.1 . Numerical data

Experimental results are plagued with uncertainties due to noise, either due to the experimental set-up or to the chain of measurements and data processing. To control them, we use a comparison with numerical simulations provided by J-P. Laval, in which Lagrangian tracers are advected by a $3d$ homogeneous flow field computed on the torus $[0, 2\pi]^3$.

The simulation corresponds to a very well resolved Direct Numerical Simulation (DNS) of decaying turbulence starting from a Taylor Green initial solution. A pseudo-spectral scheme on a 768 periodic cubic box of length 2π is used to solve the Navier-Stokes equations. It provides us synthetic data onto which we can apply our whole chain of processing, allowing us to separate the contribution due to experimental noise. We select times where Re changes the least to ensure the non-variability of our measurements. We also pick times that are statistically independent. We focus on the case of $Re \sim 137$ with $60M$ particles advected. We define here a grid $N_x = N_y = N_z$ for histograms that we adapt to the scale we want to investigate.

The computation of local standard deviations requires a minimum amount of particles for convergence of statistics. We arbitrarily select voxels that have at least $d_\epsilon = 8$ particles

Re	Re_λ	N_x	l_c (η)	Density	τ^* / τ_η
137.1	60	200	3.9	7.5	0.2
		150	5.2	17.8	0.2
		100	7.8	60	0.2
		70	10.7	175	0.2
		50	15.6	480	0.2

Table 8.1: Summary of DNS parameters and investigated scales. Density here being the number of particles per voxel.

Figure 8.1: Picture of the 'Giant Von Kármán' experiment. The black motors on the left drive the belts above and below the aluminium case, rotating the impellers inside.

regardless of the grid size. The large density in this simulation allows us to study a large range of scales that are reported in Table 8.1.

8.1.2 . Experimental data

Presentation of the experimental setup – We use experimental data partly obtained from the 'Giant Von Kármán' (GVK) experiment in the Saclay laboratory. GVK is a $1.5m$ high cylindrical experiment with radius $R = 0.5m$. Two impellers, situated on top and bottom of the experiment, are rotating in opposite directions, moving a ton of water. The created mean flow is, in the simplest case, divided into two circulation cells with a shear layer oscillating in the middle of the cylinder (see Figure 8.2). The resulting flow in the centre of the experiment is close from homogeneous and isotropic turbulence. Optical measurements are taken at this location. Because of the first law of thermodynamics, dissipation is converted into heat in the experiment, which can induce spurious variation of the viscosity due to temperature increase. The flow is therefore cooled down by two cooling systems situated above and below each turbine, keeping the water at constant temperature at all times. Two configurations are available in this setup: the contra and anti configurations with their two associated mean torques. When the impellers are in contra-rotation, the back of the curved blades pushes water. When the impellers are in anti-rotation, the front of the curved blades pushes water. The latter case can lead to a random bifurcation in the flow (for constant motor velocity inputs) where the two cells can merge, forming one turbulent cell as depicted on Figure 8.2 [70, 64, 74]. We made sure to look at data from non-bifurcated runs in order to keep the same two cells configuration as in the contra case.

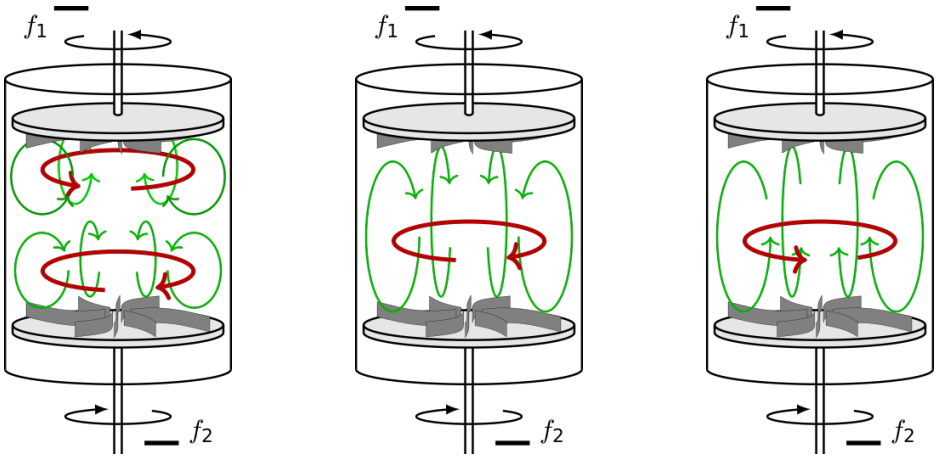

Figure 8.2: Flow configurations in the Von Karmàn setup. The non-bifurcated case (Left) is a symmetric flow composed of two circulation cells (red arrows). In the anti-rotation case, the flow might bifurcate. This leads to one of the two configurations (Middle and Right) where the two circulation cells merge together. Either the bottom impeller gets carried by the top one (Middle) or the opposite (Right). Schematics taken from Damien Geneste's thesis [48].

In the following, we also used data from the 'Small Von Kármán' (SVK) experiment that is 5 times smaller than the GVK. Consequently, at the same rotation rate, η becomes 5 times smaller than before while Re becomes 5 times larger. The created flow is identical and totally comparable to the one obtained in GVK. Since we must look at different scales and Reynolds numbers, the two experiments are complementary. In particular, we have two cases from SVK that have the same Reynolds number but two different flow configurations (anti and contra). It will give us some information about the influence of the flow configuration on the transition deviation criterion.

Lagrangian tracers are particles of diameter $\sim 10\mu m$ and about the same density as water and are placed inside the tank[1]. A high frequency laser, points at the internal tank, providing an intense light sheet of size $0.05 \times 0.044 \times 0.006m^3$. The laser light, scattered by the particles within the flow, is then retrieved by four cameras situated on the sides of the experiment (see Figure 8.3). The light is then diffracted on the camera aperture, resulting in typical diffraction pattern, i.e. Airy disk, representing the particle image, encoding both intensity and position.

Using the images from the four cameras, we are able to reconstruct the $3d$ positions of Lagrangian particles in time (see Figure 8.4). This is done by using the commercial algorithm 'Shake-the-Box' (STB), from 'LaVision'. See Damien Geneste's thesis for further information[48, 14].

Parametrisation – The different Reynolds numbers and associated investigated scales

[1]The type of particle and their diameter depends on the experiment and what is needed to achieve specific densities. Further information can be found in Paul Debue's thesis [23].

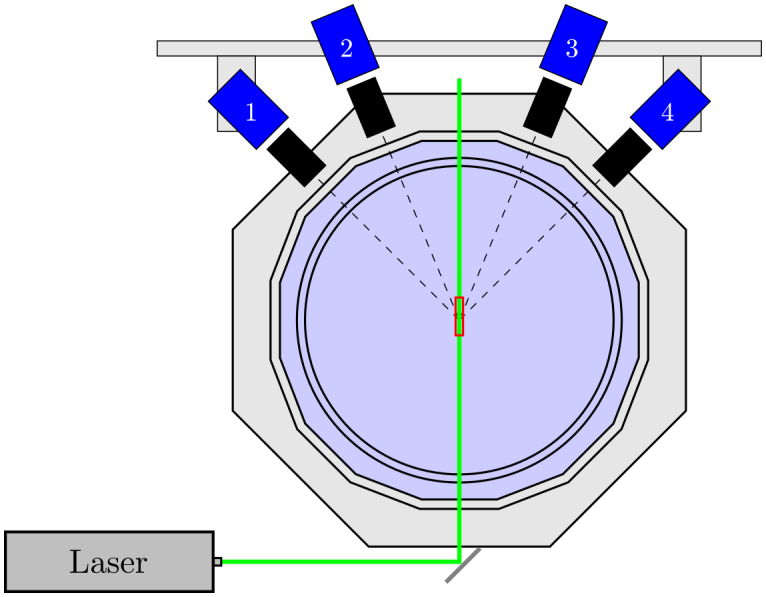

Figure 8.3: Experimental setup for 'Particle Tracking Velocimetry' (PTV) measurements. A laser is calibrated using optics to be focused to form a sheet. Particles, placed inside the flow, scatter the incoming light. The red area is recorded by cameras outside the experiment. Particle tracking post-processing leads to the $3d$ reconstruction of particle trajectories. Schematic by Damien Geneste [48].

Cases	C7-1	C7-2	C7-3	C7-4	C15-1	C15-2	C15-3
l_c (η)	7.78	7.72	7.76	7.78	15.3	15.6	15.3
Type	anti	contra	anti	contra	anti	contra	contra
Re	6300	6300	39 000	157 000	6300	31 000	157 000
N_x	48	37	38	100	24	62	50
Density	2.6	5.7	5.2	1.0	12.5	1.0	12
τ^*/τ_η	0.17	0.21	0.21	0.22	0.17	0.2	0.22
d_ϵ chosen	6	8	6	5	8	8	6

Table 8.2: Summary of GVK/SVK parameters and investigated scales. Density here being the number of particles per voxel.

are summarised in Table 8.2. For the computation of the histogram's grid, we set N_x and deduce N_y and N_z from the domain defined by the laser sheet. We have $N_y = 0.88N_x$ and $N_z = 0.12N_x$. To compute the transition deviation criterion, we must select voxels that have enough particles inside, to have meaningful standard deviations. For that, we set a threshold d_ϵ such that if the local density $d < d_\epsilon$, then the associated voxel is discarded. We note that in some experimental cases, on average, the number of particles per voxel can get very low (see Table 8.2). As a result, we decrease d_ϵ a bit, case-by-case, in order to capture more voxels for the final statistics. This can potentially alter the value of

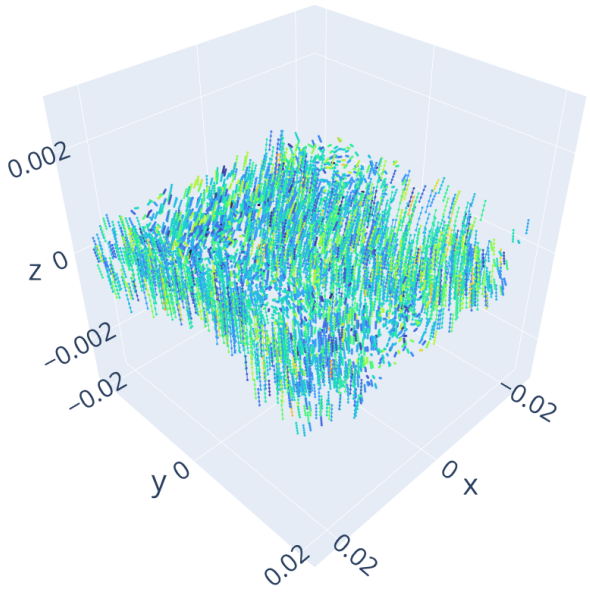

Figure 8.4: Lagrangian trajectories from the SVK experiment coloured by their velocity. Only 10 percent of the trajectories are represented here.

transition standard deviations, possibly leading to errors in the final results.

We only look at times that are considered to be statistically independent from each others just as for synthetic data. We note that densities here are way lower than in DNS. We can indeed reach at most 90 000 particles per instant, limiting the number of possible investigated scales.

Finally, the Eulerian grid N_x^Π, N_y^Π and N_z^Π was chosen to be the one used by D. Geneste, performing at a density of 0.05 particles per voxel [16].

STB Limitations – The Shake-the-Box algorithm may induce the outcome of outliers in the Lagrangian data. Those outliers can, for instance, have large displacement vectors (in norm) compared to the other particles. Taking the minimum and maximum of particle displacements to define the Cartesian decomposition can lead to wrong results: more weight is given to the larger values (thus not representing the whole data). We shall perform an outlier detection first in order to remove the spurious vectors. This method is explained in Appendix I.

8.2 . FlowMapFit: from trajectories to Eulerian fields

8.2.1 . Introduction

Presentation – We presented above the way to get Lagrangian trajectories from PTV measurements. We also need the Eulerian velocity field for the calculations of Π_l and D_ν^l. To get it, we use the Lagrangian data that we interpolate onto an Eulerian grid. The FlowHisto method is able to do this task but is a highly coarse-grained method,

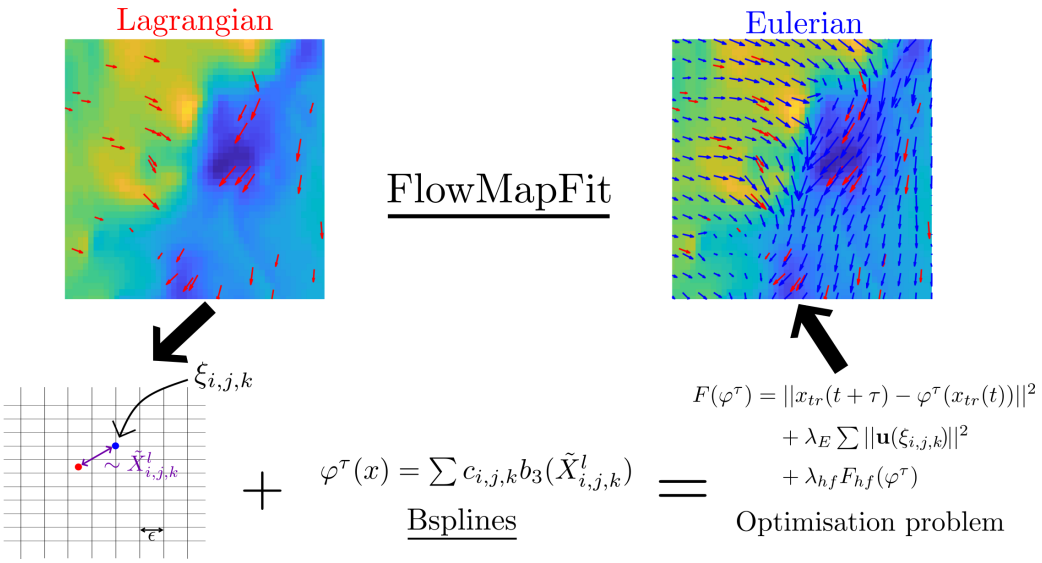

Figure 8.5: Schematic illustrating the FlowMapFit algorithm. The aim of this algorithm is to deduce an Eulerian field (here φ^τ) from a given Lagrangian distribution (here displacements). We select a grid which will represent the B-Splines centers. The Eulerian field is then deduced from an optimisation problem. The goal is to find the best $c_{i,j,k}$ coefficients so that the Eulerian field is as close as possible as the Lagrangian one, under some constraints.

as such, the computations of velocity increments are very noisy. Instead, we opt for an interpolation of the local displacements of particles using B-spline interpolations. We introduce the displacement field $\boldsymbol{\varphi}_t^{t+\tau}$ (called flowmap in the following) such as: if we consider any particle that starts at position $\boldsymbol{x}_1$ at t and ends at position $\boldsymbol{x}_2$ at $t+\tau$, we have

$$\boldsymbol{\varphi}_t^{t+\tau}(\boldsymbol{x}_1) = \boldsymbol{x}_2 - \boldsymbol{x}_1. \tag{8.1}$$

For the sake of simplicity, we omit the t dependence in the following: $\boldsymbol{\varphi}^\tau = \boldsymbol{\varphi}_t^{t+\tau}$. We therefore deduce the approximation for τ small

$$\boldsymbol{u} \underset{\tau \to 0}{\simeq} \boldsymbol{\varphi}^\tau / \tau \tag{8.2}$$

This subsection will be dedicated to introducing the full methodology to obtain $\boldsymbol{\varphi}^\tau$ from Lagrangian particles. A test on the ABC flow will then be presented.

Methodology – We consider particle trajectories with associated positions along time $\boldsymbol{x}_{tr}^i(t)$. We also consider an Eulerian grid of dimensions N_x^Π, N_y^Π, N_z^Π and grid width ϵ_Π where $\boldsymbol{\xi}_{i,j,k}$ will be the corresponding reference centres of B-splines. We call 'weights', the $c_{i,j,k}^\tau$ coefficients such that, multiplied by B-splines, they perform an interpolation of all local advections performed by the considered flowmap:

$$\boldsymbol{\varphi}^\tau(\boldsymbol{x}_{t_0}) = \boldsymbol{x}_{t+\tau} - \boldsymbol{x}_t = \sum_{i=1}^{N_x}\sum_{j=1}^{N_y}\sum_{k=1}^{N_z} \boldsymbol{c}^\tau_{i,j,k} \prod_{n=1}^{3} b_3(\tilde{X}^n_{i,j,k}), \tag{8.3}$$

where $\tilde{X}^n_{i,j,k} = \frac{x_n - \xi_{i,j,k}}{N_n \epsilon}$ the distance between the particle and nodes, $N_n \in (N_x^\Pi, N_y^\Pi, N_z^\Pi)$, and

$$b_3(y) = \begin{cases} \frac{4}{6} - |y|^2 + \frac{1}{2} & \text{if } y \leq \epsilon \\ \frac{1}{6}(2 - |y|^2) & \text{if } \epsilon < y \leq 2\epsilon \\ 0 & \text{otherwise.} \end{cases} \tag{8.4}$$

The goal is to learn the weights $\boldsymbol{c}^\tau_{i,j,k}$ from the positions of particles at each considered time. Their small displacement serves as a reference that we shall try to reproduce with the interpolation. This becomes an optimisation problem with the following functional:

$$F\left[\boldsymbol{\varphi}^\tau\right] = \sum_{i=1}^{N_{tr}} \left|\left| \boldsymbol{x}^i_{tr}(t+\tau) - \boldsymbol{\varphi}^\tau(\boldsymbol{x}^i_{tr}(t)) \right|\right|_2^2 + \lambda_{hf} F_{hf}(\boldsymbol{\varphi}^\tau), \tag{8.5}$$

where the velocity $\boldsymbol{u} \underset{\tau \to 0}{\approx} \pm \boldsymbol{\varphi}^\tau \tau$. A summary of the method can be found in Figure 8.5. A regularisation using a low-pass filter which is used to limit the effect of high frequencies on the computations of the flowmap. It has been proven to be efficient in order to limit experimental noise contamination [8, 49]. It is defined as follows:

$$F_{hf}(\boldsymbol{\varphi}^\tau) \doteq \sum_{i,j,k}^{N_x,N_y,N_z} ||\tilde{\boldsymbol{c}}_{i,j,k}||_2^2 \,, \tag{8.6}$$

with

$$\tilde{\boldsymbol{c}}_{i,j,k} = \frac{1}{3}\left(3\boldsymbol{c}_{i,j,k} - \sum_{l=-1}^{1} w(l+2)(\boldsymbol{c}_{i+l,j,k} + \boldsymbol{c}_{i,j+l,k} + \boldsymbol{c}_{i,j,k+l}) \right), \tag{8.7}$$

which corresponds to a spatial low-pass filter with a kernel $w = \left[\frac{1}{4}, \frac{1}{2}, \frac{1}{4}\right]$.

Hyperparameters and regression – The hyperparameter λ_{hf} should be determined by learning them from the data either using some physical arguments or by using some training data [63]. Such study has not been lead though, and we arbitrarily chose our parameter in order to match with the PTV data for experiments. In most cases, the choice of $\lambda_{hf} = 1$ was qualitatively ideal.

We use a least-square algorithm to optimise the resulting linear functional. We make sure to have this method converge before a limiting number of steps. We observe that a tolerance of 10^{-8} was generally a good choice for both good performances and reasonable computation time.

With the regularisation of the high frequencies, one is able to reconstruct the Eulerian field with a low density of particles [78]. This is particularly convenient in experiments since we cannot track as many particles as we want and the Eulerian field is harder to get from direct measurements.

8.2.2 . Verifying the method

We here verify the methodology by comparing with the integrated ABC flow, using the relation

$$\boldsymbol{\varphi}^{\tau}(\boldsymbol{x}) = \int_{t}^{t+\tau} \boldsymbol{u}(\boldsymbol{x}(t'))dt' \tag{8.8}$$

We choose $\lambda_{hf} = 1$. Slices of absolute value of φ_x^τ are presented in Figure 8.6. We observe that both flowmaps are almost identical with an overall error of 10%. Sides of the the domain are less correct due to a lack of data on the borders. Just like the FlowHisto method, the range of scales that can be correctly modelled is limited. This effect can be observed on the under-resolved band of zeros depicted on the maps.

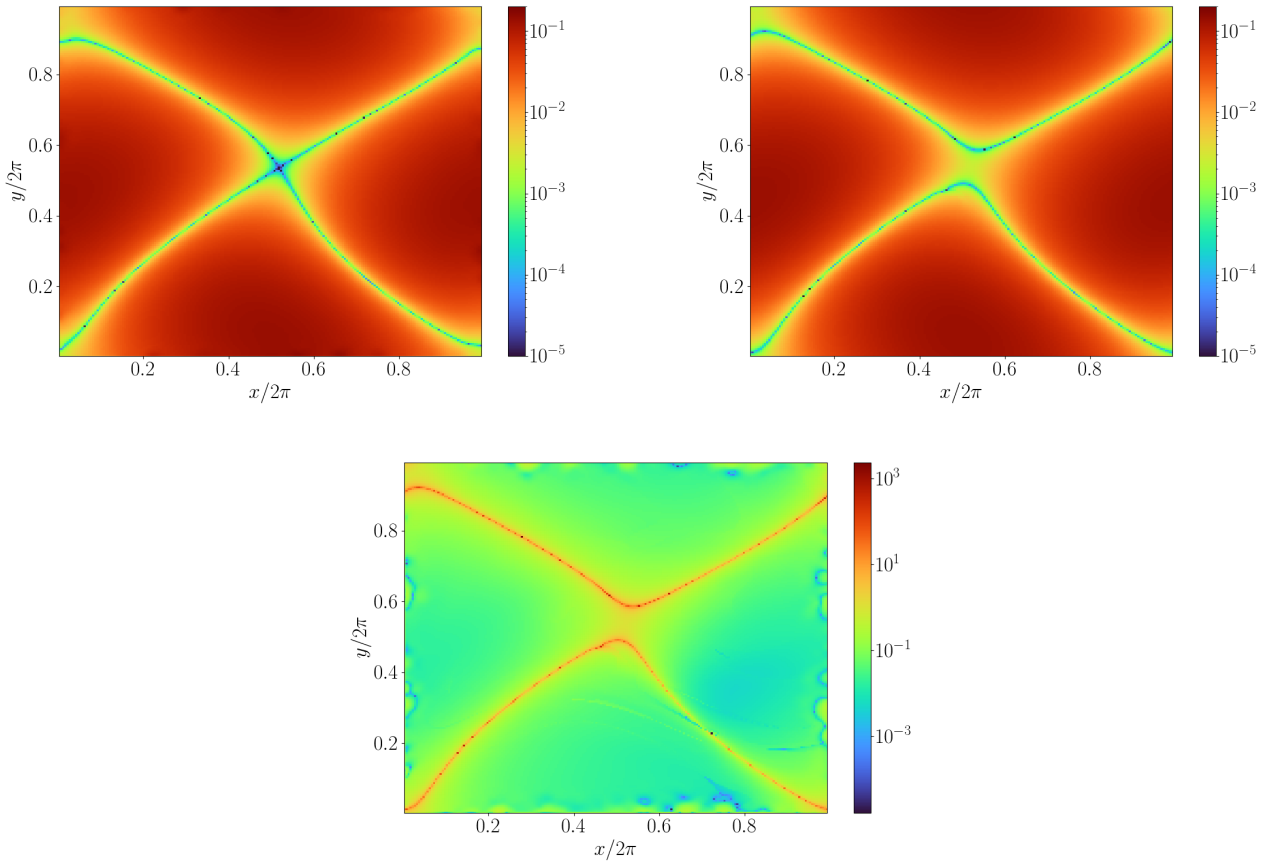

Figure 8.6: Slices of $|\varphi_x^\tau|$ for $z = \pi$ in ABC flow. The FlowMapFit methodology (top left) is compared to the theoretical value (top right). The comparison between the two maps through their difference is provided on the lower picture.

8.3 . DNS and Experimental results

This section is dedicated to the analysis of the results regarding the study of the transition standard deviation compared to Π^l and D^l_ν. We first analyse the structures and then move on to studying the statistics of σ^{ϵ,τ^o}. Some discussions and comparison with the WABC will be presented in the end of this section.

8.3.1 . Main results

Structures analysis – As a preliminary approach, we analyse the structures of the transition standard deviation and compare them with the terms in Duchon-Robert's theorem. We perform this study on the DNS data only: the lack of particles and the strong coarse-graining prevented us from studying the structures in the current experimental data we have. We present in Figure 8.7, slices (at $z = \pi$) of D^l_ν, Π^l, $(\Pi^l + D^l_\nu)$ and σ^{ϵ,τ^o} at one instant for $l_c = 3.9\eta$. We observe that places of strong σ^{ϵ,τ^o} correspond mostly to places of strong Π^l and D^l_ν. In particular, we notice similar structures between $(\Pi^l + D^l_\nu)$ and σ^{ϵ,τ^o}. Those two seem more similar than with Π^l or D^l_ν alone. We note that subtle differences can still be observed between the two maps, in particular for low $(\Pi^l + D^l_\nu)$.

Analysis of joint probabilities – We here analyse the joint probabilities between Duchon-Robert coefficients and the transition standard deviation. We present the cases where $l_c \sim 15.5\eta$ (beginning of inertial range) in Figure 8.8.

The DNS provides less statistics for the joint probability distributions than the experimental data. We however notice that without the experimental noise, the joint probability distribution between σ^{ϵ,τ^o} and D^l_ν seems more centred around the 1/2 law from equation (5.20). Overall, the distributions are more centred for the comparison with D^l_ν than with Π^l. In particular, we notice that the distributions stretch for the low Π^l, indicating that only the largest Π^l correlate with the transition standard deviation. The σ^{ϵ,τ^o} associated with the largest Π^l appear to stick close to the 1/3 scaling from equation (5.19).

The $Re = 31\ 000$ case shows however very round distributions, a very different behaviour from the others Reynolds numbers which we believe is due to the lack of statistics in this case. Regardless of this case, we observe that the distributions seem to be similar regardless of the Reynolds number.

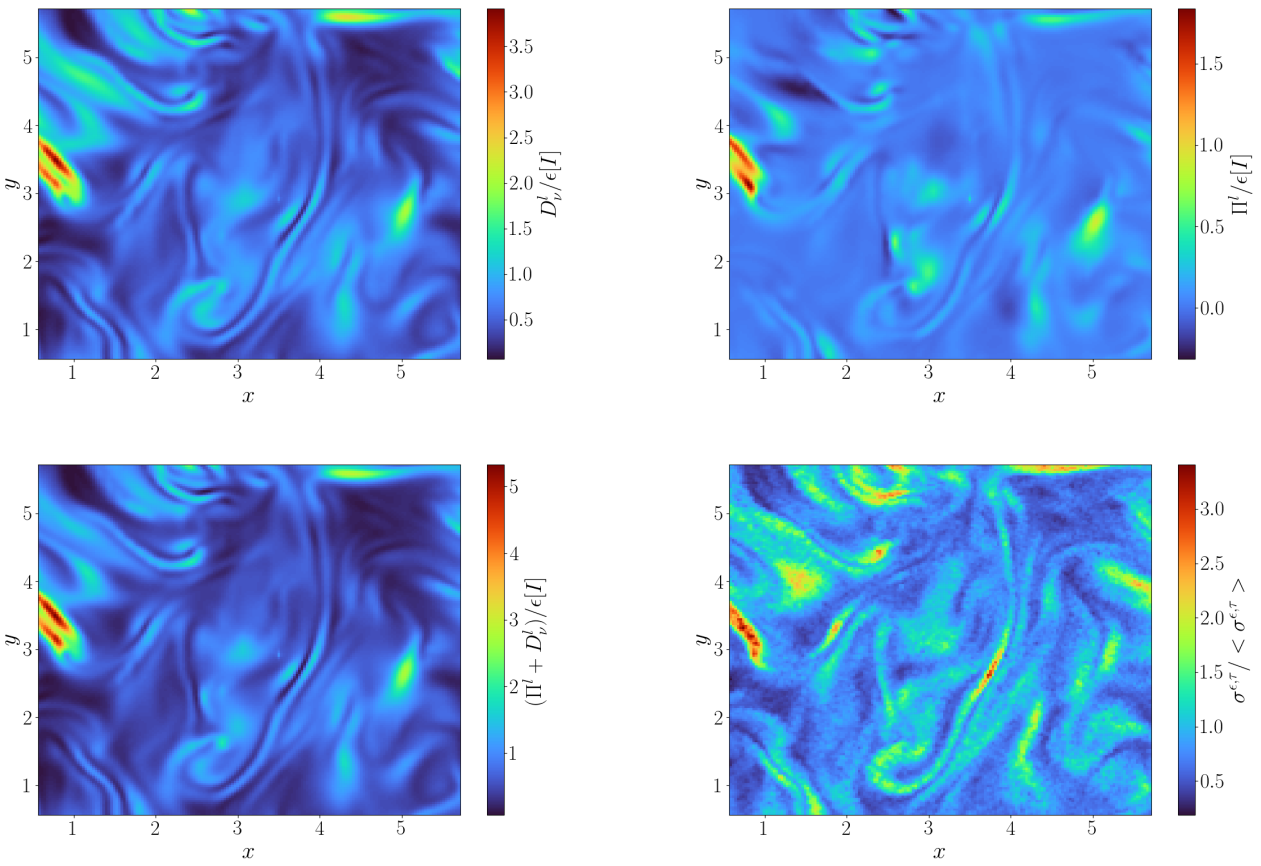

Figure 8.7: Slices of $D^l_\nu/\epsilon[I]$ (top left), $\Pi^l/\epsilon[I]$ (top right), $(D^l_\nu + \Pi^l)/\epsilon[I]$ (bottom left) and $\sigma^{\epsilon,\tau^o}/\left\langle\sigma^{\epsilon,\tau^o}\right\rangle$ (bottom right) for $z = \pi$ and $l_c = 3.9\eta$ in the numerical simulation.

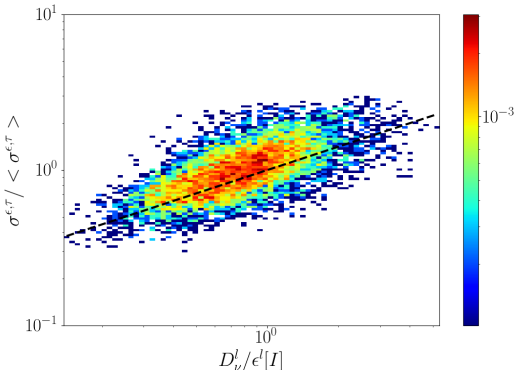

(a) D^l_ν in DNS, $Re = 137.1$

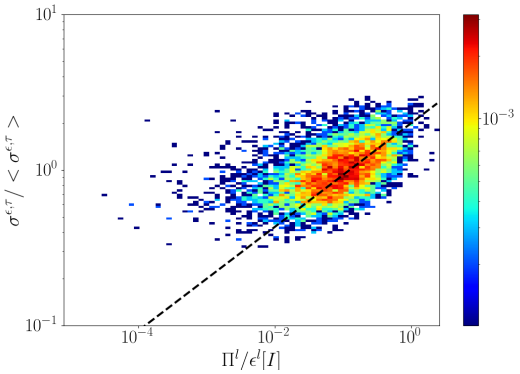

(b) Π^l in DNS, $Re = 137.1$

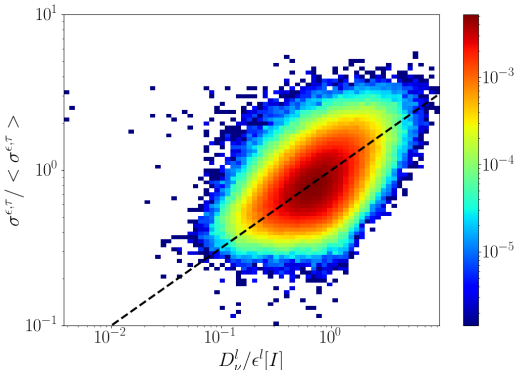

(c) D^l_ν in C15-1, $Re = 6300$

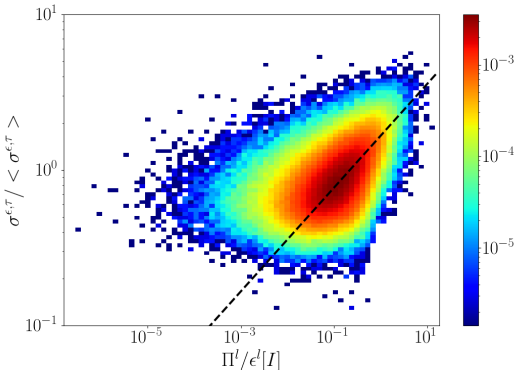

(d) Π^l in C15-1, $Re = 6300$

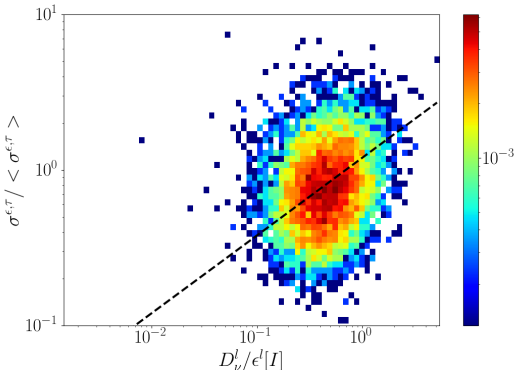

(e) D^l_ν in C15-2, $Re = 31\ 000$

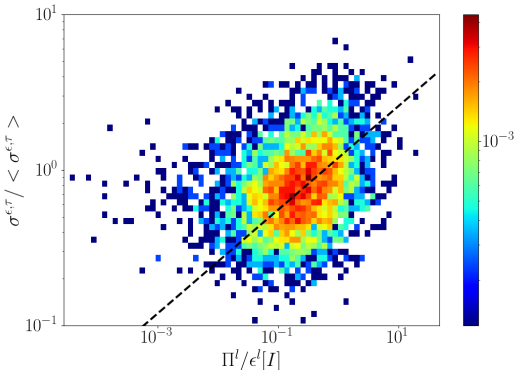

(f) Π^l in C15-2, $Re = 31\ 000$

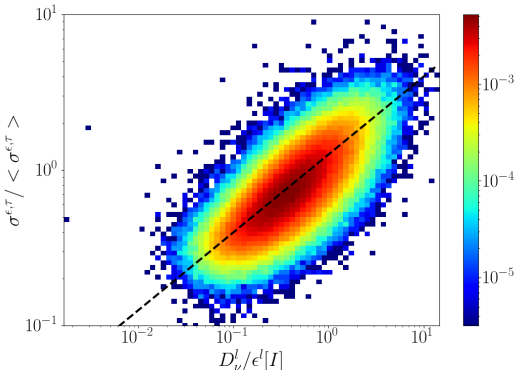

(g) D^l_ν in C15-3, $Re = 157\ 000$

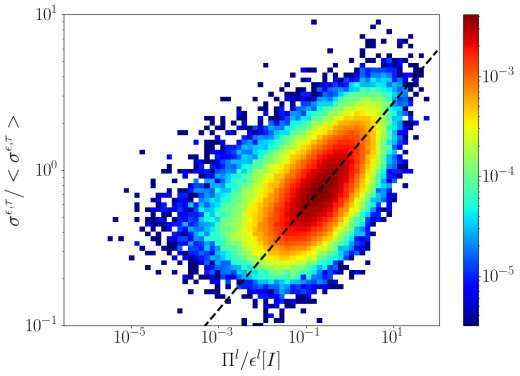

(h) Π^l in C15-3, $Re = 157\ 000$

Figure 8.8: Joint probability distributions between σ^{ϵ,τ^o} and dissipative terms $D^l_\nu/\epsilon[I]$ and $\Pi^l/\epsilon[I]$ for the different experiments and the numerical simulation in the case $l_c \sim 15.5\eta$. The dashed lines correspond to the respective $\frac{1}{2}$ and $\frac{1}{3}$ laws determined by equations (5.20) and (5.19).

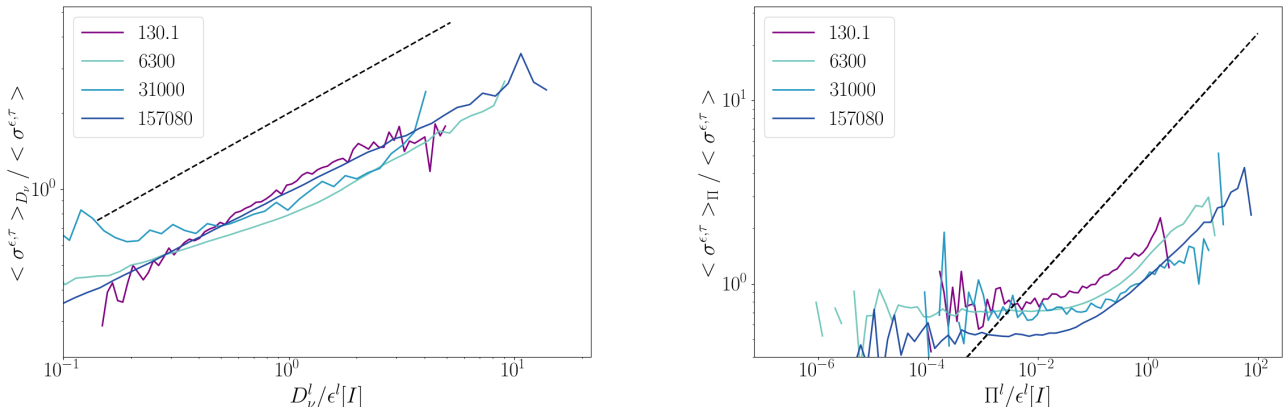

Figure 8.9: Conditioned averages $\langle \sigma^{\epsilon,\tau^o} \rangle_{D_\nu}$ (Left) and $\langle \sigma^{\epsilon,\tau^o} \rangle_\Pi$ (Right) as a function of respectively $\Pi^l/\epsilon[I]$ and $D_\nu^l/\epsilon[I]$ for an increasing Reynolds number Re, in the case $l_c = 15.5\eta$. The dashed lines correspond to the respective $\frac{1}{2}$ and $\frac{1}{3}$ laws determined by equations (5.20) and (5.19).

Transition deviation criterion – All of the above observations can be summarised with the conditioned statistics, available in Figure 8.9. As in the WABC model, in the comparison with Π^l, we observe that the curves are flat for low Π^l and becomes non-flat for large Π^l. This change of behaviour is seemingly independent of the Reynolds number. On the contrary, the comparison with D_ν^l is non-flat even for low D_ν^l as already observed in the study of joint probability distributions. The different curves in the comparison with D_ν^l seem to collapse onto a single one, regardless of the Reynolds number. The DNS data appears to especially follow the same law.

In the two comparisons (Π^l and D_ν^l), the curves seems to be close (but not equal) to the respective scaling laws given in equations (5.19) and (5.20). We note though that the scaling law fits better in the comparison with D_ν^l.

8.3.2 . Discussions

Preliminary conclusions – In the experimental results shown in the previous subsection, we identified that the transition deviation criterion seemed independent of the Reynolds number. In fact, we observed from the analysis of joint probability distributions and conditioned statistics that the curves were looking similar under normalisation. This is especially the case in the comparison with D_ν^l where strong correlation can be observed with $\langle \sigma^{\epsilon,\tau^o} \rangle_{D_\nu}$. This is particularly noticeable in the DNS data where experimental noise is absent.

We also observed that $\langle \sigma^{\epsilon,\tau^o} \rangle_\Pi > 0$ regardless of the Reynolds number and for the available probed scale. This conclusion was already reached in the study of Lagrangian trajectories in the WABC flow, for the irregular case $h < 1$. We therefore conclude that the SVK and GVK data are displaying a similar scenario as in the $h = 1/3$ case from the WABC model. In the range of the investigated Reynolds numbers, we are close to

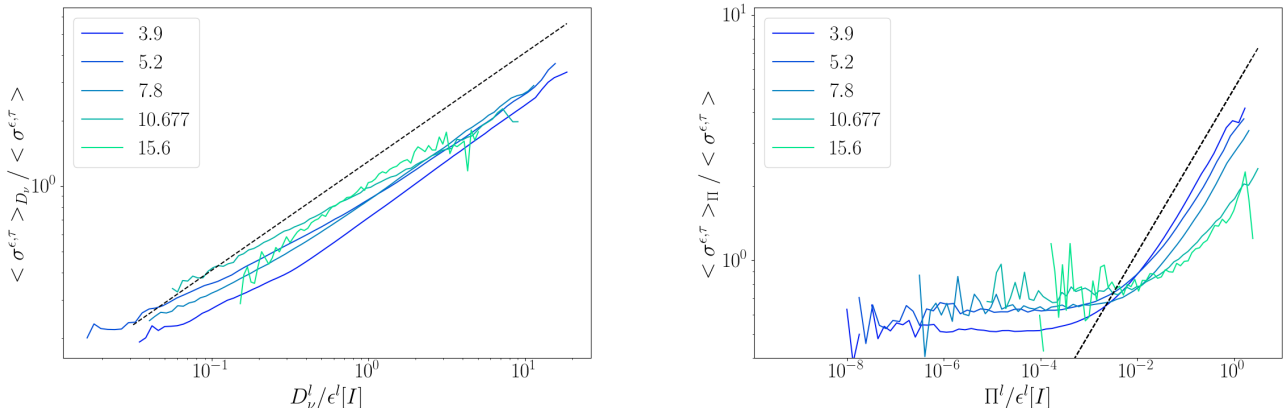

Figure 8.10: Conditioned averages $\langle \sigma^{\epsilon,\tau^o} \rangle_{D_\nu}$ (Left) and $\langle \sigma^{\epsilon,\tau^o} \rangle_{\Pi}$ (Right) as a function of respectively $\Pi^l/\epsilon[I]$ and $D_\nu^l/\epsilon[I]$ for the DNS with an increasing investigated scale l_c. The dashed lines correspond to the respective $\frac{1}{2}$ and $\frac{1}{3}$ laws determined by equations 5.20 and 5.19.

reaching the convergence in Duchon-Robert theorem (see Figure 2.1). We can therefore deduce that we almost reached the vanishing regularisation limit imposed in the transition deviation criterion.

The lack of statistics in our data prevents us from truly concluding about the existence of spontaneously stochastic events for the experimental trajectories. We should first comfort the observed tendencies in the low Reynolds numbers ($Re \leq 31\ 000$). We should then include more cases with higher Reynolds numbers in order to derive quantitative evolution laws.

Scale dependence – One may argue that the observed results are only valid in the inertial range. We here test this remark by analysing the influence of scales on the transition deviation criterion. This is performed on the DNS data which presents a very large amount of particles. The results are shown in Figure 8.10. We observe that all the curves in the comparison with D_ν^l appear close to each other. We note that the lower l_c, the closer the curves are to the $1/2$ scaling law. Similarly, the comparison with Π^l gets closer to the $1/3$ scaling law as l_c decreases. The dependence on l appears to be more important in the comparison with Π^l than with D_ν^l. Finally, all the curves seem to show the typical change of regime above a common critical Π^l.

We now check if the transition deviation criterion shows similar results across the Reynolds numbers for $l_c = 7.75\eta$, i.e. in the dissipative range. The results regarding the joint probability distributions are displayed in Figure 8.11. The associated conditioned statistics are represented in Figure 8.12. We observe that, overall, the distributions are more centred around their respective scaling laws than in the $l_c = 15.5\eta$ case. The comparison with D_ν^l still shows a better correlation than the comparison with Π^l. This

can be particularly observed in the DNS where the correlation is clear between $\langle \sigma^{\epsilon,\tau^o} \rangle$ and D_ν^l.

From the conditioned statistics, we observe that the transition deviation criterion appears to be closer to the respective scaling laws for large Π^l and D_ν^l, as already observed in the DNS above. We particularly note that those curves seem to collapse onto single ones. This underlines the fact those do not change when the Reynolds number increases, which confirms the preliminary observations reached in the inertial case.

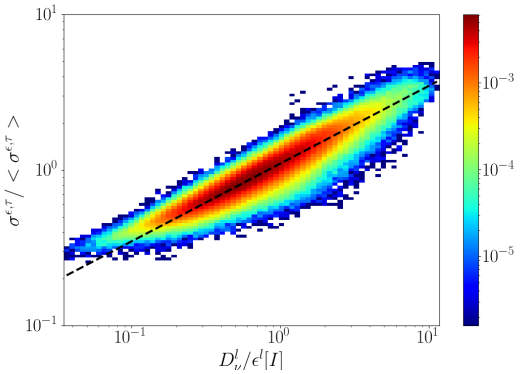

(a) D^l_ν in DNS, $Re = 137.1$

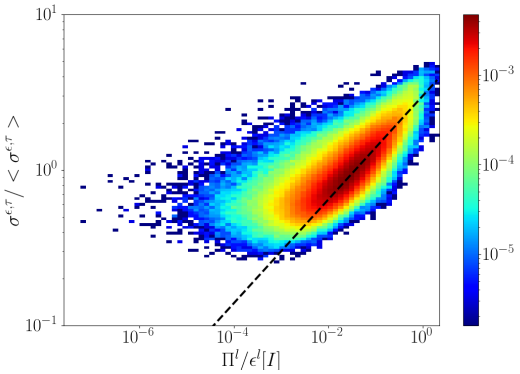

(b) Π^l in DNS, $Re = 137.1$

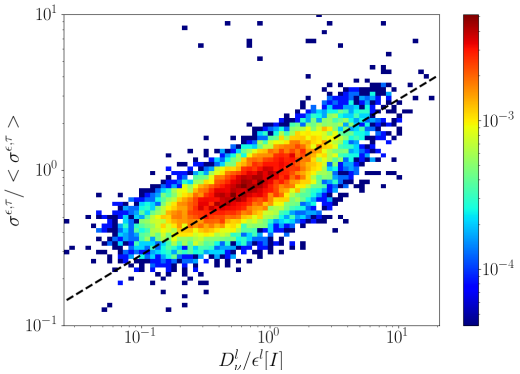

(c) D^l_ν in C7-1, $Re = 6300$

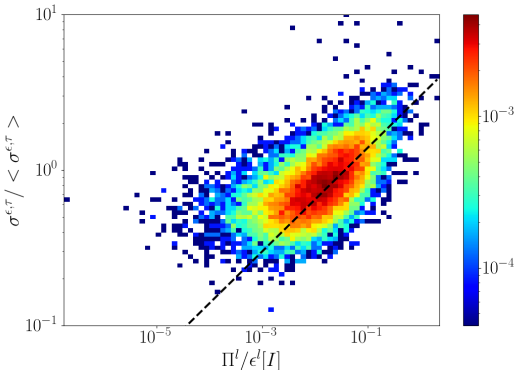

(d) Π^l in C7-1, $Re = 6300$

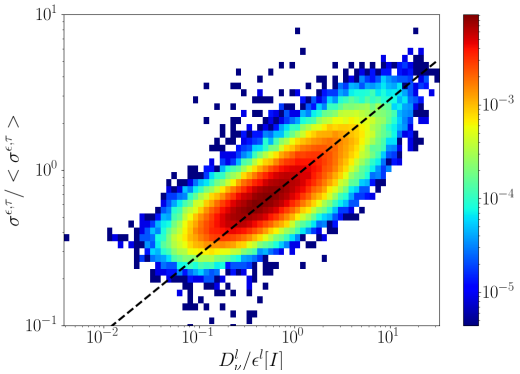

(e) D^l_ν in C7-3, $Re = 39\ 000$

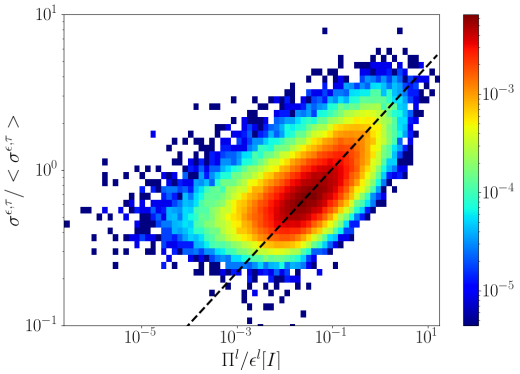

(f) Π^l in C7-3, $Re = 39\ 000$

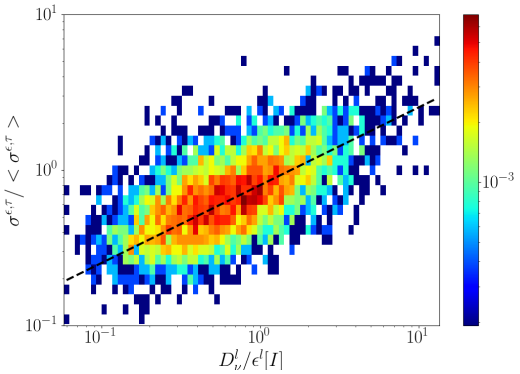

(g) D^l_ν in C7-4, $Re = 157\ 000$

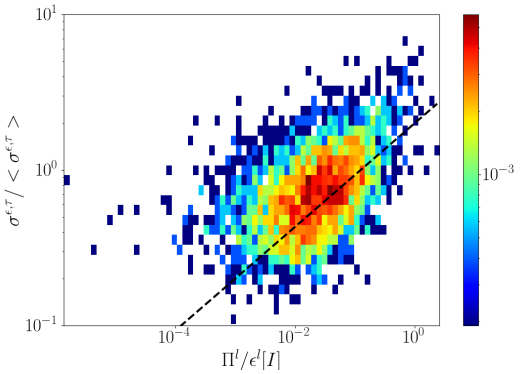

(h) Π^l in C7-4, $Re = 157\ 000$

Figure 8.11: Joint probability distributions between σ^{ϵ,τ^o} and dissipative terms $D^l_\nu/\epsilon[I]$ and $\Pi^l/\epsilon[I]$ for the different experiments and the numerical simulation in the case $l_c \sim 7.75\eta$. The dashed lines correspond to the respective $\frac{1}{2}$ and $\frac{1}{3}$ laws determined by equations (5.20) and (5.19).

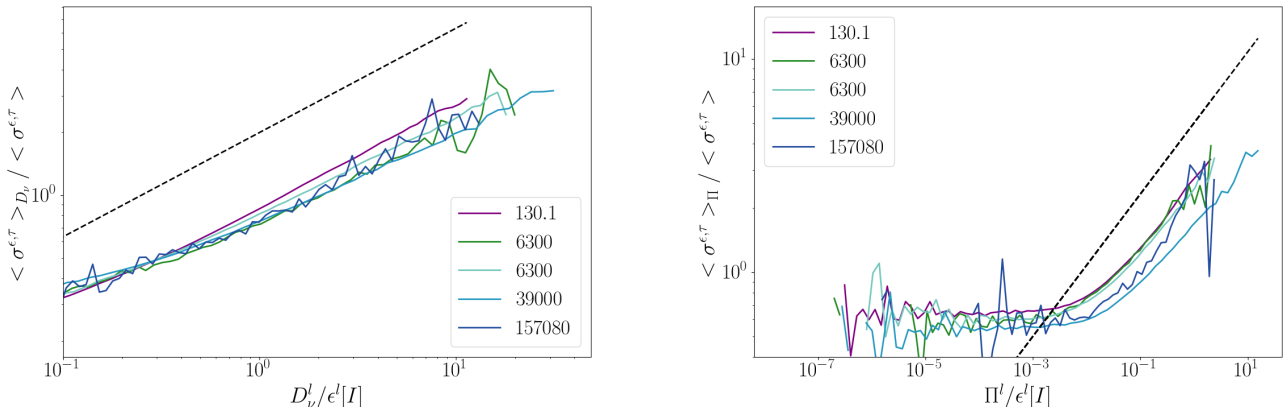

Figure 8.12: Conditioned averages $\langle \sigma^{\epsilon,\tau^o} \rangle_{D_\nu}$ (Left) and $\langle \sigma^{\epsilon,\tau^o} \rangle_{\Pi}$ (Right) as a function of respectively $\Pi^l/\epsilon[I]$ and $D^l_\nu/\epsilon[I]$ for an increasing Reynolds number Re, in the case $l_c = 7.75\eta$. The dotted curves correspond to the respective $\frac{1}{2}$ and $\frac{1}{3}$ laws determined by equations 5.20 and 5.19.

Flow dependence – We also check here if switching flow type also changes the transition deviation criterion. We check this on cases C7-1 (anti configuration) and C7-2 (contra configuration) that share the same Reynolds number. Results are displayed in Figure 8.12. We observe that from the conditioned average perspective, the two curves seem identical. This highlights that this criterion gives similar results in both the contra and anti configurations, at least at the small investigated scales.

8.4 . Conclusions

In this chapter, we analysed data from two Von Kármán experiments and from a DNS. We were able to compute the transition deviation criterion for different Reynolds numbers and probed scales. We identified a strong correlation between large anomalous dissipation and the transition standard deviation. In particular, we observed that this correlation appears to be independent of the Reynolds number, similar to what was obtained for the rough WABC model. As global dissipation almost becomes anomalous for the largest Re investigated, we therefore conclude that the transition deviation criterion might be pointing at spontaneously stochastic events. It is the first observation of traces of Lagrangian spontaneous stochasticity in experimental data.

Some tests were performed in order to check that the investigation scale does not change the results. We observed that the lower this scale is, the closer the transition deviation criterion is from the expected scaling laws (i.e. $(\Pi^l)^{1/3}$ and $(D^l_\nu)^{1/2}$). We saw that the evolution through the Reynolds numbers is unchanged when the investigation scale is lowered.

The obtained results need though to be refined in order to confirm the above observations. We should gather more experimental data to quantify the convergence of the

transition deviation criterion through the Reynolds numbers. In particular, we note that a high density of particles is needed in order to correctly evaluate the transition standard deviation with the FlowHisto algorithm. Switching this method for a convolution-based method could probably allow for more experiments to be represented for the same scale.

Part IV

Conclusions and perspectives

In this thesis, we explored the real physics behind the notion of spontaneous stochasticity. Our goal was to create a criterion that would allow us to experimentally observe such phenomenon. From Richardson's intuitions to Onsager's conjecture, we identified the potential relationship between irregularities and the Lagrangian dispersion. The criterion we propose is based on this relationship.

To get some insights and verify the correctness of our reasoning, we built a model based on the Weierstrass irregular function. The WABC flow, was shown to be irregular everywhere and to exhibit some of fundamental properties of turbulence. We observed for instance the presence of a Richardson regime for pair dispersion, in the long-time dynamics. Using numerical stochastic methods, we were able to simulate regularised Lagrangian trajectories in the WABC flow. In the limit of vanishing regularisation, these trajectories appeared to remain stochastic. This was confirmed by their statistical analysis, which exhibit convergence to non-trivial distributions (i.e. non Dirac distributions) in the same limit. Altogether, this prompt us to conclude that the WABC flow builds Lagrangian spontaneous stochasticity. We numerically verified that this conclusion was universal under the change of regularisation type, initial position, or Hölder exponent. One would need however to dig deeper in order to quantitatively verify those conclusions.

We note that the A, B and C for the WABC model were chosen to display chaotic behaviour even in the regular case. It is still unclear whether chaos is absolutely necessary for this model to display spontaneous stochasticity. Heuristic models [80, 10] show that the Richardson regime can be produced from accumulation of ballistic motions with Lyapunov dispersion. If this is the case, the possible necessary condition for the occurrence of spontaneous stochasticity in this WABC model could be to have positive diverging Lyapunov exponents but not necessarily chaos. To check such a conjecture, one should lead a systematic investigation by varying the parameters A,B and C that control the chaotic properties of the basic flow. This could also be helpful in searching for transition towards spontaneous stochasticity in the context of a deterministic flow. This transition has, so far, only be observed in the Kraichnan model.

In the framework of this thesis, the WABC flow helped us identify the traps hindering the evidence of spontaneous stochasticity in experiments. Using transition probabilities and coarse-graining, we were able to build a candidate criterion that can be computed in real flows. The transition deviation criterion was then tested in the WABC flow. We showed that it is well-defined and is sensitive to spontaneous stochasticity: the criterion fails, as expected, when the flow becomes regular. We applied this criterion to experimental data obtained from Von Kármán experiments. We showed that experimental results display similar features than in the case of the rough WABC flow, which is spontaneously stochastic. This result can thus be seen as the first qualitative experimental evidence of spontaneous stochasticity in turbulence. More cases with higher Reynolds numbers are needed in order to quantitatively confirm what was observed.

Comparison with numerical data showed that experimental noise is not the main trouble-shooter in the quest for statistical convergence. The main limitation for appli-

cation of this criterion to experimental data is in fact the density of the particle tracers, that needs to be high enough for the convergence of the statistics within each voxels. This particle density also drives the range of scales that are accessible for the analysis. With the method described in the present thesis, and the present experimental tracer densities, we were only able to compute a very limited amount of scales. This makes the gathering of several results with different Reynolds numbers difficult. One needs to change the numerical methodology to compute the transition deviation criterion in order to overcome this difficulty. In particular, the use of kernel filtering might give some smooth evaluation of local transition standard deviation.

In the end, this thesis represents a proof of concept for exploring spontaneous stochasticity experimentally. This could be useful in order to test the incoming thrilling theories and numerical properties. Many outstanding interesting questions regarding Lagrangian spontaneous stochasticity remain also to be explored, both from a numerical and experimental point of view, such as the influence of the particle path history, or the dependence on the initial position. This may require adaptation of our transition deviation criterion, using the WABC flow as a useful guide for intuition.

Appendices

A - Measuring thermal noise in turbulence

A.1 . Introduction

A.1.1 . Theoretical considerations

If spontaneous stochasticity exists in real turbulence, then it is thermal noise that regularises the smallest scales. It was shown by G. Eyink [4], using arguments from statistical physics, that this noise should appear at

$$k_{th}\eta \approx 10. \tag{A.1}$$

The dissipative regime in the energy spectrum (characterised by an exponential decrease) should break at this length scale, where energy is injected again by thermal fluctuations (with the typical k^2 law). For now, those considerations are only theoretical, and one may wonder why such regime has never been observed experimentally?

A.1.2 . Scales and measurements

While the PTV (Particle Tracking Velocimetry) techniques are very useful to precisely get the Lagrangian or Eulerian fields, they fail to correctly solve the smallest scales. It is a chimera for now to consider reaching the scale (A.1) with those methods. A more successful technique to reach small scales is hot-wire measurements. Crudely, a current goes through a thin tin wire which heats up due to Joule's heat. This heat is dissipated due to convection when this wire is placed inside a flow. In CTA (Constant Temperature Anemometry) mode, the difference of tension e needed to keep the wire at the same temperature is an image of the flow's velocity through King's law:

$$e = \sqrt{\alpha + \beta\sqrt{u}}, \tag{A.2}$$

where α and β are two constants dependant on the experimental setup (geometry, mean velocity, Prandtl number, etc.). The smallest length scale measured by a hot-wire is given by its dimensions $\sim 100\mu m - 1mm$

In most cases however, this technique is insufficient to reach scales below (A.1). In most wind tunnels (like Modane, see Figure A.2 [9, 50]), $\eta \sim 1\mu$m. The creation of a wire that small is impossible in practice. However, in the GVK experiment (see Chapter 8), $\eta \sim 1$ mm. As such, it would be possible, with the proper hot-wire, to reach the desired scales.

A.2 . Experimental issues

One should note that in practice, such technique is hard to set up. A good calibration is first needed to correctly find the α and β coefficients in the King's law. This step is important in order to get proper results, in particular because it is a non-linear law. In addition, measuring thermal noise come with some new constraints:

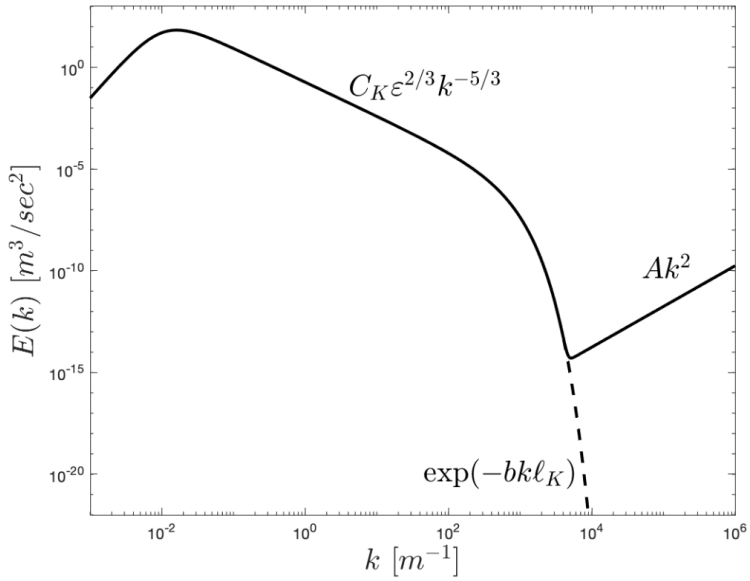

Figure A.1: Image taken from G. Eyink's paper representing the theoretical energy spectrum of atmospheric turbulence. The full line represents the scenario where thermal noise is considered in the computations. The dash line is the classical dissipative spectrum.

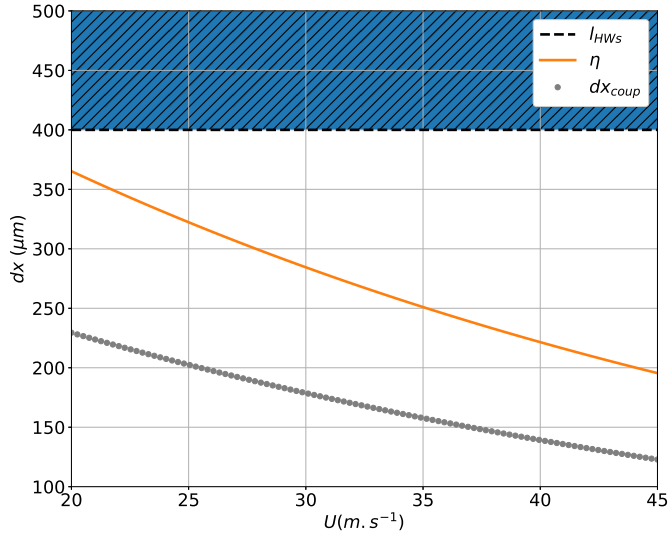

Figure A.2: Evolution of the thermal-noise's cut-off scale $dx_{coup} = k_{th}^{-1}$ as a function of the velocity in the Modane wind tunnel [9, 50]. The blue zone corresponds to the scale actually investigated with their hot-wires. In orange is represented the Kolmogorov scale as an indication.

- *Limits of sampling:* In the dissipative regime, we need to be able to resolve energies at an exponential rate. This is highly problematic since the ADC[1] can only sample data on a finite range (usually in laboratories, on 14 to 16 bits). An undersampled signal appears to be noisy and saturated, which can be confused with real experimental noise.
- *Electrical noise:* The power grid experiences fluctuations in time which can affect such precise measurements. The use of batteries is, in that case, recommended.
- *Internal noise:* The CTA retroaction device is made from various non-linear electrical components. As such they can alter the velocity spectrum. This needs to be controlled and filtered.
- *Heat noise:* For short wires, the King's law may be altered due to unperfect convective dissipation. This can also have a large impact on the desired energy spectrum.
- *Burning wire:* A high temperature combined with the stress imposed by the flow can break the wire. The CTA device needs to be tweaked in order to precisely control temperature and avoid any damage made to the wire.

A.3 . Perspectives

Taking into account the above constraints, we propose here some technical solutions to perform such measurements in the GVK experiment. To characterise the noise induced by both the unperfect convection and the retroaction device, we would impose a modulated laser to artificially heat the wire (without any flow). Knowing the laser's modulating signal, we could therefore determine the transfer function of the whole setup [8]. This would give us insightful information about the frequencies that are affected by the device.

The measurements would be achieved with a home-made retroaction CTA device that is presented in Figure A.3. It includes a decoupling of frequencies in order to treat low scales independently (to limit sampling errors). This device should also be accessible in order to tweak the components and ease the control of the wire's temperature.

[1] Analog-Digital Converter.

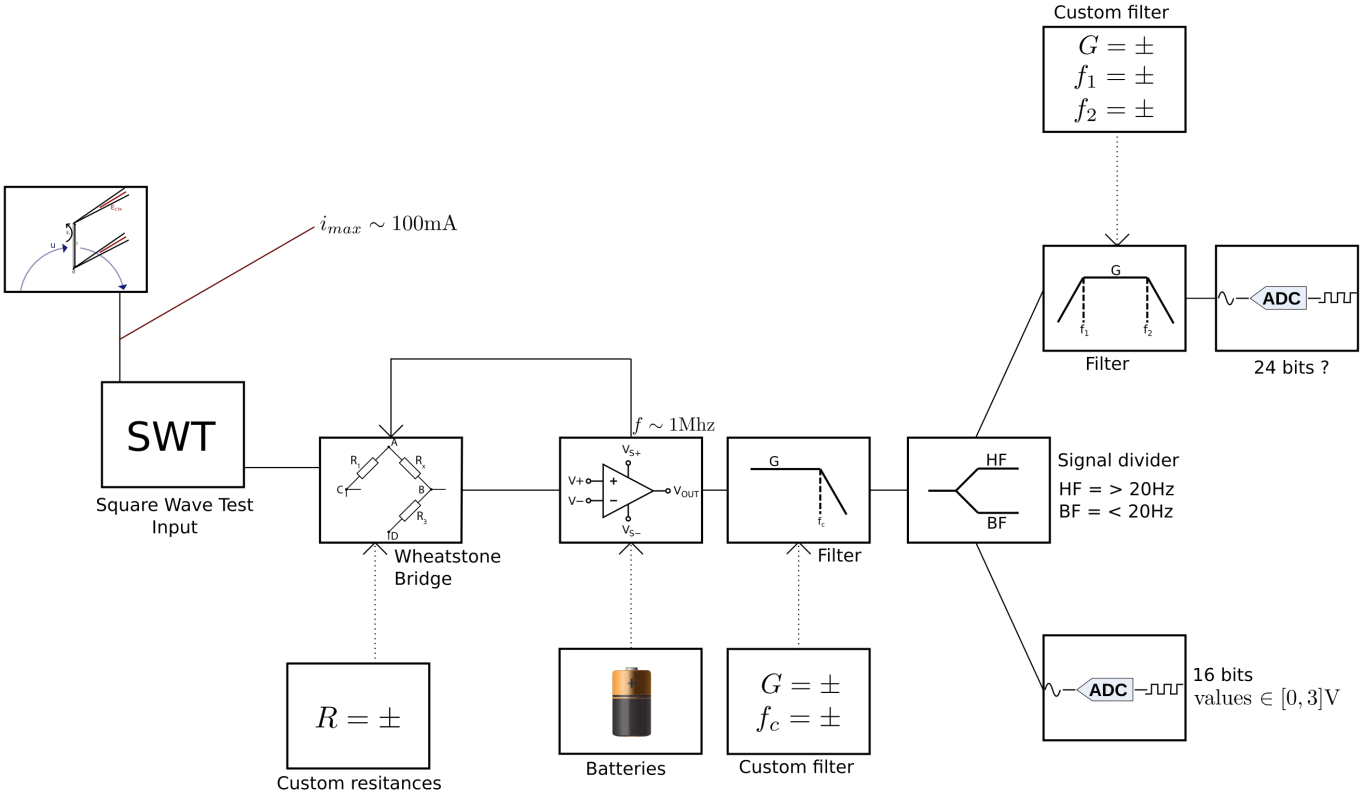

Figure A.3: Schematic of the desired CTA device designed specifically for measuring thermal noise in turbulence. The retroaction loop is performed with the Wheatstone bridge which checks any changes of resistance (i.e. temperature) in the wire (on the left). The difference of tension is then sent to an amplifier to limit the CTA's non-linear components to affect the signal. A decoupling of the latter is then performed, isolating the small scales from the large scales. The acquisition is therefore performed on two different ADCs, with another potential amplification. This final amplification could matter, in order to isolate the scales that would show the k^2 law from equipartition of energy.

B - Unpredictability and entropies

B.1 . Introduction

B.1.1 . Preamble

From a classical physics perspective, deterministic and stochastic phenomena lie at two different ends on the spectrum of complexity. Deterministic processes characterise the behaviour of small systems, allowing for predictions through ordinary differential equations and smooth dynamical systems. In contrast, stochastic phenomena, characterised by randomness, reveal a level of complexity that arises from coarse-graining over an underlying, often incomputable many-body Hamiltonian dynamics. For example, diffusion processes including but not limited to Brownian motion and standard Wiener processes, can formally be derived from microscopic dynamics within the Mori-Zwanzig framework. We saw in Chapter 1 that even low-dimensional systems may spontaneously generate randomness. We observed that chaos involve the exponentiation of nearby trajectories and their convergence onto a strange attractor [32]. This means that long time limits of such chaotic systems need to be described in terms of probability measures. The stochastic framework there offers a natural language for describing long-time limits as invariant measures, which loosely said quantify amounts of time typical trajectories spend in a given attractor. It also provides a selection mechanism to identify the physically meaningful measures as those resistant to noise perturbations.

The complexity of dynamical systems can be quantified and those can then be categorised. The underlying theorems allowing for such classification are of stochastic nature. The quantification of complexity could then be extended to stochastic systems, provided the stationarity of the processes [44]. Spontaneous stochasticity appears to lie in between the deterministic and stochastic worlds. In this Appendix, written in collaboration with Simon Thalabard, we question the possibility of quantifying and characterising the complexity of spontaneously stochastic processes. This work intends to provide some intuitions on the deep connections between dynamical systems theory, stochastic processes and spontaneous stochasticity.

B.1.2 . Scope

We wish to study in particular the distinction between chaotic and spontaneously stochastic randomness in terms of the concept of $\epsilon-$entropies. Those entropies are close analogues to Shannon entropy in information theory and have been used in a series of recent works to classify the complexity of arbitrary physical signals, in terms of their level of randomness when probed with a small, but finite ϵ precision. Such metric is sensitive to the strength of the stochastic component of the underlying dynamics. In particular, it diverges for continuous-time random signals, including but not limited to Markov processes, and takes finite values for low-dimensional smooth deterministic systems, where it is prescribed by the fractal geometries of the attractors. We here extend the classification to include

spontaneously stochastic systems. We characterise by direct or numerical means the ϵ-entropies of a variety of systems possessing such mechanism, obtained by considering various types of particles trapped in rough wells. We particularly show that relative entropies are more useful tools in the continuous limit. Those can be used to compare experimental data with spontaneously stochastic models (e.g. the Kraichnan model).

B.2 . From Shannon to Epsilon entropy for stochastic systems

This section provides a short background on information theory, and defines entropy rates of stochastic processes as suitably defined conditional Shannon entropies. Those definitions will serve as a basis for understanding both chaos and spontaneous stochasticity.

B.2.1 . Stochastic setup

Countable random variables – Given a probability space $(\Omega, \mathbb{P})$ [1] , the Shannon entropy of a (discrete) random variable $X : \Omega \to \mathbb{Z}$, is defined as

$$H[X] = -\sum_{i\in\mathbb{Z}} P_X(i) \log P_X(i) \doteq -\mathbb{E}_X \log \mathbb{P}(X) \tag{B.1}$$

in terms of the distribution $P_X(i) = \mathcal{P}(X = i)$ and the expectation $\mathbb{E}_X$ [21]. It quantifies the amount of randomness of X. For example, $H[X] = -p \log p - (1-p)\log(1-p)$ for a Bernouilli distribution $P_X = p\mathbf{1}_{X=0} + (1-p)\mathbf{1}_{X=1}$, ranging from 0 for the deterministic cases ($p = 0$ and $p = 1$) to $\log 2$ for the uniform case $p = 1/2$.

Definition B.1 naturally extends to the case of a joint variable $X = (X_1, X_2)$ as

$$H[X_1, X_2] = -\sum_{i,j\in\mathbb{Z}} P_{X_1,X_2}(i,j) \log P_{X_1,X_2}(i,j) \doteq -\mathbb{E}_X \log \mathbb{P}(X), \tag{B.2}$$

from which we define the conditional entropy

$$H[X_1|X_2] = H[X_1, X_2] - H[X_2] \tag{B.3}$$

and the mutual information

$$I[X_1, X_2] = H[X_1, X_2] - H[X_1] - H[X_2] \tag{B.4}$$

The vocabulary stems from the usual framework of information theory [21]. One interprets the conditional entropy (B.3) as the uncertainty of X_1 given X_2 and the mutual information (B.4) as the reduction of uncertainty of X_1 knowing X_2.

B.2.2 . Case of stochastic processes

Discrete-time (countable) stochastic process – We can now extend the definitions (B.1),(B.3), (B.4) to define entropy rates associated to discrete-time stochastic processes

[1] As in Frisch, we choose not introduce σ-algebras in order to avoid discussing measure-theoretic issues.

defined on a countable set, that is a sequence $X = (X_i, i \in \mathbb{N})$ where each of the $X_i : \Omega \to \mathbb{Z}$ are countable random variables. Writing $X_{\leq n}$ the joint distribution up to time n, that is

$$X_{\leq n} = (X_0, X_1 \cdots X_n), \tag{B.5}$$

we define the entropy rate as

$$h(n) = H[X_{n+1}|X_{\leq n}] \tag{B.6}$$

In words, the entropy rate quantifies the uncertainty of the state X_{n+1} knowing the history $X_{\leq n}$. We observe that combining Definition (B.6) with equations (B.1),(B.4), we identify

$$h(n) = H[X_{\leq n+1}|X_{\leq n}] = H[X_{\leq n+1}] - H[X_{\leq n}] \tag{B.7}$$

For example, the deterministic process such that $\forall i X_i = X_0$ prescribed by the realisation at time 0, has constant $h(n) = 0$, while the white-in-time process with independent $X_i \sim X_0$ has constant $h(n) = H[X_0]$. Introducing Markov property as:

$$P(X_n|X_{n-1}, \ldots, X_0) = P(X_n|X_{n-1}), \tag{B.8}$$

one can prove that entropy follows the same property using relation B.3

$$H(X_n|X_{n-1}, \ldots, X_0) = H(X_n|X_{n-1}). \tag{B.9}$$

In the case of a Markov chain, the entropy rate then is

$$h(n) = H(X_{\leq n+1}) - H(X_{\leq} n) = H(X_{n+1}|X_n, \ldots, X_0) + H(X_n, \ldots, X_0) - H(X_{\leq} n), \tag{B.10}$$

which is, using (B.9)

$$h(n) = H(X_{n+1}|X_n). \tag{B.11}$$

The homogeneous case simply becomes $h(n) = H(X_1|X_0)$.

Continuous Stochastic processes – For continuous output, one cannot introduce a meaningful entropy unless some type of space discretization is introduced. To that end, given a random variable $X : \Omega \to \mathbb{R}$, with distribution P_X, we introduce the ϵ-entropy as

$$H_\epsilon[X] = -\int_{\mathbb{R}} P_X(dx) \log P_X[B(x, \epsilon)], \quad B(x, \epsilon) \doteq \{y \in \mathbb{R},\, |x - y| \leq \epsilon\}, \tag{B.12}$$

where we use the shorthand $P_X(dx) \doteq \mathbb{P}(X \in B(x, dx))$.

Similarly, for a joint process $\boldsymbol{X} = (X_1, X_2)$

$$H_\epsilon[\boldsymbol{X}] = -\int_{\mathbb{R}^2} P_{\boldsymbol{X}}(dx_1, dx_2) \log P_{\boldsymbol{X}}[B(\boldsymbol{x}, \epsilon)], \quad B(\boldsymbol{x}, \epsilon) \doteq \left\{\boldsymbol{y} \in \mathbb{R}^2, \|\boldsymbol{x} - \boldsymbol{y}\|_2 \leq \epsilon\right\}; \tag{B.13}$$

The conditional and mutual ϵ-entropies between X_1 and X_2 are then respectively:

$$H_\epsilon[X_1|X_2] = H_\epsilon[\boldsymbol{X}] - H_\epsilon[X_2], \text{ and } I_\epsilon[X_1, X_2] = H_\epsilon[\boldsymbol{X}] - H_\epsilon[X_1] - H_\epsilon[X_2]. \tag{B.14}$$

We can define the same way an entropy rate being

$$h(n, \epsilon) = H_\epsilon(X_{\leq n+1}) - H_\epsilon(X_{\leq n}). \tag{B.15}$$

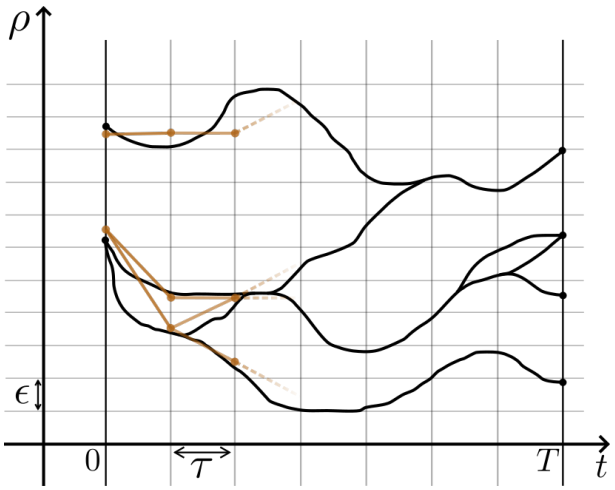

Figure B.1: Schematic illustrating the coarse-graining methodology for the (ϵ, τ)-entropy.

We finally consider the case of continuous-time stochastic process: $X = (X_t, t \in \mathbb{R}^+)$. We first discretise time (as illustrated in Figure B.1), define the discrete-time process $\hat{X}^\tau = (X_{i\tau}, i \in \mathbb{N})$ and use the above definitions

$$h(n, \epsilon, \tau) \doteq \frac{1}{\tau} \left(H_\epsilon(\hat{X}^\tau_{\leq n+1}) - H_\epsilon(\hat{X}^\tau_{\leq n}) \right) \tag{B.16}$$

B.2.3 . Computations and limitations

Monte-Carlo estimates – The numerical and analytical estimations of the above entropies are not simple in the general case. Some algorithms can however give either boundaries or estimates of those quantities. They essentially rely on Monte-Carlo simulations. Among the different available methods we have:

- The Cohen-Procaccia methodology introduced in details in Appendix C.
- The Abel-Biferale [1] methodology which uses exit-times to estimate (ϵ, τ) entropies. They evaluate the time t_ϵ for a trajectory to escape a box of size ϵ which they show to be related to entropy production by $h(n, \epsilon, \tau) \sim \frac{1}{<t_\epsilon>}$ using Shannon-McMillan-Breiman theorem (introduced later). This method has the advantage to be computationally efficient while giving pretty good boundaries for the estimation of the above entropies.

Examples of direct computations – The epsilon-tau entropy defined that way quantifies the amount of uncertainty created per unit time, as explained by Gaspard and Wang [44]. We introduce below some direct examples:

- $X \sim U([0,1])$: then $P_{\boldsymbol{X}}[B(\boldsymbol{x}, \epsilon)] \underset{\epsilon \to 0}{\simeq} \epsilon \mathbb{1}_{B(\boldsymbol{x}, \epsilon)}$, which leads to $H_\epsilon(X) = \log(1/\epsilon)$ for $\epsilon << 1$.

- $X \sim \mathcal{N}(0,\sigma)$: then $P_X[B(x,\epsilon)] \underset{\epsilon\to 0}{\simeq} \frac{\epsilon}{\sqrt{2\pi\sigma^2}} e^{\frac{-x^2}{2\sigma^2}}$, leading to $H_\epsilon(X) = \log(\sqrt{2\pi\sigma^2}/\epsilon)$ for $\epsilon << 1$.

- Diffusions: extending the result of Markov chains to Markov processes, we deduce that entropy rate for those Gaussian processes are given by probability densities transitions. Writing $\boldsymbol{Y}_X = (Y|X)$ for a jump in time τ, we have

$$P_{\boldsymbol{Y}_X}[B(\boldsymbol{x},\epsilon)] \underset{\epsilon\to 0}{\simeq} \frac{\epsilon}{\sqrt{2\pi D\tau}} e^{\frac{-(x-y)^2}{2D\tau}}. \tag{B.17}$$

  All calculations done, one obtains an entropy rate that does not depend on time $n\tau$ any more

$$h(n,\epsilon,\tau) \simeq 1 + \log\left(\frac{\epsilon}{\sqrt{2\pi D\tau}}\right). \tag{B.18}$$

  We note that this last result is however false when the number of considered states is low enough compared to ϵ. As Gaspard and Wang observed in the context of Gaussian processes, for small enough τ, correlations become much stronger and make the approximation in equation (B.17) fail. This was already reported by Kolmogorov who identified the influence of correlations as a need to push the Taylor expansion in ϵ of (ϵ,τ)-entropy further in case of $\epsilon \to 0$. In the case of Gaussian processes, one can therefore observe the rise of ϵ^2 scaling in the limit of finer and finer coarse-graining [47, 44].

B.2.4 . Numerical results

Yaglom process – We test here the numerical computation of the (ϵ,τ)-entropy through the Cohen-Procaccia methodology with the Yaglom processes. Those are stationary centred Gaussian processes with a correlation function prescribed by:

$$C_H(r) \doteq \frac{1}{Z_H}|r|^H K_H(|r|), \tag{B.19}$$

where K_H is a modified Bessel function of the second kind and

$$Z_H = \begin{cases} \Gamma(H)2^{H-1} \text{ for } H > 0 \\ 1 \text{ if } H = 0. \end{cases} \tag{B.20}$$

We note that the H coefficient is called the 'Hurst exponent' and characterises the smoothness of a random process (just as the Hölder exponent h does for deterministic systems). It was shown by Gaspard and Wang that the (ϵ,τ)-entropy should be for those processes:

$$h(\epsilon,\tau) \underset{\epsilon\to 0}{\sim} \epsilon^{-\frac{1}{H}}. \tag{B.21}$$

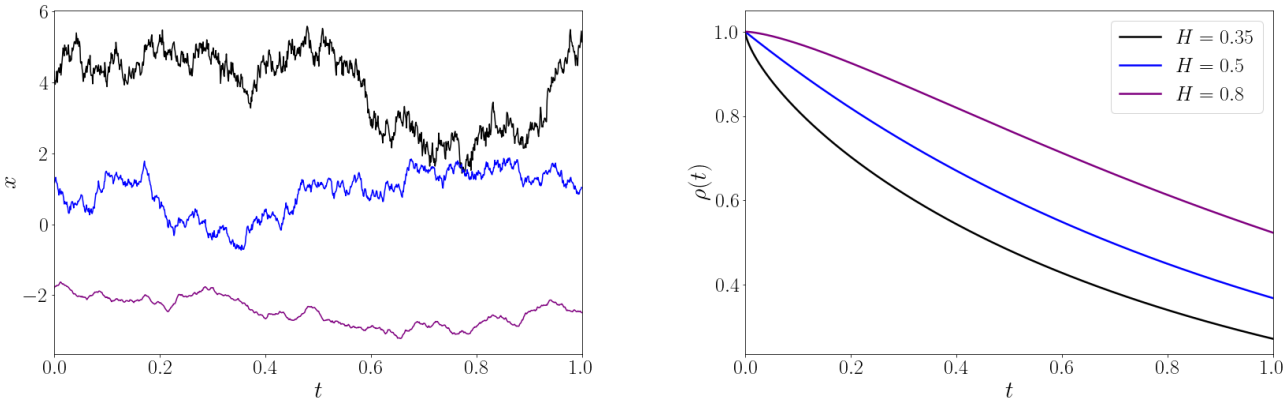

Figure B.2: Left: Realisations of Yaglom processes with $H = 0.35$ (black), $H = 0.5$ (blue) and $H = 0.8$ (purple). Right: Associated auto-correlation functions $\rho(t)$.

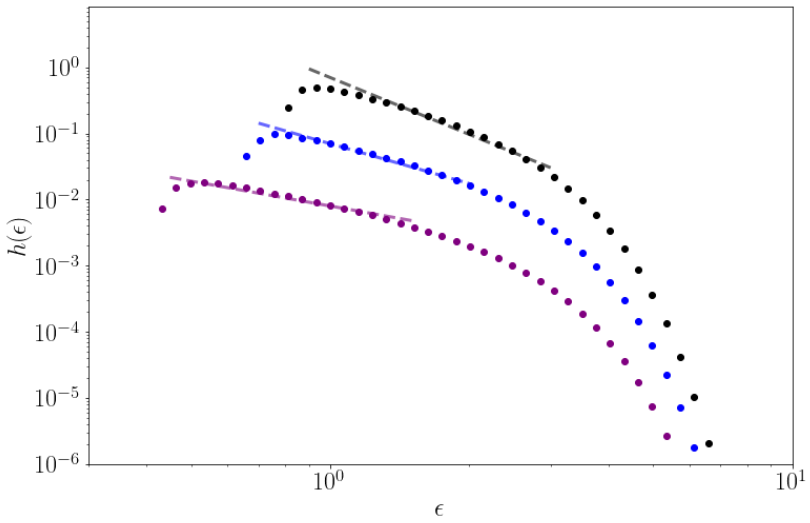

Figure B.3: (ϵ, τ)-entropy as a function of ϵ for the Yaglom processes with $H = 0.35$ (black), $H = 0.5$ (blue) and $H = 0.8$ (purple). Those are numerical computations obtained with the Cohen-Procaccia methodology (see Appendix C). The dashed lines correspond to the $\epsilon^{-1/H}$ predictions given by Gaspard and Wang [44].

Observations – We show in Figure B.2 three realisation of Yaglom processes for $H = 0.35$, $H = 0.5$ and $H = 0.8$ and their auto-correlation functions. Intuitively, we can observe that the more regular the realisation, the 'less complex' it appears. We verify this statement by computing their respective (ϵ, τ)-entropies with the Cohen-Procaccia algorithm. Those results are displayed in Figure B.3.

We observe that the predicted scaling (B.21) seems to be satisfied in the cases $H = 0.35$ and $H = 0.5$. The case $H = 0.8$ does not seem to be converged however, probably because of the long-time correlations of the process. We nonetheless note that the larger H, the larger $h(\epsilon, \tau)$ gets for small ϵ. The entropy production is therefore linked to the apparent complexity of the signals.

Those observations could even be extended in the case of non-stationary processes as expressed by M. Abel and L. Biferale [1] as they show that their exit times are deeply related to multi-fractal exponents that they derive using large deviations theory. Applying those computations to turbulent data, they find a scaling in ϵ that follows the above conclusion with a mean Hurst exponent being the one derived from K41 theory $h = 1/3$.

B.2.5 . Conclusions

In this section, we defined the statistical tools that are necessary to quantify the amount of information created by a stochastic process per unit of time. They particularly offer a quantification of the apparent complexity of signals. We however observed that the computation of (ϵ, τ)-entropies are not trivial in the general case. Numerical tools can help getting some estimates of those entropies. The inner correlations of the system is the main limiting factor to obtain proper analytical or numerical results. Those entropies are however important since they characterise the dynamical systems, as we shall now investigate.

B.3 . Chaos, the long smooth road

We previously observed that the complexity of signals can be measured and quantified using analogues of Shannon entropies. For smooth dynamical systems, the connection between complexity and path entropy is mathematically well defined. One can cite for instance Pesin's theorem, which relates the geometry of attractors to entropy production through the use of Lyapunov spectrum.

As in the case of stochastic processes, we need to be able to define stationary measures. In dynamical system theory, this is achieved by taking large enough time in order to let the system evolve towards an attractor in which it will be (almost) stuck. Once those so called invariant measures defined or computed, one is able to calculate entropy production using the same framework as the one introduced in the previous section. Some useful theorems, that will be presented below, prove the good existence of such mathematical objects. In practice, those entropies are more easily computed through the evaluation of the Lyapunov spectrum or Cohen-Proccacia methodology.

More importantly, mathematicians were able to prove that entropy production in such cases is unique and should not change if the system is transformed by any isomorphism. This characterisation is essential in dynamical system theory as it allows one to classify systems using their complexity. An extension of this was proposed by Gaspard and Wang, where they introduce a ranking of stochastic processes by their entropy production. While this classification goes beyond chaos and dynamical system theory, it is still evaluated for the long-time dynamics.

B.3.1 . Definitions

Lyapunov spectrum – The definition of Lyapunov exponent can be generalised to the different other growth directions. We assume that Φ_t is actually a diffeomorphism and, to that regard, we define the evolution matrix $T_{x,t}$ such as $T^{i,j}_{x,t} = \partial_i \Phi^j_t$. Using the multiplicative Oseledets theorem [72], we can define the following matrix,

$$\Lambda_x \doteq \lim_{t\to\infty} (T^\dagger_{x,t} T_{x,t})^{1/2t}, \tag{B.22}$$

from which we can get the logarithmic values of its eigenvalues $\lambda_1 \leq \dots \lambda_d$. Those coefficients represent growth rate in every eigen-direction, and are called 'characteristic exponents' (often confused as 'Lyapunov exponents'). In the case of an ergodic measure μ, one can show that Lyapunov exponents are invariant under the change of initial position and characterise the geometry of local attractors.

Fractal dimension – In that sense, the fractal dimension D of attractors can be related to characteristic exponents using the Kaplan-Yorke conjecture: by arranging them in increasing order $\lambda_1 \geq \lambda_2 \geq \dots \geq \lambda_d$ and defining index k such as $\sum_{i=1}^k \lambda_i > 0$ and $\sum_{i=k+1}^d \lambda_i < 0$, we define

$$D = k + \frac{\sum_{i=1}^k \lambda_i}{|\lambda_{k+1}|}. \tag{B.23}$$

Kolmogorov-Sinai entropy – To extend the definitions of entropies above, we introduce a small stochastic perturbation of the dynamical system, modifying the dynamics equation 1.3 into Langevin-type equation:

$$d\boldsymbol{x} = \boldsymbol{f}(\boldsymbol{x}(t))dt + \sqrt{2\kappa}\, d\boldsymbol{W}, \tag{B.24}$$

where we recover the initial system by taking the limit of vanishing diffusion $\kappa \to 0$. Using the above definition for continuous stochastic processes, we define entropy rate for the modified dynamics (B.24) such as:

$$h^\kappa(n, \epsilon, \tau) \doteq \frac{1}{\tau}\left(H^\kappa_\epsilon(\hat{X}^\tau_{\leq n+1}) - H^\kappa_\epsilon(\hat{X}^\tau_{\leq n})\right) \tag{B.25}$$

The characteristic entropy rate of attractors is however represented by the so-called Kolmogorov-Sinai entropy which can be obtained by taking the following limits (assuming they exist):

$$h_{KS} \doteq \lim_{\epsilon\to 0}\lim_{\kappa\to 0}\lim_{n\to\infty} h^\kappa(n, \epsilon, \tau) \tag{B.26}$$

Two observations arise from this definition:

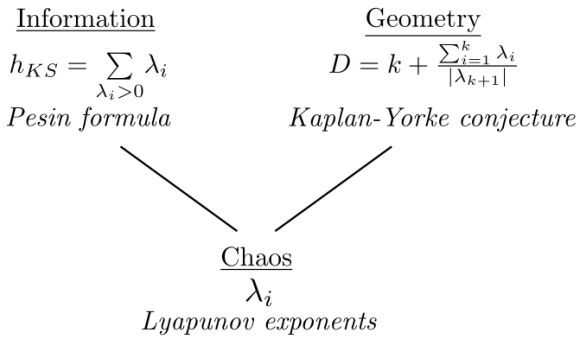

Figure B.4: Schematic summarising the deep connection between chaos, information theory and geometry of attractors in dynamical systems.

- While it is not the usual way to define this entropy in ergodic theory, we should note that both definitions shall be equivalent. Let us consider a system with a single basin of attraction (such as the Lorenz system). In the limit of vanishing noise $\kappa \to 0$, trajectories tend to get trapped in the system's basin of attraction, having the probabilistic stationary measure μ_κ converging to the invariant measure μ. This convergence provides a physical measure, also called 'Kolmogorov measure' [32]. As such, entropies defined by the probability measure or the invariant one are equal in the limit of vanishing noise. The general case is however more difficult to study since a small fluctuation can always make the trajectories jump from one basin of attraction to another, which makes the definition of an invariant measure in this context complicated. In practice, for small enough noise, the system will remain in the same basin of attraction as long as the prescribed simulation duration is not too high. In that sense, we shall converge to an invariant measure in this context and fall back on the above remark. To that reason, we assume in the above definition that we always converge to a Kolmogorov measure, bridging with ergodic theory's definition.

- In the limit $\epsilon \to 0$, this entropy does not depend on τ any more as we study smooth deterministic systems [7].

B.3.2 . Properties/Theorems

The existence of h_{KS} is in general provided by two theorems: given the existence of an invariant measure μ, Shannon-McMillan-Breiman and Kolmogorov-Sinai theorems justify the respective convergence of limits $n \to \infty$ and $\epsilon \to 0$. One can particularly show that this entropy is invariant under any transformation of the dynamical system by an isomorphism. In other words, dynamical systems are entirely characterised by their rate of information production. Assuming that we can write $\forall A,\ \mu(A) = \int_A \rho(x) dx^d$, i.e that μ admits a density ρ, then Pesin's theorem states that geometry of attractors is related to

the Kolmogorov-Sinai entropy by the following formula:

$$h_{KS} = \sum_{\lambda_i > 0} \lambda_i, \tag{B.27}$$

where the sum is over the positive Lyapunov exponents only. This shows the intimate relation between production of information and chaos, falling under the mantra: the more chaotic, the more unpredictable. But with Kaplan-Yorke's interpretation, we can also see how deep is the link between creation of information and local geometry of attractors. We summarise the link between chaos, information theory and geometry of attractors in a schematic presented in Figure B.4.

To determine Kolmogorov-Sinai entropy in practice, one can either compute Lyapunov exponents and use Pesin's formula or use Cohen-Procaccia method.

B.3.3 . Two illustrations: Lorenz 63 and the ABC model

We illustrate here some of the properties and theorems broached above. We first come back to the Lorenz 63 system (defined in Chapter 1) which we explore from the scope of entropies. We then analyse the ABC flow case, which shows the limitations of the introduced entropies.

Lorenz 63: a well known system – Once on the attractor, the distribution of positions falls into the invariant measure of the system. The Kolmogorov-Sinai theorem can be applied and we can determine entropy production using Pesin's formula. We set $(\sigma, \rho, \beta) = (16,\ 45.92,\ 4)$ and compute (ϵ, τ)-entropy using Cohen-Proccacia methodology to compare with Pesin's formula, for which results are presented in Figure B.5. Several curves are displayed, where we used an increasing number of points for the statistics, ranging from 10^7 to 1.6×10^8 particles.

We observe that the curves reach a supremum, being equal to the dashed line. This corresponds to the computed positive Lyapunov exponent. We can therefore see a good agreement between Pesin's formula and the Cohen-Procaccia estimates. In practice, it is way easier to compute the Lyapunov exponents ($\sim$ 1h) than entropies directly ($\sim$ 2 weeks parallelised).

ABC model: first limitations – As presented in Chapter 4, determining the ABC model's Lyapunov exponents is a challenge. The system presents many different attractors. As such, the selected trajectory used for computing the spectrum, eventually ends up in another attractor for long enough time. This is why we opted for short-time statistics like the instantaneous Lyapunov exponents to analyse the WABC flow's properties. In practice, the long-time limit is therefore not suited for systems that possess more than one invariant measure.

B.3.4 . The GW classification: a generalisation towards stochastic processes?

In their 1995's article [44], Gaspard and Wang proposed a classification of dynamical systems based on the Kolmogorov-Sinai entropy. The invariance of this entropy under the

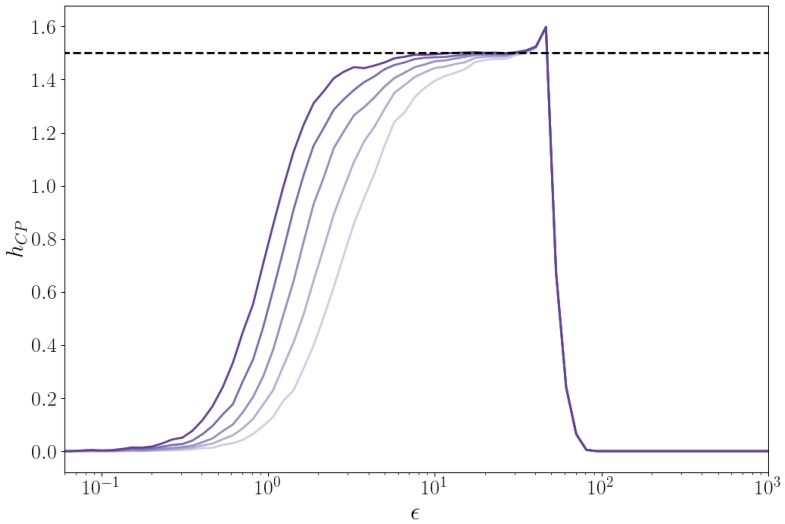

Figure B.5: (ϵ, τ)-entropy as a function of coarse-graining ϵ of the Lorenz system in the chaotic case $(\sigma, \rho, \beta) = (16, 45.92, 4)$. The curves use a number of points ranging from $N_p = 10^7$ (light purple) to $N_p = 1.6 \times 10^8$ (deep purple). The dashed line corresponds to the only positive Lyapunov exponent, determined numerically with equation (B.22). We here verify Pesin's formula where the supremum of $h(\epsilon, \tau)$ corresponds to the sum of positive Lyapunov exponents.

effect of any isomorphism justifies these observations. As such, we can divide dynamical systems into two groups: the non-chaotic systems for which the Kolmogorov-Sinai entropy is 0 and the chaotic ones for which this entropy is non-zero. One can scale the different complexities of chaotic systems by comparing the entropies. In that sense, a numerical determination of those quantities can be useful when studying an unknown system, using Monte-Carlo methods.

Since those methods are well defined for stochastic processes, one may wonder if it is possible to reach the same classification for such systems? In other words, is it possible to classify complexity of stochastic processes, and especially in the so common non-stationary case?

B.4 . Spontaneous stochasticity, the short rough road

Gaspard and Wang, in their article, try to tackle the problem of classifying complexity of stochastic processes. They first observe that the absence of local attractors in such systems inevitably leads to a diverging Kolmogorov-Sinai entropy. They however argue that even though those entropies shall diverge, their way of diverging should implicitly determine the complexity of those systems. As such, evaluating their asymptotic behaviours in the limit of vanishing scales could be categorised as well.

While the scope of Gaspard and Wang goes beyond chaos (i.e. smooth dynamical systems), complexity is still evaluated for long times. No observations has indeed been lead regarding non-stationary systems for which evaluating complexity is still to be correctly understood. Here we would like to discuss the evaluation of complexity for a transient stochastic behaviour that can arise from some deterministic settings: spontaneous stochasticity.

An analysis over simple examples will be lead in order to uncover the eventual failures of the determination of the Kolmogorov entropy in this framework. The failures and needed properties would be analysed to give some crude answers to the above problems.

B.4.1 . Examples with direct but gentle estimates

We recall the definition of the singular double well potential (represented in Figure B.6):

$$V(x) = (1 - ||x||^{1+h})^2. \tag{B.28}$$

In the following series of examples, we consider a damped particle of mass m under the effect of the above potential:

$$m\ddot{x} = -\nabla_x V - \gamma m\dot{x} + \sqrt{2\kappa}\,\xi(t), \tag{B.29}$$

where ω is the damping coefficient. We would like to study the effect such potential has on entropy determination through different simple cases:

1. When we are considering the over-damped dynamics in one dimension ($\gamma >> 1$).

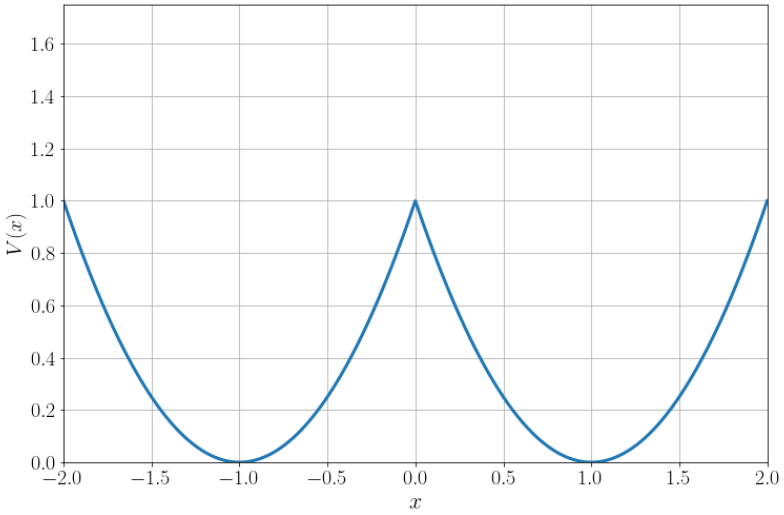

Figure B.6: Singular double-well potential.

2. When we are considering a massive particle that has its energy conserved exactly, being equal to the energy barrier ($\gamma = 0$), still in one dimension.

3. When we are considering the same case but in two dimensions (Mexican hat style).

Over-damped dynamics – We suppose that the damping is leading the dynamics, $\gamma >> 1$. We consider a particle on top of the potential. As we have already seen, we are able to find a correct scaling for which a transient stochasticity appears in the limit of vanishing noise: an infinitesimal perturbation will make the particle jump into one of the two wells. At time $t = 0$, the particle is able to choose between two paths that become deterministic at infinite time (the particle stays in the chosen well), corresponding to all possible realisations. We therefore deduce that entropy in the spontaneously stochastic limit is exactly

$$H = \Theta_H(t) \log 2, \tag{B.30}$$

with Θ_H the Heaviside function. The entropy rate is thus zero unless in $t = 0$ where:

$$\dot{H} = \delta(t) \log 2. \tag{B.31}$$

In Gaspard-Wang's definition (i.e. the one from dynamical system theory), one finds that entropy rate in that case is 0 as the $t \to \infty$ cancels $H = cte$. Spontaneous stochasticity is not necessarily a stationary process, which complicates its study.

1D conserved dynamics – We suppose this time that energy E_m is conserved, i.e. $\gamma = 0$ and that $E_m = V(0)$. We consider the initial position $x_0 = -1$ with an initial velocity pointing at the barrier.

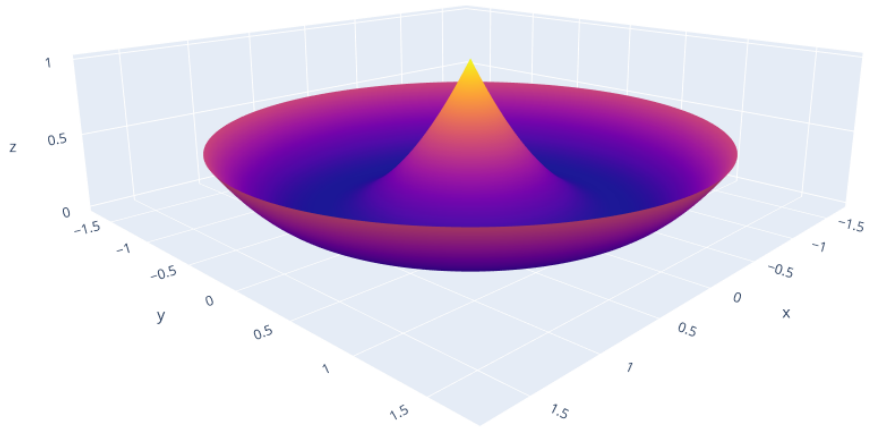

Figure B.7: Singular Mexican hat potential.

In the case of $h = 1$, in such situation, a particle would take an infinite amount of time to change well. But in the case $h < 1$, a particle would not only take a finite amount of time to reach the top but then will have two possible paths to choose, just as in the previous example. We will therefore have an amount of possible paths that depends on the number of times we reached the top, therefore leading to an entropy

$$H \sim \left\lfloor \frac{t}{T_p} \right\rfloor \log 2, \tag{B.32}$$

where T_p is the time period for a particle to stay in one well. In the case of Gaspard and Wang, we have to impose a coarse-graining ϵ to compute this entropy. One can however show that this entropy goes to infinity in the limit of vanishing ϵ.

2D conserved dynamics – We suppose here that $\boldsymbol{x}$ is instead of dimension 2 (which is represented in Figure B.7). We take the example of a particle on top of the potential and that has therefore an infinity of angles where to fall. The probability of a path is not finite any more and one should consider probability densities instead. This example shows that our definition of entropy struggles in correctly describing the singularity as it shall be infinite as well.

A good measure of complexity should give us something similar as in the previous example, which is $H \sim \left\lfloor \frac{t}{T_p} \right\rfloor$. The same way as in the other two cases, following Gaspard and Wang's point of view leads to a diverging entropy for the limit $\epsilon \to 0$.

Conclusions and requirements – Through those three different examples we were not always able to capture the spontaneous stochastic event occurring in the dynamic. Especially, Gaspard and Wang's point of view was totally unable to get the right measure of complexity of those transient regimes. They were mainly interested in knowing the stationary measure in those systems. However, we are interested in evaluating transition probabilities, finite-time quantities that could eventually require to be in a continuous

description of space. As such, spontaneous stochasticity differs from chaos and therefore inevitably makes ergodic theory fail in those regimes.

The main issue that one faces in spontaneous stochasticity is to determine if the considered regularised processes (such as 3.1) are still stochastic in the limit of vanishing noises. The study of properties of such transient systems is in full generality hard.

One may though want to characterise such behaviours in an approximate fashion. Our definition of entropy was not suitable to describe complexity in the case of the two dimensional double well potential. The argument was actually made clear by Jaynes in the 70's [55]. He showed that the Shannon entropy is ill-defined in the continuous limit and an additional normalisation term should be added. The good normalisation to consider is however not trivial.

One way to avoid this problem is to having a look into inference theory. Using tools like the Kullback-Leibler entropy, one may compare measurements to an inferred model. As such, in our case, if we infer that the probability measure to be expected is $p \sim 2\pi$, then our entropy becomes finite or eventually 0. The physical interpretation should equally be changed. The computation of those relative entropies answer the question: 'Is my considered system more complex than my reference one?'. A diverging relative entropy would therefore mean that the two processes are not comparable in terms of complexity. As such we should find a model that has a comparable complexity compared to the studied system.

B.4.2 . Turbulent-inspired models: more violent estimates

Following the ideas from inference theory, it is possible to check for spontaneous stochasticity in turbulence by comparing with well-chosen models. We only give, in this thesis, some perspectives which we did not have time to fully check.

Pair dispersion – As an example, we know that the Kraichnan model is able to reproduce faithfully the statistics of pair dispersions in turbulence. The $1d$ distributions of pair dispersion can be modelled by Richardson's distribution [77]:

$$P_{Ric}(r,t) \propto \frac{r^2}{\langle r^2(t)\rangle^{3/2}} \exp\left\{-b\left(\frac{r}{\langle r^2(t)\rangle^{1/2}}\right)^{2-\xi}\right\}, \tag{B.33}$$

where $r(t) = ||\boldsymbol{x}_2(t) - \boldsymbol{x}_1(t)|| \sim t^{2/(2-\xi)}$ the pair dispersion, which imposes $\xi = 4/3$. This distribution can be formally recovered in the Kraichan model [39, 46] and was observed in DNS [75]. We could extend those investigations by considering the whole random process. The Kraichan model can indeed serve as a reference model, which n-times statistics are written $p^n_{Ric}(r_0, \ldots, r_{n-1})$ [2]. The underlying random process in pair dispersion $p^n_{exp}(r_0, \ldots, r_{n-1})$ would then be compared numerically to this model, as we now know

[2]For the sake of simplicity, the random variables will be forgotten in this part. We aim at giving some insights only.

that

$$H_{KL}(p^n_{exp},\, p^n_{Ric}) = 0 \;\;\Leftrightarrow\;\; \forall (r_1,\,\ldots,\,r_n) \in \mathbb{R}^n,\;\; p^n_{exp}(r_1,\,\ldots,\,r_n) = p^n_{Ric}(r_1,\,\ldots,\,r_n). \tag{B.34}$$

Markov hypothesis – The n-times statistics are hard to compute in practice. Instead we would rely on using a Markov hypothesis, which simplifies the above entropy as we shall now introduce. We consider the general case where we compare two n-times probability distributions $p(\rho_0,\,\ldots,\,\rho_{n-1})$ and $q(\rho_0,\,\ldots,\,\rho_{n-1})$. We assume that the Markov hypothesis applies here. Therefore :

$$\forall i \;\; p(\rho_i|\rho_{i-1}\rho_{i-2}\ldots\rho_0) \doteq p(\rho_i|\rho_{i-1}). \tag{B.35}$$

Also, we note that for any function f,

$$\forall i \sum_{\rho_0,\,\ldots,\,\rho_{n-1}} p(\rho_{i+1}\ldots\rho_{n-1}|\rho_0\ldots\rho_i) f(\rho_0\ldots\rho_i) = \sum_{\rho_0\ldots\rho_i} f(\rho_0\ldots\rho_i) \tag{B.36}$$

since that all possible paths starting at a time $i\tau$ does not depend on previous paths. Using Bayes scheme and the above property of Markov processes, we obtain the following simplification :

$$p(\rho_0\rho_1\ldots\rho_{n-1}) = p(\rho_0)\prod_{i=0}^{n-1} p(\rho_{i+1}|\rho_i). \tag{B.37}$$

This leads to consider a separation in two terms of the entropy :

$$H_{KL}(p,q) = \int d\rho_0\,\ldots\int d\rho_{n-1}\, p(\rho_0\ldots\rho_{n-1})[\log\frac{p(\rho_0)}{q(\rho_0)} + \sum_{i=0}^{n-1}\log\frac{p(\rho_{i+1}|\rho_i)}{q(\rho_{i+1}|\rho_i)}]. \tag{B.38}$$

Since $p(\rho_0,\,\ldots,\,\rho_{n-1}) = p(\rho_1\ldots\rho_{n-1}|\rho_0)p(\rho_0)$, the first term can be actually reduced to only $\sum_{\rho_0} p(\rho_0)\log\frac{p(\rho_0)}{q(\rho_0)}$ using property (B.36). Thus :

$$H_{KL}(p,q) = \int d\rho_0\, p(\rho_0)\log\frac{p(\rho_0)}{q(\rho_0)} - \sum_{i=0}^{n-1}\int d\rho_0\,\ldots\int d\rho_{n-1}\, p(\rho_0\ldots\rho_{n-1})\log\frac{p(\rho_{i+1}|\rho_i)}{q(\rho_{i+1}|\rho_i)}. \tag{B.39}$$

We note $K_i = \int p(\rho_0\ldots\rho_{n-1})\log\frac{p(\rho_{i+1}|\rho_i)}{q(\rho_{i+1}|\rho_i)}$. Let us focus on K_3. We have :

$$\begin{aligned} K_3 &= \int_{\rho_0\ldots\rho_{n-1}} p(\rho_0\ldots\rho_{N-1})\log\frac{p(\rho_4|\rho_3)}{q(\rho_4|\rho_3)} \\ &= \int_{\rho_0\ldots\rho_{n-1}} [p(\rho_5\ldots\rho_{N-1}|\rho_4\ldots\rho_0)\, p(\rho_1\rho_2|\rho_3\rho_4)\, p(\rho_4|\rho_3)\, p(\rho_3|\rho_0)\, p(\rho_0)]\,\log\frac{p(\rho_4|\rho_3)}{q(\rho_4|\rho_3)}. \end{aligned} \tag{B.40}$$

When using property (B.36), we then obtain that :

$$K_3 = \int\int\int_{\rho_0\rho_3\rho_4} p(\rho_4|\rho_3)p(\rho_3|\rho_0)p(\rho_0)\log\frac{p(\rho_4|\rho_3)}{q(\rho_4|\rho_3)}. \tag{B.41}$$

More generally, we deduce that

$$K_i = \int d\rho_0 \int d\rho_i \int d\rho_{i+1}\, p(\rho_{i+1}|\rho_i) p(\rho_i|\rho_0) p(\rho_0) \log \frac{p(\rho_{i+1}|\rho_i)}{q(\rho_{i+1}|\rho_i)}, \tag{B.42}$$

and

$$H_{KL}(p,q) = \int d\rho_0\, p(\rho_0) \log \frac{p(\rho_0)}{q(\rho_0)} - \sum_{i=0}^{n-1} K_i. \tag{B.43}$$

Perspectives – Using the Markov property, we could therefore evaluate the deep difference between the Kraichnan model and the turbulent pair dispersion. One could indeed only evaluate the transition probabilities and use equation (B.43) to compare the two processes. This comparison would be interesting to perform since the Kraichnan model is known to present Lagrangian spontaneous stochasticity. Also, its solvability could lead to interesting developments towards finding new ways to analyse the experimental Lagrangian data, especially in the perspective of unveiling spontaneous stochasticity.

B.5 . General discussion: Spontaneous stochasticity versus Chaos

From the above analysis of those singular potential examples, we were unable to distinguish systems that are chaotic from those that are spontaneous stochastic using path entropies in a general way. We always had to adapt our definitions to the system that we were studying. In particular, spontaneous stochasticity is, in most generality, a non-stationary process. As a consequence, we need to be able to probe finite-time non-vanishing Shannon entropies, which goes beyond the ergodic theory.

It seems that there is no clear frontier between those two worlds, and the reality is probably showing a continuous evolution of complexity going from purely stochastic processes to deterministic systems having somewhere in between both chaos and spontaneous stochasticity. We can however say that the latter is expected to be more complex than chaotic systems as two trajectories would still separate in finite-time in case of vanishing initial separation.

As underlined above, one should instead compare systems using inference theory and relative entropy, from which a more useful information would be extracted. In particular, we proposed a methodology to have a deeper analyse of turbulent pair dispersion. The link with the Kraichnan model should be exploited, as this model would serve as a reference in the entropy computations. A vanishing Kullback-Leibler divergence in that case would indicate a true correspondence between the model and the experiment.

C - Cohen-Procaccia entropy

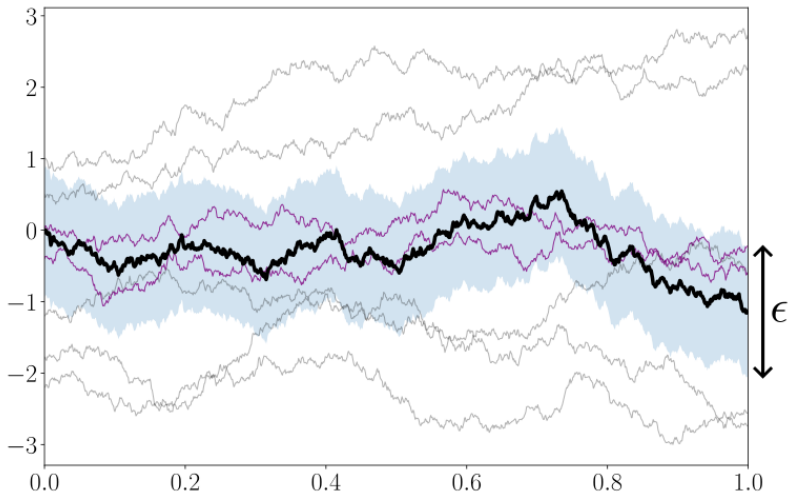

Figure C.1: Illustration of the Cohen-Proccacia methodology for computing (ϵ, τ)-entropies. Among all realisations, we count only the ones (purple) that are close to the reference trajectory (black) within a precision ϵ. We note that in the case of dynamical systems, a long trajectory is divided into pieces. They are seen as realisations of a same process, falling back onto the stochastic method.

In case of a stationary process, Monte-Carlo simulations can give an estimate of $P_\epsilon(X_{\leq n}) \doteq P_{X_{\leq n}}[B(x, \epsilon)]$. We consider R reference paths $X^r_{\leq n}$ ($r \in [1, R]$) which are chosen randomly, i.e. they should constitute typical paths the system can take, such that we efficiently coarse-grain the above probability. We define a L^∞ distance between two paths such that:

$$D_n(X_{\leq n}, X'_{\leq n}) \doteq \max\{||X_1 - X'_1||, \ldots, ||X_n - X'_n||\}. \tag{C.1}$$

We observe that the norm $||.||$ can be chosen freely and does not have an impact on the results [52]. A good estimate of the above probability, for a given reference path, should therefore be given by the number of paths generated by Monte-Carlo method that are close up to ϵ to the reference one (assuming convergence of statistics):

$$P_\epsilon(X^r_{\leq n}) \simeq \frac{\#\{X_{\leq n} \mid D_n(X_{\leq n}, X^r_{\leq n}) \leq \epsilon\}_{MC}}{\#\{X_{\leq n}\}_{MC}} \tag{C.2}$$

If R is large enough, one can also estimate (ϵ, τ)-entropy by taking the average over the

chosen reference paths:

$$H(\epsilon, \tau, n) \simeq -\mathbb{E}_r(\log P_\epsilon(X^r_{\leq n})) = -\frac{1}{R}\sum_r \log P_\epsilon(X^r_{\leq n}), \tag{C.3}$$

which can then be used to compute the entropy rate of this process.

In the case of dynamical systems, Cohen and Procaccia have proved that such strategy can also be used to efficiently compute estimates of (ϵ, τ)-entropies [18]. Instead of considering several realisations of the process however, they consider a very long trajectory (in the style of dense orbit) that is assumed to remain on the attractor. Sequences of this long trajectory are chosen and, under the use of the invariant measure, act as the independent paths used in the Monte-Carlo methodology. Dynamical systems are therefore seen as stochastic processes, and as such, this lighter method can also be used to analyse any stationary process.

One should however note that those methods largely rely on paths length and, to that regard, one should choose sequences that are large enough compared to the typical evolution time of the system. In other words, $N\tau$ should be way larger than $\min_{\lambda>0}\left(\frac{1}{\lambda}\right)$ for chaotic systems or correlation time for stochastic processes in order to correctly quantify complexity in the considered dynamics. Similarly, more statistics should be required as complexity increases.

D - Computation of instantaneous Lyapunov exponent in the WABC flow

In order to compute the instantaneous Lyapunov Exponent (iLE) λ^i in practice, we use an approximation by Nolan et al. In this section, we first introduce the notion of Finite Time Lyapunov Exponent (FTLE) and then give an approximated formula for the iLE in the WABC flow.

D.1 . Finite-time Lyapunov exponent

From the definition of flows given in Chapter 1, we here introduce the notion of 'flowmap', where

$$\boldsymbol{\Phi}_t^{t+\tau}(\boldsymbol{x}) = \boldsymbol{x} + \int_t^{t+\tau} \boldsymbol{u}(\Phi_t^{t'}(\boldsymbol{x}), t')\, dt', \tag{D.1}$$

where $\boldsymbol{u}$ is the velocity field. From this, we can define the right Cauchy-Green strain tensor:

$$C_t^{t+\tau}(\boldsymbol{x}) = (\nabla \boldsymbol{\Phi}_t^{t+\tau}(\boldsymbol{x}))^\top \nabla \boldsymbol{\Phi}_t^{t+\tau}(\boldsymbol{x}). \tag{D.2}$$

We define the $\tilde{c_i}(\boldsymbol{x})$ as being the eigenvalues of $C_t^{t+\tau}(\boldsymbol{x})$. Since $C_t^{t+\tau}(\boldsymbol{x})$ is symmetric, by spectral theorem we conclude that the $\tilde{c_i}(\boldsymbol{x})$ are real and can be ordered:

$$\tilde{c_1} \leq \tilde{c_2} \leq \cdots \leq \tilde{c_d}. \tag{D.3}$$

We can therefore define the Finite-Time Lyapunov exponent (FTLE) as:

$$\lambda_\tau^{FTLE} = \frac{1}{2\tau} \log \tilde{c_d}. \tag{D.4}$$

We know that one can get the iLE by having: $\lim_{\tau \to 0} \lambda_\tau^{FTLE} = \lambda^i$. Introducing the rate-of-strain tensor

$$\boldsymbol{S}(\boldsymbol{x}, t) = \frac{1}{2} \left(\nabla \boldsymbol{u}(\boldsymbol{x}, t) + (\nabla \boldsymbol{u}(\boldsymbol{x}, t))^\top \right) \tag{D.5}$$

with its ordered eigenvalues (since it is symmetric): $s_1 \leq s_2 \leq \cdots \leq s_d$, Nolan et. al. [65] showed that the Taylor expansion of the right Cauchy-Green strain tensor can lead to useful simplifications for the computation of iLEs. In particular, for the eigenvalues (hence the iLE), we get:

$$\lambda^i \underset{\tau \to 0}{=} s_d + o(1) \tag{D.6}$$

D.2 . WABC flow

This approximation is very convenient in the case of the WABC flow, since it is stationary. As such, we get

$$\boldsymbol{S}(\boldsymbol{x},t) = \sum_{n=1}^{N} \frac{\omega_n}{2} \begin{pmatrix} 0 & B\cos(k_n x) - C\sin(k_n y) & A\cos(k_n z) - B\sin(k_n x) \\ B\cos(k_n x) - C\sin(k_n y) & 0 & C\cos(k_n y) - A\sin(k_n z) \\ A\cos(k_n z) - B\sin(k_n x) & C\cos(k_n y) - A\sin(k_n z) & 0 \end{pmatrix}. \tag{D.7}$$

One can diagonalise numerically this matrix to get the eigenvalues s_i. Since the WABC flow is stationary, the maximum eigenvalue s_d directly gives the iLE using approximation (D.6).

E - Convergence of standard deviation with FlowHisto

To ensure statistical convergence of the transition standard deviation, we need to evaluate the number of realisations N_{FM} required from the FlowHisto method. To that aim, we compute the spatial average of the transition standard deviation

$$\langle \sigma^{\epsilon,\tau} \rangle = \int_M \sigma^{\epsilon,\tau}(\boldsymbol{x})\, d\boldsymbol{x}, \tag{E.1}$$

for different N_{FM} for the WABC flow, the DNS and the experimental data. We say that we are converged, when $\langle \sigma^{\epsilon,\tau} \rangle$ reaches a plateau qualitatively. Results are presented in Figure E.1.

We observe in all cases that the case $N_{FM} \sim 5000$ seems to be a good trade-off between computational time and statistical convergence. We also note that this does not seem to strongly depend on grid size or particle density. We therefore chose to have for all data $N_{FM} = 5000$.

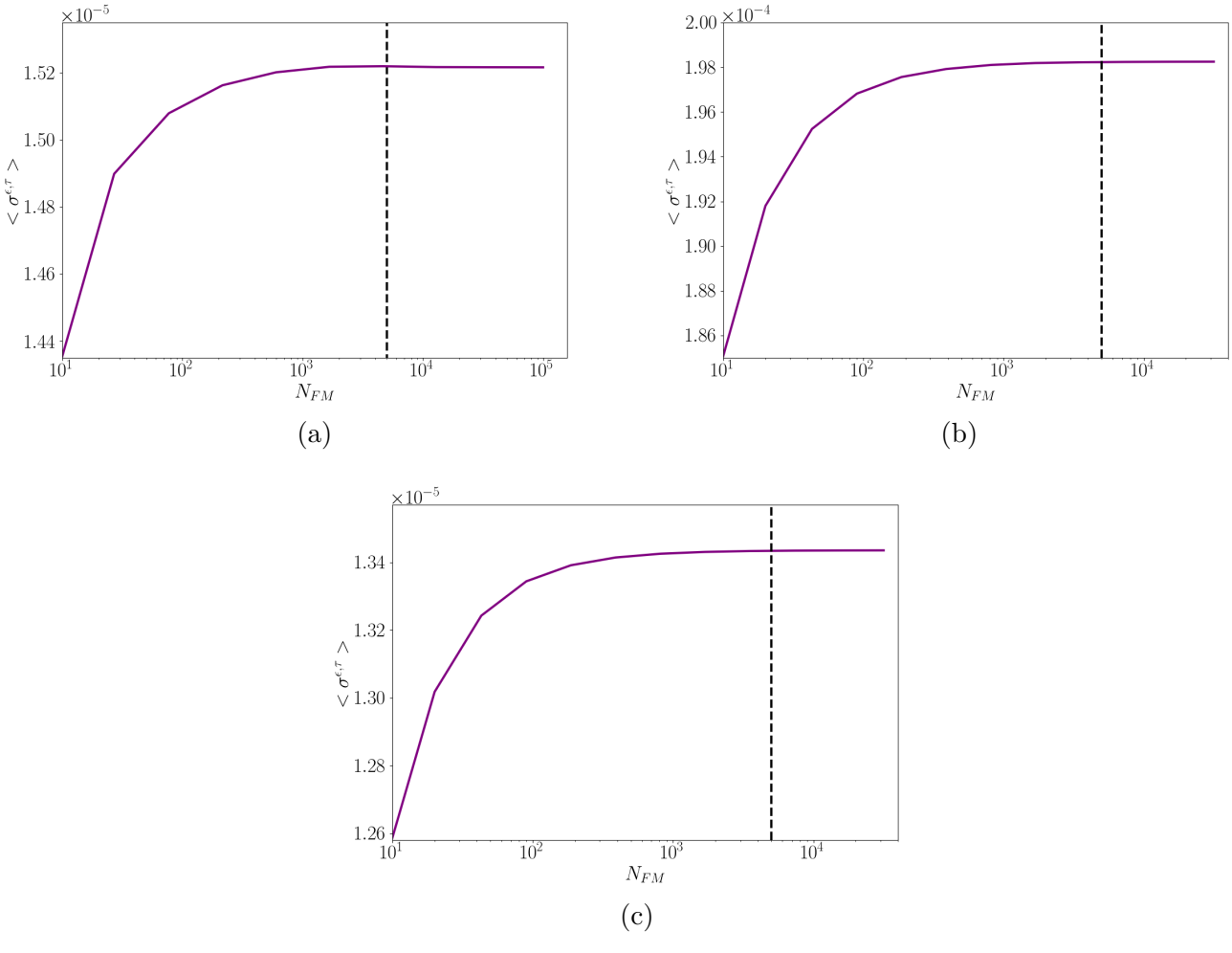

Figure E.1: Evolution of $< \sigma^{\epsilon,\tau} >$ as a function of number of generated realisations N_{FM} for the GVK experiment (a), the DNS (b) and the WABC flow (c). See data presentation (Chapters 7 and 8) for further details.

F - Decorrelations and Markov processes

F.1 . Introduction

F.1.1 . Correlations and anomalous dissipation

We introduce the auto-correlation function

$$C(\tau) = \frac{\left\langle \boldsymbol{u}^L(t).\boldsymbol{u}^L(t+\tau) \right\rangle}{\langle \boldsymbol{u}^L(t).\boldsymbol{u}^L(t) \rangle}, \tag{F.1}$$

where $\boldsymbol{u}^L$ is the Lagrangian velocity and $C(0) = 1$. It is often assumed that spontaneous stochasticity is related to a loss of memory of the trajectories' history, being a sign of a Markov property. This necessarily implies that Lagrangian velocities should decorrelate faster in places where there are spontaneously stochastic events. In this thesis, we wanted to check whether spontaneous stochasticity is experimentally related to anomalous dissipation. A way to challenge this hypothesis, is actually to check whether decorrelation is faster in places of strong anomalous dissipation.

F.1.2 . Methodology

F.1.3 . Drivas' theorem –

To evaluate the anomalous dissipation in the Lagrangian point of view, we make use of Drivas' theorem introduced in 2019 [25, 16]. This theorem relates the difference of the particle's backward and forward dispersions with anomalous dissipation. We define the deviation $\delta_{\boldsymbol{r}} \boldsymbol{X}_{t_0,t}(\boldsymbol{x}) = \boldsymbol{X}_{t_0,t}(\boldsymbol{x}+\boldsymbol{r}) - \boldsymbol{X}_{t_0,t}(\boldsymbol{x})$, where $\boldsymbol{X}_{t_0,t}(\boldsymbol{x})$ represents the position of a particle at time t knowing it was at position $\boldsymbol{x}$ at time t_0. We can then introduce the smoothed dispersion coefficient:

$$\Delta_l^{\pm\tau}(\boldsymbol{x},t) = \int d\boldsymbol{\xi}\, \Phi^l(\boldsymbol{\xi})\, ||\delta_{\boldsymbol{\xi}} \boldsymbol{X}_{t,t+\tau}(\boldsymbol{x}) - \delta_{\boldsymbol{\xi}} \boldsymbol{X}_{t,t}(\boldsymbol{x})||^2, \tag{F.2}$$

where $\Phi^l(\boldsymbol{x}i)$ is a smoothing function (just as for the Duchon-Robert theorem). Φ^l is here chosen to be a Heaviside function (see [16] for further details). Introducing the Lagrangian irreversibility indicator

$$\mathcal{I}_{\mathcal{L}}^{\tau,l} \doteq \frac{\Delta_l^{-\tau} - \Delta_l^{\tau}}{4\tau^3}, \tag{F.3}$$

T. Drivas was able to prove that it is related to anomalous dissipation as:

$$\lim_{l\to 0} \lim_{\tau\to 0} \lim_{\nu\to 0} \mathcal{I}_{\mathcal{L}}^{\tau} = \epsilon[I]. \tag{F.4}$$

It corresponds to the Lagrangian counterpart of Duchon-Robert's theorem.

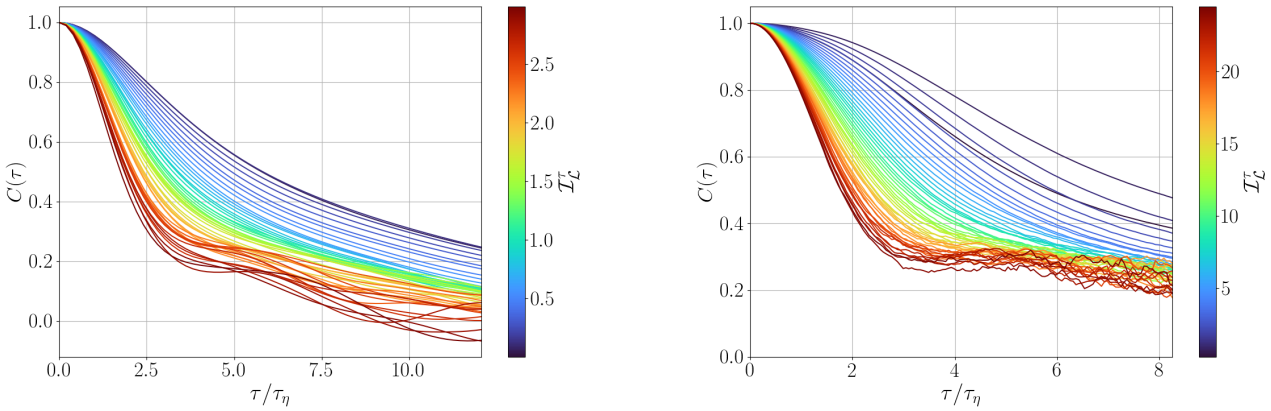

Figure F.1: Evolution of auto-correlation function $C(\tau)$ conditioned by dissipation $\mathcal{I}_\mathcal{L}^\tau$ as a function of time τ. Left: data from DNS with $Re = 131.7$ and $l_c = 11.8\eta$, Right: data from the SVK experiment with $Re = 157\ 000$ and $l_c = 28\eta$.

Conditioned averages – To check whether decorrelation is faster in places of strong anomalous dissipation, we compute the Lagrangian auto-correlation function for all trajectories in the SVK and DNS data (see Chapter 8 for more information about this data). We then compute the conditioned average of those functions $\langle C(\tau)\rangle_\mathcal{I}$ over the $\mathcal{I}_\mathcal{L}^\tau$ felt by the particles at their initial position in the flow. We then see if, in average, correlations decay much faster near strong $\epsilon^l[I]$.

We note that, in practice, the $\mathcal{I}_\mathcal{L}^\tau$ can present some artefacts due to a lack of particles locally. As such, we perform a time averaging of $\mathcal{I}_\mathcal{L}^\tau$ over some instants before and after t in order to smooth the potential artefacts.

F.2 . Results

We present in Figure F.1 the conditioned correlation functions $\langle C(\tau)\rangle_\mathcal{I}$ for the DNS and the SVK experiment. We note that the investigated scales here are $l_c = 11.2\eta$ for the DNS and $l_c = 28\eta$ for the experimental data. We observe that the average correlation function decreases faster when $\mathcal{I}_\mathcal{L}^\tau$ is larger. Those results tend to show that, indeed, places of extreme events of dissipation tend to decorrelate faster the Lagrangian velocities. This goes in favour of a scenario where spontaneous stochasticity is linked to anomalous dissipation.

G - Convergence of the Cauchy-WABC problem

G.1 . Introduction

We here provide the results concerning the convergence of the Cauchy-WABC's probability distributions, a sign of spontaneous stochasticity. We recall that the initial positions $\boldsymbol{x}_0$ are taken randomly within a ball $\mathcal{B}(\boldsymbol{x}_0^*, \eta_N)$, with $\eta_N = \frac{10}{k_N}$. All trajectories are integrated using a Runge-Kutta method of strong order 4/5. See Chapter 7 for further information.

G.2 . Results

G.2.1 . 1,2-points statistics

Qualitative approach – We introduce first the evolution of one and two-points statistics as N increases. The one-point statistics are presented in Figure G.1. The two-points ones are then introduced (by slices) in Figure G.2, Figure G.3 and Figure G.4.

We observe that in both cases, the distributions seem to converge onto non-trivial curves as in the Langevin-WABC case. Again we notice that convergence seems achieved for $N \geq 12$.

Kullback-Leibler divergence – Just as for the Langevin-WABC, we quantify this convergence using the Kullback-Leibler divergence $H_{KL}(p_{N+1}, p_N)$. We present those results in Figure G.5. We observe that this entropy decreases with N until reaching a plateau due to numerical errors.

G.2.2 . Discussions

As in the Langevin-WABC case, we observe a convergence of statistics towards non-Dirac distributions. We conclude that for this regularisation, the WABC model also shows spontaneous stochasticity, up to numerical errors. We note, again, that the limiting factor remains the number of particles.

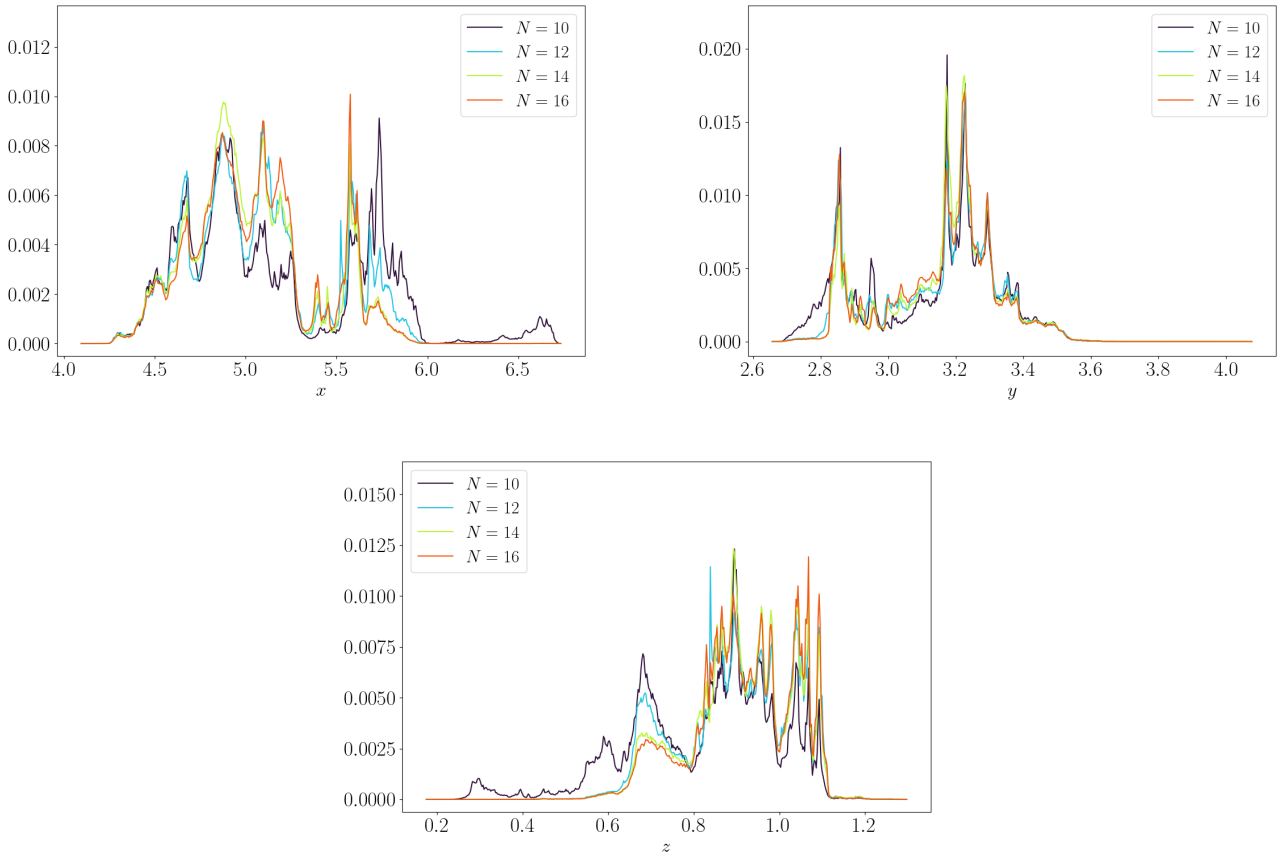

Figure G.1: Evolution of one-point statistics through the number of modes N for the Cauchy-WABC problem for $h = 1/3$ on the three different axes x, y and z.

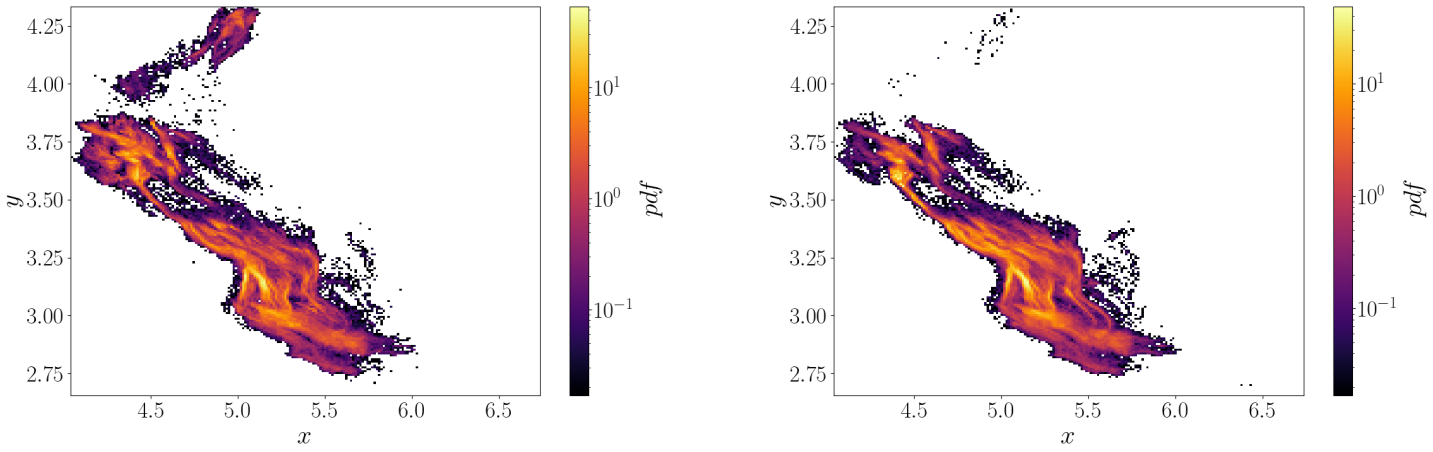

(a) $N = 10$

(b) $N = 12$

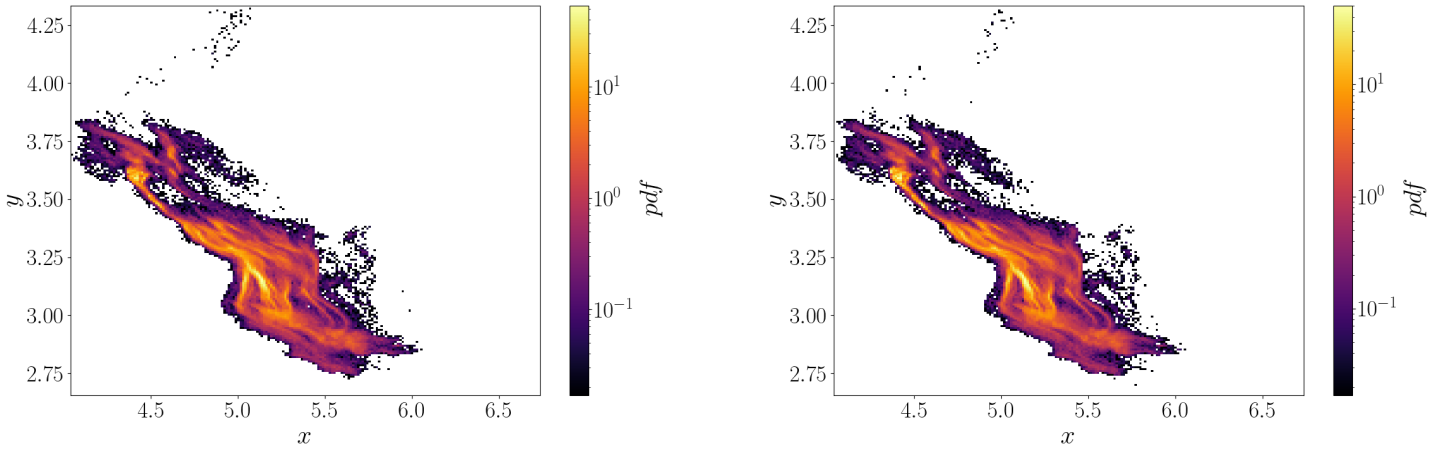

(c) $N = 14$

(d) $N = 16$

Figure G.2: Evolution of two point statistics through the number of modes N for the Cauchy-WABC problem for the XY-slice and $h = 1/3$.

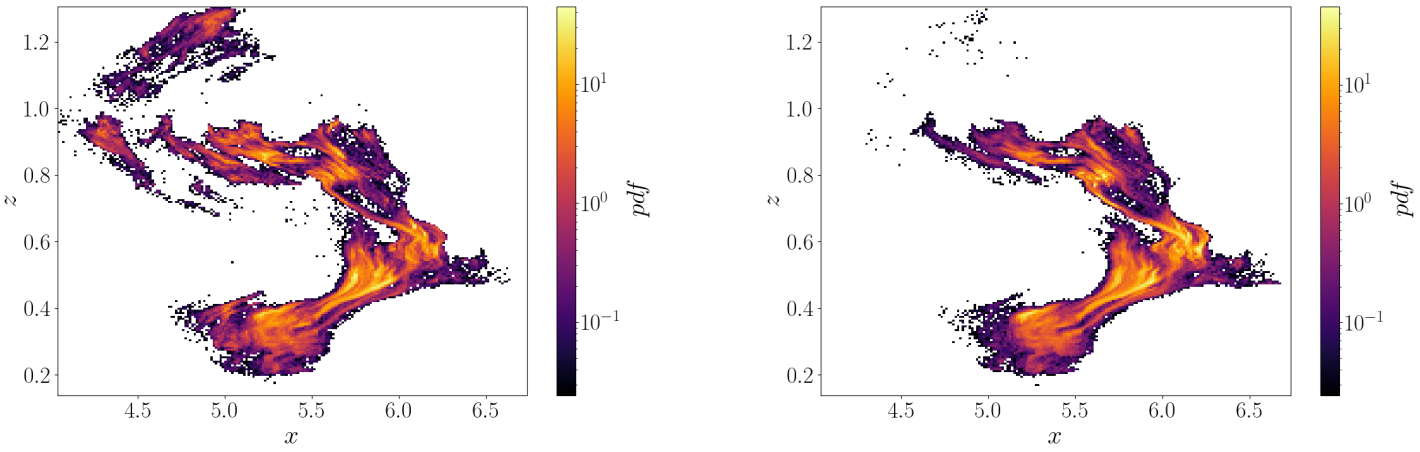

(a) $N = 10$ (b) $N = 12$

(c) $N = 14$ (d) $N = 16$

Figure G.3: Evolution of two point statistics through the number of modes N for the Cauchy-WABC problem for the XZ-slice and $h = 1/3$.

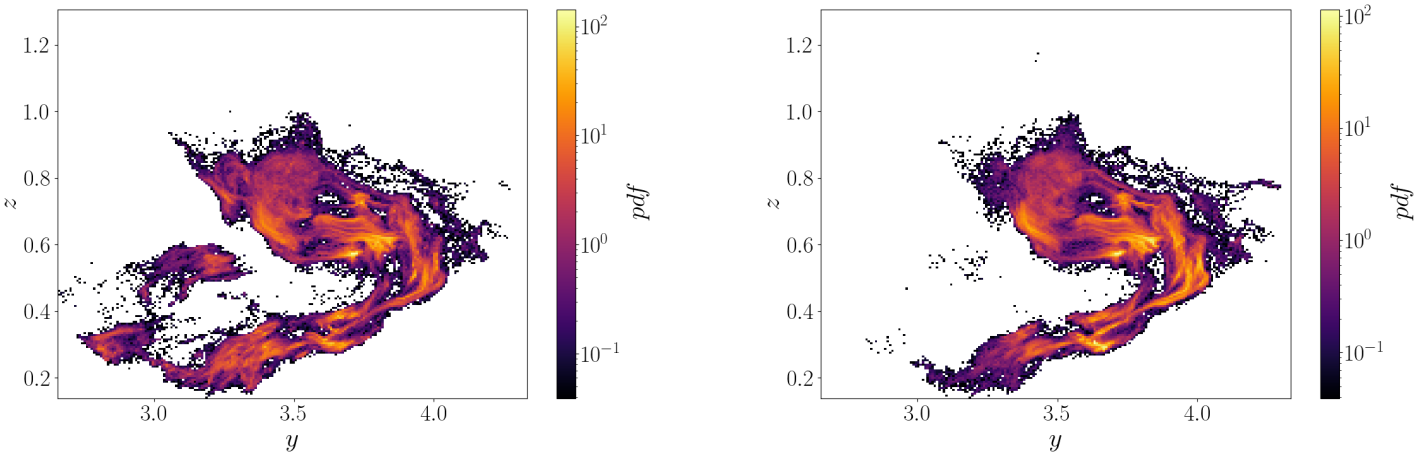

(a) $N = 10$ (b) $N = 12$

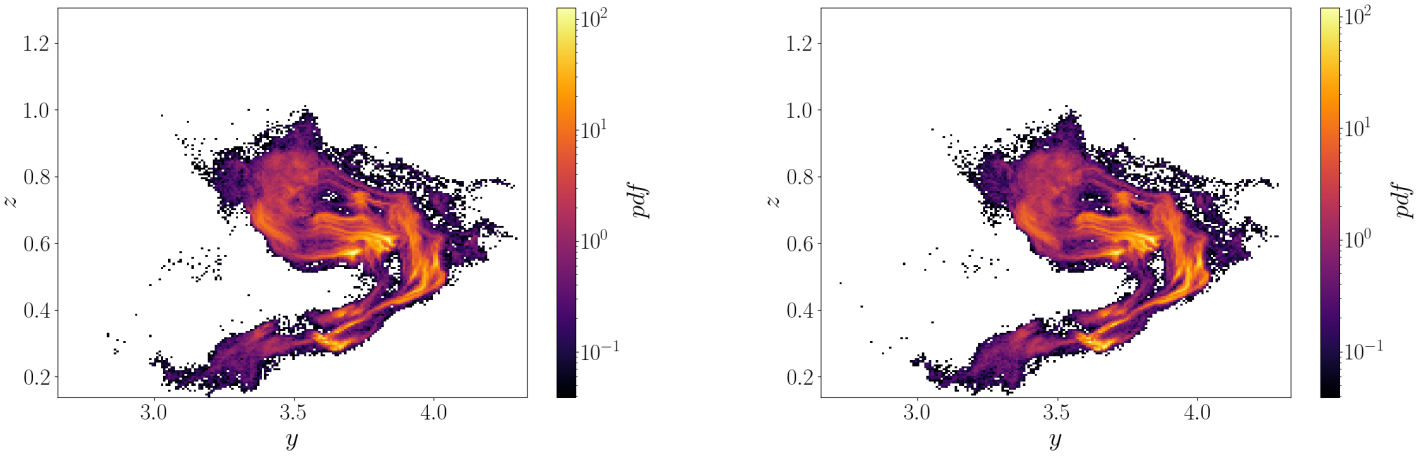

(c) $N = 14$ (d) $N = 16$

Figure G.4: Evolution of two point statistics through the number of modes N for the Cauchy-WABC problem for the YZ-slice and $h = 1/3$.

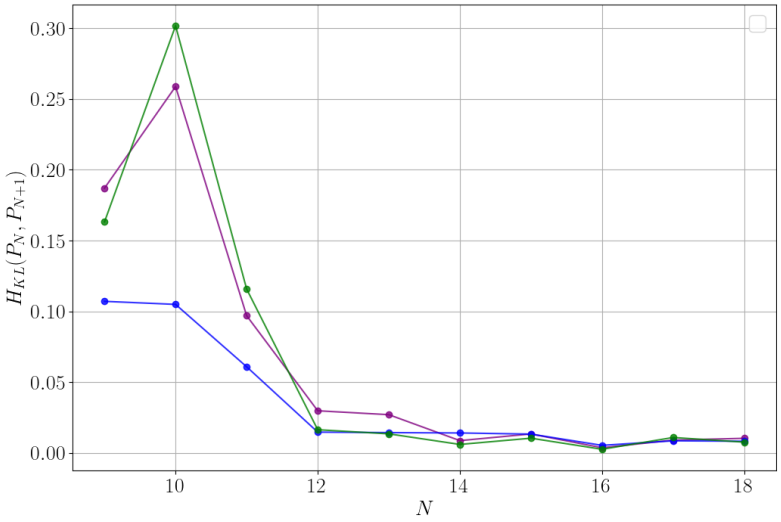

Figure G.5: Evolution of Kullback-Leibler between one-point statistics of increasing number of modes N as a function of N for Cauchy-WABC with $h = 1/3$ for the x-axis (purple), the y-axis (blue) and the z-axis (green).

H - WABC flow's noise scaling

H.1 . A non-trivial scaling

H.1.1 . A wrong scaling

Introduction – In equation (5.1), the noise term κ_N needs to decrease as N goes to infinity. Spontaneous stochasticity might not show up however if this scaling decreases too fast or too slowly compared to the cut-off. The choice for this scaling is however not obvious due to the non-linear effects in the WABC model. To illustrate this point, we derive a scaling law for κ_N based on dimensional analysis. We want the noise to scale accordingly with the smallest scale in the WABC flow. At this scale, the velocity felt is of the order $\frac{\omega_N}{k_N}$. We recall that the smallest displacement in this model was chosen to be $dx_N = k_N^{-1}$. As such, since $\boldsymbol{dW} \sim \sqrt{dt_N}$, this means that we should have

$$\kappa_N \sim \frac{\omega_N^2}{k_N^2} dt_N = \frac{\omega_N^2}{k_N^3}. \tag{H.1}$$

Results – We recall that for the WABC flow, we introduced two types of regularisations called respectively: Cauchy-WABC (uncertainty on initial position) and Langevin-WABC (stochastic process). We should expect the two regularisations to give the same results (i.e. the same probability distributions) in the limit of vanishing regularisation.

Since the Cauchy-WABC converges for $N \geq 12$, we expect the Langevin-WABC to be converged at approximately the same number of modes. We show in Figure H.3 (Left pictures) a comparison between Cauchy-WABC and Langevin-WABC's $1d$ probability distributions (for $N = 16$) with the noise scaling given in equation (H.1). We observe that the curves are mostly different between the two regularisations. In addition, we tend to observe the the probability distributions for the Langevin-WABC do not converge as N increases. We show indeed the evolution of the convergence of the Kullback-Leibler divergence $H_{KL}(p_{N+1}, p_N)$ in Figure H.1. We observe that after a reaching a plateau, this criterion rises again, symbol of non-convergence.

H.1.2 . Methodology

From the above observations, we want to find a good scaling κ_N for the Langevin-WABC problem. We introduce a general noise scaling:

$$\epsilon_N = b^2 \frac{\omega_N^2}{k_N^{p(h)}}. \tag{H.2}$$

Our goal is to determine the function $p(h)$. We here focus on $h = 1/3$. We will use the Kullback-Leibler divergence H_{KL} in order to compare the $1d$ probability distributions from: Cauchy p^C and Langevin p^L. We recall that the lowest $H_{KL}(p^C, p^L)$, the closest the two distributions are. As such, we should find the correct $p(1/3)$ when we find $H_{KL}(p^C, p^L) \approx 0$ (up to numerical errors).

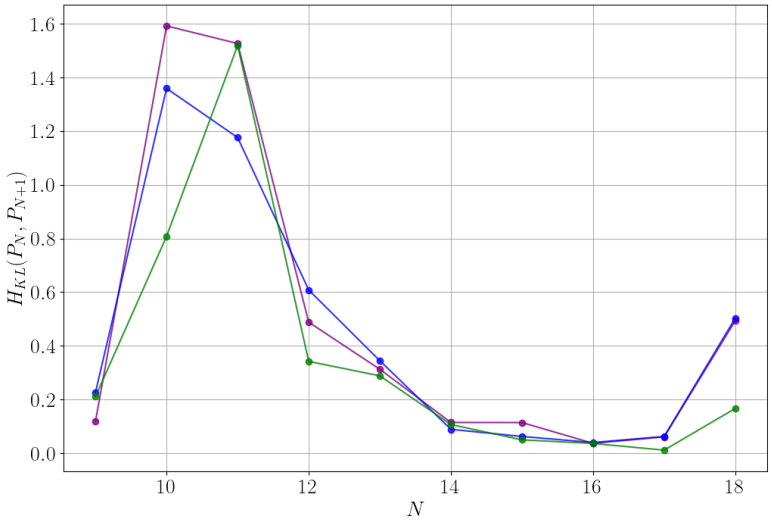

Figure H.1: Evolution of the Kullback-Leibler divergence between one point statistics of increasing number of modes N as a function of N for Langevin-WABC with $h = 1/3$ in the case of a noise scaling given by equation (H.1). The three axes are represented by different colours: purple for the x-axis, blue for the y-axis and green for the z-axis.

H.2 . Results

We perform different simulations for $p \in [2, 3]$ and evaluate the one-point probability distributions at time $t = 0.875$. The numerical methods for the integration are given in Chapter 7. Results are summarised in Figure H.2.

We notice that, within the error induced by the convergence of statistics (and numerical scheme), the curves are not flat and present some minima for all axes. The initial value $p = 3$, guessed from dimensional analysis, appears to be far from the minimum. A simple second order polynomial fit gives us a minimum value for each coordinate, all situated at $p \simeq 2.4$. The non-linearity and intrinsic chaos of such model could explain why dimensional analysis fails here, leading to non-trivial noise scalings.

H.2.1 . Discussions

In the above observations, we implicitly assumed that only one scaling should make the model converge. This assumption is based on the results obtained for the other models of spontaneous stochasticity. There is no obvious reason so far that this would always be the case however. We could for instance have a range of possible good scalings that ensures convergence of the model. We can mention for instance the work of Eyink and Bandak [36]. In their analysis of a simple model, using the renormalisation group they were able to derive a phase diagram showing the interconnection between the regularisation and the noise part. If the noise grows too fast compared to the regularisation, the dynamics

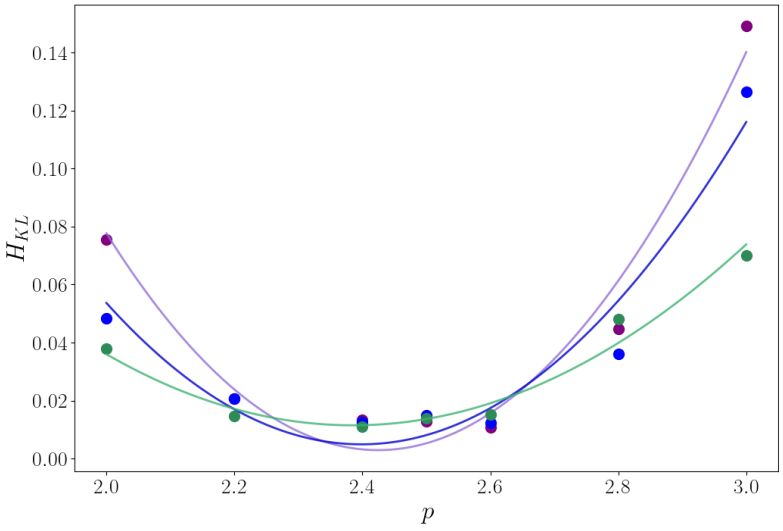

Figure H.2: Kullback-Leibler divergence between Langevin and Cauchy one-point statistics' (at time $t = 0.875$) for different exponents p in the case of $N = 16$ and $h = 1/3$. Axes are displayed by different colours: x-axis is purple, y-axis is blue and z-axis is green.

becomes essentially flooded by the noisy fluctuations. On the contrary, if the regularisation wins, the convergence towards a spontaneously stochastic phase ask for a very low regularisation. This scenario is not convenient as we could reach technical limits for the numerical simulations: large computation times, saturation of memory... Consequently, the above optimisation procedure could be used to determine a good scaling to quicker reach convergence.

We also note, that so far, there is no obvious reason that $p(h) = p(1/3)$. This would need to be further investigated. It could also depend on the A, B and C coefficients that control the appearance of chaos in the WABC model.

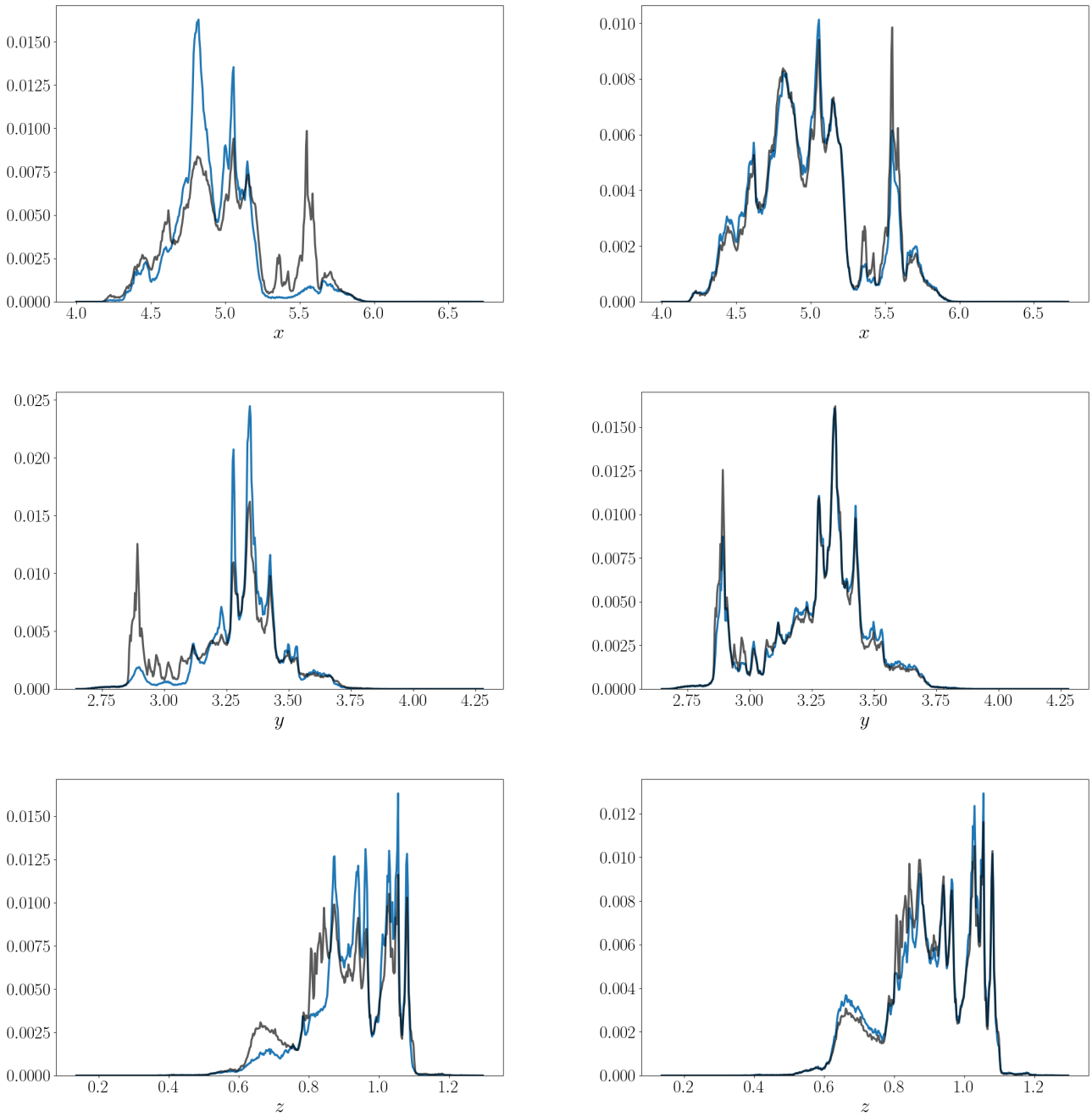

Figure H.3: Comparison of one point statistics between Cauchy-WABC (black) and Langevin-WABC (blue) for $p = 3$ (Left) and $p = 2.4$ (Right), with $h = 1/3$ and $N = 16$. The different axes x, y and z are displayed from top to bottom.

I - Outlier detection for experimental data

I.1 . Experimental issues

We introduced in Chapter 8 the STB algorithm that is able to reconstruct the Lagrangian trajectories from camera images. The reconstructed particles can be outliers, which we need to identify. In this Appendix, we introduce a methodology to determine and filter out a subtype of outliers: the reconstructed particles that have abnormal displacements norms. Those are indeed responsible for the FlowHisto method (introduced in Chapter 6) to fail: the maximum displacement among particles is too large and do not represent the real data. As a consequence, the coarse-graining becomes too rough for the real data, which leads to really low-defined Eulerian grids.

To identify those outliers, we first compute the norm of displacements and build its global probability distribution. Using a specific threshold, we are able to filter out all of the problematic outliers. This technique however filters out too many particles that we consider to be meaningful. We thus introduce, in a second part, a refined method, that is called 'Local outlier factor' (LOF), which gives a score to the particles according to how different they are from the others.

I.2 . Norm histogram

We define the particles' displacements as a $3d$ vector $\delta\boldsymbol{x} = (\delta x, \delta y, \delta z)$. We consider its norm, that we note $\delta R = ||\delta\boldsymbol{x}||_2$. As exemplified in Figure I.1, we build the probability distribution $p(\delta R)$. The extreme values outliers are visible on the right side. We observe in fact some noise next to the large decrease of probability, which corresponds to the outliers' noise. We therefore impose a threshold δR_{th} (represented by the red dashed lines on the plots), where particles having $\delta R > \delta R_{th}$ are filtered out. This also gives what we call 'the contamination factor' c_f. It corresponds to the chance of picking an outlier when randomly choosing a particle.

I.3 . Local outlier factor

As presented in Figure I.1, the norm histogram method is not sufficient as it can filter out too many particles that we consider to be real. Instead, we refine our outlier detection using the 'Local outlier factor' (LOF) algorithm. This method was first introduced by Breunig et al. in 2000 [11]. For each particle, we evaluate its number of neighbours and how far they are in the space of $\delta\boldsymbol{x}$. A score is then attributed to those particles: an isolated particle in this space gets a poor score compare to a particle surrounded by very close neighbours.

Therefore, a particle that has an extreme δR will necessarily be isolated from the other particles in the space of $\delta\boldsymbol{x}$. As such, its score given by the LOF algorithm will be low.

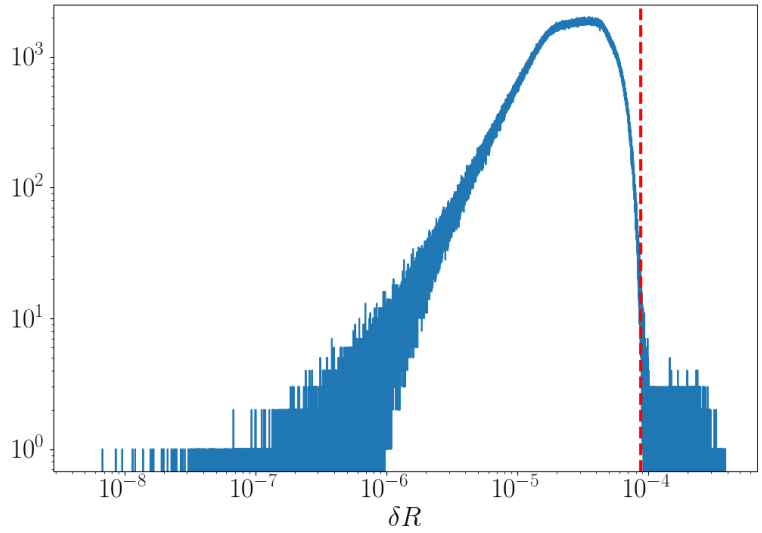

Figure I.1: Distribution of δR for a run of the GVK experiment. The noise on the right side of the histogram corresponds to the norm outliers. We automatically set a threshold (represented by the red dashed line) left to the noise.

Comparing this score to the contamination factor allows one to discriminate the particles to keep from the others.

The method works quite well for our dataset as illustrated in Figure I.2. The blue dots correspond to the detected outliers, which are the particles that we expect to be filtered out.

I.4 . Conclusions

The presented method works in our case to filter out the outliers that might drive the FlowHisto algorithm to fail. We note that this does not eliminate all outliers. In particular, the wrong vectors that have a reasonable norm are still selected. This is not a problem in our case since those are smoothed by the statistical analysis afterward.

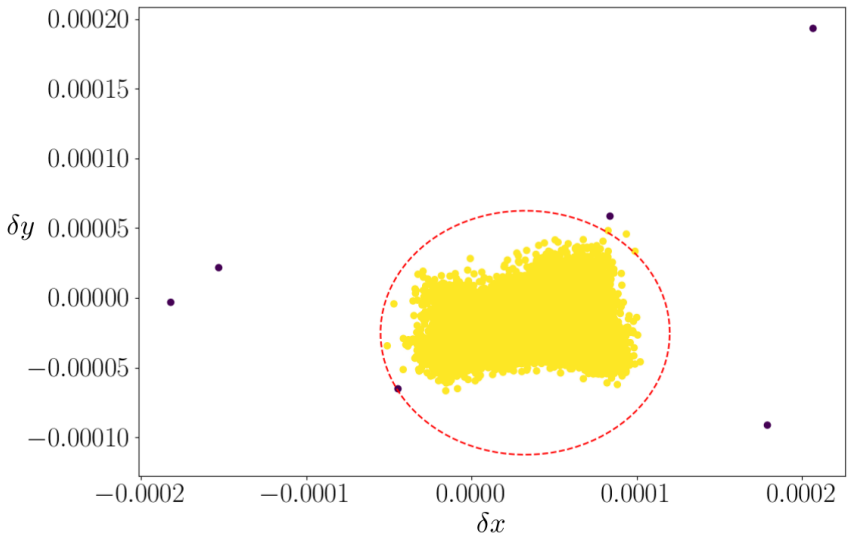

Figure I.2: Example of displacements of particles in the space of $\delta \boldsymbol{x}$. The red dashed circle corresponds to the threshold set in the distribution of δR. We notice that it filters out too many good particles (see right top corner). The blue particles are the ones identified as outliers par the LOF algorithm.

J - French summary

Depuis la découverte des systèmes chaotiques, physiciens et mathématiciens se sont succédés pour tenter d'enfin comprendre un mystère qui perdure : la turbulence. Dans cet état, les fluides présentent des structures aléatoires voire chaotiques. A ce titre, il ferait sens d'essayer de comprendre ces phénomènes au travers de nos connaissances sur les systèmes chaotiques, eux aussi semblant aléatoires dans les limites de temps longs. On observe que la turbulence échappe cependant toujours aux théories des systèmes dynamiques. Par exemple, on sait que deux solutions initialement distantes d'une amplitude ϵ vont se séparer dans l'espace des phases à un taux exponentiellement croissant dans le temps. On sait en outre que cette distance est directement proportionnelle à ϵ : les deux solutions deviennent identiques quand ϵ tend vers 0. Ce phénomène n'est pourtant pas observé en turbulence. A la place, on observe que les solutions se séparent en temps longs de manière linéaire indépendamment de la perturbation initiale ϵ donnée [79].

Cette observation fait écho à une remarque de Lorenz en 1969 [60, 67] sur le fait que certains systèmes (et particulièrement les fluides) atteindraient un plafond de verre de prédictibilité lorsque la perturbation initiale ϵ tend vers 0. Cet article met l'accent sur l'influence de la pluralité des échelles dans ces systèmes pour la construction de ces régimes paradoxaux. On sait depuis les travaux effectués dans le modèle de Kraichnan [45, 82, 39] qu'un tel phénomène est bien réel et s'apparente physiquement à une extrême amplification de bruits infinitésimaux due à la présence de singularités dans l'écoulement. Le nom de « Stochasticité Spontanée » a ainsi été donnée pour appeler ce type de comportements.

A l'heure actuelle, ces systèmes ne sont que partiellement compris. On sait qu'il est au moins nécessaire d'avoir des irrégularités, qu'elles soient régularisées localement et qu'un bruit infinitésimal soit rajouté pour obtenir un modèle présentant de tels comportements. Ainsi, dans ces systèmes, la dynamique apparaît toujours stochastique malgré que la régularisation et le bruit soient envoyés vers 0. Dans le cas lagrangien, la distribution des positions des particules semble devenir indépendante du bruit initial, à l'image des observations de Lorenz. Il apparaît cependant que ces ingrédients sont nécessaires mais pas suffisants : certains systèmes possédant ces caractéristiques ne sont pourtant pas spontanément stochastiques. On peut notamment questionner l'influence du chaos sur la construction d'un tel phénomène.

On notera enfin que la stochasticité spontanée est très difficile à observer expérimentalement. En effet, dans le cas Lagrangien, ce phénomène pourrait se manifester au travers de la célèbre loi de Richardson où les paires de particules semblent en moyenne se séparer selon une loi cubique en temps, indépendamment de la séparation initiale. Cette loi n'est pourtant pas, à ce jour, observée rigoureusement en turbulence expérimentale. Ceci est dû au fait que cette loi apparaît pour des temps trop longs par rapport au temps que les particules mettent pour sortir de la zone de mesure. Pourtant l'investigation de ces propriétés d'un point de vue expérimental est fondamental pour pouvoir confirmer ou in-

firmer les théories émergentes sur ce sujet. Il est donc important de considérer un critère spécifique de stochasticité spontanée qui pourrait être appliqué en expériences.

Dans cette thèse, nous nous intéressons à élaborer un tel critère à partir de probabilités de transition (issues des théories markoviennes). Pour vérifier son efficacité, nous introduisons un écoulement jouet, intitulé « modèle WABC », qui nous sert de terrain de jeu pour tester ces idées. Après avoir introduit ce modèle et ses propriétés dans une première partie, nous poursuivons en introduisant la définition de la stochasticité spontanée lagrangienne pour cet écoulement. En nous inspirant de cette définition, nous arrivons à élaborer notre critère, intitulé « déviation de transition ». C'est ce critère qui est testé dans le modèle WABC. Mais avant cela, nous vérifions en amont que ce modèle présente bien de la stochasticité spontanée lagrangienne. Pour ce faire, nous introduisons d'abord, dans une partie dédiée, tous les outils statistiques nécessaires pour le calcul du critère ainsi que la vérification quantitative (et pratique) de la convergence non-triviale des statistiques. Ces outils sont ensuite directement appliqués dans le cadre de la vérification de la stochasticité spontanée lagrangienne dans le modèle WABC, présenté dans une partie dédiée. Dans cette dernière, on introduit en détail la méthode d'intégration des équations stochastiques décrivant le mouvement des particules. On montre ainsi, au travers d'une analyse numérique que les statistiques convergent, où les trajectoires restent stochastiques même dans les limites de régularisation et de bruit nul. Une comparaison entre ce qui est observé dans le modèle WABC et les écoulements expérimentaux du comportement du critère de déviation de transition est enfin présentée.

Le modèle WABC u_W est un écoulement stationnaire correspondant à une somme infinie d'écoulements ABC [2] de plus en plus fins :

$$\boldsymbol{U}(\boldsymbol{x}) = \begin{cases} A\sin(z) + C\cos(y) \\ B\sin(x) + A\cos(z) \\ C\sin(y) + B\cos(x), \end{cases} \tag{J.1}$$

$$\boldsymbol{u}_W(\boldsymbol{x}) = \sum_{i=1}^{+\infty} \frac{\omega_i}{k_i}\, \boldsymbol{U}(k_i \boldsymbol{x}). \tag{J.2}$$

On montre que cet écoulement $3d$ est irrégulier partout et brise quelques symétries observées dans l'écoulement constituant. On observe en outre que, lorsque les coefficients A, B et C de l'écoulement ABC sont choisis de telle sorte à avoir du chaos lagrangien, l'écoulement WABC résultant voit également apparaître du chaos lagrangien. En toute généralité, il apparaît que les attracteurs sous-jacents semblent devenir de plus en plus nombreux (et plus petits) lorsque la somme d'écoulements ABC devient de plus en plus grande. Ceci est dû en partie à la présence d'une auto-similarité partielle de l'écoulement.

Pour ce modèle, on peut aussi définir une « dissipation anormale » non physique comme déjà observé par G. Eyink en 1994 [34]. Cette dissipation, différente de celle due à la viscosité, correspond conceptuellement dans les bonnes limites à l'anomalie de dissipation observée expérimentalement en turbulence. Le théorème de Duchon et Robert

permet de démontrer le lien entre les irrégularités et l'anomalie de dissipation [31]. Bien qu'ici cette définition n'ai pas de sens physique, elle permet de distinguer deux types de singularités : celles dissipatives (avec un coefficient de Hölder $h \leq 1/3$) et celles non-dissipative (avec un coefficient de Hölder $h > 1/3$). On montre que pour l'écoulement WABC avec $h = 1/3$, la dissipation symbolisée par le coefficient de Duchon et Robert converge vers une valeur finie pour une régularisation nulle.

Dans le cadre de la simulation de la stochasticité spontanée lagrangienne, on définit les équations régissant le mouvement des particules dans le champ WABC. Ces équations font intervenir un bruit qui peut être choisi de la manière que l'on souhaite : il est admis que les statistiques ne devraient pas dépendre du type de bruit qui est choisi dans les limites de régularisation nulle. Nous définissons donc le « Langevin-WABC » et le « Cauchy-WABC », deux types de simulations lagrangiennes pour ce modèle. On dit alors que l'on observera de la stochasticité spontanée lagrangienne dans cet écoulement si et seulement si, en considérant que toutes nos particules partent d'une même position initiale (ou boule initiale dans le cas de Cauchy-WABC), il existe un temps $t_S^{x_0}$ tel que les distributions des positions de particules à un temps $t > t_S^{x_0}$, notées $p_N^L(\boldsymbol{x}, t)$, convergent vers des distributions qui ne sont pas celles de Dirac dans la limite de régularisation et bruit nul :

$$\exists t_s^{x_0} > 0,\ \forall t > t_s^{x_0} \quad \lim_{N\to\infty} p_N^L(\boldsymbol{x}, t) = p^L(\boldsymbol{x}, t) \neq \delta(\boldsymbol{x} - \boldsymbol{m}(t)), \tag{J.3}$$

où

$$\boldsymbol{m}(t) = \mathbb{E}(\boldsymbol{x}) = \int_{\mathbb{R}^d} \boldsymbol{x}\, p^L(\boldsymbol{x}, t)\, d\boldsymbol{x}. \tag{J.4}$$

Pour construire notre critère de mesure de stochasticité spontanée en expérience, on adapte cette définition aux contraintes expérimentales : nous avons besoin d'un outil local en temps et en espace capable d'aller au-delà de la limitation de la non-répétabilité exacte (non pas au sens statistique) de l'expérience lorsque l'on change le nombre de Reynolds (représentant la régularisation en turbulence). On définit un écart-type des déplacements de particules pendant un temps τ. On dit alors qu'il y a des traces de stochasticité spontanée si et seulement si cet écart-type ne tend pas vers 0 dans la limite de régularisation et bruit nuls. Ceci indiquerait en effet que, dans ces limites, les probabilités de transition ne convergent pas de manière triviale vers la distribution de Dirac, d'écart-type strictement nul. On écarterait ainsi le scénario d'une dynamique déterministe dans le cas d'une viscosité nulle. Ce critère est par la suite légèrement raffiné de sorte à prendre en compte à la fois le caractère non-reproductible de l'expérience et l'échantillonnage spatial imposé par les techniques de mesures PIV/PTV. Ceci nous a poussé à conditionner les statistiques sur les événements extrêmes de dissipation liés à l'irrégularité du champ. Bien qu'il y ai des indices pointant dans cette direction, il n'existe pour le moment aucune preuve démontrant une relation entre stochasticité spontanée et anomalie de dissipation du champ de vitesse. Dans cette thèse, nous explorons cette hypothèse dans le modèle WABC en

même temps que l'efficacité de notre critère pour déceler des événements spontanément stochastiques.

On vérifie d'abord numériquement si le modèle WABC pour $h = 1/3$ montre des signes de stochasticité spontanée lagrangienne. Pour ce faire, on choisit une intégration stochastique dont on vérifie en amont sa précision (via l'évaluation de son ordre de convergence faible). Les distributions de probabilités sur lesquelles sont effectuées les analyses qualitatives et quantitatives sont calculées à partir des positions de particules pour un temps t donné. Des projections à un et deux points de ces distributions sont proposées de sorte à éviter toute malédiction de dimensionnalité. On montre ainsi que, dans les précisions numériques (statistique ou d'intégration) choisies, les probabilités de distributions semblent converger non-trivialement dans les limites de bruit et de régularisation nulles (voir Figure J.1). Nous vérifions ceci aussi de manière quantitative au travers de l'évaluation de la convergence des distributions de probabilités à un point. On montre ainsi numériquement que les trajectoires lagrangiennes sont toujours stochastiques même dans les limites de bruit nul. Ceci indique donc que le modèle WABC présente de la stochasticité spontanée lagrangienne pour les paramètres A, B et C choisis (ici présentant du chaos).

On remarque en outre que les deux schémas d'intégration, « Langevin-WABC » et « Cauchy-WABC » présentent les mêmes distributions de probabilités dans la limite de régularisation nulle. Ceci illustre donc les observations selon lesquelles le type de bruit/régularisation ne devrait pas avoir d'influence sur les statistiques.

On a enfin testé si un changement de coefficient de Hölder h ou de position initiale changeait la convergence des statistiques. Pour les valeurs testées ($h = 2/5$ par exemple), on observe peu de changements par rapport au cas testé avec $h = 1/3$. Ceci pointe donc dans la direction d'une universalité de cette stochasticité spontanée pour n'importe quel paramètre de simulation. Cette étude n'est cependant pas assez complète pour conclure pleinement sur le cadre de cette universalité dans ce modèle.

On note enfin, que nous ne testons pas dans cette thèse l'influence du chaos sur l'établissement (ou non) de la stochasticité spontanée lagrangienne. Ceci pourrait pourtant être raisonnablement testé en changeant les paramètres A, B et C qui permettent de contrôler la présence de chaos lagrangien ou non. Cette perspective serait intéressante à explorer puisque qu'il n'est pas encore certain que la stochasticité spontanée puisse exister sans qu'il y ai de chaos.

Nous testons enfin le critère développé précédemment, d'abord dans le modèle WABC et ensuite en expérience. L'expérience utilisée ici correspond au « Giant Von Kármán » qui est capable de créer un écoulement quasiment homogène et isotrope en son centre. Les techniques de PTV nous permettent de reconstruire en $3d$ les trajectoires de particules de polystyrène, traceurs de l'écoulement. On utilise en particulier des données produites par P. Debue et D. Geneste [23, 48].

Pour tester le lien entre la déviation de transition et la stochasticité spontanée, on compare trois scénarios : le cas $h = 1/3$ dissipatif et spontanément stochastique, le cas $h = 2/5$ non-dissipatif et spontanément stochastique et le cas $h = 1$ non-dissipatif et

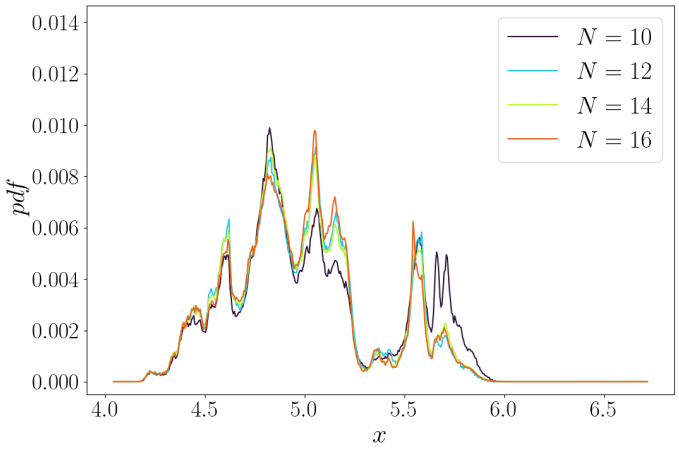

Figure J.1: Évolution des distributions de probabilité à un point selon l'axe x selon le nombre de modes N, pour des simulations de Langevin-WABC avec $h = 1/3$. On note que les distributions semblent converger vers une unique courbe pour N suffisamment grand, signe de stochasticité spontanée.

non spontanément stochastique. Dans chacun des cas, on augmente progressivement le nombre de modes et on conditionne les statistiques sur les événements de fortes dissipations (toujours selon Duchon et Robert). Dans cette étude préliminaire, on observe que dans les cas où la stochasticité spontanée devrait apparaître, notre critère semble rester identique peu importe le nombre de modes. Cependant pour le cas $h = 1$, notre critère semble changer avec le nombre de modes, se décorrélant totalement des événements de fortes dissipation. Cette observation met en évidence le lien fort entre notre critère et la présence de stochasticité spontanée lagrangienne.

On observe dans les expériences analysées dans cette thèse que le critère calculé semble être insensible à des nombres de Reynolds suffisamment grands. Ceci semble être le cas quand on considère des échelles inertielles. Mais des échelles considérées plus proches de la zone dissipative semblent mieux fonctionner. Tout indique un scénario similaire à ce qui a été observé dans le cas $h = 1/3$ pour le modèle WABC. Cette étude préliminaire pointe donc dans la direction d'une toute première observation de stochasticité spontanée lagrangienne en expérience (voir Figure J.2). On note cependant que le manque de données expérimentales ne nous permet pas de conclure parfaitement.

En résumé, ce travail a permis la réalisation d'un écoulement $3d$ développant de la stochasticité spontanée lagrangienne. Cet écoulement est facilement réalisable et permettrait d'étudier en détail l'influence du chaos sur l'établissement d'un tel phénomène. En outre, sa simplicité permet de tester des idées simples pour l'analyse de la stochasticité spontanée. En particulier, nous avons pu développer un critère de mesure pour la turbulence expérimentale. Nous avons pu vérifier de manière qualitative que ce critère fonctionne. Il nous a permis d'identifier dans une étude préliminaire des similarités entre

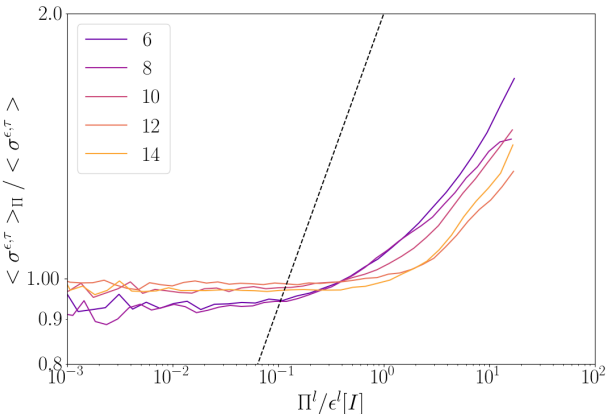

(a) WABC, $h = \frac{1}{3}$

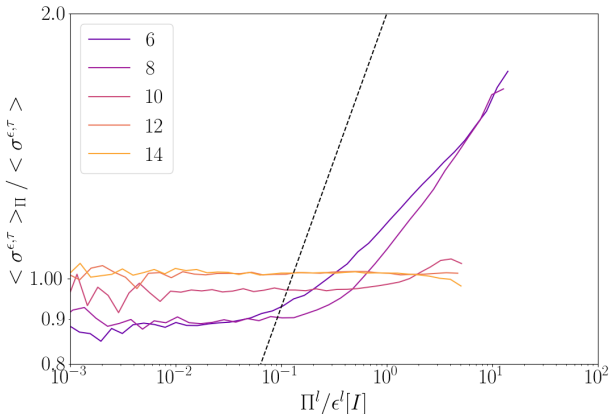

(b) WABC, $h = \frac{1}{3}$

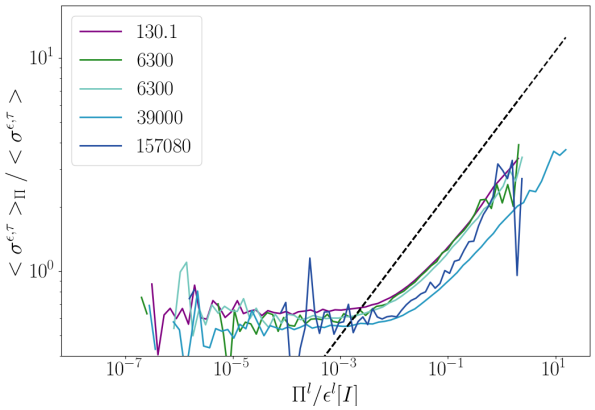

(c) Expérience GVK, $\langle h \rangle = 1/3$

Figure J.2: Le critère de déviation de transition $\left\langle \sigma^{\epsilon,\tau^o} \right\rangle_\Pi$ comme fonction de la dissipation due aux irrégularités Π^l pour : le modèle WABC avec $h = 1/3$ (gauche) et $h = 1$ (droite) et l'expérience (bas). Ces courbes sont représentées pour une régularisation de plus en plus faible, c'est à dire pour N croissant pour le modèle WABC et Re croissant pour l'expérience.

les observations expérimentales et le comportement spontanément stochastique des particules advectées dans le modèle WABC. Une étude plus approfondie permettrait d'affirmer ou infirmer les premières observations allant dans ce sens.

Bibliography

[1] M. Abel et al. “Exit-times and epsilon-entropy for dynamical systems, stochastic processes, and turbulence”. In: *Physica D: Nonlinear Phenomena* 147.1 (Dec. 2000), pp. 12–35. ISSN: 01672789.

[2] Vladimir Arnold. “Sur une proprietes topologique des applications globalment canonique de la mechanique classique”. In: *CR. Acad. Sci. Paris* 261 (1965), pp. 3719–3722.

[3] Stefano Attanasio and Franco Flandoli. “Zero-noise solutions of linear transport equations without uniqueness: an example”. In: *Comptes Rendus. Mathématique* 347.13 (2009), pp. 753–756. ISSN: 1778-3569.

[4] Dmytro Bandak et al. “Thermal noise competes with turbulent fluctuations below millimeter scales”. In: July 7, 2021.

[5] Denis Bernard, Krzysztof Gawedzki, and Antti Kupiainen. “Slow Modes in Passive Advection”. In: *Journal of Statistical Physics* 90.3 (Feb. 1, 1998), pp. 519–569. ISSN: 1572-9613.

[6] Rehab Bitane, Holger Homann, and Jérémie Bec. “Time scales of turbulent relative dispersion”. In: *Physical Review E* 86.4 (Oct. 31, 2012), p. 045302. ISSN: 1539-3755, 1550-2376.

[7] G Boffetta. “Predictability: a way to characterize complexity”. In: *Physics Reports* 356.6 (Jan. 2002), pp. 367–474. ISSN: 03701573.

[8] J. P. Bonnet and T. Alziary De Roquefort. “Determination and optimization of frequency response of constant temperature hot-wire anemometers in supersonic flows”. In: *Review of Scientific Instruments* 51.2 (Feb. 1, 1980), pp. 234–239. ISSN: 0034-6748, 1089-7623.

[9] M. Bourgoin et al. “Investigation of the small-scale statistics of turbulence in the Modane S1MA wind tunnel”. In: *CEAS Aeronautical Journal* 9.2 (June 1, 2018), pp. 269–281. ISSN: 1869-5590.

[10] Mickaël Bourgoin. “Turbulent pair dispersion as a ballistic cascade phenomenology”. In: *Journal of Fluid Mechanics* 772 (June 10, 2015), pp. 678–704. ISSN: 0022-1120, 1469-7645.

[11] Markus M. Breunig et al. “LOF: identifying density-based local outliers”. In: *SIGMOD Rec.* 29.2 (May 16, 2000), pp. 93–104. ISSN: 0163-5808.

[12] Ciro S Campolina and Alexei A Mailybaev. “Fluid dynamics on logarithmic lattices”. In: *Nonlinearity* 34.7 (July 1, 2021), pp. 4684–4715. ISSN: 0951-7715, 1361-6544.

[13] Bernard Castaing, Yves Gagne, and Muriel Marchand. “Log-similarity for turbulent flows?” In: *Physica D: Nonlinear Phenomena* 68.3 (Oct. 1993), pp. 387–400. ISSN: 01672789.

[14] Tarek Chaabo. “Optimisation d’une métrologie 4D-PTV pour la caractérisation d’un écoulement turbulent à très petites échelles”. These de doctorat. Centrale Lille Institut, Dec. 6, 2022.

[15] Marta Chaves et al. “Lagrangian Dispersion in Gaussian Self-Similar Velocity Ensembles”. In: *Journal of Statistical Physics* 113.5 (Dec. 1, 2003), pp. 643–692. ISSN: 1572-9613.

[16] Adam Cheminet et al. “Eulerian vs Lagrangian Irreversibility in an Experimental Turbulent Swirling Flow”. In: *Physical Review Letters* 129.12 (Sept. 14, 2022), p. 124501. ISSN: 0031-9007, 1079-7114.

[17] Jiajie Chen and Thomas Y. Hou. “Finite Time Blowup of 2D Boussinesq and 3D Euler Equations with $$C^{1,\alpha }$$Velocity and Boundary”. In: *Communications in Mathematical Physics* 383.3 (May 1, 2021), pp. 1559–1667. ISSN: 1432-0916.

[18] Aviad Cohen and Itamar Procaccia. “Computing the Kolmogorov entropy from time signals of dissipative and conservative dynamical systems”. In: *Physical Review A* 31.3 (Mar. 1, 1985), pp. 1872–1882. ISSN: 0556-2791.

[19] Peter Constantin, Boris Levant, and Edriss S. Titi. “Analytic study of shell models of turbulence”. In: *Physica D: Nonlinear Phenomena* 219.2 (July 2006), pp. 120–141. ISSN: 01672789.

[20] Peter Constantin, Boris Levant, and Edriss S. Titi. “Regularity of inviscid shell models of turbulence”. In: *Physical Review E* 75.1 (Jan. 16, 2007), p. 016304. ISSN: 1539-3755, 1550-2376.

[21] Thomas M. Cover and Joy A. Thomas. *Elements of Information Theory*. 1st ed. Wiley, Sept. 16, 2005. ISBN: 978-0-471-24195-9 978-0-471-74882-3.

[22] P. Debue et al. “Dissipation, intermittency, and singularities in incompressible turbulent flows”. In: *Physical Review E* 97.5 (May 3, 2018), p. 053101. ISSN: 2470-0045, 2470-0053.

[23] Paul Debue. “Experimental approach to the problem of the Navier-Stokes singularities”. These de doctorat. Université Paris-Saclay (ComUE), Sept. 25, 2019.

[24] T. Dombre et al. “Chaotic streamlines in the ABC flows”. In: *Journal of Fluid Mechanics* 167.-1 (June 1986), p. 353. ISSN: 0022-1120, 1469-7645.

[25] Theodore D. Drivas. “Turbulent Cascade Direction and Lagrangian Time-Asymmetry”. In: *Journal of Nonlinear Science* 29.1 (Feb. 1, 2019), pp. 65–88. ISSN: 1432-1467.

[26] Theodore D. Drivas and Gregory L. Eyink. “A Lagrangian fluctuation–dissipation relation for scalar turbulence. Part I. Flows with no bounding walls”. In: *Journal of Fluid Mechanics* 829 (Oct. 2017), pp. 153–189. ISSN: 0022-1120, 1469-7645.

[27] Theodore D. Drivas and Gregory L. Eyink. “A Lagrangian fluctuation–dissipation relation for scalar turbulence. Part II. Wall-bounded flows”. In: *Journal of Fluid Mechanics* 829 (Oct. 2017), pp. 236–279. ISSN: 0022-1120, 1469-7645.

[28] Theodore D. Drivas and Gregory L. Eyink. “An Onsager singularity theorem for Leray solutions of incompressible Navier–Stokes”. In: *Nonlinearity* 32.11 (Oct. 2019). Publisher: IOP Publishing, p. 4465. ISSN: 0951-7715.

[29] Theodore D. Drivas, Alexei A. Mailybaev, and Artem Raibekas. “Statistical determinism in non-Lipschitz dynamical systems”. In: *Ergodic Theory and Dynamical Systems* 44.7 (July 2024), pp. 1856–1884. ISSN: 0143-3857, 1469-4417.

[30] Bérengère Dubrulle. “Beyond Kolmogorov cascades”. In: *Journal of Fluid Mechanics* 867 (May 25, 2019), P1. ISSN: 0022-1120, 1469-7645.

[31] Jean Duchon and Raoul Robert. “Inertial energy dissipation for weak solutions of incompressible Euler and Navier-Stokes equations”. In: *Nonlinearity* 13.1 (Jan. 1, 2000), pp. 249–255. ISSN: 0951-7715, 1361-6544.

[32] J. -P. Eckmann and D. Ruelle. “Ergodic theory of chaos and strange attractors”. In: *Reviews of Modern Physics* 57.3 (July 1, 1985), pp. 617–656. ISSN: 0034-6861.

[33] Frank W. Elliott and Andrew J. Majda. “Pair dispersion over an inertial range spanning many decades”. In: *Physics of Fluids* 8.4 (Apr. 1, 1996), pp. 1052–1060. ISSN: 1070-6631, 1089-7666.

[34] Gregory L. Eyink. “Energy dissipation without viscosity in ideal hydrodynamics I. Fourier analysis and local energy transfer”. In: *Physica D: Nonlinear Phenomena* 78.3 (Nov. 15, 1994), pp. 222–240. ISSN: 0167-2789.

[35] Gregory L. Eyink. “Locality of turbulent cascades”. In: *Physica D: Nonlinear Phenomena* 207.1 (July 2005), pp. 91–116. ISSN: 01672789.

[36] Gregory L. Eyink and Dmytro Bandak. “Renormalization group approach to spontaneous stochasticity”. In: *Physical Review Research* 2.4 (Oct. 30, 2020). Publisher: American Physical Society, p. 043161.

[37] Gregory L. Eyink and Damien Benveniste. “Suppression of particle dispersion by sweeping effects in synthetic turbulence”. In: *Physical Review E* 87.2 (Feb. 19, 2013), p. 023011. ISSN: 1539-3755, 1550-2376.

[38] Gregory L. Eyink and Theodore D. Drivas. “Spontaneous Stochasticity and Anomalous Dissipation for Burgers Equation”. In: *Journal of Statistical Physics* 158.2 (Jan. 1, 2015), pp. 386–432. ISSN: 1572-9613.

[39] G. Falkovich, K. Gawedzki, and M. Vergassola. “Particles and fields in fluid turbulence”. In: *Reviews of Modern Physics* 73.4 (Nov. 19, 2001), pp. 913–975. ISSN: 0034-6861, 1539-0756.

[40] Franco Flandoli. *Topics on regularization by noise*. University of Pisa, 2013.

[41] J. M. Foucaut, J. Carlier, and M. Stanislas. “PIV optimization for the study of turbulent flow using spectral analysis”. In: *Measurement Science and Technology* 15.6 (May 2004), p. 1046. ISSN: 0957-0233.

[42] Uriel Frisch. *Turbulence: The Legacy of A.N. Kolmogorov*. 1st ed. Cambridge University Press, Nov. 30, 1995. ISBN: 978-0-521-45103-1 978-1-139-17066-6 978-0-521-45713-2.

[43] Crispin W. Gardiner. *Handbook of stochastic methods: for physics, chemistry and the natural sciences*. Study ed., 2. ed., 6. print. Springer series in synergetics 13. Berlin Heidelberg: Springer, 2002. 444 pp. ISBN: 978-3-540-61634-4 978-3-540-15607-9.

[44] Pierre Gaspard and Xiao-Jing Wang. “Noise, chaos, and (epsilon, tau)-entropy per unit time”. In: *Physics Reports* 235.6 (Dec. 1993), pp. 291–343. ISSN: 03701573.

[45] Krzysztof Gawedzki. *Easy turbulence*. Version Number: 2. 1999.

[46] Krzysztof Gawedzki. *Soluble models of turbulent advection*. Version Number: 1. 2002.

[47] I. M. Gelfand and A. M. Yaglom. “Amount of Information and Entropy for Continuous Distributions”. In: *Selected Works of A. N. Kolmogorov: Volume III: Information Theory and the Theory of Algorithms*. Ed. by A. N. Shiryayev. Dordrecht: Springer Netherlands, 1993, pp. 33–56. ISBN: 978-94-017-2973-4.

[48] Damien Geneste. “Des évènements extrêmes de dissipation aux évènements extrêmes de dispersion, une empreinte des singularités : Approche expérimentale”. These de doctorat. université Paris-Saclay, Feb. 2, 2023.

[49] S. Gesemann et al. “From Noisy Particle Tracks to Velocity, Acceleration and Pressure Fields using B-splines and Penalties”. In: 2016.

[50] Anastasiia Gorbunova et al. “Analysis of the dissipative range of the energy spectrum in grid turbulence and in direct numerical simulations”. In: *Physical Review Fluids* 5.4 (Apr. 29, 2020), p. 044604. ISSN: 2469-990X.

[51] Mihai Gradinaru, Samuel Herrmann, and Bernard Roynette. “A singular large deviations phenomenon”. In: *Annales de l’Institut Henri Poincare (B) Probability and Statistics* 37.5 (Sept. 1, 2001), pp. 555–580. ISSN: 0246-0203.

[52] Peter Grassberger. “Generalized dimensions of strange attractors”. In: *Physics Letters A* 97.6 (Sept. 1983), pp. 227–230. ISSN: 03759601.

[53] Michel Hénon. “Sur la topologie des lignes de courant dans un cas particulier”. In: *Sur la topologie des lignes de courant dans un cas particulier* 262 (1966), pp. 312–314.

[54] Thomas Y. Hou. “Potential Singularity of the 3D Euler Equations in the Interior Domain”. In: *Foundations of Computational Mathematics* 23.6 (Dec. 1, 2023), pp. 2203–2249. ISSN: 1615-3383.

[55] Edwin Thompson Jaynes. “Information theory in statistical mechanics”. In: *Lectures in theoretical physics*. Brandeis university summer institute. Brandeis university summer institute. 1962.

[56] A. Kolmogorov. “The Local Structure of Turbulence in Incompressible Viscous Fluid for Very Large Reynolds’ Numbers”. In: *Akademiia Nauk SSSR Doklady* 30 (1941), pp. 301–305. ISSN: 0002-3264.

[57] Denis Kuzzay. “Investigations on the relevance of Onsager’s conjecture in real incompressible turbulence”. These de doctorat. Université Paris-Saclay (ComUE), Oct. 5, 2016.

[58] François Ladieu. “La Physique : une science exacte où règne l’indétermination:” in: *Revue française de psychanalyse* Vol. 88.2 (Apr. 30, 2024), pp. 37–47. ISSN: 0035-2942.

[59] Jean Leray. “Sur le mouvement d’un liquide visqueux emplissant l’espace”. In: *Acta Mathematica* 63.1 (Dec. 1, 1934), pp. 193–248. ISSN: 1871-2509.

[60] Edward N. Lorenz. “The predictability of a flow which possesses many scales of motion”. In: *Tellus* 21.3 (June 1969), pp. 289–307. ISSN: 00402826, 21533490.

[61] Alexei A. Mailybaev. “Spontaneous Stochasticity of Velocity in Turbulence Models”. In: *Multiscale Modeling & Simulation* 14.1 (Jan. 2016), pp. 96–112. ISSN: 1540-3459, 1540-3467.

[62] Alexei A. Mailybaev and Artem Raibekas. “Spontaneously Stochastic Arnold’s Cat”. In: *Arnold Mathematical Journal* 9.3 (Sept. 1, 2023), pp. 339–357. ISSN: 2199-6806.

[63] Pankaj Mehta et al. “A high-bias, low-variance introduction to Machine Learning for physicists”. In: *Physics Reports* 810 (May 2019), pp. 1–124. ISSN: 03701573.

[64] Romain Monchaux. “Approche statistique des écoulements turbulents”. These de doctorat. Paris 7, Jan. 1, 2007.

[65] Peter J. Nolan, Mattia Serra, and Shane D. Ross. “Finite-time Lyapunov exponents in the instantaneous limit and material transport”. In: *Nonlinear Dynamics* 100.4 (June 1, 2020), pp. 3825–3852. ISSN: 1573-269X.

[66] L. Onsager. “Statistical hydrodynamics”. In: *Il Nuovo Cimento* 6 (S2 Mar. 1949), pp. 279–287. ISSN: 0029-6341, 1827-6121.

[67] T. N. Palmer, A. Döring, and G. Seregin. “The real butterfly effect”. In: *Nonlinearity* 27.9 (Aug. 2014). Publisher: IOP Publishing, R123. ISSN: 0951-7715.

[68] Quentin Pikeroen et al. *Tracking complex singularities of fluids on log-lattices*. Version Number: 1. 2023.

[69] Christopher Rackauckas, Qing Nie, and ,Department of Mathematics, Center for Complex Biological Systems, University of California, Irvine, CA 92697, USA. “Adaptive methods for stochastic differential equations via natural embeddings and rejection sampling with memory”. In: *Discrete & Continuous Dynamical Systems - B* 22.7 (2017), pp. 2731–2761. ISSN: 1553-524X.

[70] Florent Ravelet. “Bifurcations globales hydrodynamiques et magnétohydrodynamiques dans un écoulement de von Karman turbulent”. These de doctorat. Palaiseau, Ecole polytechnique, Jan. 1, 2005.

[71] Lewis F. Richardson. “Atmospheric diffusion shown on a distance-neighbour graph”. In: *Proceedings of the Royal Society of London. Series A, Containing Papers of a Mathematical and Physical Character* 110.756 (Apr. 1926), pp. 709–737. ISSN: 0950-1207, 2053-9150.

[72] David Ruelle. “Ergodic theory of differentiable dynamical systems”. In: *Publications Mathématiques de l’Institut des Hautes Études Scientifiques* 50.1 (Dec. 1, 1979), pp. 27–58. ISSN: 1618-1913.

[73] David Ruelle. “Strange attractors”. In: *The Mathematical Intelligencer* 2.3 (Sept. 1, 1980), pp. 126–137. ISSN: 0343-6993.

[74] Brice Saint-Michel. “L’écoulement de von Karman comme paradigme de la physique statistique hors équilibre”. These de doctorat. Paris 6, Jan. 1, 2013.

[75] Juan P.L.C. Salazar and Lance R. Collins. “Two-Particle Dispersion in Isotropic Turbulent Flows”. In: *Annual Review of Fluid Mechanics* 41.1 (Jan. 1, 2009), pp. 405–432. ISSN: 0066-4189, 1545-4479.

[76] E.-W. Saw et al. “Experimental characterization of extreme events of inertial dissipation in a turbulent swirling flow”. In: *Nature Communications* 7.1 (Aug. 31, 2016). Publisher: Nature Publishing Group, p. 12466. ISSN: 2041-1723.

[77] R. Scatamacchia, L. Biferale, and F. Toschi. “Extreme Events in the Dispersions of Two Neighboring Particles Under the Influence of Fluid Turbulence”. In: *Physical Review Letters* 109.14 (Oct. 5, 2012), p. 144501. ISSN: 0031-9007, 1079-7114.

[78] Jan F. G. Schneiders and Fulvio Scarano. “Dense velocity reconstruction from tomographic PTV with material derivatives”. In: *Experiments in Fluids* 57.9 (Aug. 16, 2016), p. 139. ISSN: 1432-1114.

[79] Simon Thalabard, Jérémie Bec, and Alexei A. Mailybaev. "From the butterfly effect to spontaneous stochasticity in singular shear flows". In: *Communications Physics* 3.1 (July 6, 2020), p. 122. ISSN: 2399-3650.

[80] Simon Thalabard, Giorgio Krstulovic, and Jérémie Bec. "Turbulent pair dispersion as a continuous-time random walk". In: *Journal of Fluid Mechanics* 755 (Sept. 25, 2014), R4. ISSN: 0022-1120, 1469-7645.

[81] D. J. Thomson and B. J. Devenish. "Particle pair separation in kinematic simulations". In: *Journal of Fluid Mechanics* 526 (Mar. 10, 2005), pp. 277–302. ISSN: 0022-1120, 1469-7645.

[82] Weinan E Vanden Eijnden and Eric Vanden Eijnden. "Generalized flows, intrinsic stochasticity, and turbulent transport". In: *Proceedings of the National Academy of Sciences* 97.15 (July 18, 2000), pp. 8200–8205. ISSN: 0027-8424, 1091-6490.

[83] Stephen Wiggins. *Introduction To Applied Nonlinear Dynamical Systems And Chaos*. Vol. 4. Journal Abbreviation: Computers in Physics Publication Title: Computers in Physics. Jan. 1, 2003. ISBN: 978-0-387-00177-7.

[84] Antoni Zygmund. *Trigonometric Series*. Google-Books-ID: W9AxAjSiIaUC. Cambridge University Press, 2002. 784 pp. ISBN: 978-0-521-89053-3.